EUROPEAN ORGANIZATION FOR NUCLEAR RESEARCH (CERN)

CERN-LHCC-2011-001
29 March 2011 (v2)

Letter of Intent for the LHCb Upgrade

The LHCb Collaboration[1]

Abstract

The primary goal of LHCb is to measure the effects of new particles or forces beyond the Standard Model. Results obtained from data collected in 2010 show that the detector is robust and functioning well. While LHCb will be able to measure a host of interesting channels in heavy flavour decays in the upcoming few years, a limit of about 1 fb^{-1} of data per year cannot be overcome without upgrading the detector. The LHC machine does not face such a limitation. With the upgraded detector, read out at 40 MHz, a much more flexible software-based triggering strategy will allow a large increase not only in data rate, as the detector would collect 5 fb^{-1} per year, but also the ability to increase trigger efficiencies especially in decays to hadronic final states. In addition, it will be possible to change triggers to explore different physics as LHC discoveries point us to the most interesting channels. Our physics scope extends beyond that of flavour. Possibilities for interesting discoveries exist over a whole variety of phenomena including searches for Majorana neutrinos, exotic Higgs decays and precision electroweak measurements. Here we describe the physics motivations and proposed detector changes for exploring new phenomena in proton-proton collisions near 14 TeV centre-of-mass energy.

---

[1] Authors are listed on the following pages.

The LHCb Collaboration

R. Aaij[23], C. Abellán Beteta[35,n], B. Adeva[36], M. Adinolfi[42], C. Adrover[6], A. Affolder[48], Z. Ajaltouni[5], J. Albrecht[37], F. Alessio[6,37], M. Alexander[47], P. Alvarez Cartelle[36], A.A. Alves Jr[22], S. Amato[2], Y. Amhis[38], J. Amoraal[23], J. Anderson[39], R.B. Appleby[50], O. Aquines Gutierrez[10], L. Arrabito[53], M. Artuso[52], E. Aslanides[6], G. Auriemma[22,m], S. Bachmann[11], D.S. Bailey[50], V. Balagura[30,37], W. Baldini[16], R.J. Barlow[50], C. Barschel[37], S. Barsuk[7], A. Bates[47], C. Bauer[10], Th. Bauer[23], A. Bay[38], I. Bediaga[1], C. Beigbeder-Beau[7], K. Belous[34], I. Belyaev[30,37], E. Ben-Haim[8], M. Benayoun[8], G. Bencivenni[18], R. Bernet[39], M.-O. Bettler[17,37], M. van Beuzekom[23], A. Bien[11], S. Bifani[12], A. Bizzeti[17,h], P.M. Bjørnstad[50], T. Blake[49], F. Blanc[38], C. Blanks[49], J. Blouw[11], S. Blusk[52], A. Bobrov[33], V. Bocci[22], B. Bochin[29], A. Bondar[33], N. Bondar[29], W. Bonivento[15], S. Borghi[47], A. Borgia[52], E. Bos[23], T.J.V. Bowcock[48], C. Bozzi[16], T. Brambach[9], J. van den Brand[24], J. Bressieux[38], D. Breton[7], M. Britsch[10], T. Britton[52], N.H. Brook[42], H. Brown[48], A. Büchler-Germann[39], A. Bursche[39], J. Buytaert[37], T. Caceres[7], J.-P. Cachemiche[6], S. Cadeddu[15], J.M. Caicedo Carvajal[37], O. Callot[7], M. Calvi[20,j], M. Calvo Gomez[35,n], A. Camboni[35], P. Campana[18], M. Campbell[37], A. Carbone[14], G. Carboni[21,k], R. Cardinale[19,i], A. Cardini[15], L. Carson[36], K. Carvalho Akiba[23], G. Casse[48], L. Castillo Garcia[37], M. Cattaneo[37], M. Charles[51], D. Charlet[7], Ph. Charpentier[37], N. Chiapolini[39], X. Cid Vidal[36], P.J. Clark[46], P.E.L. Clarke[46], M. Clemencic[37], H.V. Cliff[43], J. Closier[37], C. Coca[28], V. Coco[23], J. Cogan[6], P. Collins[37], F. Constantin[28], G. Conti[38], A. Contu[51], M. Coombes[42], G. Corti[37], G.A. Cowan[38], R. Currie[46], B. D'Almagne[7], C. D'Ambrosio[37], W. Da Silva[8], P. David[8], I. De Bonis[4], S. De Capua[21,k], M. De Cian[39], F. De Lorenzi[12], J.M. De Miranda[1], L. De Paula[2], P. De Simone[18], D. Decamp[4], M. Deckenhoff[9], H. Degaudenzi[38,37], M. Deissenroth[11], L. Del Buono[8], C. Deplano[15], O. Deschamps[5], F. Dettori[15,d], J. Dickens[43], H. Dijkstra[37], M. Dima[28], P. Diniz Batista[1], S. Donleavy[48], D. Dossett[44], A. Dovbnya[40], O. Duarte[7], R. Dumps[37], F. Dupertuis[38], P.-Y. Duval[6], R. Dzhelyadin[34], C. Eames[49], S. Easo[45], U. Egede[49], V. Egorychev[30], S. Eidelman[33], D. van Eijk[23], F. Eisele[11], S. Eisenhardt[46], R. Ekelhof[9], L. Eklund[47], Ch. Elsasser[39], D.G. d'Enterria[35,o], D. Esperante Pereira[36], L. Estève[43], A. Falabella[16,e], E. Fanchini[20,j], C. Färber[11], G. Fardell[46], C. Farinelli[23], S. Farry[12], V. Fave[38], V. Fernandez Albor[36], M. Ferro-Luzzi[37], S. Filippov[32], C. Fitzpatrick[46], F. Fontanelli[19,i], J. Fopma[51], R. Forty[37], M. Frank[37], C. Frei[37], M. Frosini[17,f,37], S. Furcas[20], A. Gallas Torreira[36], D. Galli[14,c], M. Gandelman[2], P. Gandini[51], R. Gao[51], Y. Gao[3], J-C. Garnier[37], J. Garofoli[52], L. Garrido[35], D. Gascón Fora[35], C. Gaspar[37], N. Gauvin[38], M. Gersabeck[37], T. Gershon[44], Ph. Ghez[4], A. Giachero[20], V. Gibson[43], V.V. Gligorov[37], C. Göbel[54], V. Golovtsov[29], D. Golubkov[30], A. Golutvin[49,30,37], A. Gomes[2], H. Gordon[51], C. Gotti[20], M. Grabalosa Gándara[35], R. Graciani Diaz[35], L.A. Granado Cardoso[37], E. Graugés[35], G. Graziani[17], A. Grecu[28], S. Gregson[43], B. Gui[52], E. Gushchin[32], Yu. Guz[34], Z. Guzik[27], T. Gys[37], F. Hachon[6], G. Haefeli[38], S.C. Haines[43], T. Hampson[42], S. Hansmann-Menzemer[11], R. Harji[49], N. Harnew[51], P.F. Harrison[44], J. He[7], V. Heijne[23], K. Hennessy[48], P. Henrard[5], J.A. Hernando Morata[36], E. van Herwijnen[37], A. Hicheur[38], E. Hicks[48], W. Hofmann[10], K. Holubyev[11], P. Hopchev[4], W. Hulsbergen[23], P. Hunt[51], T. Huse[48], R.S. Huston[12], D. Hutchcroft[48], D. Hynds[47], V. Iakovenko[7,41], P. Ilten[12], J. Imong[42], R. Jacobsson[37], M. Jahjah Hussein[5], E. Jans[23], F. Jansen[23], P. Jaton[38], B. Jean-Marie[7], J. Jeglot[7], F. Jing[3], M. John[51], D. Johnson[51], C.R. Jones[43], B. Jost[37], F. Kapusta[8], M. Karacson[37], T.M. Karbach[9], J. Keaveney[12], U. Kerzel[37], T. Ketel[24], A. Keune[38], B. Khanji[6], Y.M. Kim[46], M. Knecht[38], S. Koblitz[37], A. Konoplyannikov[30], P. Koppenburg[23], A. Kozlinskiy[23], L. Kravchuk[32], M. Kreps[44], G. Krocker[11], P. Krokovny[11], F. Kruse[9], K. Kruzelecki[37], M. Kucharczyk[25], S. Kukulak[25], R. Kumar[14,37], T. Kvaratskheliya[30,37], V.N. La Thi[38], D. Lacarrere[37], G. Lafferty[50], A. Lai[15], R.W. Lambert[37], G. Lanfranchi[18], C. Langenbruch[11], T. Latham[44], R. Le Gac[6], J. van Leerdam[23], J.-P. Lees[4], R. Lefèvre[5], A. Leflat[31,37], J. Lefrançois[7], O. Leroy[6], T. Lesiak[25], L. Li[3], Y.Y. Li[43], L. Li Gioi[5], M. Lieng[9], M. Liles[48], R. Lindner[37], C. Linn[11], B. Liu[3], G. Liu[37], X. Llopart Cudie[37], J.H. Lopes[2], E. Lopez Asamar[35], N. Lopez-March[38], J. Luisier[38], B. M'charek[24], F. Machefert[7], I.V. Machikhiliyan[4,30], F. Maciuc[10], O. Maev[29,37], J. Magnin[1], A. Maier[37], S. Malde[51], R.M.D. Mamunur[37], G. Manca[15,d,37], G. Mancinelli[6], N. Mangiafave[43], U. Marconi[14], R. Märki[38], J. Marks[11], G. Martellotti[22], A. Martens[7], L. Martin[51], A. Martín Sánchez[7], D. Martinez Santos[37],

A. Massafferri[1], Z. Mathe[12], C. Matteuzzi[20], M. Matveev[29], V. Matveev[34], E. Maurice[6],
B. Maynard[52], A. Mazurov[32,37], G. McGregor[50], R. McNulty[12], C. Mclean[46], M. Meissner[11],
M. Merk[23], J. Merkel[9], M. Merkin[31], R. Messi[21,k], S. Miglioranzi[37], D.A. Milanes[13,37],
M.-N. Minard[4], S. Monteil[5], D. Moran[12], P. Morawski[25], J.V. Morris[45], R. Mountain[52], I. Mous[23],
F. Muheim[46], K. Müller[39], R. Muresan[28,38], F. Murtas[18], B. Muryn[26], M. Musy[35],
J. Mylroie-Smith[48], P. Naik[42], T. Nakada[38], R. Nandakumar[45], J. Nardulli[45], A. Nawrot[27],
M. Nedos[9], M. Needham[46], N. Neufeld[37], M. Nicol[7], S. Nies[9], V. Niess[5], N. Nikitin[31],
A. Nomerotski[51], A. Oblakowska-Mucha[26], V. Obraztsov[34], S. Oggero[23], O. Okhrimenko[41],
R. Oldeman[15,d], M. Orlandea[28], A. Ostankov[34], B. Pal[52], J. Palacios[39], M. Palutan[18], J. Panman[37],
A. Papanestis[45], M. Pappagallo[13,b], C. Parkes[47,37], C.J. Parkinson[49], G. Passaleva[17], G.D. Patel[48],
M. Patel[49], S.K. Paterson[49,37], G.N. Patrick[45], C. Patrignani[19,i], C. Pavel -Nicorescu[28],
A. Pazos Alvarez[36], A. Pellegrino[23], G. Penso[22,l], M. Pepe Altarelli[37], S. Perazzini[14,c],
D.L. Perego[20,j], E. Perez Trigo[36], A. Pérez-Calero Yzquierdo[35], P. Perret[5], G. Pessina[20],
A. Petrolini[19,i], E. Picatoste Olloqui[35], B. Pie Valls[35], D. Piedigrossi[37], B. Pietrzyk[4], D. Pinci[22],
R. Plackett[47], S. Playfer[46], M. Plo Casasus[36], T. Poikela[37], G. Polok[25], A. Poluektov[44,33],
E. Polycarpo[2], D. Popov[10], B. Popovici[28], C. Potterat[35], A. Powell[51], T. du Pree[23], V. Pugatch[41],
A. Puig Navarro[35], W. Qian[3], J.H. Rademacker[42], B. Rakotomiaramanana[38], I. Raniuk[40],
G. Raven[24], S. Redford[51], W. Reece[49], A.C. dos Reis[1], F. Rethore[6], S. Ricciardi[45], K. Rinnert[48],
D.A. Roa Romero[5], P. Robbe[7], E. Rodrigues[47], F. Rodrigues[2], C. Rodriguez Cobo[36],
P. Rodriguez Perez[36], G.J. Rogers[43], V. Romanovsky[34], J. Rouvinet[38], L. Roy[37], T. Ruf[37],
H. Ruiz[35], G. Sabatino[21,k], J.J. Saborido Silva[36], N. Sagidova[29], P. Sail[47], B. Saitta[15,d],
C. Salzmann[39], A. Sambade Varela[37], M. Sannino[19,i], R. Santacesaria[22], R. Santinelli[37],
E. Santovetti[21,k], M. Sapunov[6], A. Sarti[18], C. Satriano[22,m], A. Satta[21], M. Savrie[16,e], D. Savrina[30],
P. Schaack[49], M. Schiller[11], S. Schleich[9], M. Schmelling[10], B. Schmidt[37], O. Schneider[38],
A. Schopper[37], M.-H. Schune[7], R. Schwemmer[37], A. Sciubba[18,l], M. Seco[36], A. Semennikov[30],
K. Senderowska[26], N. Serra[23], J. Serrano[6], B. Shao[3], M. Shapkin[34], I. Shapoval[40,37], P. Shatalov[30],
Y. Shcheglov[29], T. Shears[48], L. Shekhtman[33], O. Shevchenko[40], V. Shevchenko[30], A. Shires[49],
E. Simioni[24], H.P. Skottowe[43], T. Skwarnicki[52], A.C. Smith[37], K. Sobczak[5], F.J.P. Soler[47],
A. Solomin[42], P. Somogy[37], F. Soomro[49], B. Souza De Paula[2], B. Spaan[9], A. Sparkes[46],
E. Spiridenkov[29], P. Spradlin[47], F. Stagni[37], O. Steinkamp[39], O. Stenyakin[34], S. Stoica[28], S. Stone[52],
B. Storaci[23], U. Straumann[39], N. Styles[46], S. Swientek[9], M. Szczekowski[27], P. Szczypka[38],
T Szumlak[26], S. T'Jampens[4], V. Talanov[34], E. Teodorescu[28], F. Teubert[37], C. Thomas[51,45],
E. Thomas[37], J. van Tilburg[39], V. Tisserand[4], M. Tobin[39], S. Topp-Joergensen[51], M.T. Tran[38],
A. Tsaregorodtsev[6], N. Tuning[23], A. Ukleja[27], P. Urquijo[52], U. Uwer[11], V. Vagnoni[14], G. Valenti[14],
R. Vazquez Gomez[35], P. Vazquez Regueiro[36], S. Vecchi[16], J.J. Velthuis[42], M. Veltri[17,g], K. Vervink[37],
B. Viaud[7], I. Videau[7], X. Vilasis-Cardona[35,n], J. Visniakov[36], S. Volkov[29], A. Vollhardt[39],
D. Voong[42], A. Vorobyev[29], An. Vorobyev[29], H. Voss[10], K. Wacker[9], S. Wandernoth[11], J. Wang[52],
D.R. Ward[43], A.D. Webber[50], M. Whitehead[44], D. Wiedner[11], L. Wiggers[23], G. Wilkinson[51],
M.P. Williams[44,45], M. Williams[49], F.F. Wilson[45], J. Wishahi[9], M. Witek[25], W. Witzeling[37],
S.A. Wotton[43], K. Wyllie[37], Y. Xie[46], F. Xing[51], Z. Yang[3], G. Ybeles Smit[23], R. Young[46],
O. Yushchenko[34], M. Zavertyaev[10,a], L. Zhang[52], W.C. Zhang[12], Y. Zhang[3], A. Zhelezov[11],
L. Zhong[3], E. Zverev[31].

[1] *Centro Brasileiro de Pesquisas Físicas (CBPF), Rio de Janeiro, Brazil*
[2] *Universidade Federal do Rio de Janeiro (UFRJ), Rio de Janeiro, Brazil*
[3] *Center for High Energy Physics, Tsinghua University, Beijing, China*
[4] *LAPP, Université de Savoie, CNRS/IN2P3, Annecy-Le-Vieux, France*
[5] *Clermont Université, Université Blaise Pascal, CNRS/IN2P3, LPC, Clermont-Ferrand, France*
[6] *CPPM, Aix-Marseille Université, CNRS/IN2P3, Marseille, France*
[7] *LAL, Université Paris-Sud, CNRS/IN2P3, Orsay, France*
[8] *LPNHE, Université Pierre et Marie Curie, Université Paris Diderot, CNRS/IN2P3, Paris, France*
[9] *Fakultät Physik, Technische Universität Dortmund, Dortmund, Germany*
[10] *Max-Planck-Institut für Kernphysik (MPIK), Heidelberg, Germany*
[11] *Physikalisches Institut, Ruprecht-Karls-Universität Heidelberg, Heidelberg, Germany*

[12]*School of Physics, University College Dublin, Dublin, Ireland*
[13]*Sezione INFN di Bari, Bari, Italy*
[14]*Sezione INFN di Bologna, Bologna, Italy*
[15]*Sezione INFN di Cagliari, Cagliari, Italy*
[16]*Sezione INFN di Ferrara, Ferrara, Italy*
[17]*Sezione INFN di Firenze, Firenze, Italy*
[18]*Laboratori Nazionali dell'INFN di Frascati, Frascati, Italy*
[19]*Sezione INFN di Genova, Genova, Italy*
[20]*Sezione INFN di Milano Bicocca, Milano, Italy*
[21]*Sezione INFN di Roma Tor Vergata, Roma, Italy*
[22]*Sezione INFN di Roma Sapienza, Roma, Italy*
[23]*Nikhef National Institute for Subatomic Physics, Amsterdam, Netherlands*
[24]*Nikhef National Institute for Subatomic Physics and Vrije Universiteit, Amsterdam, Netherlands*
[25]*Henryk Niewodniczanski Institute of Nuclear Physics Polish Academy of Sciences, Cracow, Poland*
[26]*Faculty of Physics & Applied Computer Science, Cracow, Poland*
[27]*Soltan Institute for Nuclear Studies, Warsaw, Poland*
[28]*Horia Hulubei National Institute of Physics and Nuclear Engineering, Bucharest-Magurele, Romania*
[29]*Petersburg Nuclear Physics Institute (PNPI), Gatchina, Russia*
[30]*Institute of Theoretical and Experimental Physics (ITEP), Moscow, Russia*
[31]*Institute of Nuclear Physics, Moscow State University (SINP MSU), Moscow, Russia*
[32]*Institute for Nuclear Research of the Russian Academy of Sciences (INR RAN), Moscow, Russia*
[33]*Budker Institute of Nuclear Physics (BINP), Novosibirsk, Russia*
[34]*Institute for High Energy Physics(IHEP), Protvino, Russia*
[35]*Universitat de Barcelona, Barcelona, Spain*
[36]*Universidad de Santiago de Compostela, Santiago de Compostela, Spain*
[37]*European Organization for Nuclear Research (CERN), Geneva, Switzerland*
[38]*Ecole Polytechnique Fédérale de Lausanne (EPFL), Lausanne, Switzerland*
[39]*Physik-Institut, Universität Zürich, Zürich, Switzerland*
[40]*NSC Kharkiv Institute of Physics and Technology (NSC KIPT), Kharkiv, Ukraine*
[41]*Institute for Nuclear Research of the National Academy of Sciences (KINR), Kyiv, Ukraine*
[42]*H.H. Wills Physics Laboratory, University of Bristol, Bristol, United Kingdom*
[43]*Cavendish Laboratory, University of Cambridge, Cambridge, United Kingdom*
[44]*Department of Physics, University of Warwick, Coventry, United Kingdom*
[45]*STFC Rutherford Appleton Laboratory, Didcot, United Kingdom*
[46]*School of Physics and Astronomy, University of Edinburgh, Edinburgh, United Kingdom*
[47]*School of Physics and Astronomy, University of Glasgow, Glasgow, United Kingdom*
[48]*Oliver Lodge Laboratory, University of Liverpool, Liverpool, United Kingdom*
[49]*Imperial College London, London, United Kingdom*
[50]*School of Physics and Astronomy, University of Manchester, Manchester, United Kingdom*
[51]*Department of Physics, University of Oxford, Oxford, United Kingdom*
[52]*Syracuse University, Syracuse, NY, United States of America*
[53]*CC-IN2P3, CNRS/IN2P3, Lyon-Villeurbanne, France, associated member*
[54]*Pontifícia Universidade Católica do Rio de Janeiro (PUC-Rio), Rio de Janeiro, Brazil, associated to* [2]

[a]*P.N. Lebedev Physical Institute, Russian Academy of Science (LPI RAS), Moskow, Russia*
[b]*Università di Bari, Bari, Italy*
[c]*Università di Bologna, Bologna, Italy*
[d]*Università di Cagliari, Cagliari, Italy*
[e]*Università di Ferrara, Ferrara, Italy*
[f]*Università di Firenze, Firenze, Italy*
[g]*Università di Urbino, Urbino, Italy*
[h]*Università di Modena e Reggio Emilia, Modena, Italy*
[i]*Università di Genova, Genova, Italy*
[j]*Università di Milano Bicocca, Milano, Italy*

[k] *Università di Roma Tor Vergata, Roma, Italy*
[l] *Università di Roma La Sapienza, Roma, Italy*
[m] *Università della Basilicata, Potenza, Italy*
[n] *LIFAELS, La Salle, Universitat Ramon Llull, Barcelona, Spain*
[o] *Institució Catalana de Recerca i Estudis Avançats (ICREA), Barcelona, Spain*

Contents

Chapter 1

Introduction

1.1 Flavour physics in the era of the LHC

Studies of hadronic flavour physics observables have provided critical input in the construction of the Standard Model (SM). Flavour measurements provided the first indications of the existence and nature of the charm quark, the third generation, and the high mass scale of the top. In searching for physics beyond the Standard Model it is also evident that flavour observables will play a central role.

Many of the open questions of the SM are associated with the flavour sector. Why are there three generations (if there are only three)? What determines the hierarchy of quark masses? What is responsible for the characteristic structure of the CKM matrix? Furthermore, two of the very few observations that cannot be accommodated in the Standard Model, namely the baryon-antibaryon asymmetry of the universe, and non-zero neutrino mass, are of a flavour physics nature.

Flavour physics measurements already exert significant weight in limiting the parameter space of New Physics (NP) beyond the SM. The strongest constraints on supersymmetric Higgs bosons come not from direct searches, but from limits on, and measurements of, the rates of suppressed heavy flavour decays such as $B_s \to \mu^+\mu^-$, $b \to s\gamma$ and $B^- \to \tau^-\nu$. These observables will continue to have great importance in the era of the LHC. This can be seen in Fig. 1.1, which illustrates for a popular variant of SUSY (NUHM1 [1]), how measurements that are sensitive to values of $\mathcal{B}(B_s \to \mu^+\mu^-)$ below 1×10^{-8} have greater discovery power over the parameter space indicated than direct searches for the H and A Higgs bosons performed with up to 60 fb^{-1} [2]. Moreover, a measurement of $\mathcal{B}(B_s \to \mu^+\mu^-)$ together with any direct observation of a H or A candidate will be invaluable in elucidating the nature of the underlying physics.

The physics opportunities of the LHC in terms of direct searches are well known; its potential in flavour physics through the enormous production rate of B and D hadrons is no less rich. At the LHC observation of $B_s \to \mu^+\mu^-$ and other rare decays will be possible, as well as detailed studies of important kinematical distributions that have not been accessible at previous facilities, such as the angular distribution of the decay products in $B^0 \to K^*\mu^+\mu^-$, which are highly sensitive to the helicity structure of any NP effects [4].

A particular attraction of performing flavour physics at the LHC is the opportunity to make measurements of CP-violating asymmetries with much higher precision than has been possible

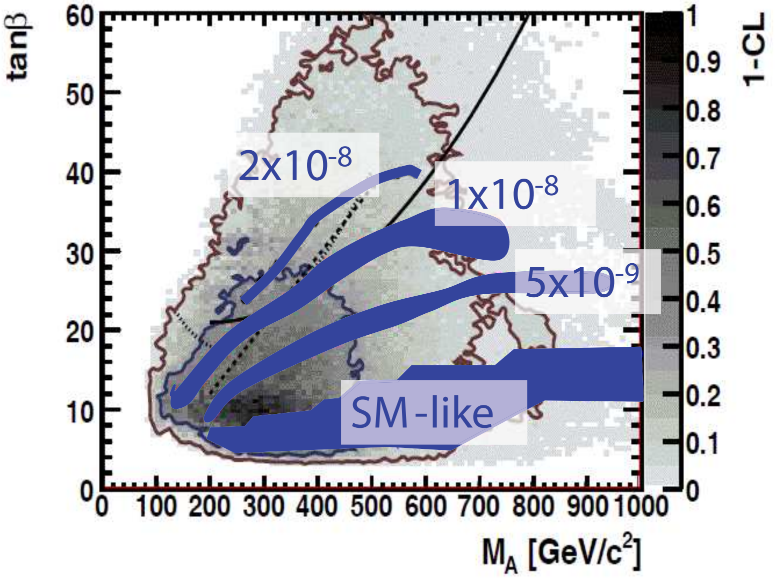

Figure 1.1: The correlations between the preferred values of M_A and $\tan\beta$ in the NUHM1 variant of MSSM [3]. Superimposed are the contours indicating the value of $\mathcal{B}(B_s \to \mu^+\mu^-)$ in this framework. Also indicated are the $5\,\sigma$ discovery contours for observing the heavy MSSM Higgs bosons H, A in the decay channels $H, A \to \tau^+\tau^-$ jets (solid line), jet + μ (dashed line), jet + e (dotted line) assuming an analysis requiring 30 or 60 fb^{-1} collected with the CMS detector [2].

hitherto. These asymmetries are a priori very sensitive to the contribution from NP effects. It is therefore surprising that the measurements of CP violation performed with B^0 and $B^\pm$ mesons at BABAR and Belle are broadly consistent with the CKM mechanism of the SM [5,6]. If new particles exist at the TeV mass scale, as is expected, then this is already an indication that the flavour couplings of the NP have a very particular structure, so as not to have given rise to effects inconsistent with the SM expectations. More precise measurements are needed to test whether the CKM description remains successful at the sub-10% level. Even more exciting is the possibility to extend this programme to the B_s sector, about which very little is known and where more visible effects may be apparent. Recent measurements from the Tevatron hint at larger than expected CP violation in $B_s \to J/\psi\phi$ [7,8] and in B_s mixing [9,10], but measurements with higher precision are required to clarify the situation. This will only be possible at the LHC.

1.2 LHCb goals with current and upgraded detector

LHCb is an experiment that has been designed to perform flavour physics measurements at the LHC. Its physics programme will be executed in two phases. A full discussion of the goals of each phase may be found in Chapter 2. Here a brief overview is given.

The aims of the first phase of the experiment can be achieved with around 5 fb^{-1} of data and will take several years to accomplish, using the current detector. With this data-set, it will be possible to extend significantly the precision of many key observables in B and D physics beyond what was possible at the B-factories, and make the first exploration of the B_s system.

To exploit fully the flavour-physics potential of the LHC will then require an upgrade to the

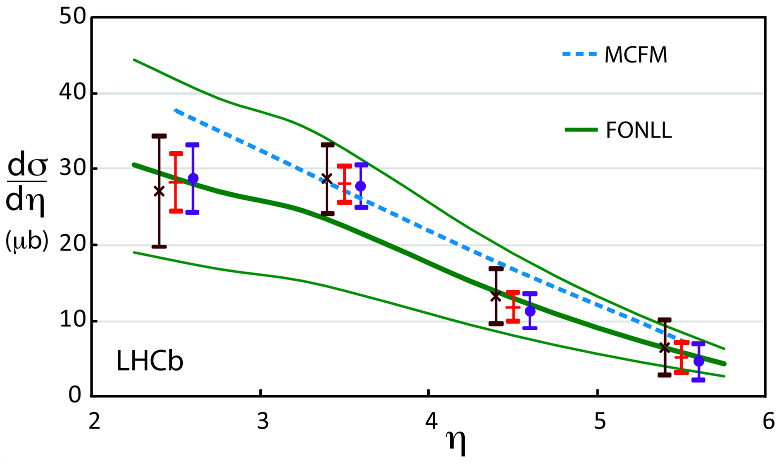

Figure 1.2: LHCb measurement of the $b\bar{b}$ cross-section at $\sqrt{s} = 7$ TeV, as a function of rapidity. In each rapidity bin measurements performed with two sets of trigger conditions are shown (black and blue), which are then averaged together to give the final result (red, with smallest error bars). Also shown are two theoretical predictions [12].

detector, as proposed in this document. The upgrade will allow the experiment to operate at higher luminosity, and will equip the detector with a fully flexible software trigger. This latter attribute will be invaluable for improving the selection efficiency for hadronic final states in B and D decays. The upgraded detector will be able to collect 50 fb^{-1} of data integrated over around ten years of operation.

The aim of both the existing experiment and the upgrade is to search for effects of processes beyond the SM, and to characterise the nature of the underlying physics. In both phases a wide programme of studies will be performed, which can be broadly divided into two equally important categories, as summarised in Table 1.1. In the first category ("Exploration") are those studies which exploit decay modes or observables which are a priori very sensitive to NP, but have not been accessible at previous experiments. The hope here is to observe large non-SM effects. The second category ("Precision Studies") encompasses measurements of known parameters with improved sensitivity, to allow for more precise comparisons with theory. The strategies for performing the studies in certain key topics with the existing detector have been mapped out using simulation [11]. The data collected in 2010 give confidence that these physics goals are achievable, as it has been observed that the detector is performing as expected and that the cross-section for heavy-flavour production agrees with the theoretical predictions (see Fig. 1.2).

In the physics exploitation of the upgraded experiment the Exploration category will be populated by important new observables and decay modes, which cannot be studied with interesting precision at the existing experiment. This means that the physics gain of the upgrade cannot be assessed by merely applying a '$1/\sqrt{N}$' scaling to the expectations of the current detector. The topics which had been classified in the Exploration category for the existing experiment will migrate to the class of Precision Studies. Improved knowledge of these observables will be essential in understanding the NP which it is hoped that the LHC will uncover.

The potential of LHCb extends far beyond quark flavour physics. Important studies are also

Table 1.1: LHCb quark flavour physics goals, illustrated with selected examples for the current and upgraded detector.

	Exploration	Precision studies
Current LHCb	Search for $B_s \to \mu^+\mu^-$ down to SM value Search for mixing induced CP violation in B_s system ($2\beta_s$) down to SM value Look for non-SM behaviour in forward-backward asymmetry of $B^0 \to K^*\mu^+\mu^-$ Look for evidence of non-SM photon polarisation in exclusive $b \to s\gamma^{(*)}$	Measure unitarity triangle angle γ to $\sim 4^\circ$ to permit meaningful CKM tests Search for CPV in charm
Upgraded LHCb	Search for $B^0 \to \mu^+\mu^-$ Study other kinematical observables in $B^0 \to K^*\mu^+\mu^-$, e.g. $A_T(2)$ CPV studies with gluonic penguins e.g. $B_s \to \phi\phi$ Measure CP violation in B_s mixing (A^s_{fs})	Measure $\mathcal{B}(B_s \to \mu^+\mu^-)$ to a precision of $\sim 10\%$ of SM value Measure $2\beta_s$ to precision $< 20\%$ of SM value Measure γ to $< 1^\circ$ to match anticipated theory improvements Charm CPV search below 10^{-4} Measure photon polarisation in exclusive $b \to s\gamma^{(*)}$ to the % level

possible in the lepton sector, including the search for lepton-flavour violating tau decays and for low mass Majorana neutrinos. Furthermore, the forward geometry, precise vertexing and particle identification capabilities of the detector give LHCb unique and exciting possibilities in the areas as diverse as electroweak physics, the search for long-lived new particles, and QCD. In all cases great benefit will come both from the increased sample sizes that will be made available with the upgrade, and the flexible software trigger. More discussion is given to these opportunities in Chapter 2.

1.3 Running LHCb with large pile-up

Recent running of LHCb, albeit at luminosities below nominal design, have approached interaction rates per bunch expected at the upgrade. The effect on the detector of much higher number of visible interactions per crossing, μ, than originally planned has therefore been observed. The detector has been run with μ values of up to 2.5, similar to those expected in the

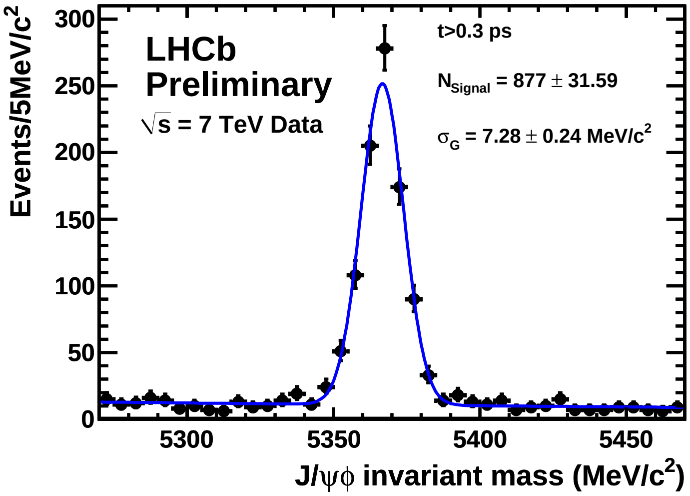

Figure 1.3: Invariant mass distribution of $J/\psi(\mu^+\mu^-)\phi(K^+K^-)$ candidates, using 35 pb^{-1} of data.

upgrade scenario, while the nominal design value was $\mu = 0.4$. However, an upgraded LHCb detector will experience larger bunch-to-bunch spillover, and track multiplicities will increase somewhat given the expected doubling of the LHC beam energy.

Running at larger than design pile-up results in an increased combinatorial background and lower reconstruction efficiency due to increased occupancy in the detector. Studies of 2010 data suggest that these effects are much smaller than might initially have been expected.

Impact on combinatorial background The impact of the large pile-up on the combinatorial background has been studied extensively [11]. The invariant mass of $J/\psi(\mu^+\mu^-)\phi(K^+K^-)$ candidates, which are used to measure the B_s mixing phase, are shown in Fig. 1.3. These candidates have been reconstructed in the data taken in 2010 with an average $\mu = 1.8$. The distribution shows a signal-to-background ratio (S/B) of around 5. This level of background results in only a very small loss in sensitivity compared to that expected in nominal LHCb conditions.

To extrapolate to even larger pile-up, Fig. 1.4 shows S/B extracted from the invariant mass distributions of $J/\psi(\mu^+\mu^-)K^\pm$ candidates as a function of the number of primary vertices (PVs) reconstructed in the 2010 run. The S/B of $B_s \to J/\psi(\mu^+\mu^-)K^\pm$ is comparable to that of $B_s \to J/\psi(\mu^+\mu^-)\phi(K^+K^-)$. However, the former decays have an order of magnitude more statistics. This allows the S/B to be investigated in events with up to five PVs. The S/B value is found to be independent of the number of PVs, due to the fact that the separation between PVs is on the order of centimetres, while the resolutions of primary and secondary vertices are $\sim 60\ \mu$m and $\sim 200\ \mu$m, respectively. For this core physics channel the LHCb detector therefore performs very well in terms of S/B, even in the presence of large pile-up. For some other channels, for example inclusive semileptonic decays such as $B \to D\mu X$, some degradation is observed.

Impact on track reconstruction efficiency To check the track reconstruction efficiency for large pile-up, the 2010 data has been used to validate the reconstruction efficiency of charged

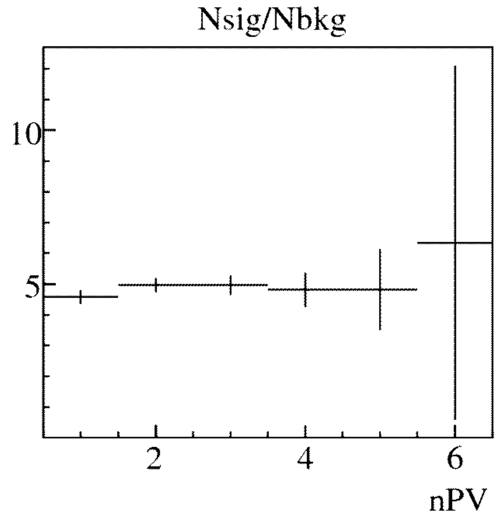

Figure 1.4: Signal-to-background ratio for the invariant mass distribution of $J/\psi(\mu^+\mu^-)K^\pm$ as a function of the number of primary vertices reconstructed in the event.

tracks in Monte-Carlo simulation. The simulation results are in good agreement with the observed efficiencies, which gives confidence in using the simulation to determine the maximum pile-up at which the reconstruction of charged tracks would still work with the present LHCb detector.

Owing to the limited number of LHC bunches in 2010, LHCb has not yet been exposed to spill-over[1] from neighbouring LHC buckets. With the nominal number of bunches, 2622, the probability that a consecutive crossing also has a pp interaction is 0.33 at $\mu = 0.4$, while at $\mu = 2$ this probability rises to 0.86.

The Outer Tracker subdetector is sensitive to spill-over and from $\mu = 0.4$ to $\mu = 2$ its occupancy rises by a factor two. Other subdetector systems which are less sensitive to spill-over, see the occupancy rise by a factor ∼1.6. To test the reconstruction efficiency, crossings have been simulated containing $B_s \to \phi(K^+K^-)\phi(K^+K^-)$ decays, and the efficiency to reconstruct the B_s was determined. Compared to running at $\mu = 0.4$, the loss in efficiency at $\mu = 2$ and 4 is respectively 13% and 36%. The deterioration in tracking efficiency due to large occupancies is therefore expected to be small compared to the luminosity increase up to $\mu = 2$. For larger μ values, the increase in luminosity would be neutralised by the loss in reconstructing multi-body final states.

1.4 Consequences for the upgrade strategy

The above would indicate that the present detector could run at luminosities $L \sim 10^{33}$ cm^{-2}s^{-1} with $\mu = 2$ if the machine reaches its nominal number of bunches. However, the present detector is limited to a maximum read-out rate of 1.1 MHz. To trigger at an increased event

---

[1] The arrival time of each particle and electronic response may span more than the time interval between consecutive bunches. The simulation takes this into account, also generating interactions in several bunches around the bunch of interest.

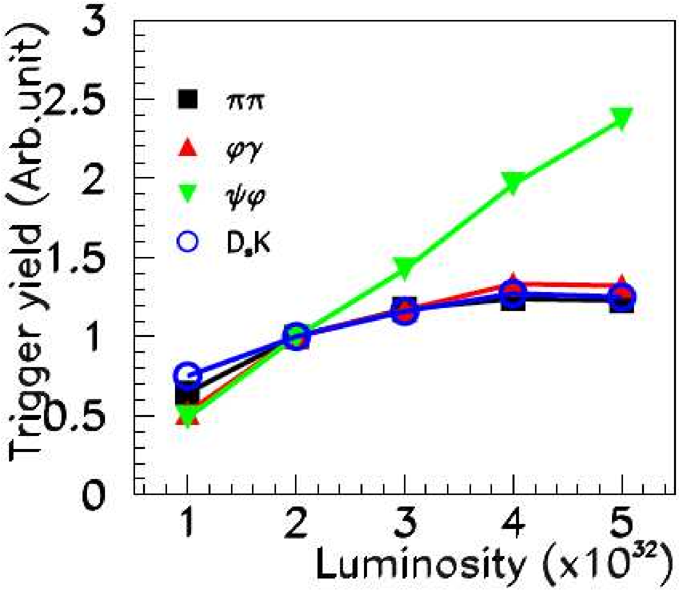

Figure 1.5: The trigger yield for different decays of B mesons. Each point is normalised to the trigger yield expected in nominal conditions at a luminosity of 2×10^{32} cm^{-2}s^{-1}.

rate requires a substantial change in the LHCb read-out architecture.

The present first level trigger (L0) is implemented in hardware [13]. Trigger selections are made at the 40 MHz beam crossing rate using either the Calorimeters or the Muon System. Criteria are based on the deposit of several GeV of transverse energy, E_{T}, by charged hadrons, muons, electrons or photons. While this provides high efficiencies on dimuon events, it typically removes half of the fully hadronic signal decays. In these hadronic decays the E_{T} threshold required to reduce the rate of triggered events to an acceptable level is already a substantial fraction of the B meson mass. Any further increase in the rate requires an increase of this threshold, which then removes a substantial fraction of signal decays. As shown in Fig. 1.5, the trigger yield therefore saturates for hadronic channels with increasing luminosity. While it was shown above that LHCb would be able to run at $L = 10^{33}$ cm^{-2}s^{-1}, the decrease in L0-efficiencies, and especially the L0-hadron efficiency, would result in an almost constant signal yield, independent of luminosity, for $L > 2$–3×10^{32} cm^{-2}s^{-1}. Unless the efficiency can be improved by removing the L0 1 MHz limitation and introducing information that is more discriminating than E_{T} earlier in the trigger, the experiment cannot profit from increasing the luminosity.

The most effective way of achieving such a trigger upgrade is to supply the full event information, including whether tracks originate from the displaced vertex that is characteristic of heavy flavour decays, at each level of the trigger. This requires reading out the whole detector at 40 MHz and then analysing each event in a trigger system implemented in software. A detector upgraded in this way would allow the yield of hadronic B decays to be increased by up to a factor of seven for the same LHC machine run-time.

In order to supply displaced vertex information at the first level of the trigger, a tracking

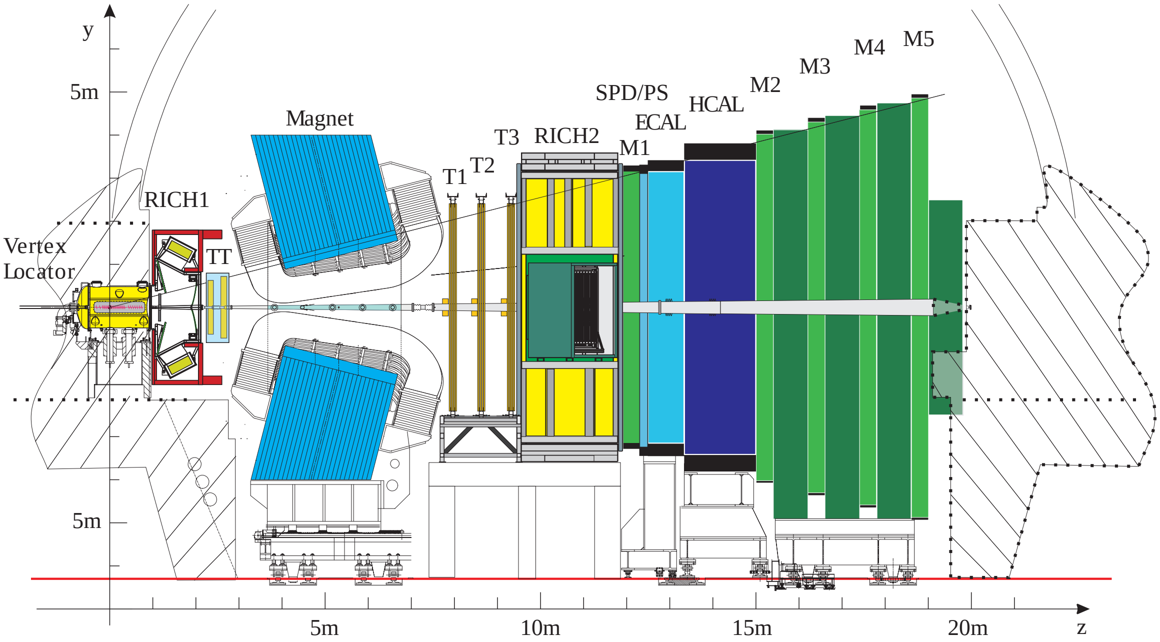

Figure 1.6: Layout of the current LHCb detector.

system which allows the pattern recognition to be performed quickly is essential. If the tracking system can also improve the efficiency and, in particular, reduce the ghost rate, it may be possible to avoid the efficiency loss for multi-body final states described above which limits the present detector to $\mu = 2$. Running at even higher pile-up would allow further gains in signal yields.

1.5 Detector modifications

The current LHCb detector is shown in Fig. 1.6. The detector elements are placed along the beam line of the LHC starting with the Vertex Locator (VELO), a silicon strip device that surrounds the proton-proton interaction region and is positioned with its sensitive area 8 mm from the beam during collisions. It provides precise locations for primary *pp* interaction vertices, the locations of decays of long-lived particles, and contributes to the measurement of track momenta. Other devices used to measure track momenta comprise a large area silicon strip detector (TT) located in front of a 4 Tm dipole magnet, and a combination of silicon strip detectors (Inner Tracker, IT) and straw drift chambers (Outer Tracker, OT) placed behind. Two ring-imaging Cherenkov (RICH) detectors are used to identify charged hadrons. Further downstream a preshower (PS), scintillating pad detector (SPD) and Electromagnetic Calorimeter (ECAL) are used for photon detection and electron identification, followed by a Hadron Calorimeter (HCAL), and a system consisting of alternating layers of iron and chambers (MWPC and triple-GEM) that distinguishes muons from hadrons (Muon System). The ECAL, HCAL and Muon System provide the capability of first-level hardware triggering.

In this document the next chapter provides a detailed physics case for the LHCb upgrade, and is followed by chapters describing the Trigger and Electronics. Implementing the 40 MHz read-out for the upgrade will require replacing all the front-end electronics. Apart from this, coping with luminosities of $10^{33}\text{cm}^{-2}\text{s}^{-1}$ does not require substantial rebuilds of the Muon System, Outer Tracker and calorimeters. For the RICH detectors, the vessels will be reused, but since the front-end electronics is encapsulated within the current photon detectors (HPDs) they will need to be replaced. The VELO sensors will also have to be replaced, due to the increased radiation dose expected in the upgrade. The possibility of equipping it with pixel sensors is under study, as discussed in Chapter 5. Replacement of the silicon tracking stations is also required, since the front-end electronics is attached to the sensors. The possibility of increasing the tracking efficiency by redesigning the stations is under investigation, as presented in Chapter 6.

In addition, owing to the higher occupancies in the upgrade environment, the RICH aerogel radiator and the first muon station (M1) will be removed. The removal of the PS and SPD is also being considered. A new component of the particle identification system based on time-of-flight (TORCH) is proposed to augment the low-momentum particle identification capabilities (see Chapter 7). Upgrades to the calorimeters and Muon System are described in the subsequent chapters, followed by a discussion of the simulations, and conclusion.

1.6 Time-line

LHCb expects to accumulate on the order of 5 fb^{-1} in the years up to 2017. At that time it is proposed to install the upgrade to allow ~ 5 fb^{-1} to be accumulated each year. This upgrade would not be tied to any luminosity increase of the LHC, as by that time it is expected that $L > 10^{33}\,\text{cm}^{-2}\text{s}^{-1}$ will already be available. The open geometry of the LHCb detector will allow portions of the upgraded detector to be installed in any reasonably long shutdown.

Chapter 2

Physics Justification

Introduction

The LHCb upgrade will pursue important and exciting physics goals in the flavour sector and beyond. The upgrade augments the established strengths of the existing detector, for example the forward acceptance, precise vertexing, and particle identification capabilities, with a flexible software trigger, and the ability to run at a luminosity of $10^{33}\,\text{cm}^{-2}\text{s}^{-1}$, which will enable a very large data sample of $\sim 50\,\text{fb}^{-1}$ to be accumulated. The improvements to the present detector will enable the detector to increase significantly the sensitivity that the experiment can attain in its study of b- and c-hadron decays, and will make possible high precision measurements and unique studies in many other areas of high energy physics.

In what follows, consideration is given first to the contribution that the upgraded experiment will bring to the field of quark flavour physics. The extremely promising results obtained with first data can already be used to extrapolate to the performance of the future detector. It is argued that measurements in the hadronic flavour sector, i.e. decays of beauty and charm hadrons, have great and wide-ranging sensitivity to New Physics effects. These measurements will be a powerful method both to search for New Physics, and to characterise its nature when found. As such, they constitute an indispensable element of LHC exploitation. The upgrade to the detector proposed in this document is necessary for this programme to proceed throughout the lifetime of the LHC.

The scientific goals of LHCb, however, extend far beyond quark-flavour physics. The upgraded experiment can be regarded as a multi-purpose detector in the forward direction. The unique acceptance, coupled with the flexible trigger, will enable LHCb to make measurements that are either complementary to, or of higher sensitivity than, those which are possible at the LHC general-purpose detectors (ATLAS/CMS) and other facilities. Examples include the search for long-lived exotic particles, and measurements in the electroweak sector such as the determination of the weak mixing angle. A brief survey is therefore made of various opportunities which exist for LHCb in the lepton sector and in non-flavour topics. In most of these areas work is only now beginning, and further study is needed to quantify more precisely the sensitivities that can be achieved. Nevertheless, a clear message emerges as to the richness of the physics possibilities that are open to LHCb beyond the studies of b and c decays.

2.1 Quark Flavour Physics

2.1.1 Motivation and strategy

The LHCb detector was constructed to study the physics of flavour and its unique capability to probe this sector remains at the core of the physics programme of the upgraded experiment. This is motivated by one of the major unsolved scientific challenges for particle physics, namely the quest to understand the origin of the asymmetry between matter and antimatter in the Universe.

Previous experiments have made a number of measurements of CP violation in the quark sector, and until now all results are compatible with a sole source of asymmetry arising in the Cabibbo-Kobayashi-Maskawa (CKM) quark-mixing matrix [14]. For reviews of the status of the field, see, for example, Refs. [15, 16]. However, it is well known that the Standard Model (SM) CP violation is insufficient to explain the magnitude of the baryon asymmetry of the Universe, and therefore further sources of CP violation must exist. It is possible that these new sources could be found in the lepton sector, or indeed in an extended gauge sector. Nonetheless, the best chance of finding non-standard CP violation effects within the next decade is in the quark sector, due to the high precision that can be achieved with an upgraded LHCb detector exploiting the copious production of charm and beauty hadrons at the LHC.

Flavour observables are also highly sensitive to physics beyond the Standard Model, even in models which do not introduce any new sources of CP violation. The suppression of flavour-changing neutral currents in the SM is one of the most severe constraints for model builders, and effects of virtual particles in rare processes can modify decay rates dramatically from their SM predictions. Historically, such observations resulted in the prediction both of the existence and the properties of the charm quark, as well as the third family (bottom and top quarks) well before colliders reached the energies necessary to produce these particles.

Indeed, there are excellent prospects for major discoveries in the first phase of LHCb operation. If, for example, the true value of the CP violation phase in B_s or D^0 oscillations, or that of the decay rate for $B_s \to \mu^+\mu^-$, is substantially altered from the SM prediction, then LHCb measurements will prove the existence of New Physics (NP). Of course, there may also be discoveries of beyond-the-SM physics at ATLAS and CMS. In these scenarios the role of the upgraded LHCb experiment will be to characterise NP, i.e. to understand what is the correct model describing the new phenomena and to measure its parameters. Examples of the impact of measurements from the upgraded LHCb experiment on some illustrative models are given below. In the less favourable scenario that there is no early discovery at the LHC that is inconsistent with the Standard Model, it will be necessary to maximise the possibility of the discovery of New Physics, leaving no stone unturned in the search. The flexible software trigger of the LHCb upgrade will be crucial for this purpose.

To illustrate the impact of the LHCb upgrade beyond the first phase of LHCb operation, we consider some of the key physics analyses discussed in the recent Roadmap document [11]. In each case, the upgraded experiment will provide a significant increase in the physics reach as new regimes of sensitivity are reached, and as the data samples become large enough to study additional decay modes.

	Measurement of mixing-induced CP violation in $B_s \to J/\psi\phi$
First phase	Find or rule out large deviations from SM
Upgrade	Precise measurement of B_s oscillation phase
	Charmless hadronic two-body B decays
First phase	Measure CP violation in two-body decays
Upgrade	Analysis of theoretically clean vector-vector final states
	The tree-level determination of the unitarity triangle angle γ
First phase	Measure with $\sim 4^\circ$ uncertainty to allow for CKM tests
Upgrade	Achieve $\leq 1^\circ$ precision to match anticipated progress in lattice QCD
	Analysis of the decay $B_s \to \mu^+\mu^-$
First phase	Find or rule out large deviations from SM
Upgrade	Make precision measurement and extend programme to $B^0 \to \mu^+\mu^-$
	Analysis of the decay $B^0 \to K^{*0}\mu^+\mu^-$
First phase	Measure the zero-crossing point of the forward-backward asymmetry
Upgrade	Exploit the NP sensitivity of the full kinematic distributions

These measurements are discussed in more detail in the remainder of this section, together with illustrative examples of other important avenues of study, such as the measurement of photon polarisation in exclusive $b \to s\gamma^{(*)}$ decays and the search for CP violation in charm.

In the first phase of the experiment, LHCb will explore areas that (some first measurements by the Tevatron experiments notwithstanding) are virgin territory. Whatever the outcome of this initial exploration, precision measurements of these important quantities will be required. Since the proposed "Super B-factory" experiments cannot compete in a number of key measurements, this can *only* be done with the LHCb upgrade. LHCb has unique potential in the B_s and b baryon sectors, since these particles are not produced in e^+e^- collisions at the $\Upsilon(4S)$ resonance. It will be the only experiment that can perform time-dependent CP violation measurements in the B_s system. Moreover, in exclusive final states composed solely of charged particles, LHCb will accumulate enormous numbers of events, far in excess of what will be available at any other facility. These will allow for super-precise measurements of fundamental quantities such as the CP violating angle γ, and unchallenged sensitivity to CP violation in charm. A summary of the achievable sensitivities for some key channels is given in Table 2.1, based on the studies presented in [11] and recent updates.

2.1.2 Impact on New Physics models

In any scenario, the LHCb upgrade will provide measurements that will be essential to understand the physics landscape that this decade will unveil. In this section we provide some brief examples of the impact of the experiment.

The minimal flavour violation (MFV) hypothesis [17] has been proposed to resolve the tension between the need for physics beyond the SM to manifest at the TeV scale in order to resolve the hierarchy problem, and the apparent absence of effects from new TeV-scale particles in flavour observables (see Refs. [18, 19] for reviews). MFV requires that all sources of flavour- and CP-violation in the quark sector have the same pattern as those of the SM, namely the CKM matrix. This can be (albeit sometimes rather unnaturally) satisfied in a range of NP models, including supersymmetry. While such models predict that all measurements of CP violation will be consistent with the SM, large enhancements are possible in rare decays. A

Table 2.1: Sensitivities of the LHCb upgrade to key observables. For each observable the current sensitivity is compared to that expected after LHCb has accumulated 5 fb^{-1} and that which will be achieved with 50 fb^{-1} by the upgraded experiment, all assuming $\sqrt{s} = 14$ TeV. (Note that at the upgraded experiment the yield/fb^{-1} in hadronic B and D decays will be higher on account of the software trigger.)

Type	Observable	Current precision	LHCb ($5\ \text{fb}^{-1}$)	Upgrade ($50\ \text{fb}^{-1}$)	Theory uncertainty
Gluonic penguin	$S(B_s \to \phi\phi)$	-	0.08	0.02	0.02
	$S(B_s \to K^{*0}\bar{K}^{*0})$	-	0.07	0.02	< 0.02
	$S(B^0 \to \phi K^0_S)$	0.17	0.15	0.03	0.02
B_s mixing	$2\beta_s\ (B_s \to J/\psi\phi)$	0.35	0.019	0.006	~ 0.003
Right-handed currents	$S(B_s \to \phi\gamma)$	-	0.07	0.02	< 0.01
	$\mathcal{A}^{\Delta\Gamma_s}(B_s \to \phi\gamma)$	-	0.14	0.03	0.02
E/W penguin	$A_T^{(2)}(B^0 \to K^{*0}\mu^+\mu^-)$	-	0.14	0.04	0.05
	$s_0\, A_{\text{FB}}(B^0 \to K^{*0}\mu^+\mu^-)$	-	4%	1%	7%
Higgs penguin	$\mathcal{B}(B_s \to \mu^+\mu^-)$	-	30%	8%	$< 10\%$
	$\frac{\mathcal{B}(B^0\to\mu^+\mu^-)}{\mathcal{B}(B_s\to\mu^+\mu^-)}$	-	-	$\sim 35\%$	$\sim 5\%$
Unitarity triangle angles	$\gamma\ (B \to D^{(*)}K^{(*)})$	$\sim 20°$	$\sim 4°$	0.9°	negligible
	$\gamma\ (B_s \to D_s K)$	-	$\sim 7°$	1.5°	negligible
	$\beta\ (B^0 \to J/\psi\, K^0)$	1°	0.5°	0.2°	negligible
Charm CPV	A_Γ	2.5×10^{-3}	2×10^{-4}	4×10^{-5}	-
	$A^{dir}_{CP}(KK) - A^{dir}_{CP}(\pi\pi)$	4.3×10^{-3}	4×10^{-4}	8×10^{-5}	-

striking example is the branching fraction of the decay $B_s \to \mu^+\mu^-$, which in the CMSSM at large values of $\tan\beta$ (the ratio of Higgs vacuum expectation values) is proportional to $\tan^6\beta$ [20]. Enhancements above the SM prediction of $\mathcal{B}(B_s \to \mu^+\mu^-) = (3.6 \pm 0.3) \times 10^{-9}$ [21] right up to the current experimental upper limit of 5.1×10^{-8} [22] are therefore possible.

Although MFV can easily be disproved (for example by any measurement of CP violation that is inconsistent with the SM), it will be difficult to establish for certain if it is an underlying feature of nature. Yet if NP does respect MFV, it will be crucial to know this for sure, since it will provide insight into the underlying physics at very high energies. For example, in supersymmetry MFV is realised if the supersymmetry breaking terms are flavour-blind at the appropriate scale. A proof of the MFV hypothesis can be achieved only by showing that physics beyond the SM exhibits its characteristic flavour-universality pattern. In particular, it is crucial to measure the ratio $\mathcal{B}(B^0 \to \mu^+\mu^-)/\mathcal{B}(B_s \to \mu^+\mu^-)$, since MFV predicts that this is given by its SM value, $|V_{td}/V_{ts}|^2$. This correlation is shown in Fig. 2.1, where MFV is contrasted against a range of other NP models. Observation of $B^0 \to \mu^+\mu^-$ requires huge statistics and excellent control of backgrounds, and can only be made by the upgraded LHCb experiment.

As an alternative to MFV, we consider a model that has received a lot of attention in the literature recently (see, for example, Refs. [24]), namely the Standard Model extended to four families (SM4). In the quark sector, this model has an extra seven parameters compared to the Standard Model: the masses of the two new quarks (t', b') plus five new quark-mixing

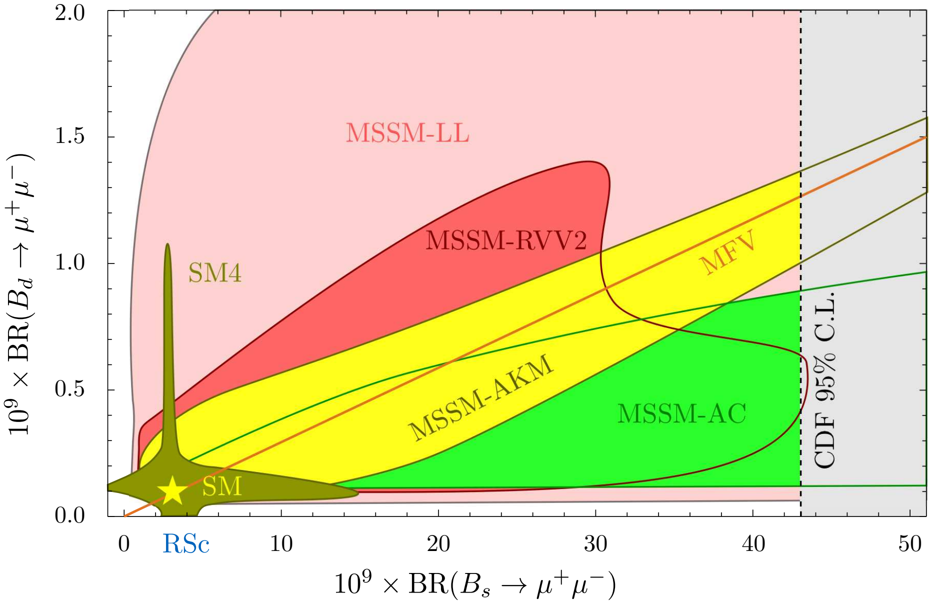

Figure 2.1: Correlations between $\mathcal{B}(B_s \to \mu^+\mu^-)$ and $\mathcal{B}(B^0 \to \mu^+\mu^-)$ in models respecting the MFV hypothesis (straight line) and in a range of alternative models. From Ref. [23], which gives a full definition of the various models. The vertical dashed line represents the experimental limit. The allowed values in the SM are restricted to the region of the yellow star.

parameters, related to the fact that the four-family version of the CKM matrix has nine free parameters instead of just four as in the SM. These five new quark-mixing parameters can be written as three mixing angles plus two new CP-violating phases. The consistency of current flavour measurements with the SM places limits on the sizes of the new mixing angles, while direct searches and electroweak fits constrain the masses of, and the mass difference between, the t' and b' quarks.

In contrast to models with MFV, in SM4 new CP-violating phenomena can be expected due to the two new phases. Measuring the underlying parameters of the model becomes a significant challenge due to their strong correlations in most observables. Particularly crucial due to their relatively clean interpretations are the CP-violating asymmetries of D^0, B^0 and B_s oscillations and the phase γ [25]. The latter, in particular, can be determined from $B \to DK$ processes with negligible theoretical uncertainty—it yields the SM value of γ even in extended models. Only the LHCb upgrade can make the complete set of these measurements with the precision necessary to disentangle the underlying parameters of the model.

As an aside, we note that it is natural to expect that, if there is a fourth family of quarks, the lepton sector will be similarly extended. This can lead to some interesting phenomenology that the LHCb upgrade would be well-placed to explore, as discussed in Section 2.2.1.

2.1.3 CP violation

CP Violation in B_s Oscillations

One of the primary goals of LHCb is to probe NP in B_s mixing. The golden channel for this analysis is $B_s \to J/\psi\phi$, which is dominated by a $b \to c\bar{c}s$ tree diagram, and therefore is sensitive to the weak phase $\beta_s = \arg\left(-V_{ts}V_{tb}^*/V_{cs}V_{cb}^*\right)$ with little theoretical uncertainty. The measurement proceeds by analysis of the time-dependent and angular decay distributions of B_s mesons. The time-evolution of a B_s meson that is tagged as $\bar{B}_s$ or B_s at time $t = 0$ to a final state f is given by [26]

$$\begin{aligned}
\Gamma_{\bar{B}_s \to f}(t) &= \frac{\mathcal{N}_f e^{-t/\tau(B_s)}}{4\tau(B_s)} \Bigg[\cosh\left(\frac{\Delta\Gamma_s t}{2}\right) \\
&\qquad + S_f \sin(\Delta m_s t) - C_f \cos(\Delta m_s t) + \mathcal{A}_f^{\Delta\Gamma} \sinh\left(\frac{\Delta\Gamma_s t}{2}\right) \Bigg], \\
\Gamma_{B_s \to f}(t) &= \frac{\mathcal{N}_f e^{-t/\tau(B_s)}}{4\tau(B_s)} \Bigg[\cosh\left(\frac{\Delta\Gamma_s t}{2}\right) \\
&\qquad - S_f \sin(\Delta m_s t) + C_f \cos(\Delta m_s t) + \mathcal{A}_f^{\Delta\Gamma} \sinh\left(\frac{\Delta\Gamma_s t}{2}\right) \Bigg], \qquad (2.1)
\end{aligned}$$

where

$$S_f = \frac{2\,\mathrm{Im}(\lambda_f)}{1+|\lambda_f|^2}\,, \quad C_f = \frac{1-|\lambda_f|^2}{1+|\lambda_f|^2}\,, \quad \mathcal{A}_f^{\Delta\Gamma} = -\frac{2\,\mathrm{Re}(\lambda_f)}{1+|\lambda_f|^2}\,, \quad \text{and} \quad \lambda_f = \frac{q}{p}\frac{\bar{A}_f}{A_f}\,.$$

Note that $(S_f)^2 + (C_f)^2 + \left(\mathcal{A}_f^{\Delta\Gamma}\right)^2 = 1$ by definition, and that in contrast to the CP-violating asymmetry parameters S_f and C_f, the parameter $\mathcal{A}_f^{\Delta\Gamma}$ appears with the same sign in both $\bar{B}_s$ and B_s decay time distributions, and can therefore be determined from untagged analysis.

The parameters $\bar{A}_f$ and A_f are the complex amplitudes for the decay of $\bar{B}_s$ and B_s to the final state f, respectively. For a CP eigenstate decay, λ_f takes a single value (so that if, for a decay to a CP-even eigenstate, the $b \to c\bar{c}s$ tree diagram is dominant, $S_f = \sin(2\beta_s)$ and $\mathcal{A}_f^{\Delta\Gamma} = -\cos(2\beta_f)$) but for a vector-vector final state λ_f is written as a function of the contributing helicity amplitudes, appropriately weighted for each particular point in phase space, giving a more complicated dependence on β_s [26]. The parameters q and p describe the eigenstates of the effective weak Hamiltonian of the B_s–$\bar{B}_s$ system (see Eq. 2.2 below). The constant $\mathcal{N}_f$ is a normalisation factor.

In the Standard Model, the value of β_s is constrained from global fits to the CKM matrix to be close to zero (see, for example, Refs. [5,6]), $2\beta_s = -2\eta\lambda^2 = -0.0363 \pm 0.0017\,\mathrm{rad}$, where η and λ are the Wolfenstein parameters [27] of the CKM matrix. Although first measurements of β_s have been made by CDF [7] and D0 [8], the results to date do not provide a very significant constraint.

The signals of $J/\psi K^{(*)}$ and $J/\psi\phi$ decays seen in the early LHCb data shown in Fig. 2.2 are in line with the expected yields. Moreover, it has already been possible with 2010 data, and using hadronic final states such as $B_s \to D_s\pi$, to resolve the very rapid B_s oscillations and measure Δm_s, the parameter which determines the mixing frequency. The likelihood scan as a function of Δm_s is shown in Fig. 2.3. A clear minimum is seen, and the preliminary analysis yields $\Delta m_s = 17.63 \pm 0.11\,(\mathrm{stat}) \pm 0.04\ \mathrm{ps}^{-1}$ [28], in good agreement with the value from the Tevatron of $17.77 \pm 0.12\ \mathrm{ps}^{-1}$ [29].

Given these encouraging first results from data, and from the results of simulation sensitivity studies [11], we can be confident that with 5 fb^{-1} accumulated during the first phase of LHCb, β_s will be determined with a statistical precision comparable to the central value of the Standard

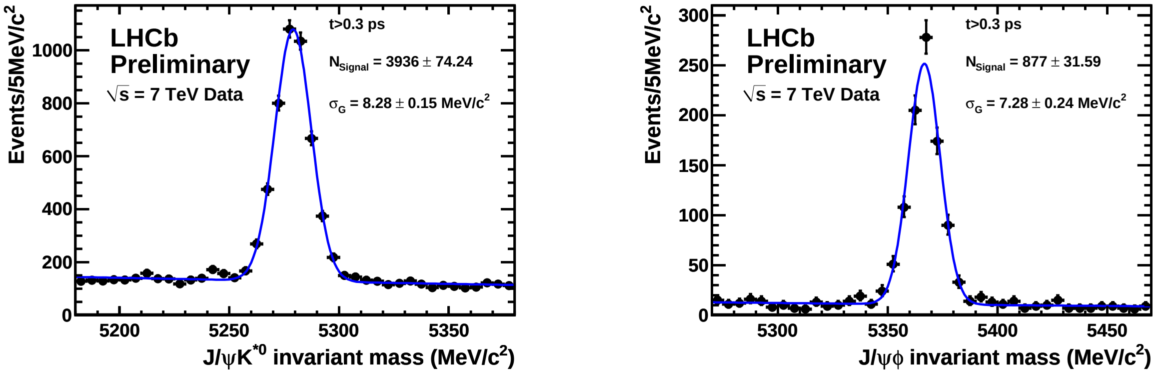

Figure 2.2: Signals for (left) $B^0 \rightarrow J/\psi K^{*0}$ and (right) $B_s \rightarrow J/\psi\phi$ seen in ~ 34 pb^{-1} of LHCb data accumulated in 2010.

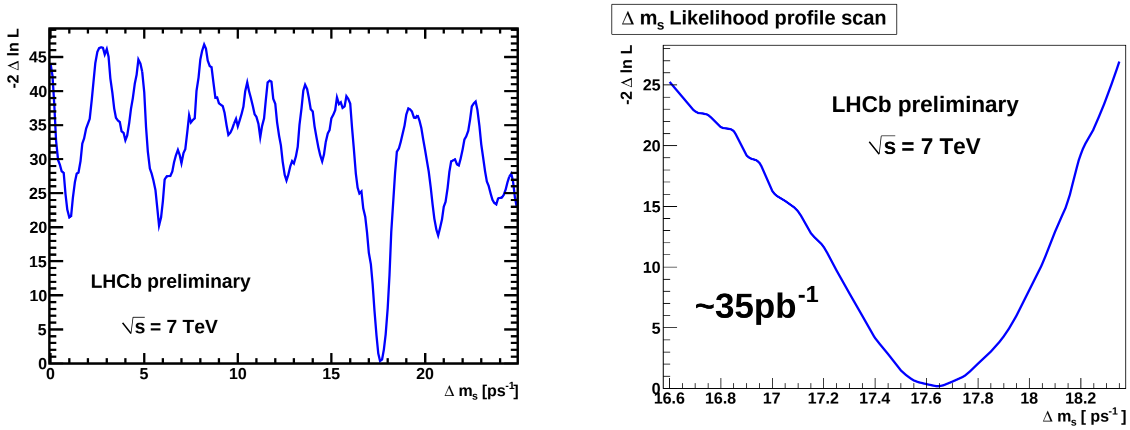

Figure 2.3: LHCb preliminary likelihood profile scans for Δm_s for a wide Δm_s range (left) and a narrower one (right). Only statistical uncertainties are considered for these scans [28].

Model prediction [11]. This accuracy is good enough to establish a New Physics effect if it is only three times larger than the SM.

If no anomalous effect is seen, it will be necessary to improve the precision to be able to observe CP violation at the SM level. In this case, and also if anomalies are found, it will be necessary to control both experimental (systematic) and theoretical uncertainties. These challenges can be tackled in the upgraded experiment using several complementary approaches.

- The measurement using $J/\psi\phi$ decays can suffer systematic uncertainties from acceptance effects since an angular analysis of the vector-vector final state is required:
  $\hookrightarrow$ β_s can be measured using B_s decays via $b \rightarrow c\bar{c}s$ transitions to pure CP eigenstates such as $D_s^+ D_s^-$ and $J/\psi f_0(980)$, which has recently been observed for the first time by LHCb, as shown in Fig. 2.4 [30].

- Contributions from S-wave K^+K^- under the ϕ peak can bias the measurement if not properly accounted for [31]:
  $\hookrightarrow$ the additional amplitudes can be included in the fit, which will remove the bias [32].

- Uncertainties arise in the SM prediction due to suppressed (penguin) contributions to the

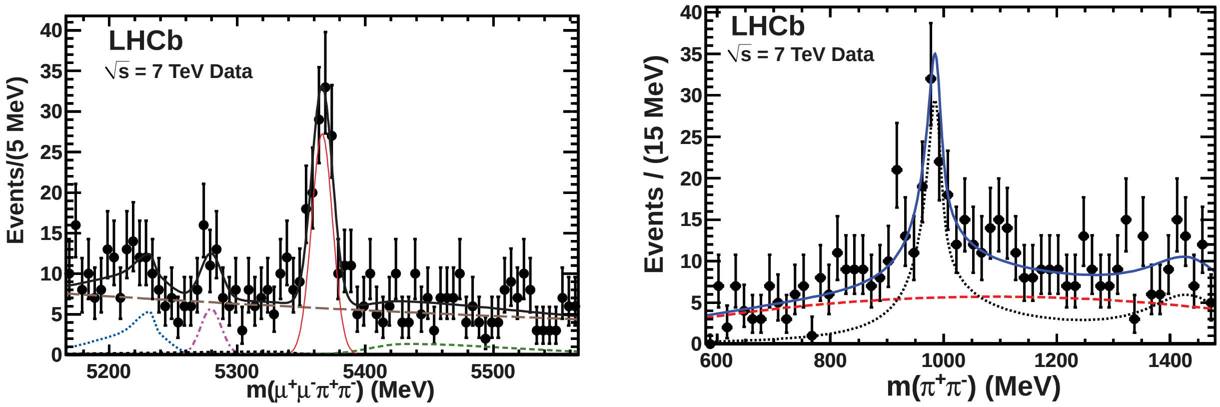

Figure 2.4: Signal for $B_s \to J/\psi f_0(980)$ seen in ~ 33 pb^{-1} of LHCb data accumulated in 2010 [30]. (Left) B_s candidate invariant mass distribution for candidates with $|m(\pi^+\pi^-) - 980 \text{ MeV}| < 90$ MeV; (right) $m(\pi^+\pi^-)$ distribution for candidates with $|m(J/\psi\pi^+\pi^-) - 5366 \text{ MeV}| < 30$ MeV.

decay amplitude:
$\hookrightarrow$ the SM uncertainties can be bounded from data using the $B_s \to J/\psi K^{(*)0}$ decays [33, 34]; β_s can be measured in the penguin-free $B_s \to D^0\phi$ channel [35].

The upgraded LHCb experiment will also allow for a significant improvement in the knowledge of the CP violating phase in B^0 oscillations, β. While the measurement of $\sin 2\beta$ using the decay $B^0 \to J/\psi K^0_S$ will be a calibration measurement in the early period of LHCb data taking, the very high statistics of the upgraded experiment will allow for a significantly better sensitivity than the present world average. Similar strategies to those discussed above for the B_s oscillation phase can be used to control theoretical uncertainties.

A complementary approach to search for New Physics effects in B_s oscillations is through the measurement of CP violation that arises in the mixing amplitude itself (as opposed to the effects discussed above, which correspond to CP violation in the interference of mixing and decay). The parameters p and q introduced in Eq. 2.1 are defined by writing the mass eigenstates of the effective weak Hamiltonian [26]

$$|B_L\rangle = p\,|B_s\rangle + q\,|\bar{B}_s\rangle \qquad |B_H\rangle = p\,|B_s\rangle - q\,|\bar{B}_s\rangle \tag{2.2}$$

where $|p|^2 + |q|^2 = 1$. CP violation in mixing occurs when $|q/p| \neq 1$, and a CP violation parameter can be defined in analogy with the kaon system as $\varepsilon_{B_s} = (p-q)/(p+q)$. This can be measured using flavour-specific decays where the quantity determined is the so-called flavour-specific asymmetry, $A_{\text{fs}}(B_s)$. Inclusive semileptonic decays provide a convenient high-statistics sample with which to determine this quantity,

$$A_{\text{fs}}(B_s) = \frac{\Gamma\left(B^0_s\bar{B}^0_s \to l^-l^-X\right) - \Gamma\left(B^0_s\bar{B}^0_s \to l^+l^+X\right)}{\Gamma\left(B^0_s\bar{B}^0_s \to l^-l^-X\right) + \Gamma\left(B^0_s\bar{B}^0_s \to l^+l^+X\right)} = \frac{|p/q|^2 - |q/p|^2}{|p/q|^2 + |q/p|^2} \approx \frac{4\,\text{Re}\left(\varepsilon_{B_s}\right)}{1 + |\varepsilon_{B_s}|^2}\,. \tag{2.3}$$

The SM prediction is $A_{\text{fs}}(B_s) = (2.06 \pm 0.57) \times 10^{-5}$ [36], and hence any asymmetry larger than $\sim 10^{-4}$ could only be a consequence of NP.

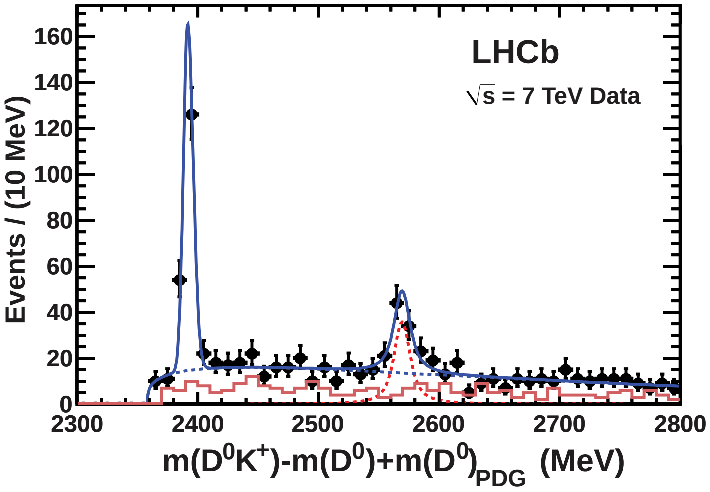

Figure 2.5: Signal for $B_s \to D^{*+}_{s2}\mu^-\nu X$ seen in ~ 20 pb^{-1} of LHCb data accumulated in 2010 [37].

If the inclusive approach is applied in a hadronic environment, the quantity measured is a linear combination of the flavour-specific asymmetries in B^0 and B_s decays. This approach has recently been used by the D0 collaboration [9, 10], with the result

$$\begin{aligned} A^b_{\rm sl} &= (0.506 \pm 0.043) \times A_{\rm fs}(B^0) + (0.494 \pm 0.043) \times A_{\rm fs}(B_s) && (2.4) \\ &= -0.00957 \pm 0.00251\,(\text{stat.}) \pm 0.00146\,(\text{syst.})\,, && (2.5) \end{aligned}$$

which is 3.2 standard deviations from the Standard Model prediction (the SM gives $A_{\rm fs}(B^0) = \left(-4.8\,^{+1.0}_{-1.2}\right) \times 10^{-4}$ [36], so that $A^b_{\rm sl}(\text{SM}) = \left(-2.3\,^{+0.5}_{-0.6}\right) \times 10^{-4}$ [9]).

One urgent goal of the first phase of LHCb is to confirm or rule out this anomaly. Large yields of semileptonic decays have already been recorded and have been used to measure the $b\bar{b}$ production cross-section [12] and to make the first observation of the decay $B_s \to D^{*+}_{s2}\mu^-\nu X$ [37], shown in Fig. 2.5. Due to the high precision required, it is necessary to use methods with intrinsically low levels of systematic uncertainty. The favoured approach in early data taking is to examine the difference between the B^0 and B_s flavour-specific asymmetries, identifying B^0 and B_s by their decays to $D^-\mu^+X$ and $D^-_s\mu^+X$ respectively, using the identical final state $K^+K^-\pi^-$ for both D^- and D^-_s decays, thereby suppressing biases from any detector asymmetries. A very precise measurement is possible with 5 fb^{-1} [38, 39].

If NP is found in this measurement, it will be necessary to perform separate measurements of $A_{\rm fs}(B^0)$ and $A_{\rm fs}(B_s)$, rather than their combination, to isolate the origin of the effect. While more precise measurements of $A_{\rm fs}(B^0)$ could potentially be made at future e^+e^- B-factories, competitive measurements of the B_s system can only be made at LHCb. Here it will be difficult to use semileptonic decays, since the systematic uncertainty due to intrinsic detector asymmetry will be hard to control. However, the hadronic decay $B_s \to D^-_s\pi^+$ is flavour-specific, and gives a symmetric final state when the $D^-_s \to K^+K^-\pi^-$ decay is used [39]. This analysis will require both very large statistics and a flexible trigger with high efficiency on hadronic decay modes, and therefore can only be carried out at the upgraded LHCb experiment.

As an aside, we mention that among the broad physics programme that can be achieved using semileptonic decays, the upgraded LHCb experiment has promising sensitivity to the

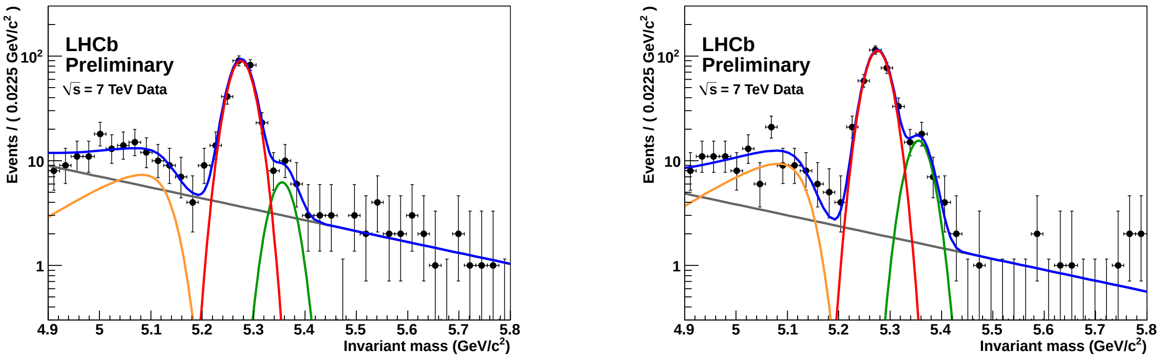

Figure 2.6: Signals for (left) $B_{(s)} \to K^-\pi^+$ and (right) $B_{(s)} \to K^+\pi^-$ seen in ~ 35 pb^{-1} of LHCb data accumulated in 2010. Signals for both B^0 and B_s decays are visible at the expected levels, and the uncorrected CP asymmetries are consistent with previous measurements [43].

decays $B \to D^{(*)}\tau\nu$. The rates of these decays are sensitive to New Physics in two-Higgs-doublet models, including supersymmetry, since tree-level diagrams involving charged Higgs bosons can interfere with the W-mediated SM amplitude [40]. The $B \to D^{(*)}\tau\nu$ decays hence probe the same physics as the e^+e^- B-factory golden channel $B^+ \to \tau^+\nu$, but in addition allow for the study of kinematical observables that provide further NP sensitivity [41]. The signature of $B \to D^{(*)}\tau\nu$ decays at LHCb is a three-prong τ decay together with a $D^{(*)}$ meson, both displaced from a B vertex that is itself displaced from the primary vertex. The decay has a large branching fraction, so very large statistics are in principle available. However, owing to the high multiplicity of the final state, the efficiency for the decay to pass a transverse energy threshold in the trigger is suppressed. This analysis will therefore benefit significantly from the flexible trigger strategy of the LHCb upgrade.

CP violation in charmless hadronic decays

Charmless hadronic B decays are in principle highly sensitive to NP, since they proceed through rare decay topologies such as penguin diagrams. However, it is an experimental and theoretical challenge to control SM uncertainties to the precision necessary. In the first phase of LHCb, the emphasis is on decays to two charged particles, where clear signals have already been observed [42], as shown in Figs. 2.6 and 2.7. In early data, we expect to make the world's first observations of direct CP violation in B_s and Λ_b decays, and to measure time-dependent CP violation in $B_s \to K^+K^-$ decays, which is sensitive to NP. We also expect to observe many new interesting decay channels, such as $B_s \to K^{*0}\bar{K}^{*0}$.

In the upgraded experiment, it will be possible to measure time-dependent CP violation in channels that have only recently been discovered, and even in some that have not yet been observed. In particularly, the penguin-dominated decays $B_s \to \phi\phi$ and $B_s \to K^{*0}\bar{K}^{*0}$ are particularly sensitive to NP [44]. For the former, the SM prediction for the time-dependent CP violation is very close to zero due to a cancellation of the B_s mixing and decay phases [45]. A SM calculation using QCD factorisation gives a theoretical upper limit of a 2% effect [46]. After collecting 5 fb^{-1} of data with the LHCb experiment, the statistical sensitivity to CP violation in $B_s \to \phi\phi$ is expected to be about 0.08 [47]. The lifetime resolution and acceptance, the angular acceptance, the B_s lifetime and mass differences and the background model will

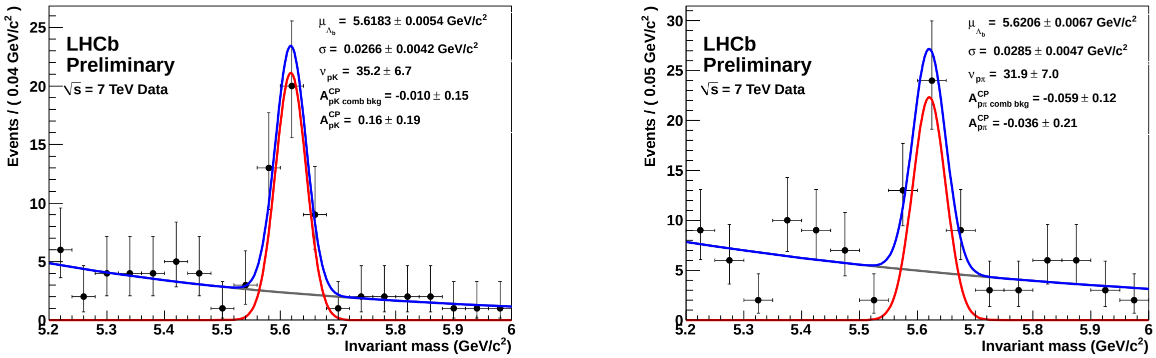

Figure 2.7: Signals for (left) $\Lambda_b \to pK^-$ and (right) $\Lambda_b \to p\pi^-$ (both including charge conjugate modes) seen in ~ 35 pb^{-1} of LHCb data accumulated in 2010.

contribute to a total systematic error of about 0.01. Therefore the precision will be at about the same level as achieved by the B-factories for the related modes $B^0 \to \phi K_S$ and $B^0 \to \eta' K_S$, and more statistics will be necessary for further improvement.

The LHCb upgrade will substantially improve the measurement of CP violation in $B_s \to \phi\phi$, since this a hadronic mode which will benefit maximally from the detached vertex trigger. To reach the highest precision it will be necessary to remove the possible S-wave contributions from non-resonant $B_s \to \phi K^+K^-$ and $B_s \to \phi f_0$ decays [31]. Studies have shown that these can be incorporated into the analysis without causing a bias, albeit with an increase in statistical error of less than 15% [32]. With 50 fb^{-1} of data accumulated with the upgraded experiment, a sensitivity of a few percent, comparable to current estimates of the theoretical uncertainty, is achievable.

The decay $B_s \to K^{*0}\bar{K}^{*0}$ has similar phenomenology to $B_s \to \phi\phi$, and the experimental sensitivities that can be reached in the two cases are also comparable. The advantage of this mode is that the SM contribution can be determined from data in a model-independent analysis that uses information extracted from the related $B^0 \to K^{*0}\bar{K}^{*0}$ decays [48].

The polarisation of the decays $B_s \to \phi\phi$ and $B_s \to K^{*0}\bar{K}^{*0}$ is also of great topical interest, due to the so-called "polarisation puzzle", i.e. the unexpectedly large transverse polarisation observed in $B \to \phi K^*$ and $B \to \rho K^*$ decays (see Ref. [49] for reviews). The polarisation of B_s decays to charmless vector-vector final states can be measured to high precision since the analysis does not require flavour-tagging.

The LHCb upgrade will also improve the precision of several interesting measurements involving ϕ mesons, such as $B^0 \to \phi K^0_S$ and $B^0 \to \phi K^{*0}$. The CP violating asymmetry in ϕK^0_S can be measured to an accuracy of 0.03 and is expected to be similar to the theoretical uncertainty.

The LHCb upgrade will also be uniquely capable of making the first detailed analyses of multibody decays of the B_s meson, such as $B_s \to K_S\pi^+\pi^-$ and $B_s \to K_S K^\pm\pi^\mp$. Together with the related B^0 and B^+ channels, analyses of the Dalitz plot distributions provide several exciting prospects for NP searches [50].

Measurement of the CKM Unitarity Triangle angle γ

Searches for New Physics in CP violation effects require precise measurements of Standard

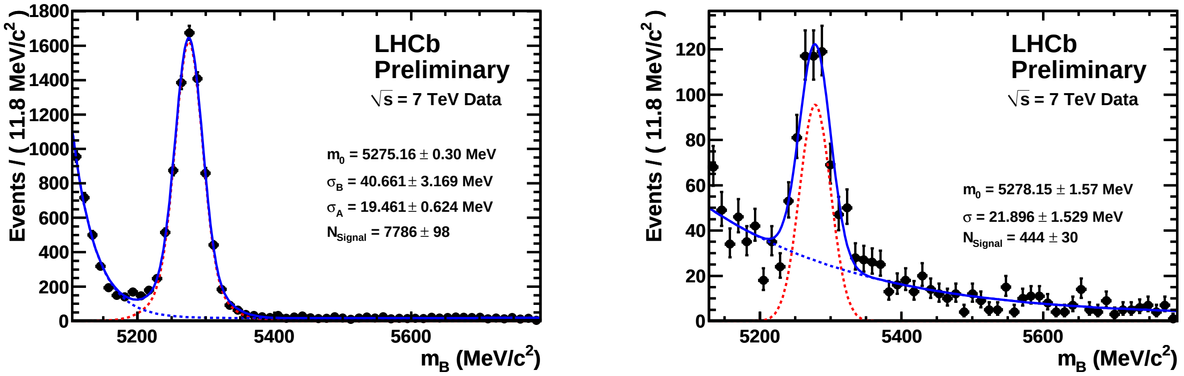

Figure 2.8: Signals for (left) $B^+ \to \bar{D}^0\pi^+$ and (right) $B^+ \to \bar{D}^0 K^+$ seen in ~ 34 pb^{-1} of LHCb data accumulated in 2010. In both cases the $\bar{D}^0 \to K^-\pi^+$ decay is used.

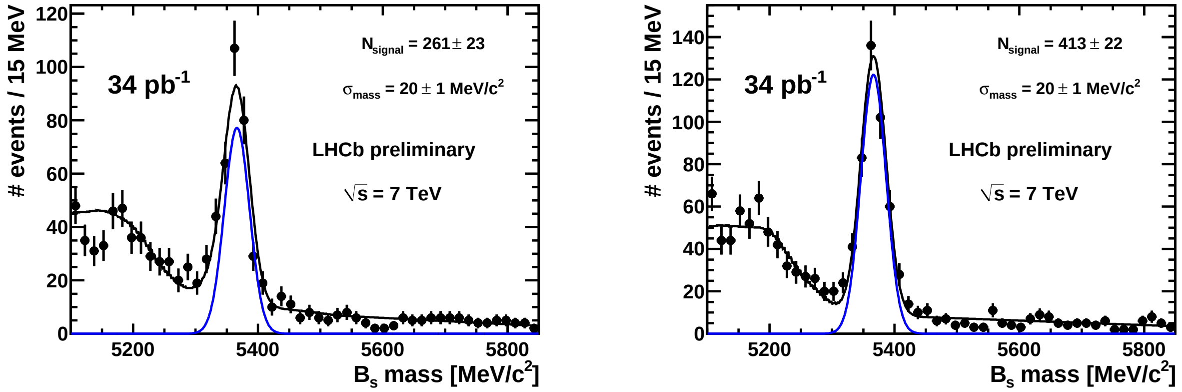

Figure 2.9: Signals for $B_s \to D_s\pi$ with (left) $D_s \to K^*K$ and (right) $D_s \to \phi\pi$ seen in ~ 34 pb^{-1} of LHCb data accumulated in 2010.

Model benchmarks to compare against. Key to this programme is the measurement of the CKM Unitarity Triangle angle γ, which can be determined with negligible theoretical uncertainty using $B \to DK$ decays such as $B^+ \to DK^+$ [51], $B^0 \to DK^{*0}$ [52] and $B_s \to D_s^{\mp}K^{\pm}$ [53].

At present, γ is the least well-determined of the three angles of the Unitarity Triangle, and does not provide any significant constraint in global fits fits to the CKM matrix carried out by groups such as CKMfitter [5] and UTfit [6]. This situation will change when results become available from LHCb.

The signals of $B \to D\pi$ and $B \to DK$ decays already seen by LHCb, shown in Figs. 2.8 and 2.9, illustrate the impact on γ that LHCb will make with early data. By combining γ measurements from $B \to DK$ and $B_s \to D_s^{\mp}K^{\pm}$, a sensitivity of 3° is expected with 5 fb^{-1}. However, precision at the level of one degree or below is necessary to avoid limiting the sensitivity of the global CKM fits to New Physics. Specifically, the indirect constraint on γ from the magnitude of the CKM matrix element V_{ub} and the ratio of mass-differences in the neutral B systems, $\Delta m_d/\Delta m_s$, is expected to reach sub-percent accuracy as more advanced lattice calculations become available [54]. This motivates a concerted effort to provide the best possible measurement of γ.

Only the LHCb upgrade will provide the huge statistics needed to reach the precision that is necessary to remove the Standard Model uncertainty in New Physics searches. Indeed, the measurement of γ is ideally suited for LHCb, since it is based largely on analyses (i) that do not require flavour-tagging, and (ii) that exploit LHCb's unique capability to trigger on fully hadronic decay modes. Due to this second reason, the measurement will benefit greatly from the improved trigger strategy of the upgraded experiment. With 50 fb^{-1}, γ will be determined to better than 1° precision. This will allow to test the consistency of the SM at the percent level. Moreover, as discussed in Section 2.1.2, once new sources of CP violation are established the measurement of γ will be particularly important to disentangle the parameters of the underlying model.

2.1.4 Rare decays

Measurement of $B_s \to \mu^+\mu^-$ and $B^0 \to \mu^+\mu^-$

One area where the impact of the increased statistical power of the upgraded LHCb experiment is profound is in rare decays. There are several key modes that offer large discovery potential. One of the most interesting is the very rare decay $B_s \to \mu^+\mu^-$. As discussed in Section 2.1.2, this flavour-changing neutral current is heavily suppressed in the SM, and is highly sensitive to New Physics [55]. In particular, in the CMSSM at large $\tan\beta$, the branching fraction $\mathcal{B}(B_s \to \mu^+\mu^-)$ increases as $\tan^6\beta$, where $\tan\beta$ is the ratio of Higgs vacuum expectation values, and depends on the gaugino mass, $m_{1/2}$ and the trilinear soft supersymmetry-breaking parameter A_0. The predictions of Ellis *et al.* [56] are shown in Fig. 2.10. The measurement of this branching fraction provides one of the strongest constraints on the parameters of this model at high $\tan\beta$.

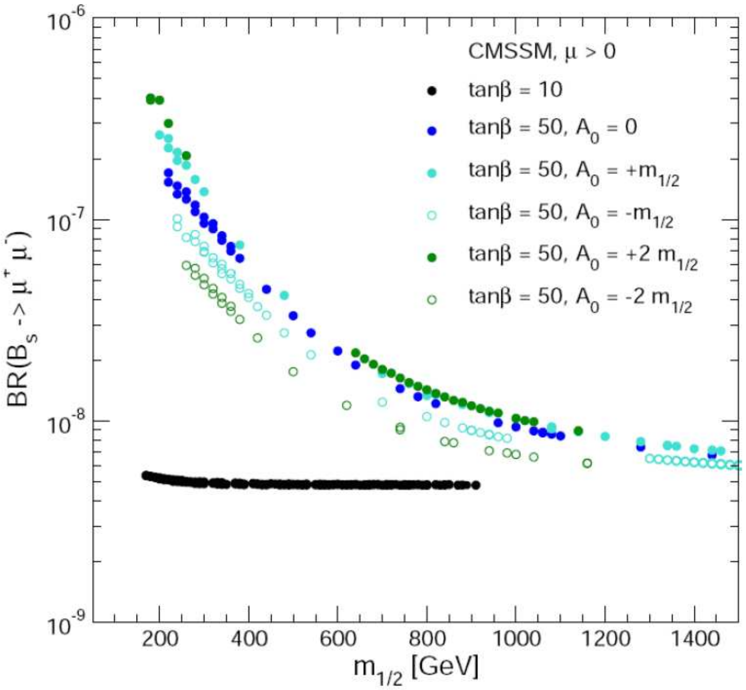

..

Figure 2.10: Predictions for $\mathcal{B}(B_s \to \mu^+\mu^-)$ as a function of the gaugino mass $m_{1/2}$ for selected values of $\tan\beta$ and the A_0 mass. From Ref. [56].

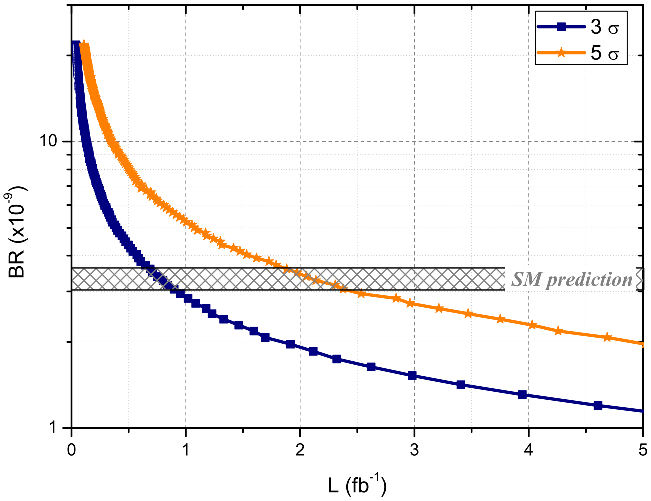

Figure 2.11: Discovery potential of LHCb to $\mathcal{B}(B_s \to \mu^+\mu^-)$ as a function of integrated luminosity for 14 TeV centre-of-mass energy collisions. The upper (lower) curve shows the data sample necessary to discover the decay with 5 (3) σ significance.

LHCb has searched for $B_s \to \mu^+\mu^-$ using about 40 pb^{-1} collected in 2010 [57]. No signal is found, and an upper limit is set at the 90% C.L. of 43×10^{-9}. This is already very similar to the corresponding limits placed by the Tevatron experiments, which are 36×10^{-9} [58] and 42×10^{-9} [59], obtained by CDF and D0 with 3.7 fb^{-1} and 6.1 fb^{-1} respectively.

The sensitivity of the first LHCb result agrees with the expectations from the Monte Carlo, and gives confidence for the future of this search over the coming years. The discovery potential of LHCb is shown in Fig. 2.11 as a function of integrated luminosity. The figure is made assuming a centre-of-mass energy of 14 TeV. Although the sensitivity of the Tevatron experiments will rapidly be surpassed, a $5\,\sigma$ discovery will require several years of operation if $\mathcal{B}(B_s \to \mu^+\mu^-)$ is at the SM level, or below. (It is also worth drawing attention to the possibility that in several NP models, in particular those with a Higgs singlet, the branching ratio may indeed be *suppressed* with respect to the SM value [60].)

Whether or not the decay is observed in early LHC data, further improvement will be necessary in the knowledge of its branching fraction. It is important to note that the measurement is expected to be statistically limited. Until recently the knowledge of the ratio of fragmentation fractions, f_s/f_d, was thought to provide a limiting factor. However, LHCb has already measured this ratio with semileptonic decays to 10% accuracy [61], and further improvement will occur. Alternative methods to measure f_s/f_d using hadronic decays have also been proposed [62].

With a 50 fb^{-1} data sample the upgraded LHCb experiment would be able to measure the branching ratio $\mathcal{B}(B_s \to \mu^+\mu^-)$ to about 8% precision if it is at the SM level. This will provide unique insights into the flavour properties of NP, and will put very stringent constraints on SUSY models in the large $\tan\beta$ regime. In the ideal scenario that SUSY particles are discovered at ATLAS and CMS, the combination of their results with those from the LHCb upgrade will allow the best constraints on the parameter space.

As soon as $B_s \to \mu^+\mu^-$ is observed for the first time, attention will turn to its sister channel,

$B^0 \to \mu^+\mu^-$. As discussed in Section 2.1.2, the correlation between the branching fractions of these two channels is extremely useful to distinguish between different NP models, and is essential to confirm or rule out the MFV hypothesis [63]. The B^0 decay is both much rarer than the B_s decay, and suffers from a larger background from pion misidentification and decay-in-flight, since the branching fraction for $B^0 \to \pi^+\pi^-$ (5×10^{-6} [43]) is much larger than that for $B_s \to \pi^+\pi^-$ ($< 1.2 \times 10^{-6}$ [64]). Therefore the full statistics of the upgraded LHCb experiment, together with excellent control of this background, will be necessary to measure the $B^0 \to \mu^+\mu^-$ decay.

Analysis of $B^0 \to K^{*0}\mu^+\mu^-$ and related decays
Exclusive decays of the type $H_b \to H_s\mu^+\mu^-$, where H_b is a b-flavoured hadron and H_s is a hadronic system containing an s quark produced in a $b \to s$ flavour-changing neutral current transition as well as the spectator quark(s) from H_b, have a high sensitivity to New Physics. Many of these can be reconstructed in large quantities at LHCb: the archetypal channel in this category is $B^0 \to K^{*0}\mu^+\mu^-$, but other decays such as $B^+ \to K^+\mu^+\mu^-$, $B^+ \to K_1^+\mu^+\mu^-$, $B^0 \to K_2^{*0}\mu^+\mu^-$, $B_s \to \phi\mu^+\mu^-$ and $\Lambda_b \to \Lambda^{(*)}\mu^+\mu^-$ will be available in large quantities at the upgraded LHCb experiment, and provide complementary New Physics sensitivity.

One of the characteristic features of the $B^0 \to K^{*0}\mu^+\mu^-$ decay is the forward-backward asymmetry in the angular distribution of the muons in the dimuon rest-frame (relative to the B^0 direction) as a function of the dimuon invariant mass, q^2. This asymmetry arises as a consequence of interference between the contributing electroweak diagrams, and can be expressed in terms of the Wilson coefficients $C_{7\gamma}$, C_9 and C_{10} (see Ref. [4] for a review). Since the relative amplitudes of the interfering diagrams vary as a function of q^2, there is a point at which the forward-backward asymmetry crosses zero, usually denoted $q^2 = s_0$. Due to a cancellation of hadronic uncertainties, the value of s_0 is cleanly predicted in the SM to be $s_0 = \left(4.36\,^{+0.36}_{-0.33}\right)$ GeV^2 [65]. First measurements of the differential distributions have been made by the B-factories and CDF, with results providing an exciting hint of a deviation from the SM prediction [66].

One of the main objectives of the first phase of LHCb data taking is a precise measurement of the forward-backward asymmetry in $B^0 \to K^{*0}\mu^+\mu^-$ decays. LHCb expects to collect 2100 $B^0 \to K^{*0}\mu^+\mu^-$ decays per 1 fb^{-1} at $\sqrt{s} = 14$ TeV, allowing s_0 to be measured with precision comparable to the theory error after a few years of data-taking [11]. If large NP effects are present, as hinted at by the current measurements, LHCb will measure a deviation from the SM prediction with high significance. Whether or not NP effects manifest themselves in the early data, it will be necessary to perform higher statistics studies in order to exploit the full sensitivity of these decays.

The $B^0 \to K^{*0}\mu^+\mu^-$ decay provides extremely rich phenomenology due to the many different kinematic observables that can be studied. In addition to the forward-backward asymmetry, one particularly interesting observable is the transversity asymmetry $A_T^{(2)}$ that can distinguish between different New Physics models [67, 68]. $A_T^{(2)}$ is highly sensitive to new right-handed currents to which the forward-backward asymmetry is blind. In the theoretically favoured region, 1 GeV^2 $< q^2 <$ 6 GeV^2, the resolution in $A_T^{(2)}$ is estimated at 0.14 with 5 fb^{-1} of integrated luminosity [68]. This is illustrated in Fig. 2.12 where we show $A_T^{(2)}$ versus q^2 for the SM and a NP model as well as the experimental sensitivity. It is clear that a larger data sample will be necessary in order to probe the full parameter space. These measurements can

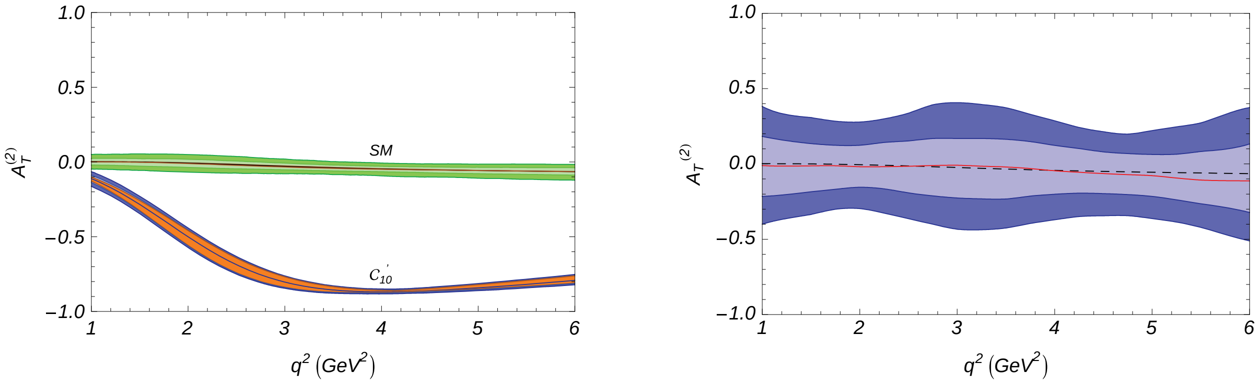

Figure 2.12: (Left) $A_T^{(2)}$ in the SM in green and with NP in blue. The inner line corresponds to the central value of each curve. The dark orange bands surrounding it are the NLO results and the external dark green/blue bands correspond to a 10% correction for each spin amplitude. (Right) expected experimental sensitivity, assuming the SM central values. The inner and outer bands correspond to 1σ and 2σ statistical errors with a yield corresponding to a 10 fb^{-1} data set from LHCb.

only be performed at the upgraded LHCb experiment, since no other experiment can reach the necessary level of statistics.

Among related modes, several provide interesting complementary NP searches. The forward-backward asymmetry in $B^+ \to K^+\mu^+\mu^-$ is zero in the SM, but can take different values in models with new scalar or pseudoscalar couplings to the leptons [69]. It is also of interest to study the ratio $R_K = \mathcal{B}(B^+ \to K^+e^+e^-)/\mathcal{B}(B^+ \to K^+\mu^+\mu^-)$, which is equal to unity to good accuracy in the SM, and can be affected by NP [70]. Signals for the $B^+ \to K^+\mu^+\mu^-$ decay have already been seen by LHCb, as shown in Fig. 2.13. Similarly, the $B^+ \to K_1^+\mu^+\mu^-$ and $B^0 \to K_2^{*0}\mu^+\mu^-$ decays provide means to search for NP effects when the meson in the final state is an axial-vector or a tensor, respectively. Similarly, the baryons involved in $\Lambda_b \to \Lambda^{(*)}\mu^+\mu^-$ provide another handle on potential NP amplitudes. The unique feature of $B_s \to \phi\mu^+\mu^-$ is that it allows CP violation in interference between mixing and decay amplitudes to be probed. The upgraded LHCb experiment has unsurpassed potential for all of these analyses.

Measurement of photon polarisation in exclusive $b \to s\gamma^{(*)}$ decays

Since $b \to s\gamma$ is a theoretically clean flavour changing neutral current transition, decays mediated by this amplitude are highly sensitive to NP. (We include here the $K^*e^+e^-$ final state.) One particularly interesting feature of this system is that in the SM, the emitted photon is highly polarised. However, this is not the case in extensions of the SM that introduce new right-handed currents. It is therefore of great importance to measure the emitted photon polarisation, which is an experimental challenge.

One particularly promising approach is to study the time-dependent decay distribution of $B_s \to \phi\gamma$ [71]. The key feature of the analysis is that if the emitted photons are polarised, there is no interference between B_s and $\bar{B}_s$ decays (since the final states are, in principle, distinguishable). However, if the photons are not fully polarised, CP violation effects can occur at rates that depend on the level of polarisation as well as on the weak phase. Two particularly attractive features of the analysis of $B_s \to \phi\gamma$, compared to similar measurements in the B^0 system, are that (i) the $\phi \to K^+K^-$ decay provides a clean signature, with the tracks

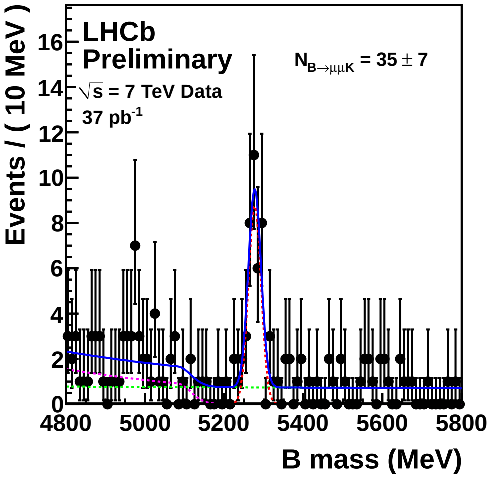

Figure 2.13: Signal for $B^+ \to K^+\mu^+\mu^-$ seen in ~ 37 pb^{-1} of LHCb data.

originating from the B_s vertex; (ii) the sizable B_s width difference allows the measurement of both $S_{\phi\gamma}$ and $\mathcal{A}^{\Delta\Gamma}_{\phi\gamma}$ (defined in Eq. 2.1) [72]. These are proportional to $\sin 2\psi \sin 2\beta_s$ and $\sin 2\psi \cos 2\beta_s$ respectively, where $\tan\psi$ describes the polarisation ($\tan\psi = 0$ for fully polarised decays). Hence the polarisation can be measured even if the weak phase $2\beta_s$ is small, as in the SM.

LHCb expects a yield of 5.5k $B_s \to \phi\gamma$ events in 1 fb^{-1} of data with a background to signal ratio $< 0.6 - 0.9$ at 90% C.L. [11]. The related decay $B^0 \to K^{*0}\gamma$ has already been seen in LHCb data, as shown in Fig. 2.14. The data from the first phase of LHCb operation will allow the photon polarisation to be measured to about 0.10. This will be a significant improvement on the existing measurements by the B-factories using $B^0 \to K_S\pi^0\gamma$ [43], but will still leave a large region of phase space unexplored. The analysis will benefit maximally from the flexible software trigger of the LHCb upgrade, allowing data samples of over 40,000 $B_s \to \phi\gamma$ decays to be collected per year. With 50 fb^{-1} of data, the sensitivity to the photon polarisation will be improved to the percent level, and will probe the theoretically most interesting region of phase space.

Other approaches to determine the photon polarisation are also under study. The decay $B^0 \to K^{*0}e^+e^-$ at low values of the dilepton invariant mass-squared (either via virtual photons or by real photons converting in detector material) can be used [73]. Another approach uses analysis of the multibody final state in $B^+ \to K_1^+\gamma \to K^+\pi^+\pi^-\gamma$ [74]. A similar analysis of $B^+ \to \phi K^+\gamma$ decays has also been proposed [75]. All of these analyses are well-suited for the upgraded LHCb experiment.

Rare hadronic B decays

Finally, it is worth noting that there are several rare hadronic B decays that are of considerable theoretical interest, for which only the LHCb upgrade will provide sufficient statistics to allow useful measurements. For example, pure annihilation decays such as $B^+ \to D^+K^{*0}$ and $B^+ \to D_s^+\phi$ could be observed at their SM branching fractions with the LHCb upgrade [76]. These observations would provide unique insight into the dynamics of hadronic B decays.

Similarly, the isospin violating decays $B_s \to \phi\rho^0$ and $B_s \to \phi\pi^0$ provide a clean handle on

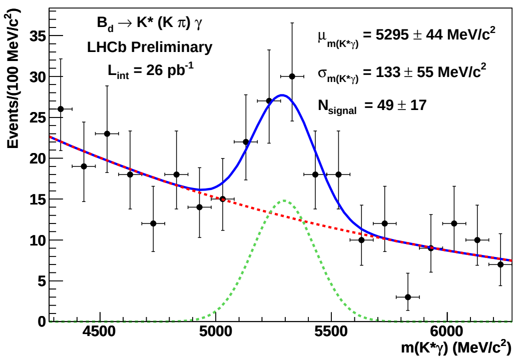

Figure 2.14: Signal for $B^0 \to K^{*0}\gamma$ seen in ~ 26 pb^{-1} of LHCb data.

electroweak penguin decays [77]. The branching fractions for these decays are $\mathcal{O}(10^{-7})$ in the SM, but can be significantly modified in various NP scenarios, for example those with extended gauge sectors (i.e. with a Z' boson). These decays can only be studied at LHCb, and require the flexible software trigger of the upgraded experiment.

On the other hand, the decays $B^+ \to K^+K^+\pi^-$ and $B^+ \to K^-\pi^+\pi^+$ are negligibly small in the SM, but can be enhanced by NP to observable levels. These rare decays are complementary to B^0 and B_s oscillations in providing sensitivity to NP at very high energies [78].

2.1.5 Charm physics

The study of charm is an essential component in the flavour physics programme. The extremely small level of CP violation expected in charm mixing and in decays offers the opportunity for very sensitive null tests of the CKM picture to be performed. Many New Physics models predict significant enhancement in these quantities, as well as distinctive correlations between observables in the charm sector and those accessible in the B system [79]. Charm therefore is a laboratory in which New Physics can both be discovered, and its nature characterised.

Outstanding charm physics will be performed with the present LHCb detector. Already with the 37 pb^{-1} of data collected during the 2010 run the experiment has accumulated samples of $D^0 \to h^+h^-$ decays of similar size to those of the B-factories. These samples are of high purity, as can be seen in Fig. 2.15 for the example mode $D^{*+} \to D^0\pi^+$, $D^0 \to K^+K^-$. The yields in higher multiplicity modes are however significantly lower, due to the constraints of enforcing a p_{T} requirement at the earliest trigger level, with a threshold that is tuned to the needs of B physics. This problem will very likely be accentuated in the 2011 run, where the increased interaction rate may necessitate raising the threshold still higher. The full software-based trigger strategy of the upgraded detector, however, will allow decays of all topologies to be selected with high efficiency.

The upgraded detector will accumulate yields of D decays that are two-to-three orders of magnitude larger than those collected at BABAR and Belle. These enormous samples will allow for a dramatic improvement in sensitivity to the mixing-related CP-violating parameters ϕ_D and $(|q/p|_D - 1)$ which are currently measured to be -0.18 ± 0.16 and -0.10 ± 0.18 respectively [43]. Similar improvements will also come in the search for direct CP-violating effects, which are final state specific, and are most promisingly searched for in singly-Cabibbo

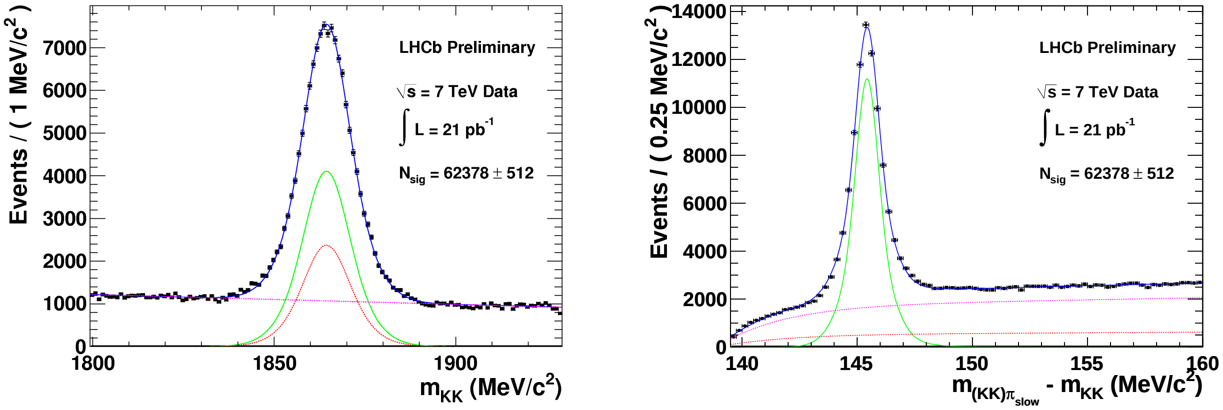

Figure 2.15: The D^0 mass and $D^{*+} - D^0$ mass distributions for $D^{*+} \to D^0\pi^+$, $D^0 \to K^+K^-$ events (plus charge conjugate) for $21\,\text{pb}^{-1}$ of 2010 LHCb data.

suppressed decays [80]. In such modes Standard Model CP-violation may occur at the 10^{-3} level, whereas the statistical precision of the LHCb measurements will be 10^{-4}. Therefore it will be essential to study these effects across a wide range of decays in order to categorise the underlying physics.

There are good reasons to believe that the enormous statistical power of the upgraded experiment can be complemented by the necessary control of systematic uncertainties. In time-dependent analyses the excellent resolution of the detector will contribute negligible uncertainty, in contrast to the situation at e^+e^- machines. The backgrounds lying under the signal peaks are already known to be low, and can be understood from side-band studies. Since biases such as detection asymmetries can be measured from data, it can be assumed that the understanding of these effects will improve in step with the increased statistical precision. Finally, many analyses can be pursued which are intrinsically robust against both experimental and theoretical uncertainty. A few examples are listed below.

- The observable A_Γ, which is the lifetime asymmetry between $D^0 \to K^+K^-$ and $\overline{D}^0 \to K^+K^-$ decays, probes CP-violation in mixing-related phenomena, and is not biased at first-order by any acceptance effects.

- The *difference* in the raw time-integrated CP-asymmetry between $D^0 \to K^+K^-$ and $D^0 \to \pi^+\pi^-$ provides a probe of direct CP-violation that has *no* systematic uncertainty arising from production or detection efficiencies.

- Dalitz plot analyses provide a sensitive and systematically robust way both to search for and measure CP-violating effects. Direct CP violation can be probed for in singly-Cabibbo suppressed decays, such as $D^+ \to K^+K^-\pi^+$ in a model independent manner [81], and exploiting Cabibbo-favoured modes such as $D_s \to K^+K^-\pi^+$ and $D^+ \to K^-\pi^+\pi^-$ for systematic control. In four-body modes such as $D^0 \to K^+K^-\pi^+\pi^-$ measurements exploiting T-odd correlations [82] are also model independent and experimentally robust.

- Similarly the CP-violating parameters ϕ_D and $(|q/p|_D - 1)$ can be measured from a time-dependent analysis in $D^0 \to K^0_S h^+h^-$ decays in a model independent binned fit [83], making use of strong-phase measurements that already exist from CLEO-c [84] and will be further improved at BES-III.

The upgraded detector will also allow for improved sensitivity to important rare charm decays. The present experimental upper limit on the branching ratio for $D^0 \to \mu^+\mu^-$ is 1.4×10^{-7} at the 90% C.L. [85], still six orders of magnitude above the Standard Model prediction [86]. Significant enhancements to this decay may come about through R-parity violating supersymmetry [86] or the contribution of leptoquarks [87]. Similar possibilities exist with the lepton-flavour violating decay $D^0 \to e^\pm\mu^\mp$. These super-rare or forbidden modes will be searched for with a sensitivity far in excess of that achievable at present facilities. Other less suppressed decays such as $D^0 \to \rho\mu^+\mu^-$ and $D^+ \to \pi^+\mu^+\mu^-$ may possibly be first observed with the existing detector. However the high statistics that the upgraded experiment will accumulate will allow kinematic distributions to be mapped out in detail, such as the lepton forward-backward asymmetry and the invariant mass spectrum of the dimuon pair, which are powerful discriminants between the Standard Model and New Physics [86].

2.2 Lepton Flavour Physics

One of the most promising frontiers to explore in the hunt for NP is that of flavour violating phenomena in the lepton sector. Neutrino oscillations are now an established experimental fact, but the very low mass scale of neutrinos remains to be understood. NP models predict the existence of flavour-violating charged lepton decays, but no such decays have so yet been observed. The upgraded LHCb detector can make significant contributions to these studies, through the search for heavy Majorana neutrinos and lepton flavour-violating τ^- decays.

2.2.1 Searches for ~ 1 GeV Majorana neutrinos

The existence of heavy Majorana neutrinos is a natural occurrence in a wide range of models, from left-right symmetric gauge theories [88], to those with extra dimensions [89]. In most models it is quite possible for these particles to exist in the ~ 1 GeV/c^2 mass range. One interesting example is the "Neutrino Minimal SM" (νMSM) [90], in which such a scenario is indeed preferred. Majorana neutrinos of mass ~ 1 GeV/c^2 can be searched for in decays of D and B mesons, and constitute an exciting physics goal for an upgraded LHCb experiment.

In the νMSM three Majorana singlet fermions are added to the SM particles. The lightest of the three new leptons is expected to have a mass of 1–50 keV/c^2 and would form a viable dark matter candidate. The two other neutral fermions, which are essentially heavier, sterile neutrinos, can give masses to the SM neutrinos via the see-saw mechanism at the electroweak scale. They would also play a key role in generating the baryon asymmetry of the universe (for a review see [91]). Thus the νMSM is able to explain three known deficiencies of the SM (dark matter, the baryon asymmetry of the universe and the problem of neutrino mass), and has the further appealing feature that every left-handed fermion then has a right-handed counterpart. The masses of these heavy sterile neutrinos and their coupling to ordinary leptons are constrained by direct searches at particle physics experiments and, importantly, by cosmological considerations, as shown in Fig. 2.16. The requirement that baryogenesis occurs necessitates that the masses of the heavier two neutrinos be almost degenerate and $\mathcal{O}(1)$ GeV/c^2 [92].

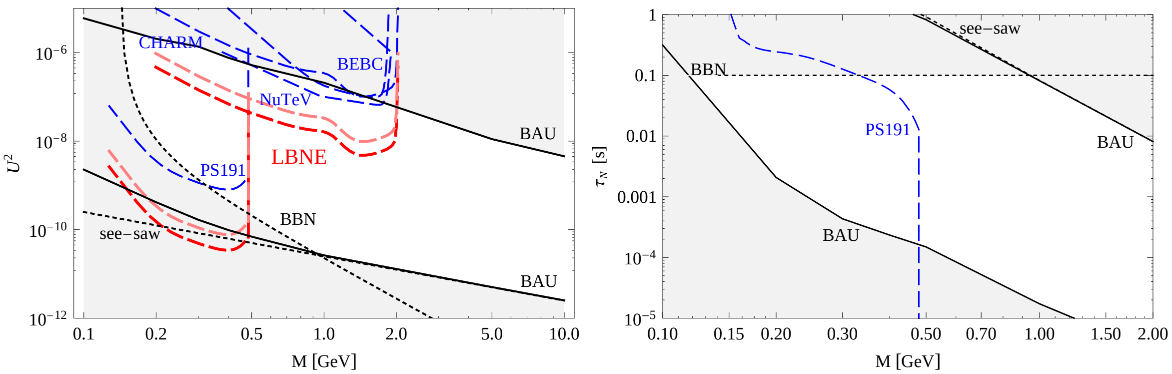

Figure 2.16: Constraints on the sterile-to-active neutrino mixing angle squared, U^2, and on the sterile neutrino lifetime, τ_N. These come from the baryon asymmetry of the Universe (solid lines); from the see-saw formula (dotted line); and from requiring Big Bang nucleosynthesis (dotted line). These constraints are shown for the case of an inverted hierarchy in the active neutrino sector. The regions excluded by direct experimental searches are indicated by the blue dashed lines [96, 97]. The pink and red curves indicate the expected sensitivity of the proposed LBNE detector at FNAL in two possible configurations.

A powerful approach to searching for ~ 1 GeV/c^2 Majorana neutrinos is in the decay of heavy flavours [93, 94, 95]. Two main strategies exist that are accessible to LHCb:

1. **Direct search**: looking for long lived neutrinos produced in the decay of D and B mesons;
2. **Indirect search**: looking for production of same-sign charged leptons in D, B and τ decays.

Both of these methods are well suited to the upgraded experiment, the former on account of the benefits that a fully software trigger will bring to the search, the latter because of the very large data samples that will be accumulated, allowing for very low branching ratios to be accessed.

Direct search Sterile neutrinos could be produced in the weak decays of charm and beauty hadrons, in which mixing occurs between the SM neutrinos and the new particles. Relevant examples of two- and three-body decays are shown in Fig. 2.17. The presence of the massive sterile neutrinos in the decay eliminates the chirality suppression that would otherwise be present. Interesting branching ratios therefore start at the level of 10^{-7} (see [97, 95] for details). Since such sterile neutrinos would be very weakly interacting, they would cover a relatively large distance before decaying, but as long as $\sim 10^{-4}$ or more of decays occur within 0.5 m of the production point, this signature would be observable with the upgraded experiment, where the software trigger would provide excellent efficiency for the long lifetime and distinctive topology. Charm decays would provide higher sensitivity for lower mass neutrinos.

Indirect search Heavy sterile neutrinos could also be probed by searching for resonant contributions to lepton number violating processes such as $D_s^\pm \to \pi^\mp \ell^\pm \ell^\pm$ or $B^\pm \to \pi^\mp \ell^\pm \ell^\pm$ [93, 94], as indicated in Fig. 2.18. Here the heavy quark annihilates with the spectator antiquark to

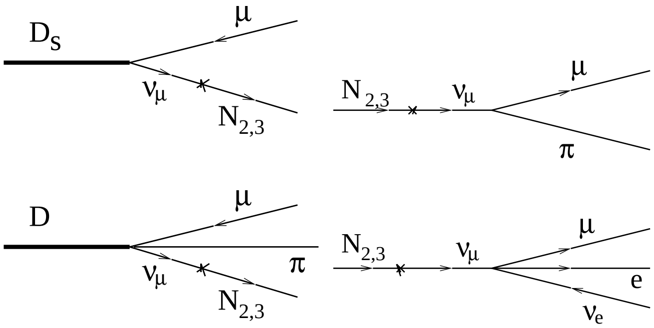

Figure 2.17: Left: Feynman diagrams of charm meson decays producing heavy sterile neutrinos. Right: Feynman diagrams of sterile neutrino decays.

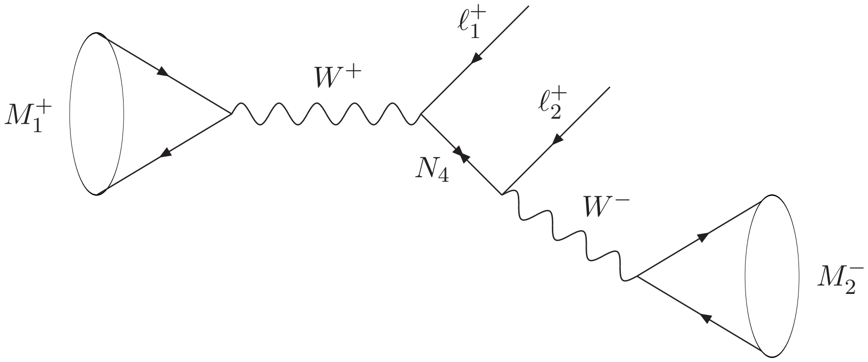

Figure 2.18: The Feynman diagram for meson decay via a lepton number violating process involving Majorana neutrinos. From Ref. [93].

produce a virtual W that can form a lepton-neutrino pair. Assuming so far only SM neutrinos, this process has been used to measure decay constants in such processes as $D_s^+ \to \mu^+\nu$ or constrain CKM elements and charged Higgs contributions in the decay $B^- \to \tau^-\nu$. If, however, the neutrino is Majorana, it can mix into a heavier neutrino that can decay into the same sign W as it was produced in association with, and the W can transform into a like-sign lepton and a hadron, as indicated in the figure. (In this figure and Fig. 2.19 N_4 indicates a fourth Majorana neutrino with mass m_4 at the GeV scale.) Looking for such a signature is analogous to laboratory based experiments which search for neutrino-less double β-decay.

The branching ratio of such decays is suppressed by the mixing between the light flavour and heavy neutrinos, $V_{\ell N}$. In the sterile neutrino mass range of $\mathcal{O}(1)$ GeV/c^2 accessible with B decays, strong constraints on V_{eN} are imposed by the non-observation of neutrino-less double beta decay ($|V_{eN}|^2 < 10^{-7}$). Searches for the decay products of heavy sterile neutrinos at LEP constrain the equivalent mixing angle for muons, $V_{\mu N}$, to be $|V_{\mu N}|^2 < 10^{-4}$. This could give branching ratios for decays such as $B^\pm \to \pi^\mp\mu^\pm\mu^\pm$ at the level of $10^{-8} - 10^{-9}$ which would be accessible at an upgraded LHCb. Other beauty and charm hadron decays can be included in the search. A particularly attractive choice is the mode $B^\pm \to D_s^\mp\mu^\pm\mu^\pm$ where the backgrounds are expected to be very low, allowing the statistical power of the upgraded experiment to be fully exploited. Existing bounds in coupling-mass space from heavy flavour decays are shown in Fig. 2.19.

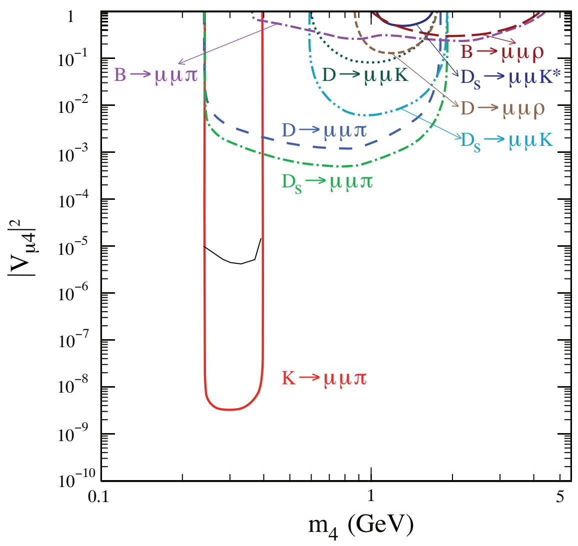

Figure 2.19: Existing bounds on $|V_{\mu 4}|^2$ versus m_4 from meson data, from Ref. [93].

2.2.2 Lepton flavour-violating τ^- decays

No lepton flavour-violating tau or muon decay has yet been observed. Such decays are forbidden in the classical SM, are vanishingly small in the SM extended to include neutrino mixing, but can be enhanced up to observable values in many NP models. The LHC is a prolific source of τ leptons, with an expected production cross-section of ~ 0.1 mb at $\sqrt{s} = 14$ TeV. The majority of produced τ leptons come from the decay of D_s mesons and B hadrons. The LHCb upgrade will use this sample to search for lepton flavour violating decays to charged track final states.

The current 90% C.L. upper limits from the B-factories on branching ratios for the channels $\tau^\mp \to \mu^\mp\gamma$ and $\tau^\mp \to \mu^\mp\mu^+\mu^-$ are at 4.4×10^{-8} and 2.1×10^{-8} [98]. In supersymmetric extensions of the SM, e.g. in the so-called constrained MSSM, lepton flavour violation in τ decays is predicted at a level of 10^{-9} for $\tau^\mp \to \mu^\mp\gamma$ and at 10^{-10} to 10^{-12} for $\tau^\mp \to \mu^\mp\mu^+\mu^-$ and $\tau^\mp \to \mu^\mp e^+e^-$ [99]. In other models, such as the so-called Non Universal Higgs Masses (NUHM) SUSY scenario, or the MSSM with R-parity violation and the Little Higgs Models with T parity (LHT) or Z' models with non-vanishing LFV couplings, the rate of $\tau^\mp \to \mu^\mp\mu^+\mu^-$ can be enhanced to the extent that it matches or even exceeds $\tau^\mp \to \mu^\mp\gamma$ [100].

Sensitivity studies for $\tau^\mp \to \mu^\mp\mu^+\mu^-$ are ongoing. With the existing analysis strategy LHCb will be able to match the B-factory sensitivity with a few fb^{-1}. The very large integrated luminosity that will be collected by the upgraded experiment will provide a sensitivity corresponding to an upper limit of the order of 10^{-9}. Searches will also be conducted in modes such as $\tau^\mp \to \mu^\mp\phi$ where the existing limits are much weaker, and very low contamination is expected in the LHCb sample.

Finally, searches will be performed for decays such as $\tau^\mp \to \mu^\mp h_1^\pm h_2^\pm$ $(h_i = \pi, K)$. The physics interest of these topologies is identical to those meson decays discussed in Sec. 2.2.1. The best limit obtained from the B-factories is 3.7×10^{-8} for the mode $\tau^\mp \to \mu^\pm\pi^\mp\pi^\mp$ [101]. The upgraded LHCb experiments will be able to attain an order of magnitude higher sensitivity.

2.3 Physics Beyond Flavour

An upgraded LHCb has the potential to make important contributions to non-flavour physics. The forward-acceptance, flexible software trigger, powerful vertexing and particle identification capabilities provide the experiment with the opportunity to perform very significant measurements in topics far beyond the core programme, and high sensitivity in certain direct particle searches. A few illustrative examples are now given, selected from the diverse areas of electroweak physics, exotic searches, and QCD.

2.3.1 Electroweak physics

Two of the most important quantities in electroweak physics are the sine of the effective electroweak mixing angle for leptons, $\sin^2\theta_{\rm eff}^{\rm lept}$, and the mass of the W-boson, m_W. Until the ILC or CLIC is operational, responsibility for improving our knowledge of these parameters rests with the LHC. Thanks to its unique forward coverage, an upgraded LHCb can make critical contributions to this programme.

The value of $\sin^2\theta_{\rm eff}^{\rm lept}$ can be extracted from $A_{\rm FB}$, the forward-backward asymmetry of leptons produced in Z decays. The raw value of $A_{\rm FB}$ at the LHC is about five times larger than at an e^+e^- collider and so, in principle, it can be measured with a better relative precision, given equal amounts of data. The measurement however requires knowledge of the direction of the matter and antimatter partons that created the Z boson, and any uncertainty in this quantity results in a dilution of the observed value of $A_{\rm FB}$. This dilution is very significant in the central region, as there is an approximately equal probability for each proton to contain the quark or anti-quark that is involved in the creation of the Z, leading to an ambiguity in the definition of the axis required in the measurement. However, the more forward the Z boson is produced, the more likely it is that it follows the quark direction; above rapidities $y > 3$, the Z follows the quark direction around 95% of the time. Furthermore, in the forward region, the partonic collisions that produce the Z are nearly always between u-valence and $\bar{u}$-sea quark or d-valence and $\bar{d}$-sea quark. The $s\bar{s}$ contribution, with a less well known parton density function (PDF), is smaller than in the central region.

Consequently, the forward region is the optimum environment in which to measure $A_{\rm FB}$ at the LHC. Preliminary studies have shown that with a 50 fb^{-1} data sample collected by the LHCb upgrade, $A_{\rm FB}$ could be measured with a statistical precision of around 0.0004. This would give an uncertainty on $\sin^2\theta_{\rm lept}$ of better than 0.0001, which is a significant improvement in precision on the current world average value. It is also worth remarking that the two most precise values entering this world average at present, the forward-backward $b\bar{b}$ asymmetry measured at LEP ($\sin^2\theta_{\rm eff}^{\rm lept} = 0.23221 \pm 0.00029$), and the left-right asymmetries measured at SLD with polarised beams ($\sin^2\theta_{\rm eff}^{\rm lept} = 0.23098 \pm 0.00026$), exhibit a three-sigma discrepancy [102]. LHCb will be able to clarify this unsatisfactory situation.

More work is needed to identify the important systematic uncertainties on the $A_{\rm FB}$ measurement. One source of error is the uncertainty in the PDFs. With current knowledge this contribution would lead to an uncertainty of almost double the statistical precision estimated above, but this will reduce when the differential cross-section measurements of the W and Z bosons and Drell-Yan lower mass dimuon production measured at the LHC are included in the PDF global fits. LHCb has already embarked on this measurement programme. Figure 2.20 (left)

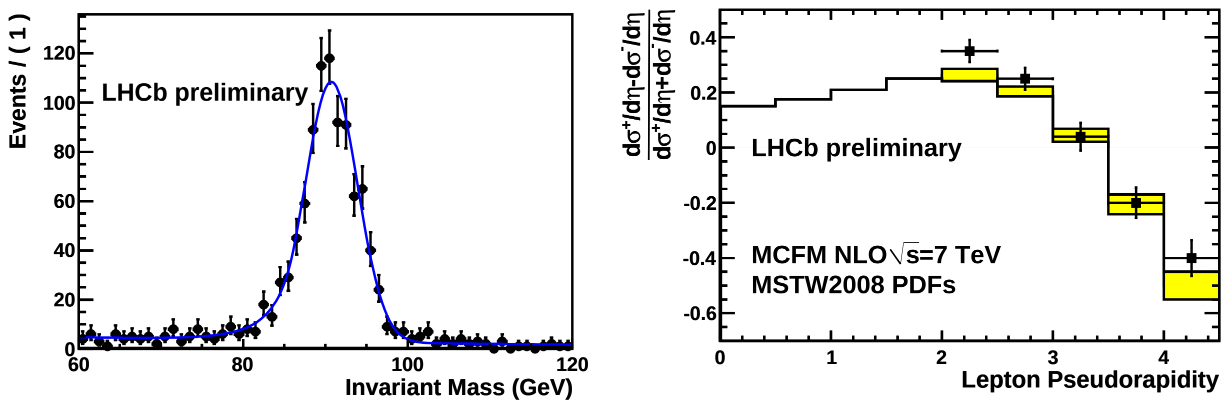

Figure 2.20: LHCb preliminary Z and W results for 16 pb^{-1} at $\sqrt{s} = 7$ TeV. Left: $Z \to \mu^+\mu^-$ peak. Right: $W^+ - W^-$ production asymmetry, where the points with error bars are the data and the boxes are the theoretical predictions with their uncertainties (only indicated within the LHCb acceptance).

shows the $Z \to \mu^+\mu^-$ peak obtained with 16 pb^{-1} of data. Figure 2.20 (right) shows the measured asymmetry between W^+ and W^- production as a function of lepton pseudorapidity. This measurement is already approaching the accuracy of the theoretical uncertainties. The range of the ATLAS and CMS experiments only extends up to lepton pseudorapidities of 2.5.

Decreasing the uncertainty on m_W from its present error of 23 MeV/c^2, (which may be reduced further at the Tevatron) is one of the most challenging tasks at the LHC. Although no studies have yet been made of determining m_W with LHCb itself, it is evident that the experiment can give important input to the measurements being made at ATLAS and CMS [103]. A significant and potentially limiting external uncertainty on m_W will again come from the knowledge of the PDFs, and several commentators consider the existing projections to be optimistic [104]. The PDFs are less constrained in the kinematical range accessible to LHCb, and high statistics, precise measurements of W^+, W^-, Z and low-mass Drell-Yan production in this region, in particular the shapes of the differential cross-sections, can be used to improve the global picture. One specific area of concern arises from the knowledge of the heavy quarks in the proton. Around $20 - 30\%$ of W production in the central region is expected to involve s and c quarks, making the understanding of this component very important for the m_W measurement. LHCb can make a unique contribution to improving the knowledge of the heavy-quark PDFs by tagging the relatively low-p_{T} final-state quarks produced in processes such as $gs \to Wc$, $gc \to Zc$, $gb \to Zb$, $gc \to \gamma c$ and $gb \to \gamma b$.

2.3.2 Exotics

A major goal of experiments at the LHC is to solve the so-called "hierarchy problem": why is the mass of the Higgs boson at the sub-TeV scale, instead of being at the Planck scale, driven there by radiative corrections? Different theoretical paradigms have been proposed, the most discussed being Supersymmetry. There are, however, many other ideas including Extra Dimensions (large, warped, Higgs-less), Technicolour and Little Higgs. These models focus on a strong dynamics type of solution to the problem [105].

A common feature of many such models is the prediction of new states at the TeV scale. In recent years there have been many proposals including Z', 4th quark generation, Leptoquarks, Hidden Valleys, etc. The latter class of models contains low mass states in a new sector with its own quantum number. This new sector is termed the "Hidden Valley", as it lies beyond the energy reach of present experiments. The light states in these hidden sector(s) are connected to the Standard Model sector via massive particles such as the Higgs boson, Supersymmetry sparticles or Kaluza-Klein states of Extra Dimensions. The Hidden Valley class of models is illustrated in Fig. 2.21 where they are labelled "The dark valley Universe" for their possible dark matter content. These models are a very general consequence of string theories [106].

Many proposals exist for the new physics that lies in the hidden valley. A large fraction of these these models predicts the production at the LHC of new particles with long lifetimes, which may decay into b-quark jets. These signatures are well suited to LHCb, and in particular the upgraded experiment, which will be able to select events with displaced vertices in the trigger.

Hidden valley particles, or "v-flavoured hadrons", can be produced directly via, for example, a Z′. The details of the decay depend on the properties of the hadrons. In one specific model [107], the v-sector contains two new heavy quarks the U and C. These can combine, in the case where they are close in mass to form either v-isospin 1 hadrons, denoted as either $\pi_v^{\pm}$ for $v = \pm 1$ or π_v^0 for $v = 0$. All these particles are electrically neutral but the $\pi_v^{\pm}$ hadrons carry 'v-charge', are stable and constitute dark matter candidates. The 'neutral' member of the isotriplet, the π_v^0, can decay into ordinary particles. If the mass of the spinless π_v^0 is below ZZ threshold it will decay dominantly into $b\bar{b}$ pairs due to helicity conservation. Then, as shown in Fig. 2.22, many such v particles can be produced in a single event.

The manifestations of such models are many. Here, by way of example, we discuss a possible scenario in which LHCb would observe the Higgs boson through its coupling to Hidden Valley

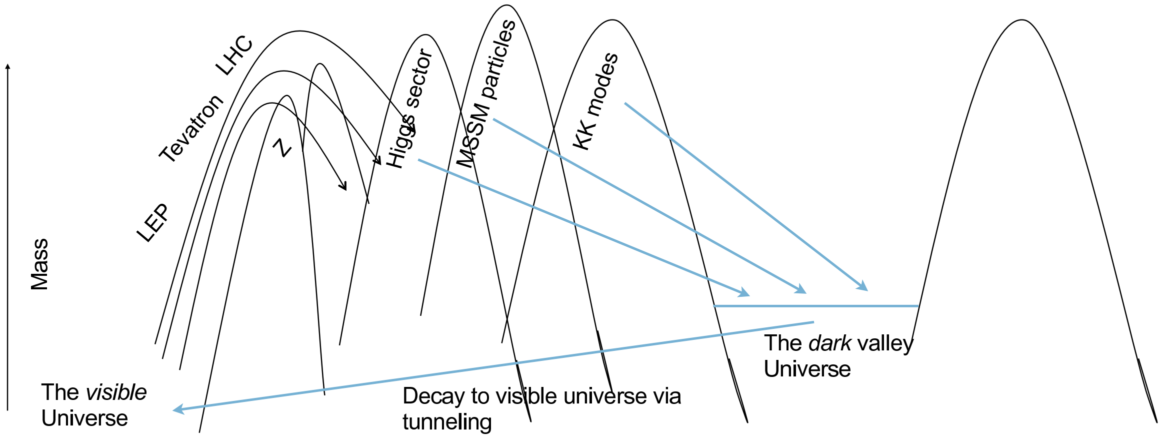

Figure 2.21: An overview of Hidden Valleys. The peaks show possible massive states that could connect the Hidden Sector to Standard Model particles (from Ref. [105]). While the hidden sector is SM neutral, the connector sector is charged under both the SM and the hidden sector.

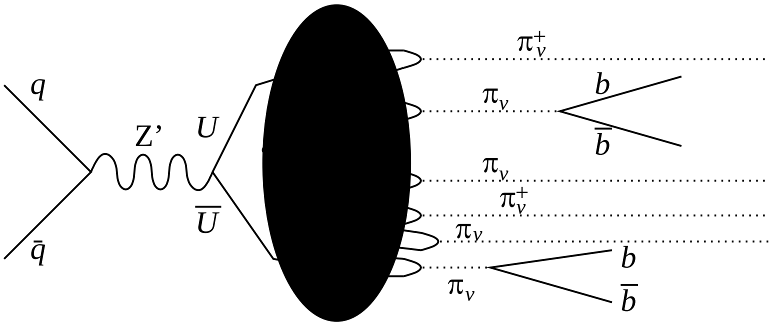

Figure 2.22: Production of electrically neutral v-flavored hadrons, π_v, and their decay. (Taken from [107].)

particles. In Strassler and Zurick [108] it is suggested that the Higgs could decay with a significant branching fraction as follows

$$H^0 \to \pi_v^0 \pi_v^0, \tag{2.6}$$

with each $\pi_v^0 \to b\overline{b}$ as illustrated in Fig. 2.23. Here the π_v^0 widths are determined by their lifetime which could be very long, resulting in narrow states. The final state would consist of four b-jets. If these decays exist, then the lower limit on the Higgs mass set by LEP may be misleading, as it assumes the prompt decay of the Higgs to $b\overline{b}$ to be dominant.

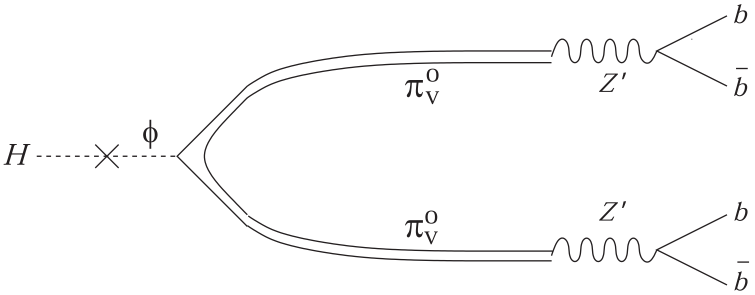

Figure 2.23: Decay of a Higgs via a scalar field ϕ into two π_v^0 particles, with π_v^0 charge equal to zero, that subsequently decay into $b\overline{b}$ jets. (Taken from [108].)

To investigate the potential of LHCb to search for these exotic Higgs decays a simulation has been performed, assuming an average of 0.4 interactions per crossing, basing the trigger and subsequent analyses on the following set of cuts: (1) consider events with at least two reconstructed secondary vertices; (2) use only charged tracks from a jet that are consistent with coming from a secondary vertex; (3) require that the two dijet masses should be equal within $3\,\sigma$. The invariant jet masses are computed for events passing this selection.

In Fig. 2.24 the distributions are shown for both the invariant mass of the dijets (left), and for the four-jet invariant mass (right) for those combinations where the dijet masses are very similar (right). The input parameters for the simulation are $\tau_{\pi_v^0} = 10$ ps, $m_{\pi_v^0} = 35$ GeV/c^2 and a Higgs mass of 120 GeV/c^2. No generator information has been used in the analysis or reconstruction. For both the dijet and four-jet reconstruction peaks are evident close to the

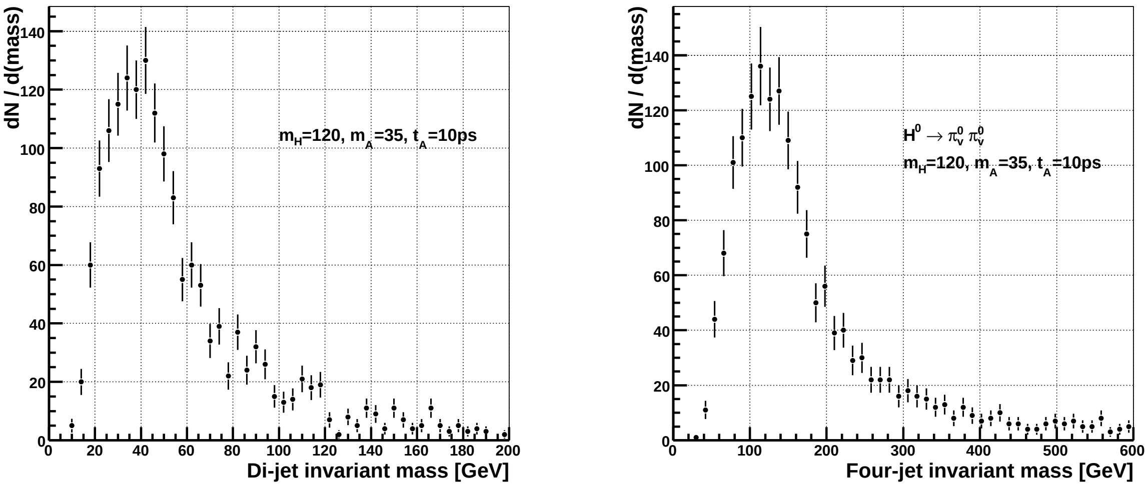

Figure 2.24: Results of signal simulation of the process $H \to \pi_v^0\pi_v^0$, $\pi_v^0 \to b\bar{b}$. Left: Reconstructed dijet invariant mass. Right: the mass of both dijets, that peaks at the putative Higgs mass; here two equal dijet masses are required. The input masses to the simulation are 35 GeV/c^2 for the π_v^0 and 120 GeV/c^2 for the Higgs.

correct mass. It will be possible to improve further by refining the jet definition and calibration, and by imposing constraints, for example that the masses of the two π_v^0 candidates be equal.

Assuming a Higgs production cross-section at 14 TeV of 50 pb, an integrated luminosity of 50 fb^{-1} and a geometric efficiency of 10%, 250,000 Higgs bosons will be produced in LHCb. If $H^0 \to \pi_v^0\pi_v^0$ is a dominant decay mode, then LHCb will be in an excellent position to observe this signal, taking advantage of the software trigger's ability to select high multiplicity events with good efficiency. Backgrounds to this signal from other processes, such as the production of two pairs of $b\bar{b}$ quarks, have been considered and found to be negligible.

Long-lived particles, which would give rise to secondary vertices that would be a suitable signature for the trigger of the upgraded experiment, are found in many Supersymmetric theories. Examples include the bilinear R-parity violating SUSY models of de Campos *et al.* [109] that predict long-lived SUSY particles such as neutralinos decaying into W + lepton, or Z + ν, or $b\bar{b}$+ ν, and the proposal of Carpenter *et al.* [110], in which the Higgs dominantly decays to a pair of long-lived neutralinos, each of which subsequently decays to three quark jets.

2.3.3 Central exclusive production

Central exclusive production (CEP) processes provide a promising and novel way to study QCD and the nature of new particles, from low mass glueball candidates up to the Higgs boson itself. The CEP of an object X in a $pp(\bar{p})$ collider may be written as follows

$$pp(\bar{p}) \to p + X + p(\bar{p}),$$

where the + signs denote the presence of a large rapidity gap. At high energies the t-channel exchanges giving rise to these processes can only be zero-charge colour singlets. Known exchanges include the photon and the Pomeron. Another possibility, allowed in QCD, but not yet observed, is the Odderon, a negative C-parity partner to the Pomeron with at least three

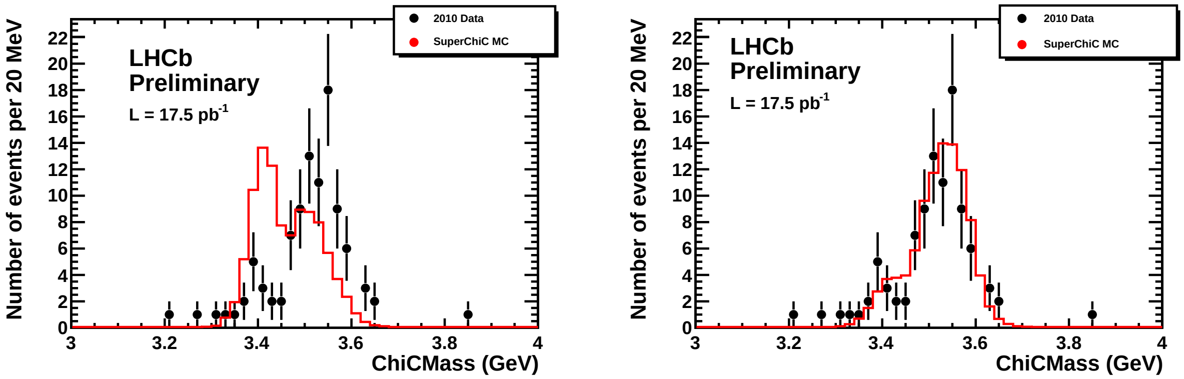

Figure 2.25: Preliminary LHCb results on central exclusive χ_c production. Also shown is the expectation of the SuperCHIC Monte Carlo [114], which has been normalised to the number events observed in the data. The relative proportions of χ_{c0}, χ_{c1} and χ_{c2} in the Monte Carlo are 52%, 36% and 12% respectively in the left plot, and 12%, 36% and 52% respectively in the right plot. (The data points are the same.)

gluons. The most attractive aspect of CEP reactions is that they offer a very clean environment in which to measure the nature and quantum numbers of the centrally produced state X.

Central exclusive $\gamma\gamma$ [111], dijet [112] and χ_c [113] production has been observed at the Tevatron. Already in the 2010 run LHCb has collected candidate dimuon events compatible with CEP. In Fig. 2.25 the invariant mass of CEP χ_c candidates is shown. These are events in which only a $J/\psi \to \mu^+\mu^-$ decay and γ candidate are reconstructed, with no other activity (inconsistent with noise) seen elsewhere in the detector. An important observable in CEP is the relative production rates of χ_{c0}, χ_{c1} and χ_{c2}. As is evident from Fig. 2.25, the invariant mass resolution of LHCb is sufficient for this measurement to be made.

These early results make clear the promise of CEP measurements at LHCb. Additional instrumentation can be considered which will help in these studies, should results with the current detector prove interesting. For example, the inclusion of Forward Shower Counters (FSCs) on both sides of the interaction point [115], would be able to detect showers from very forward particles interacting in the beam pipe and surrounding material. The absence of a shower would indicate a rapidity gap and be helpful in increasing the purity of a CEP sample. The deployment of semiconductor detectors very close to the beam within Roman pots, several 100 m away from the interaction point, as proposed for ATLAS and CMS [116] could also be beneficial for LHCb. Several important physics goals may already by identified for the LHCb CEP programme:

- To accumulate and characterise large samples of exclusive $c\bar{c}$ and $b\bar{b}$ events. A full measurement programme of these “standard candles” will be essential to understand better the QCD mechanism of CEP [117], and may provide vital input if CEP is used for studies of Higgs and other new particles [118].

- Searches for structure in the mass spectra of decay states such as K^+K^-, $2\pi^+2\pi^-$, $K^+K^-\pi^+\pi^-$ and $p\bar{p}$. A particular interest of this study would be the search for glueballs, which are a key prediction of QCD.

- Observation and study of exotic particles in CEP processes would be illuminating as to their nature. For example, a detailed study of the CEP process $pp \to p + X(3872) + p$

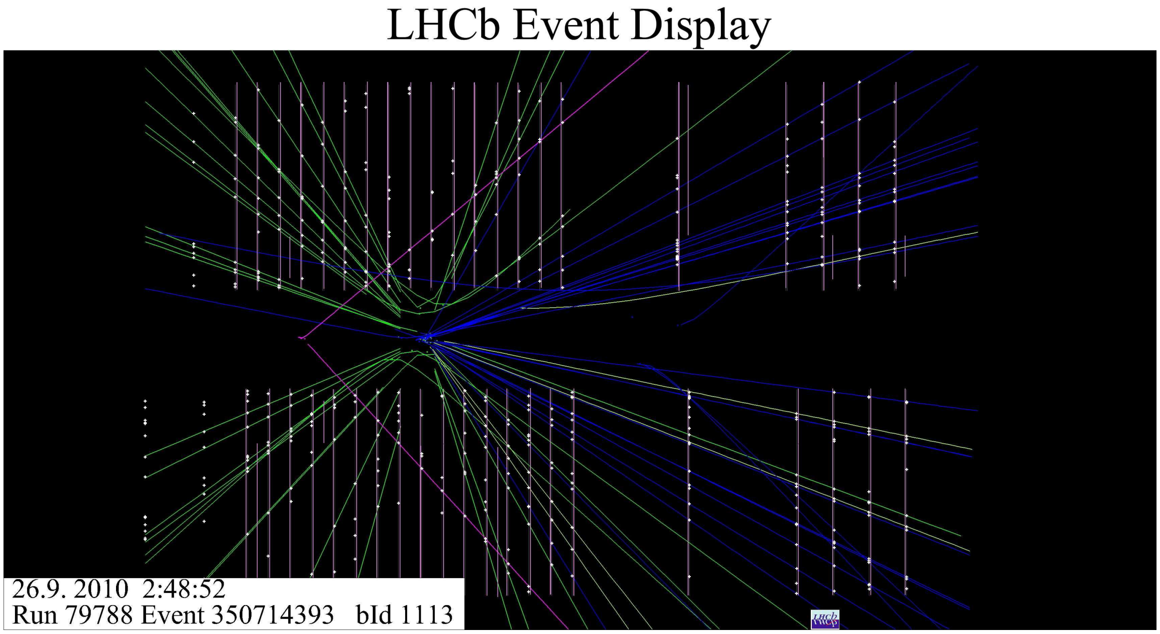

Figure 2.26: Event display in the VELO region of candidate CEP $J/\psi \to \mu^+\mu^-$ event with pile-up. The horizontal scale is 1 m, and the vertical scale is around 8.5 times smaller. The sensors are indicated either side of the beam region, together with the detected hits. Reconstructed tracks are superimposed. A primary vertex arising from one interaction can be seen, slightly left of centre, from which most tracks originate. Left of this (upstream), and clearly isolated, is the vertex of two tracks which form a $J/\psi \to \mu^+\mu^-$ candidate.

would provide a valuable new tool to test the quantum numbers of this state. This and other states could also be searched for in, for example, decays containing $D\bar{D}$, which if observed would shed light onto the nature of the parent particle [117, 119].

There are several reasons which make LHCb a suitable detector for performing such studies, particularly with the upgraded experiment:

- Even when running at a luminosity of 10^{33} cm^{-2}s^{-1} LHCb will have much less pile-up than ATLAS or CMS, which will be operating in a much more severe regime. This will be advantageous in triggering and reconstructing low mass CEP states. Not only will there still be a significant fraction of CEP interactions produced in isolation, but it will also prove possible to select CEP interactions in the pile-up environment. This has already been demonstrated with the 2010 data, as shown in Fig. 2.26, where a J/ψ vertex can be seen completely separated from, and upstream of, the primary vertex of another interaction. The software trigger of the upgrade will be used to select such events, not only containing $J/\psi \to \mu^+\mu^-$ but also two, three and four charged-track CEP decays.

- The higher integrated luminosity that will be collected by the upgraded detector will allow studies to be performed on states that are inaccessible with only a few fb^{-1}. This is true, for example, of central exclusive χ_b production, which is expected to be a factor of ~ 1000 down with respect to that of χ_c mesons [117].

- The particle identification capabilities of the LHCb RICH system allow centrally produced states to be cleanly separated into decays involving pions, kaons and protons.
- The low p_{T} acceptance of LHCb, and high bandwidth trigger, will allow samples of relatively low mass states to be collected and analysed.

Summary

The LHCb upgrade is necessary to take the next step in sensitivity that will be required in flavour physics after the first period of exploration and measurement that the experiment will perform over the coming five years. The sample sizes in most exclusive B and D final states will be far larger than those that will be collected elsewhere, for example at the upgraded e^+e^- B-factories. The performance of the existing detector, and the purity of the samples already accumulated, gives confidence that measurements of very high sensitivity will be possible with these samples. The experiment will have no serious competition in its study of B_s decays and CP violation.

The upgraded experiment will in addition have exciting opportunities to perform studies that will shed light on the lepton sector, and in topics beyond flavour physics. LHCb will be best-placed of all the LHC experiments to make an improved determination of $\sin^2\theta_{\mathrm{eff}}^{\mathrm{lept}}$, and to combat the PDF systematic uncertainties that may limit the ATLAS and CMS efforts to measure m_W. LHCb will have high sensitivity in the search for new particles with long lifetimes, and will be able to make QCD studies which are complementary to those possible in the central region.

Chapter 3

Trigger

The current LHCb trigger architecture [120, 13] has two levels: Level-0 (L0) is a trigger implemented in hardware while the High Level Trigger (HLT) consists of a software application which runs on every CPU of the event-filter farm (EFF). The purpose of L0 is to reduce the rate of crossings with interactions to below a rate at which the HLT can process the events. For the current detector this maximum rate is determined by the front-end (FE) electronics, and is 1.1 MHz. The FE-electronics will be upgraded to allow reading events at the LHC clock rate. In principle the upgrade should allow to perform data acquisition and event building on the EFF at the full rate of 40 MHz. However the upgrade is designed to be able to cope with a staged DAQ system which cannot yet handle the full rate, occupancy fluctuations which prevent the full readout, and insufficient CPU power in the EFF. Hence the upgrade will also contain a Low Level Trigger (LLT), which like L0 should not just pre-scale to a rate acceptable by the DAQ and EFF, but enrich the selected sample with interesting events. The LLT corresponds closely to the current L0, but with a tunable output rate higher than the current 1.1 MHz limit; it will be described in the next section.

During 2010 running the trigger performed as expected [121], but needed to adapt to running conditions very similar per crossing to those expected for the upgraded LHCb detector. As a result the HLT [122, 123] has evolved significantly from the implementation described in [120], profiting from the excellent detector performance both in efficiency and alignment. The HLT is subdivided in two stages HLT1 and HLT2, which are briefly introduced below and are described in detail in Sections 3.2.1 and 3.2.2 respectively. HLT1 reconstructs particles in the VELO and determines the position of the primary vertices (PV) in the event. To limit the CPU consumption, a selection of VELO tracks is made based on their smallest impact parameter (IP) to any PV, and their quality. For these selected VELO tracks their track-segment in the T-stations are sought to determine their momentum (p), so-called forward tracking. HLT1 selects events with at least one track which satisfies minimum requirements in IP, p, p_{T} and track quality. It reduces the rate to a sufficiently low level to allow forward tracking of all VELO tracks. HLT2 searches for secondary vertices, and applies decay length and mass cuts to reduce the rate to the level at which the events can be written to storage.

The trigger for the upgrade is the basically same as the trigger which LHCb has currently deployed, with the exception of allowing a much larger LLT rate, and correspondingly a much larger rate to storage. Figure 3.1 gives an overview of the trigger levels of the upgrade, the components used to select events and the trigger rates. The LLT output rate is expected to

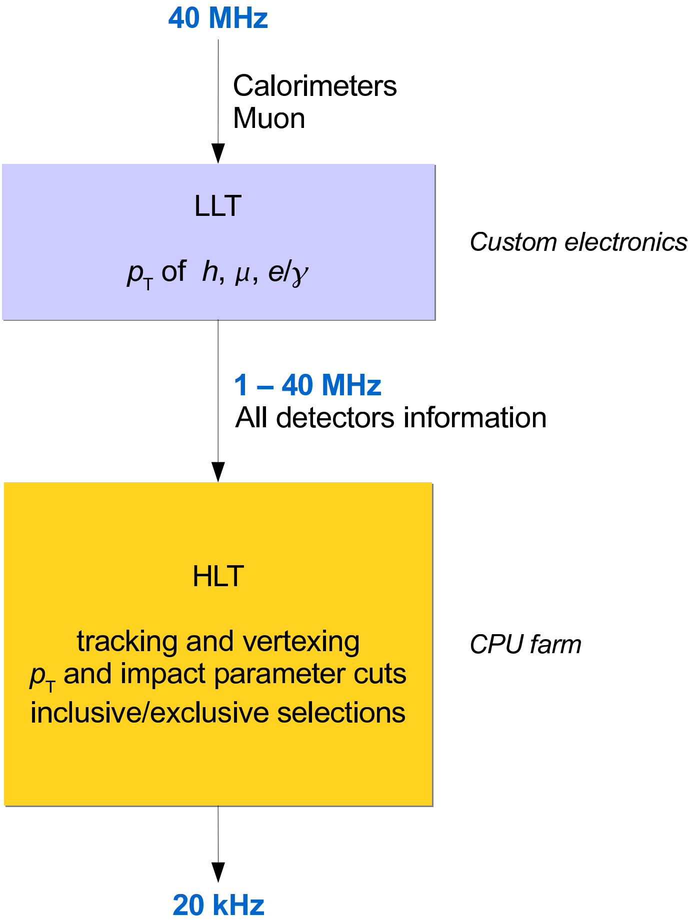

Figure 3.1: Overview of the upgraded LHCb trigger.

typically be between 5–10 MHz, while the rate to storage will be $\sim$ 20 kHz. The expected performance of the overall trigger system at a luminosity of 10^{33} cm^{-2}s^{-1} is based on trigger code which is actually running in LHCb today, and will be given in Section 3.3.

3.1 Low Level Trigger (LLT)

The present L0 reconstructs the highest E_{T} hadron, electron and photon, and the two highest p_{T} muons. L0 is able to distinguish between electron and photon candidates by using the Scintillating Pad Detector (SPD) in front of the ECAL, and reduce the hadron contamination requiring Pre-Shower (PS) energy deposition. The upgraded calorimeter trigger is not expected to contain the SPD nor PS, so the LLT will not distinguish between photons and electrons nor have a veto on hadron-induced showers. The LLT muon trigger will use the same hardware as the L0 muon trigger [120], with the distinction that the first muon station (M1) will no longer

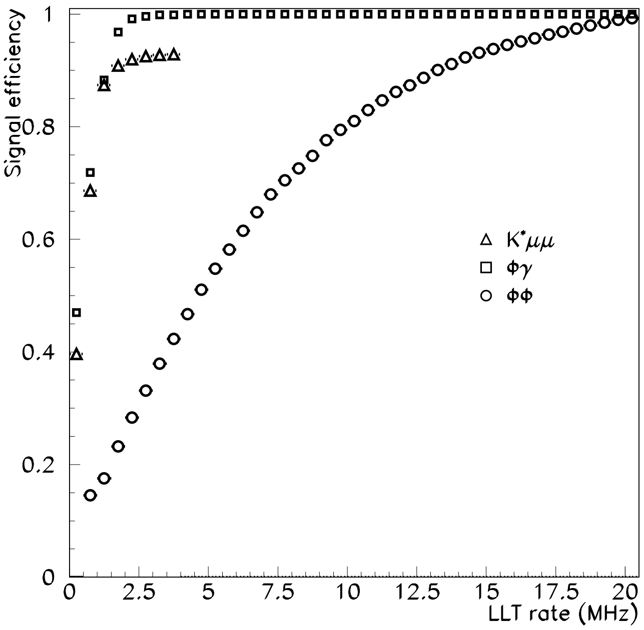

Figure 3.2: LLT efficiency for $B_s \rightarrow \phi\phi$, $B^0 \rightarrow \mu\mu\mathrm{K}^*$ and $B_s \rightarrow \phi\gamma$ as a function of the LLT trigger rate at a luminosity of 10^{33} cm^{-2}s^{-1}. For each signal the efficiency and rate are for a single LLT type, i.e. $\phi\phi$, $\mu\mu\mathrm{K}^*$ and $\phi\gamma$ are triggered by respectively LLT-hadron, LLT-μ and LLT-electromagnetic.

be present, hence the momentum will be determined by M2 and M3.

Figure 3.2 shows the performance of LLT for three selected signal channels. At a luminosity of 10^{33} cm^{-2}s^{-1} the rate of crossings with at least one visible pp interaction is 26 MHz. For $B_s \rightarrow \phi\phi$ the LLT efficiency rises almost linearly with increasing LLT output rate for the LLT-hadron trigger, clearly showing the limitations of the present L0 1.1 MHz output rate limit. The trigger based on electromagnetic clusters exhibits a sharp rise for $B_s \rightarrow \phi\gamma$ decays, and plateaus at lower output rates due to the offline requirement[1] that the photon has an $E_\mathrm{T}^\gamma > 2.4$ GeV. Channels with muons in the final state reach their LLT$-\mu$ efficiency plateau at about 1 MHz output rate. Table 3.1 gives an indication of the improvement which can be achieved with the upgraded trigger. It assumes a luminosity of 10^{33} cm^{-2}s^{-1}, and the thresholds in the LLT have been chosen to give the relative rates of the three LLT triggers in the ratios LLT-μ: LLT-hadron: LLT-e/γ = 1:3:1. It shows the efficiency for signal channels for three different LLT

Table 3.1: Signal efficiencies for three LLT-accept rates.

LLT-rate (MHz)	1	5	10
$B_s \rightarrow \phi\phi$	0.12	0.51	0.82
$B^0 \rightarrow K^*\mu\mu$	0.36	0.89	0.97
$B_s \rightarrow \phi\gamma$	0.39	0.92	1.00

---

[1] All trigger efficiencies are quoted relative to events which have been accepted after offline cuts have been applied, to assure a sufficient signal-to-background ratio.

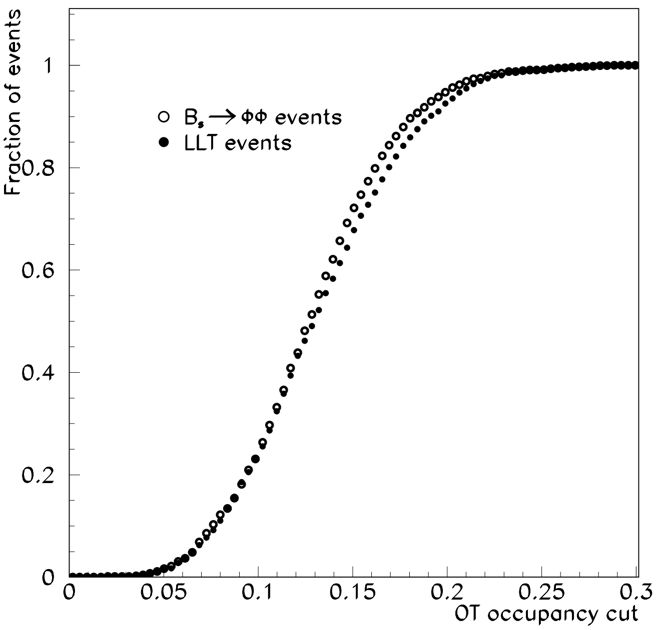

Figure 3.3: Fraction of all events, and $B_s \to \phi\phi$ events, which are triggered by LLT as a function of a cut on the OT occupancy.

accept rates: 1, 5 and 10 MHz. The 1 MHz rate has been chosen to compare with the present situation. While LHCb has already shown in 2010 to be able to run with a pile-up per bunch crossing similar to that of the pile-up at 10^{33} cm^{-2}s^{-1}, it cannot profit from a luminosity larger than ~ 2–3×10^{32} cm^{-2}s^{-1} due to the L0 1 MHz limitation, since the decrease in L0-efficiencies, and especially the L0-hadron efficiency, results in an almost constant B yield independent of luminosity. Table 3.1 shows that the upgraded trigger will result in a yield increase of up to a factor 7 for hadronic B decays for the same LHC machine run-time.

3.2 High Level Trigger

3.2.1 HLT1

A small fraction of the events in LHCb have large detector occupancies, especially in the OT. Some of these events take even seconds to reconstruct in HLT1, and are rejected before any reconstruction to be able to keep the average processing time below $\sim$ 20 ms per event[2]. Figure 3.3 shows the fraction of all events, and of $B_s \to \phi\phi$ events, as a function of the average OT straw occupancy. This is for events simulated at a luminosity of 10^{33} cm^{-2}s^{-1}, after applying $\mathrm{LLT}^{\mathrm{hadron}}_{E_\mathrm{T}} > 3$ GeV. Events are rejected if the OT occupancy is larger than 20%, which removes 5% of the $B_s \to \phi\phi$ events and 7% of the LLT triggered events.

For the remaining events the reconstruction strategy is determined by the following considerations:

---

[2] With an EFF five times the size installed for 2011, and 20 ms per event HLT processing time, the allowed LLT output rate would be 5 MHz.

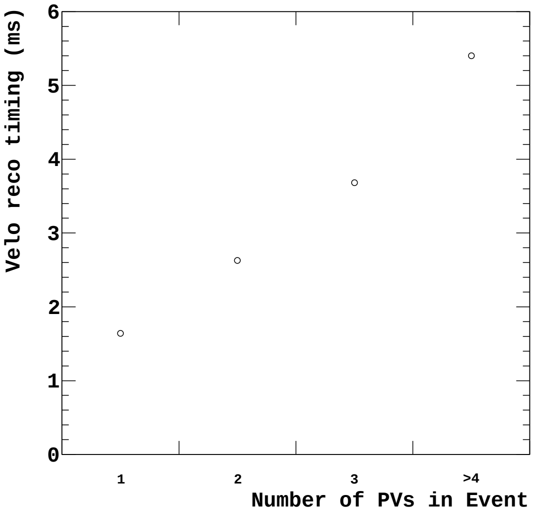

Figure 3.4: The timing of the VELO 3D pattern recognition as a function of the off-line reconstructed number of PVs in the event. The entry at 4 PVs contains all events with more than 3 PV.

- All B meson decays studied at LHCb contain at least two charged tracks in their final state;
- B mesons are heavy, and their average momentum in the LHCb acceptance is ~ 100 GeV/c, so their decay products will have a large momentum (p) and transverse momentum[3] (p_{T}) compared with light-quark hadrons originating from the PV;
- The average decay length of B mesons produced in the LHCb acceptance is ~ 1 cm so that their decay products will have a large impact parameter (IP) with respect to their PV.
- The VELO reconstruction is fast enough to allow a full 3D pattern recognition and PV finding to be performed for all events entering the HLT.

This last point is illustrated in Fig. 3.4: the timing increases linearly with the number of PV in the events, and is low enough to allow sufficient time for the subsequent reconstruction and event selection. The event reconstruction therefore begins with the VELO pattern recognition and PV finding.

Because of timing constraints, the momentum can only be determined for a limited number of VELO tracks. It is necessary to select those tracks which are most likely to come from a B decay. Three selection criteria are used: the IP of the VELO track with respect to the closest PV, the number of hits assigned to the VELO track, and the difference between the number of hits assigned to the VELO track and the number of hits expected given the track direction and the first measured point on the track (missed hits). Figures 3.5 and 3.6 compare the distributions of the latter two criteria for tracks from a minimum bias event and for the highest p_{T} B daughter track in $B_s \to \phi\phi$ decays.

---

[3] Transverse is defined perpendicular to the beam-pipe, in the plane formed by the track and the beam-pipe.

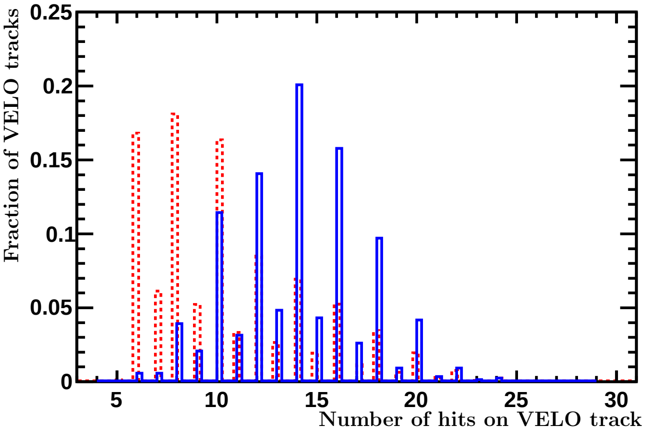

Figure 3.5: The number of hits on the VELO track for minimum bias (dashed red) and the highest p_{T} offline-selected $B_s \to \phi\phi$ daughter (solid blue).

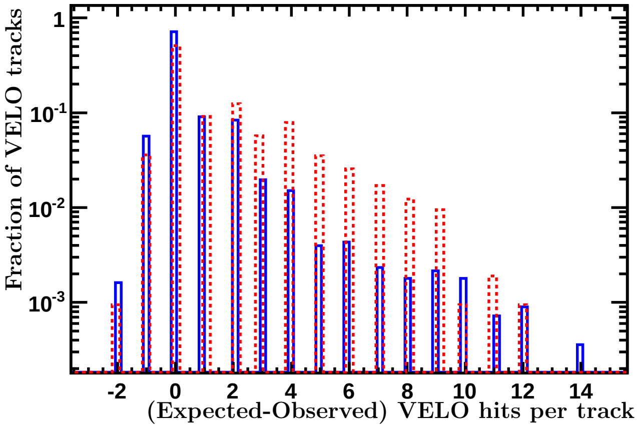

Figure 3.6: The difference between the expected and observed number of hits on a VELO track for minimum bias (dashed red) and the highest p_{T} offline-selected $B_s \to \phi\phi$ daughter (solid blue). Note the logarithmic scale.

It can be seen that both the number of hits on a VELO track and the number of missed hits are good discriminants, especially since they can be applied before any forward reconstruction, thus saving CPU time by having to consider fewer VELO tracks. Requiring $|\mathrm{IP}| > 125\ \mu\mathrm{m}$, and number of VELO hits and missing hits > 9 and < 3 respectively, is very efficient at selecting the highest p_{T} daughter from a $B_s \to \phi\phi$ decay. Figure 3.7 shows the number of VELO tracks per event for which the momentum needs to be determined.

The VELO tracks thus selected are extrapolated to the tracking stations using the PatForward [124] algorithm. Imposing a minimum momentum and transverse momentum (p, p_{T}) in the forward tracking significantly reduces the search windows which have to be opened in the IT and OT tracking stations and consequently reduces the required CPU power. This is illustrated in Fig. 3.8, which shows the reconstruction time per event of the forward tracking as a function of the minimum (p, p_{T}) cutoff imposed.

Figure 3.9 shows the transverse-momentum distributions of $B_s \to \phi\phi$ decay products which have been selected by the VELO IP and quality cuts. Hence, imposing a minimum (p, p_{T}) of

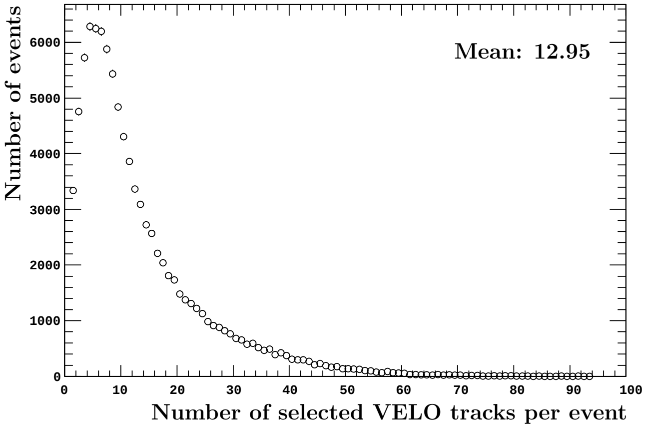

Figure 3.7: Number of VELO tracks per event which enter the forward reconstruction to have their momentum determined.

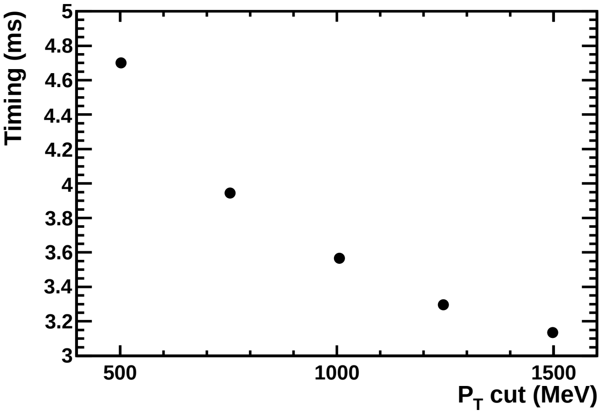

Figure 3.8: The CPU time of the forward tracking as a function of the minimum p_{T} imposed. The corresponding minimum p is always taken as ten times the minimum p_{T}.

(12, 1.2) GeV/c results in a negligible loss of signal, while the CPU time per event is acceptable.

The final track selection proceeds in two stages. First, (p, p_{T}) cuts are used in order to reduce the rate. The remaining tracks are fitted using a Kalman filter with outlier removal, in order to obtain an offline-quality value for the track χ^2 as well as an offline-quality covariance matrix at the first state of the track, allowing a cut on the IP significance squared (IP χ^2). The number of tracks which have to be fitted is low enough by this stage that the contribution of the track fit to the overall timing is negligible. The track χ^2 is a powerful tool for ghost rejection [125] in the trigger; however, being particularly sensitive to the detector performance, it needs to be verified with real data. Figure 3.10 shows the distribution of the online track χ^2/ndf for minimum bias events recorded in 2010 surviving to this stage of the trigger, as well as the highest momentum daughter from offline selected real data $D^+ \to h^+h^+h^-$ decays. The data demonstrate that LHCb achieved an excellent reconstruction performance with very low online track χ^2 values for genuine signal tracks. The track χ^2 and IP χ^2 are therefore used to achieve the final required rate reduction. Figure 3.11 shows the fraction of events which are triggered by at least one ghost track as a function of the OT occupancy, imposing a track

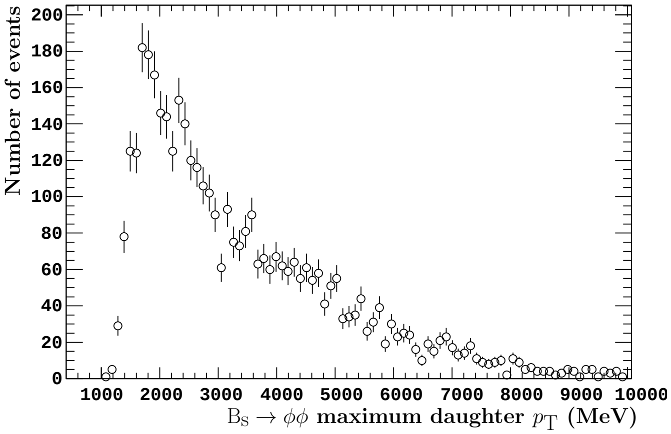

Figure 3.9: Distribution of the largest transverse momentum per event of $B_s \to \phi\phi$ decay products which have been selected by the VELO IP and quality cuts.

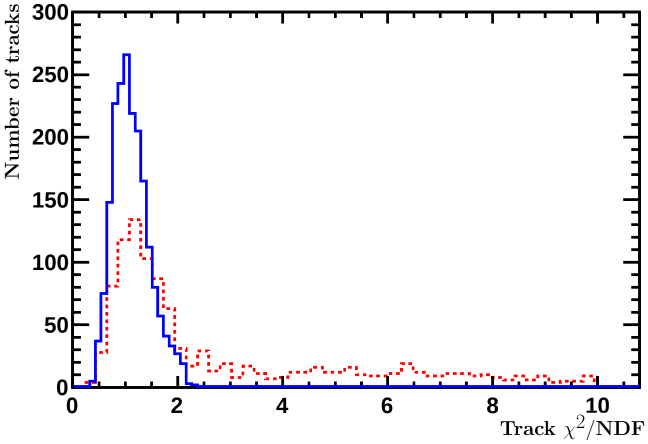

Figure 3.10: The track χ^2/ndf of forward reconstructed tracks in the trigger in real data minimum bias events (dashed red) and of the highest momentum daughter from offline selected real data $D^+ \to h^+h^+h^-$ decays (solid blue).

$\chi^2/\mathrm{ndf} < 3$ cut for minimum bias events surviving to this stage of the trigger. On average 15% of the events accepted by HLT1 are triggered due to a ghost track.

For decays involving muons an additional cut is available: the muon ID algorithm [126] which is in itself a powerful ghost and background rejection tool. This fact is exploited in a parallel trigger line which is run only on those events passing the LLT muon trigger, and hence most of the above cuts can be relaxed for muon candidates.

For radiative B decays, e.g. $B_s \to \phi\gamma$, the requirements of the offline background rejection [127] impose a tight LLT electromagnetic cut of 2.4 GeV, so that LLT electromagnetic triggers make up only a small fraction of the total LLT rate. Therefore HLT1 contains another parallel line only running on LLT electromagnetic triggered events for which the (p, p_T) cuts are significantly reduced. In addition, as this trigger line searches for lower momentum tracks, the track χ^2 cut is loosened.

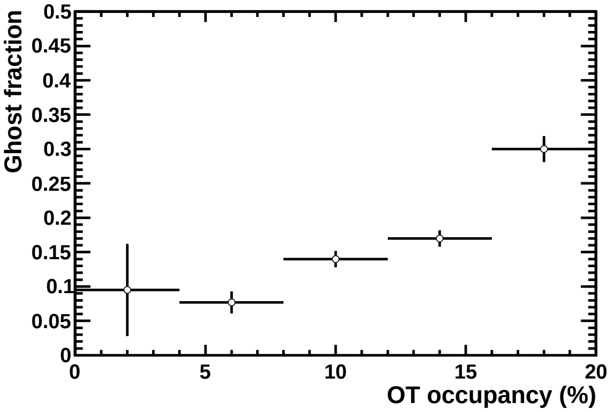

Figure 3.11: Fraction of HLT1 accepted events which are triggered by at least one ghost track as a function of the OT occupancy, imposing a track $\chi^2/\text{ndf} < 3$ cut.

3.2.2 HLT2

HLT2 is mainly based on three inclusive trigger lines, so-called topological lines [123]. These lines in principle cover all B decays with a displaced vertex, and with at least two charged particles in the final state. In addition HLT2 contains trigger lines which exploit the presence of muons, and a few lines which aim at exclusively reconstructing golden B-decay modes.

The topological lines are designed to have:

- high efficiency for any B decay with at least two charged daughters, due to the inclusive nature of the trigger lines;
- an excellent timing performance and background rejection, due to the small number of trigger lines;
- excellent data-mining properties due to their inclusive nature;
- trigger redundancy for golden modes, for which a few more exclusive selections will be deployed.

In an inclusive trigger cuts must be avoided on quantities such as the mass of the B candidate or how well the direction of its momentum agrees with the direction defined by the primary and secondary vertices. To trigger efficiently on B decays with long-lived resonances (such as D mesons), tight cuts on the quality of the vertices must also be avoided. Instead, quantities that preserve the inclusiveness of the trigger while also providing large background rejection factors are used. All VELO tracks are extrapolated to the tracking stations to have their momentum measured, imposing a minimum (p, p_{T}) of (5000, 500) MeV/c in the PatForward algorithm to save CPU time. To reduce the background rate due to ghosts, all tracks are required to have a track χ^2/ndf value less than 5. To reduce the background rate due to prompt particles, all tracks are required to have an IP χ^2 value greater than 16. Due to the inclusive nature of the HLT2 topological lines, this does not mean that all of the B daughters need to satisfy these criteria. The trigger is designed to allow for the omission of one or more daughters when forming the trigger candidate. Processing time is saved in the HLT2 topological lines by simply assigning each input particle a kaon mass.

The multibody candidates are built as follows: two input particles are combined to form a two-body object; another input particle is added to the two-body object to form a three-body object, and so on. An n-body candidate is thus formed by combining an $(n-1)$-body candidate and a particle, not by directly combining n particles. The importance of this distinction is in how the distance of closest approach (DOCA) cuts are made. When a 2-body object is built, a DOCA$<$ 0.15 mm cut is imposed for the object to either become a 2-body candidate or to become the seed for a 3-body candidate. When a 3-body object is made by combining a 2-body object and another particle, another DOCA$<$ 0.15 mm cut is imposed for the object to either become a 3-body candidate or input to a 4-body candidate. This DOCA is of the 2-body object and the additional particle, not the maximum DOCA of the three particles. This greatly enhances the efficiency of the HLT2 topological lines on $B \to DX$ decays. A similar procedure is followed when making 4-body candidates from 3-body objects and an additional particle. All n-body candidates that pass these DOCA cuts are then filtered using a number of other selection criteria. If a trigger candidate only contains a subset of the daughter particles, then the mass of the candidate will be less than the mass of the B. Thus, any cuts on the mass would need to be very loose if the trigger is to be inclusive. Instead a cut is made on the corrected mass obtained as follows [128]:

$$m_{\text{corr}} = \sqrt{m^2 + |p'_{\text{T miss}}|^2} + |p'_{\text{T miss}}| \tag{3.1}$$

where $p'_{\text{T miss}}$ is the missing momentum transverse to the direction of flight, obtained using the primary and secondary vertices, of the trigger candidate. The quantity m_{corr} would be the mass of the parent if a massless particle was omitted from the trigger candidate, i.e. it is the minimum correction to the trigger-candidate mass if any daughters are missing. Figure 3.12 demonstrates the performance of m_{corr}. For cases where there are missing daughters, the m_{corr} distributions are fairly narrow and peak near the B mass. When the trigger candidate is formed from all of the daughters, the m_{corr} distributions are slightly wider and shifted upwards by a small amount as compared with the mass distributions, as expected. Thus, the performance of m_{corr} is ideal for an inclusive trigger line. The HLT2 topological lines require $4 < m_{\text{corr}} < 7$ GeV/c^2. The HLT2 topological lines further reduce the background retention rate by requiring the p_{T} of the hardest daughter be greater than 1.5 GeV/c and also that the sum of the daughter p_{T} values be greater than 4.0, 4.25 and 4.5 GeV/c for the 2-body, 3-body and 4-body lines, respectively. To further reduce the background rate from candidates with ghost tracks the HLT2 topological lines require that at least one daughter particle has a track $\chi^2/\text{ndf} < 3$. The trigger candidate's flight-distance significance value is required to be greater than 8, and its vertex must be downstream of the closest PV. The sum of the daughter IP χ^2 values should be greater than 100, 150 and 200 for the 2-body, 3-body and 4-body lines, respectively. One of the larger background contributions to the HLT2 topological lines comes from prompt D mesons, which is suppressed by requiring that all $(n-1)$-body objects used by an n-body line either have a mass greater than 2.5 GeV/c^2 or that they have an IP $\chi^2 > 16$. A complete list of the cuts used in all three of the HLT2 topological lines is given in Table 3.2.

In addition to the topological lines, HLT2 contains a set of lines which exploit tracks which have been identified as muons. Dimuon candidates are formed and, depending on their mass,

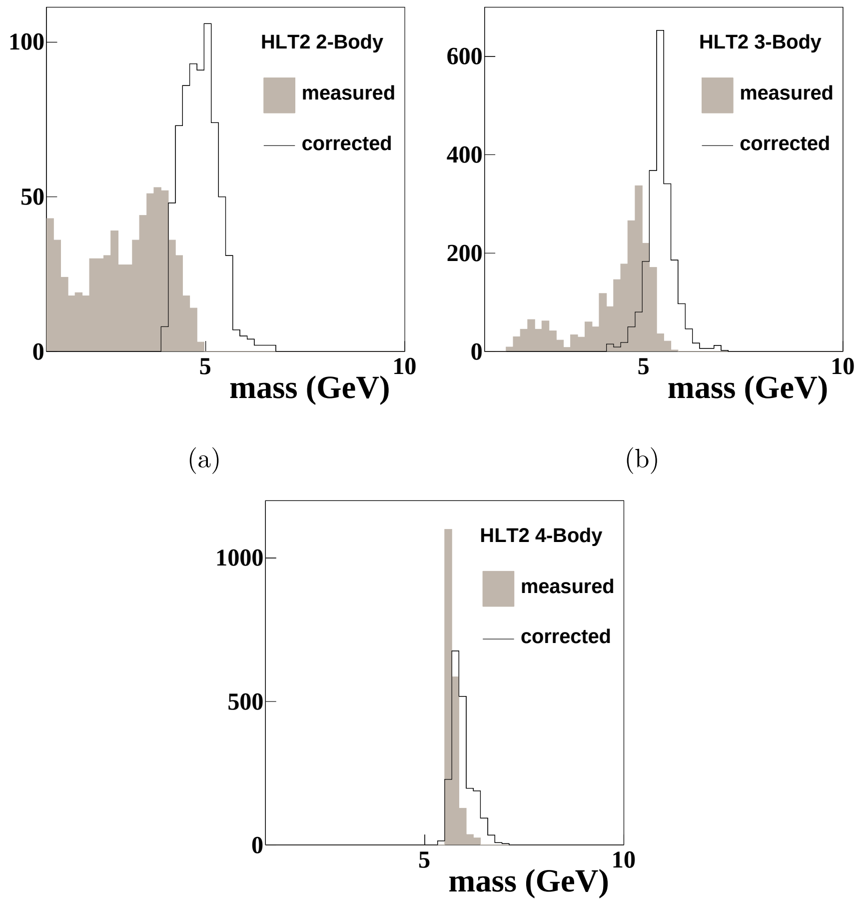

(a) (b)

(c)

Figure 3.12: B candidate masses from $B \to K^{*}\mu\mu$ decays: (a) HLT2 2-body topological trigger candidates; (b) HLT2 3-body topological trigger candidates; (c) HLT2 4-body topological trigger candidates. In each plot, both the measured mass of the $n = 2$, 3, 4 particles used in the trigger candidate (shaded) and the corrected mass obtained using Eq. 3.1 (unshaded) are shown.

cuts are applied on the flight distance and p_{T} of the dimuon candidate. Single muon candidates are accepted either requiring large p_{T}, or a combination of IP χ^2 and p_{T} cuts.

3.3 Trigger Performance

As shown in Fig. 3.2 the trigger efficiency is very sensitive to the accept rate of LLT, and especially hadronic B decays would profit from larger LLT rates. This rate is mainly limited by the size of the EFF, or rather by its size and the amount of CPU time needed by the HLT. The expected trigger efficiencies will be evaluated for two assumed EFF performances: five and ten times the CPU power which is available for LHCb in 2011. As is also shown in Fig. 3.2 channels triggered by muons or photons require much less band-width than hadronic B decays, hence the maximum allowed input rate to the EFF has to be divided among the different B decays of interest. The available bandwidth will be divided over LLT and HLT lines using

Table 3.2: The selection criteria used in the HLT2 topological lines, as explained in the text.

Quantity	Selection Criteria
all input particle transverse momenta	$p_{\mathrm{T}}^{\mathrm{min}} > 500$ MeV/c
all input particle momenta	$p^{\mathrm{min}} > 5$ GeV/c
all input particle track χ^2/ndf	χ^2/ndf < 5
all input particle IP χ^2	IP $\chi^2 > 16$
B candidate corrected mass	$4 < m_{\mathrm{corr}} < 7$ GeV/c^2
largest daughter transverse momentum	$p_{\mathrm{T}}^{\mathrm{max}} > 1.5$ GeV/c
best daughter track χ^2/ndf	χ^2/ndf < 3
sum of daughter transverse momenta	$\Sigma p_{\mathrm{T}} > 4.0,\ 4.25,\ 4.5$ GeV/c (2, 3, 4-body)
sum of daughter IP χ^2	IP $\chi^2 > 100,\ 150,\ 200$ (2, 3, 4-body)
n-body DOCA	DOCA$<$ 0.15 mm
B candidate signed flight distance χ^2	FD $\chi^2 > 64$
prompt D veto	$m_{n-\mathrm{body}} > 2.5$ GeV/c^2 or 2, 3-body IP $\chi^2 > 16$

the following benchmark channels: $B_s \to \phi\phi$, $B^0 \to \mu\mu\mathrm{K}^*$ and $B_s \to \phi\gamma$. These channels are representative both in giving access to CKM and new physics parameters, and in the way they rely on the different trigger components, i.e. they contain purely hadronic decays, soft muons and radiative decays, respectively. Note that apart from LLT the whole trigger chain is in software, and hence is able to adapt to any physics challenge which will be topical in the second half of this decade and beyond. As a matter of fact, during 2010 the HLT had to adapt to running conditions which had not been foreseen, i.e. high luminosity per bunch and a limited initial CPU power, and the HLT algorithms were adapted in a very short time to cope with the new challenge [122].

The bandwidth division minimises the overall loss in efficiency by minimising:

$$\chi^2 = \sum_{\text{channels}} \sum_{\text{lines}} \left(1 - \frac{\varepsilon^{\text{channel, line}}}{\varepsilon_{\text{max}}^{\text{channel, line}}}\right)^2 \quad , \tag{3.2}$$

where $\varepsilon_{\text{max}}^{\text{channel, line}}$ is the L0×HLT trigger efficiency for a channel when the full bandwidth is dedicated to that channel and a specific trigger line, and $\varepsilon^{\text{channel, line}}$ is obtained using one fixed set of thresholds for all channels simultaneously. The cuts in all trigger lines are varied by running an emulation of LLT and executing the HLT application. The size of the EFF is imposed as a throttle condition. Table 3.3 shows the efficiencies obtained for the benchmark channels assuming a luminosity of 10^{33} cm^{-2}s^{-1}, and 2622 colliding bunches at the LHCb interaction point, with a centre-of-mass energy of 14 TeV.

In the first phase of the upgrade, with an EFF power five times larger than available in 2011, LHCb will increase the instantaneous luminosity by a factor five to 10^{33}cm^{-2}s^{-1}. The corresponding trigger will leave cut values practically unchanged from running at lower luminosity, and hence the trigger rates increase by a factor five for LLT, and a factor eight for HLT. With these trigger settings the signal efficiencies remain unchanged compared to low luminosity running, and hence in the first phase the gain of the upgrade is roughly equivalent to the increase in integrated luminosity. A further increase in the EFF by a factor two would

Table 3.3: Expected signal efficiencies for EFF sizes 5 and 10 times the size which is installed for the 2011 run.

EFF size	5×2011	10×2011
LLT-rate (MHz)	5.1	10.5
HLT1-rate (kHz)	270	570
HLT2-rate (kHz)	16	26
Total signal efficiency		
$B_s \to \phi\phi$	0.29	0.50
$B^0 \to K^*\mu\mu$	0.75	0.85
$B_s \to \phi\gamma$	0.43	0.53

allow to relax the trigger cuts, and results in 70% larger efficiencies for hadronic decays at the same luminosity of $10^{33}\mathrm{cm}^{-2}\mathrm{s}^{-1}$, while leptonic and radiative decays would still improve their efficiencies by respectively $\sim$ 10% and $\sim$ 20%. Hence the 40 MHz readout of the FE-electronics allows LHCb not only to profit from larger instantaneous luminosity, but in addition to significantly increase the trigger efficiency, in particular for hadronic B decays.

Chapter 4

Electronics

Introduction

A new electronics architecture is required to satisfy the requirements of reading data from every bunch-crossing in the upgraded LHCb. The existing architecture, as described in [129], includes a Level-0 pipeline buffer and derandomiser. These limit the readout speed and hence the trigger rate to 1 MHz, so any increase beyond 1 MHz requires their removal and a re-design of the electronics. Many of the challenges of the 40 MHz readout scheme can be met by the use of modern technologies adapted for high energy physics. For example, high-speed optical links will be installed to accommodate the increase in data volume from the detector. Data compression schemes will be implemented on the detectors to minimise the number of these links. Though the aim is to eliminate the hardware-based part of the trigger, a throttling mechanism will be designed to control the data flow into the data acquisition. This throttle can also be enhanced with physics information in a manner similar to the existing LHCb L0 trigger, and is known as the Low Level Trigger (LLT), as discussed in the previous chapter.

Although the upgrade will require major changes to the electronics of the detector, a number of measures will be taken to minimise cost, development time and installation effort, namely:

1. Re-use parts of the existing front-end electronics that can satisfy the upgrade requirements;
2. Develop common devices and modules to be used by all sub-detectors;
3. Re-use as much of the existing infrastructure as possible.

This chapter describes the generic electronics architecture and the parts common to all sub-detectors. The front-end electronics unique to each sub-detector are described in the relevant chapters.

4.1 Readout architecture

The general architecture is shown in Fig. 4.1. The front-end (FE) amplifies and shapes the signals generated within the detectors. These signals are digitised, compressed, formatted and

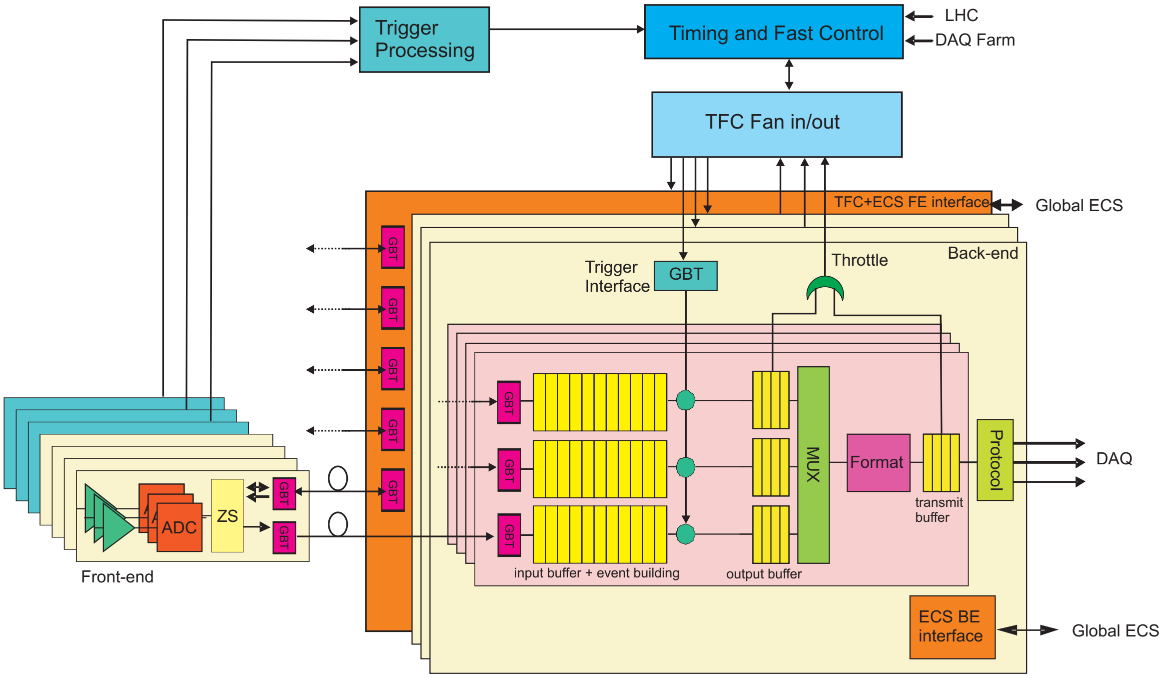

Figure 4.1: The general electronics architecture of the LHCb upgrade.

then transmitted down a high-speed optical link. The back-end electronics (BE) sit in the counting room and receive the data from the optical links. After buffering and filtering by the LLT, data are formatted for transmission to the data-acquisition system. Data from the Calorimeter and Muon sub-detectors are extracted via an independent transmission system to the trigger processors where the LLT is generated. Transmission of trigger information is through a Timing and Fast Control (TFC) system and takes the form of bunch-crossing identification numbers for which the LLT gave a positive decision. Configuration and monitoring of the BE and FE electronics are through an interface to the Experiment Control System (ECS). More details of the architecture and the specifications can be found in [130].

Compression of the data is advantageous for cost reasons, although in some regions of certain detectors the channel occupancy is such that zero-suppression is not economical and will not be used. Following any compression step, a buffer will absorb statistical fluctuations in the data size and allow an optimal use of the data band-width provided by the link. However, this implies that data from different FE modules will arrive asynchronously at the BE modules. Additional information is therefore attached as a header to the data packets to allow selection by the LLT and reconstruction of the complete events. This is based on a bunch-counter within the FE module running synchronously with the LHC clock. If the FE buffer is full, then data will be truncated until the buffer recovers. However, to maintain synchronicity, empty data packets containing only header words will still be transmitted. To minimise the risk of de-synchronisation, resets of the bunch counters will be issued once every orbit of the LHC machine.

The implementation of zero-suppression or data compression in the FE electronics implies that detector parameters such as the channel occupancy must be well understood before the

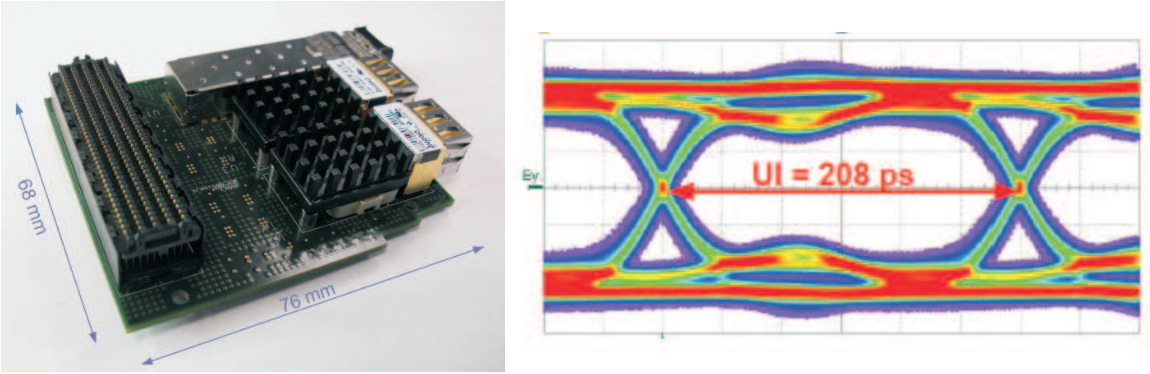

Figure 4.2: Left: prototype mezzanine board with high density serial links. This contains a 12-way transmitter, 12-way receiver, a single-channel transceiver, and a high density connector for plugging into a motherboard. Right: the eye-diagram from one channel operating at 4.8 Gbit/s.

hardware is designed and constructed. The efficiency of the algorithms and the amount of buffering are currently being tested using data from Monte Carlo simulations of the detector at the luminosities foreseen for the upgrade.

The hardware and protocol chosen for the links supports bi-directional transmission. However, the data band-width from the detector far outweighs that for TFC and ECS transmission to the detector. For this reason and to allow a cost-effective modular approach, it has been chosen to use the link in simplex mode for data transmission, and in duplex mode for combined TFC and ECS communication.

4.2 Implementation

Details of the FE modules can be found in the relevant sub-detector chapters. The relatively modest radiation levels in some sub-detectors of LHCb allow the use of commercial devices to carry out the data-compression algorithms, and flash-programmable devices manufactured by Actel [131] are the favoured components. These offer the flexibility of re-programming and faster development time compared to Application Specific Integrated Circuits (ASICs), and readily provide useful features such as internal memory. They must, however, withstand the radiation environment and a test programme is in progress to assess this. Preliminary results indicate that the device most-suited to our needs can resist up to 30 krad of ionising radiation.

Data links to and from the detector will be implemented using components from the Gigabit Transceiver (GBT) [132] and Versatile Link [133] projects developed for the upgrades of the LHC experiments. These offer a user band-width of 3.2 Gbit/s per link with a serial bit-rate of 4.8 Gbit/s, and are radiation tolerant. The LHCb sub-detector systems are being designed to drive and receive data according to the GBT protocol. Around 13,000 links will be used in the system.

The BE will be implemented as a module known as TELL40, a development of the TELL1 module that is successfully employed in the current experiment. It will be used by all sub-detectors, and its main processing task will be building the events from fragments arriving on the different data links from the detector. This processing will be done in field-programmable gate-arrays (FPGAs). The choice of format for TELL40 is Advanced-TCA [134], following trends both in industry and high energy physics. The implementation follows a modular, mezzanine-based approach. Thus data receivers, FPGAs and data transmitters will sit on pluggable cards mounted on a motherboard designed to optimise channel density. This offers the advantage of using different types of mezzanine for different tasks but all mounted on the same type of motherboard. This technique will be used in, for example, the hardware of the LLT, as described below. A prototype board has already been designed to test the density of high-speed serial links achievable on a mezzanine. Fig. 4.2 shows the mezzanine equipped with a 12-way optical transmitter and receiver together with the eye diagram from a data channel operating at the GBT serial rate. The good performance indicates that 24 channels can be integrated into one mezzanine, and up to 96 channels using four mezzanines on an ATCA motherboard. Most of the data compression will be already carried out by the FE electronics so the BE output band-width will be similar to its input band-width. The favoured option for transmission to the data acquisition system is 10 Gigabit Ethernet.

The experimental control system (ECS) interfaces for the FE modules will be based on the GBT. An ancillary chip, known as the GBT-SCA [135] translates a portion of the GBT frame into standard protocols such as I2C to configure the components on the detector. However, many of the existing systems in LHCb used for slow controls and environmental monitoring will be maintained. Each BE module will be configured through an Ethernet interface, implemented as either a credit-card PC or embedded within an FPGA.

4.3 Low Level Trigger hardware

The LLT will be based on the hardware used for the existing LHCb Level-0 trigger [136] and is shown in Fig. 4.3. The ECAL and HCAL detectors are read out by new FE boards equipped to handle the new architecture but with a separate data path for the trigger, following the present architecture. These transmit data to the present Validation Card where initial selection is carried out. Data are then transmitted off-detector to two TELL40 modules, known as TRIG40 and equipped with mezzanines compatible with the data protocol of the Validation Card. Further processing is done by the TRIG40s and results are transmitted directly to the TFC system. The Muon trigger is based almost entirely on the present L0-muon system, where data from the off-detector electronics (ODE) are transmitted to the counting room for processing. Decisions are sent to a third TRIG40 for further processing and then to the TFC.

The main role of the LLT is as a controlled throttle. It can also be used as a staging mechanism to allow the running of upgraded sub-detectors together with systems still operating with the classical Level-0 architecture whose upgrade would come later. This would restrict the upgraded electronics to 1 MHz operation during this initial period.

4.4 Infrastructure

It is intended to re-use as much of the existing electronics infrastructure as possible for the upgrade. LHCb currently uses radiation- and magnetic-field-qualified power supplies situated close to the detector, and these will still survive the radiation environment at the upgraded luminosity. However, it is expected that additional supplies will have to be purchased. Much

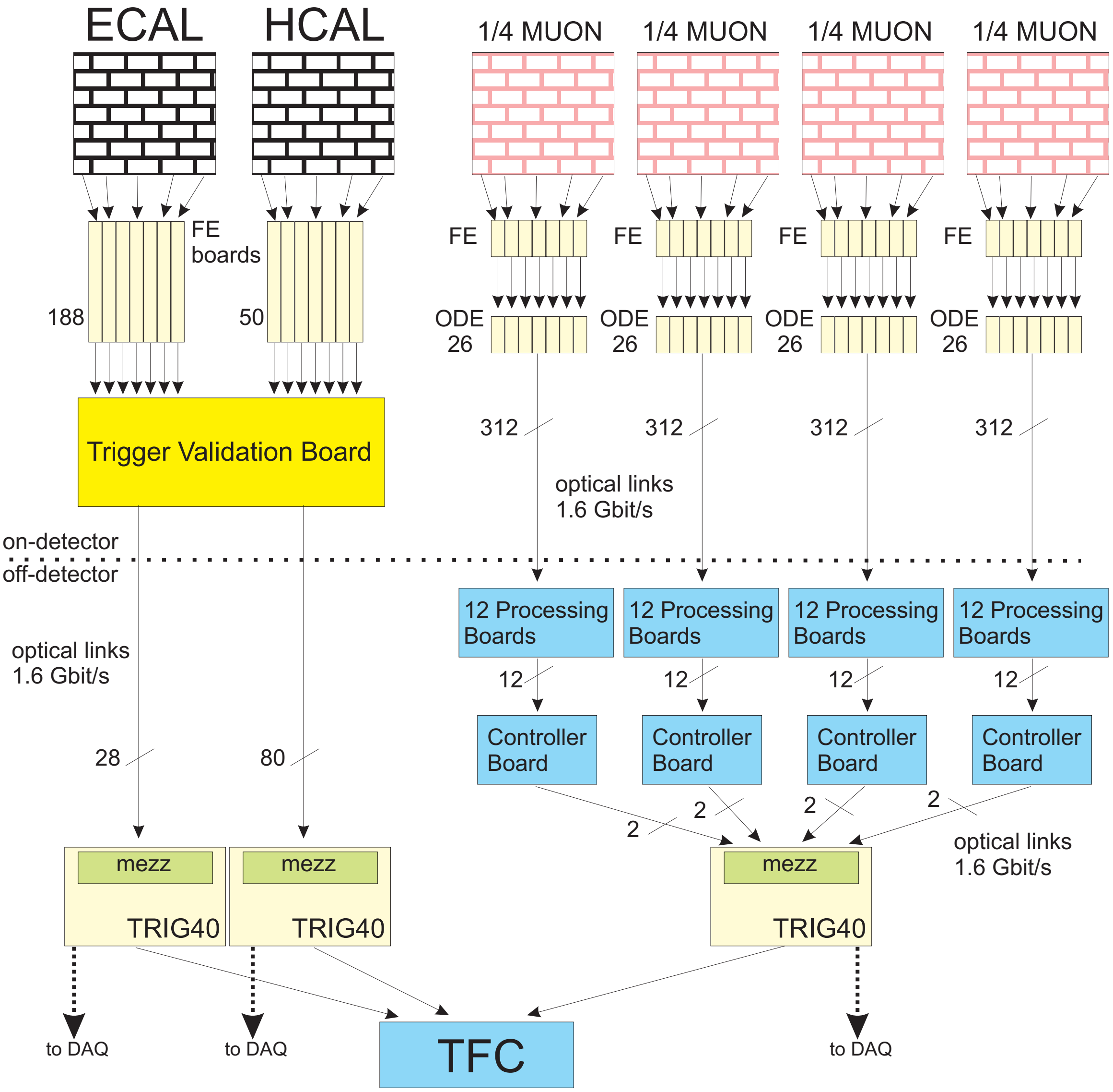

Figure 4.3: The hardware used to generate the Low Level Trigger.

of the electrical cabling in the cavern can be re-used. Around 8,000 optical fibres, rated for a band-width of 600 MHz km, are already installed in the cavern and can support the band-width of the GBT transmission.

Chapter 5

Vertex Locator (VELO)

Introduction

The physics programme of the LHCb upgrade requires an extremely performant vertex detector with fast pattern recognition capabilities, excellent vertex resolution and two track separation, and sufficient radiation hardness to guarantee excellent performance throughout the upgrade data-taking period. In particular, the trigger performance, which relies heavily on the vertex detector data, must be fast and flexible enough to adapt to the evolving physics needs of the experiment. The move to a 40 MHz readout necessitates the construction of a new Vertex Locator (VELO) with appropriate electronics and sufficient radiation hardness. Pixels are an attractive choice for the upgraded VELO due to the high granularity and the relative ease of pattern recognition. In order to provide 40 MHz readout, the Timepix chip, from the Medipix family of chips [137] has been identified as an excellent candidate from which the final pixel FE electronics, dubbed "VELOPIX" could be developed. The principal challenges of the pixel module design are to keep the module sufficiently light and to control the power consumption and cooling to the required levels. The alternative of an upgraded VELO strip detector would be similar to the current VELO design, but require improved cooling and a new ASIC, with possible synergies with the Silicon Tracker upgrade silicon option. In the following sections we outline the VELO design requirements, and the R&D programme which is underway to develop the upgraded VELO detector. For more details about the VELO upgrade see [138].

5.1 VELO evolution and design issues

The current VELO is manufactured with 84 R and ϕ measuring strip sensors operated in a secondary vacuum inside the LHC beampipe. The sensors are grouped by $R\phi$ pairs into 42 modules, each with 32 readout chips. The detector is divided into two movable halves, allowing it to retract during LHC injection, and separated from the primary vacuum with a 300μm thin foil of aluminium alloy, which is corrugated in such a manner as to reduce as far as possible the material traversed by particles before the first measured point. For a more complete description of the VELO see [139] and references therein. The upgraded VELO will retain the current vacuum system together with its control system, and also most of the movement mechanics, however the modules must be completely redesigned to be compatible with the 40 MHz readout and to be able to withstand thermal runaway after high irradiation. The cooling is envisaged to be a mixed-phase CO_2 system similar to the current VELO, with the cooling capillaries at approximately -40°C running around the edge of the silicon as far as possible out of the acceptance. In order to drain heat away from the most irradiated innermost portions of the module a diamond cooling spine is envisaged.

The major design issues for the VELO upgrade are outlined below:

Irradiation issues The upgraded VELO must be designed to withstand an integrated luminosity of at least 40 fb^{-1} and accumulate a maximum flux of up to approximately $0.3 \times 10^{16} n_{\text{eq}}\text{cm}^{-2}$ at the innermost portions of the modules. After this dose, we would expect currents of approximately 120 $\mu\text{A/cm}^2$ at -15°C at a bias voltage of 900 V at the innermost radius, equivalent to roughly 4 nA for 55×55 μm square pixels, or 200 nA for an innermost strip. At these doses and currents, the tip of the silicon is exposed to the risk of thermal runaway, from the bulk current and from the heat injected by the pixel ASICs. The most challenging issue will be to provide effective cooling without introducing too much material into the acceptance. The electronics will also be required to be extremely radiation hard and tolerant of single-event upsets.

Geometry issues The trigger algorithms of LHCb in both the current detector and the upgrade rely on an impact parameter cut, hence the impact parameter resolution is an excellent benchmark performance number for the detector. From our previous studies [140] we know that the impact parameter resolution is well described to first order by the following expression:

$$\sigma_{\text{IP}}^2 = \frac{r_1^2}{p_{\text{T}}^2\sqrt{2}}\left(0.0136\sqrt{\frac{x}{X_0}}\left(1 + 0.038\ \ln\left(\frac{x}{X_0}\right)\right)\right)^2 + \frac{\Delta_{02}^2\sigma_1^2 + \Delta_{01}^2\sigma_2^2}{\Delta_{12}^2} \tag{5.1}$$

In this formula r_1 is the radius of the first measured point, p_{T} is the transverse momentum of the track in MeV/c, x/X_0 is the fractional radiation length before the second measured point, which includes the foil, any dead area of silicon traversed, and the material of the first measured point, σ_1 and σ_2 are the measurement errors on the first and second point respectively, and Δ_{ij} represents the distance between x and y, where i and j can be 0 (the interaction region), 1 (the first measured point), or 2 (the second measured point). This formula gives an indication of the driving factors behind the design. The presence of the r_1^2 term indicates that the first measured point should be as close to the interaction point as possible, which is achieved by designing the minimum possible inner dimensions, reducing the size of the guard rings, and having as many stations as possible. The impact of varying the minimum radius of the first measured point is illustrated in Fig. 5.1 (left). The presence of the $\sqrt{\frac{x}{X_0}}$ term shows, on the other hand, the importance of reducing the number of stations, of having the stations as thin as possible, and of reducing the material contribution of the RF foil which encapsulates the detector secondary vacuum volume. The impact of this material term on the impact parameter resolution as a function of transverse momentum is illustrated in Fig. 5.1 (right). The final term in Eq. 5.1 illustrates the importance, for high momentum tracks, of maintaining the best possible precision. There are additional considerations which enter into the design, in particular the importance of having stations surrounding the interaction region on both sides, in order to measure the primary vertices as accurately as possible. In addition the overall performance of

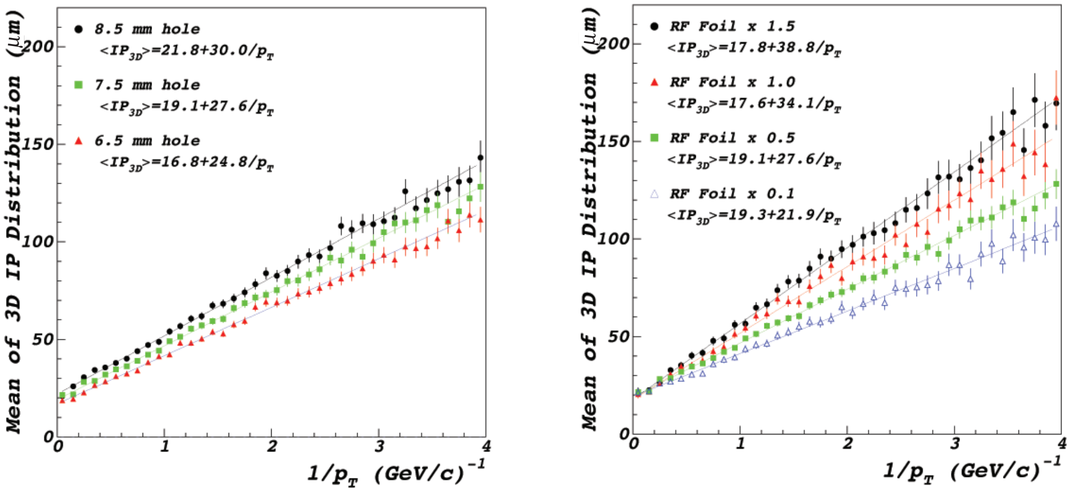

Figure 5.1: Illustration of the importance of some sample design parameters of the VELO on the impact-parameter resolution performance. Each plot shows the impact-parameter resolution as a function of $1/p_{\mathrm{T}}$. The left plot shows the impact of varying the innermost radius of the first measured point. The right plot shows the effect of decreasing the material in the foil. One of the goals of the upgrade R&D is to decrease the foil material by a factor of up to two. The plots shown here use the pixel straw-man design as input.

the detector in terms of the trigger algorithm and the time taken to execute this algorithm in the computer farm must be taken into consideration.

Data rates Imposing a 40 MHz readout results in a high data rate output needed from the front end chip, with the particle density per crossing reaching $\approx 2.5 \times r^{-1.9}/\mathrm{cm}^2$ at the highest luminosity, where r is the radius in cm. Taking the model of a 256×256 matrix pixel detector (as outlined in the following sections), and assuming an average cluster size of 2 leads to the conclusion that from the innermost chip the data rate would be approximately 13 Gbit/s with a total data rate of around 3000 Gbit/s for the entire detector. This would require a minimum of 940 data links running at 3.2 Gbit/s. On top of this, extracting the data from the pixel matrix to the pixel periphery becomes non-negligible at these rates and a fundamental design change is needed for the front-end chip. This is discussed in the following sections. In the case of the strip design, the total data rate is similar.

Mechanical constraints The presence of the detector within the LHC beampipe imposes additional design considerations. In the baseline design, the concept of the separation of the primary and secondary vacua is preserved, which imposes requirements on the foil leak tightness, as well as its mechanical stability up to a small pressure difference of 5 mbar, which is a safety factor required for the venting/pump-down procedures. The modules themselves cannot be manufactured out of material which causes excessive out-gassing, and great care must be taken with the integrity and leak tightness of the cooling connections. In addition the overall constraints on the detector geometry, such as the horizontal opening movement of 30 mm, and the total allowed detector length of 1.2 m, remain in place.

Figure 5.2: Front view and exploded schematic of the VELO straw-man module, shown in an "open" configuration; for normal running the module edges will overlap slightly. The 3 × 1 chip + sensor components can be seen with the chips in yellow and the sensor in orange, mounted on either side of the light blue, partially transparent diamond substrate. Eight of these components make up one complete plane. The sensitive region is outlined with the dashed line.

5.2 Straw-man pixel design

A "straw-man", or working hypothesis for the pixel detector layout, has been designed to serve as input to simulation studies of the upgrade detector design. Its concept follows a conservative estimate of the available technologies and may be revised following further R&D results. The layout comprises two detector halves which can be accommodated by the current motion system. Each half consists of 26 modules with varying spacing along the beam axis, the minimal pitch being 24 mm.

A single module contains twelve VELOPIX chips (see Fig. 5.2). The chips are grouped in rows of three which are bump bonded to a common silicon sensor. Each group of six chips containing two such rows are mounted on opposite sides of the substrate such that they can overlap in the transverse plane to create a gap-less acceptance.

The two blocks of six chips are mounted at right angles such that one block is read out towards the top or bottom of the module and the other to the left or right. This results in the readout columns of the chips being oriented pointing towards the beam-hole instead of being laterally exposed. This configuration is chosen in order to produce a more uniform hit occupancy in the columns and as a consequence a lower maximal column hit occupancy, which is an important consideration in the design of the chip readout architecture. The outer row of three chips has to be slightly displaced as it is mounted on the same side as the inner row of the other block of six chips. This results in a small acceptance gap in the outer part of the transverse plane of this layout; however there is complete coverage in the internal part, which is essential to optimise the impact parameter resolution.

The sensors and chips are supported by a diamond substrate which extends about 1 cm beyond the edge of the active area to serve as a cooling interface. The diamond extends to the innermost edge of the silicon. The diamond substrate is framed by a TPG substrate which also acts as a support for the cooling and readout infrastructure.

The innermost edge of the silicon is at 7 mm from the beam, as for the current VELO detector. The guard ring is assumed to have a width of 0.5 mm such that the active area starts at 7.5 mm from the beam. Any possible reduction in either the distance of material to the beam or the width of the guard ring would improve the performance of the detector. The material of the RF foil also has significant impact on the performance as it contributes to most of the multiple scattering between the origin vertex of a track and its first measured point. The foil design is discussed in detail in Section 5.3.5.

The material thickness of the module will be dominated by the following components: 400 μm diamond substrate, 150 μm thinned ASIC, 200 μm thick silicon sensor, 50 μm glue, and kapton traces over half of the active region dominated in thickness by 60 μm kapton foil and 120 μm Al power and signal traces. From these contributions the total material thickness in the sensitive region of the module can be estimated at roughly $0.8\%\,X_0$. The impact-parameter resolution performance has been estimated using a standalone GEANT3 simulation which uses parameters close to these values. Assuming that a material contribution of the upgraded foil of half the current foil is achievable, then the layout described here should achieve a nominal impact parameter resolution performance of $(19 + 28/p_{\mathrm{T}})\mu$m where p_{T} is the track transverse momentum expressed in GeV/c. In case this foil thickness is not achievable, the degradation in the material term would evolve as shown in Fig. 5.1. The efficiency for reconstructing all four tracks from a $B_s \to D_s K$ decay has been simulated to be 98.3% (99.7)% if 4 (3) hits are demanded per track.

5.2.1 Cooling Studies

A critical aspect of any pixel detector design is the cooling. Because of the large particle fluence the silicon closest to the beam will draw large current, $I_{\mathrm{leak}} \simeq O(100)\,\mu\mathrm{A/cm}^2$. The corresponding power dissipation, $I_{\mathrm{leak}}V$ heats the silicon, which in turn results in larger leakage current. This thermal runaway can be avoided if the silicon is kept sufficiently cool, below about -10° to -15°C.

The module will nominally incorporate a 400 μm-thick CVD diamond substrate which extends from the innermost edge of the silicon out to a cooling channel, which is about 1 cm from the outermost edge of the silicon. ANSYS [141] thermal simulations of a pixel module assuming two-phase CO_2 cooling (as in the current VELO) have been performed, capable of maintaining the temperature of the cooling channel at -35°, a conservative estimate of what will be possible. The simulations included readout chip (ROC) heat loads, temperature and radial-dependent silicon heating[1], and nominal thicknesses and thermal conductivities of the various materials.

The thermal performance of the module has been studied by varying the ROC power, the diamond thickness, glue-joint thicknesses, and thermal conductivities of the diamond substrate and epoxy interfaces. The main conclusions of these simulations, in order of importance are: (1) The cooling line must be as close to the silicon as possible; (2) The ROC power must be minimized. For a 400 μm thick diamond substrate with thermal conductivity, κ = 1600

---

[1] I_{leak} falls as $\sim r^{-1.9}$.

W/m K, a maximum ROC power of ∼3.0–3.5 W/chip can be tolerated, assuming all other design parameters are held at nominal values. (3) In general, all thermal impedances between the cooling line and the silicon must be minimized.

Other factors in the module design, such as moving the cooling channels closer, exact values of thermal conductivities and material thicknesses, inner diamond detector region, etc, could allow for somewhat higher ROC power, or provide more or less safety margin with regard to thermal runaway. For ROC power below 3.0–3.5 W/chip, CO_2 cooling should be sufficient to avoid thermal runaway up to a dose of $\sim 10^{16}\ n_{\mathrm{eq}}/\mathrm{cm}^2$, giving a safety factor of two above the expected upgrade fluence.

5.3 R&D towards the upgraded VELO module

5.3.1 Module structure

A guiding principle of the module construction is to aim for a balanced two-sided design in order to keep the structure planar for ease of construction, and to minimise distortion resulting from temperature changes both during construction and operation. The proposed module will be constructed around a central High Thermal Conductivity (HTC) CVD diamond or alternatively a carbon-fibre clad TPG spine. Four tiles consisting of a sensor bump-bonded to three chips will be precisely positioned, two each side, using similar jigging and techniques to those used in construction of the present VELO. In order to meet the required operating temperature at the highly irradiated inner edges of the sensor and avoid possible thermal runaway the spine is required to extend under the whole of the active area of the module, and thus the thickness of the spine must be kept as low as possible. Thermal simulations suggest that an HTC spine of 400 μm thickness may be adequate, however minimisation of the thermal gradients in the interfaces between the tiles and spine, and the spine and the biphase CO_2 cooled heat-sink attached at the outer edges, are critical in achieving this. Identification of adhesives and a process to achieve repeatably very thin glue layers capable of resisting shear from CTE differences between the silicon tiles and the substrate will be investigated. As the detector is operated in a secondary vacuum, closely coupled with the primary vacuum, leakage from the cooling system is avoided by providing a pre-engineered leak tight system and attaching the heat-sinks during module installation. Development of a demountable low-mass heat-sink structure compatible with the substrate CTE and adequate thermal performance is a priority.

To reduce mass in the active area both the chips and sensors can be thinned after production. It is possible to thin the silicon down to 150 μm, or to 100 μm for sensors and even less for readout chips, if a support structure is used, however bowing and handling difficulties may limit what can be achieved here. There are three alternatives under consideration for the sensor technology, described in the following section.

5.3.2 Sensor options

Planar silicon sensors A substantial amount of experimental data has been accumulated in recent years (see for example [142] and references therein) to show a surprisingly large charge collection in severely irradiated silicon detectors, compared to the parameterisation of the radiation damage accepted at the time. The discrepancy between these results and the predictions led to a reanalysis of the model describing the charge collection. The currently accepted explanation for the enhanced charge collection in highly irradiated silicon sensors involves a charge multiplication effect for irradiated detectors biased at high voltage. The data show that planar silicon sensors can provide adequate charge collection for detecting minimum ionising particle even after doses as high as $2 \times 10^{16} n_{\rm eq}{\rm cm}^{-2}$ if coupled to low-noise electronics. The data also show that after this level of irradiation, detectors of reduced thickness ($\sim$150 μm) exhibit better charge collection than standard ones (300 μm) at the same bias voltage. This feature makes thin devices particularly interesting for the LHCb upgrade, because a signal of about 6000 e^- can be measured at 900 V with a 150 μm detector after $\sim 2 \times 10^{16} n_{\rm eq}\,{\rm cm}^{-2}$, corresponding to double the dose expected at the upgrade. This implies that very good tracking efficiency can be maintained, particularly when coupled to the low noise electronics that will be made available for the upgrade. It should be noted that the charge multiplication effects can also increase the noise levels, and so it is essential to pursue R&D to guarantee the expected performance.

The charge multiplication mechanism that enhances the signal after high doses can have an impact on the charge sharing, though, and therefore on resolution in segmented sensors. The charge sharing is expected to be reduced with irradiation. One of the aims of the R&D on planar sensors will be to determine the changes of the charge sharing between adjacent readout channels as a function of the irradiation. Planar silicon sensors will need high bias voltages, and the system needs to be designed to be able to sustain up to about 1000 V bias for efficient tracking performance after the higher doses. This will in turn lead to significant detector leakage current. The leakage current can be reduced by lowering the operation temperature and by annealing the sensors for limited amount of time at temperature around or above 20°C. The scenario for optimal operations (sensor temperature during data taking and during shut-down periods) will be studied. One of the drawbacks of the planar technology is the need to keep a significant distance between the active area and the cut edge to prevent voltage breakdown through the sensor edges. This distance is, for present designs, as large as $\sim$1 mm. An optimised design of the implanted ring structures that surround the active region to provide protection against low resistive paths between the active region and the edge of the sensors (biased at high voltage) can considerably reduce the inactive region. Here a further advantage can be found with thin devices, because the width of this area can be further reduced with respect to standard devices. Widths of the inactive area of 400 μm or below seem to be possible. The investigation of planar silicon sensors will use various types of devices (diodes, pixel and microstrip sensors) from different manufacturers, and will use different characterisation methods (lab measurements with IV-CV bridges, radioactive sources and beam tests with high resolution beam telescopes).

Diamond sensors Chemical Vapor Deposition (CVD) diamond has some appealing properties as a sensor element for hybrid pixel modules operating at the kind of radiation fluences which are envisaged for LHCb upgrade operation. It has been demonstrated to be extremely radiation tolerant, and in addition the leakage currents remain low after irradiation, so that the risk of thermal runaway and the associated cooling challenges of the upgraded VELO modules might be reduced with the use of diamond for the sensors closest to the beam. In addition its large thermal conductivity (between four and five times that of copper at room temperature) may be exploited for intelligent integrated cooling concepts, thus leading to an overall optimization of the material budget in the innermost region of the detector.

The challenges of this technology include producing wafers with uniform charge collection distance sufficient to produce an adequate signal-to-noise ratio throughout the expected detector lifetime, spatial resolution, and minimization of the horizontal polarization fields induced by grain structure effects.

The RD42 collaboration has worked for the last 20 years to improve the quality of polycrystalline CVD (pCVD) diamond, and of single crystal diamonds. The latter have excellent charge collection and spatial resolution properties, however the production of single crystal diamonds in the size needed for our application appears too expensive. We have started an R&D programme to establish the suitability of pCVD diamonds, by acquiring some pCVD diamond samples suitable for bump-bonding with Timepix devices. We have measured the collection length of five samples with a ^{90}Sr source, obtaining collection lengths between 200 and 250 μm. Test beam studies to validate these measurements and to study other properties such as efficiency and spatial resolution are under way.

The next steps are:

1. An assessment of the performance of CVD detectors developed for the ATLAS insertable B-layer project, in conjunction with the Timepix ASIC.

2. The construction of pCVD hybrid pixel modules with Medipix3 readout to evaluate their radiation resilience.

3. The production of a wafer optimized for our application in terms of thickness and charge collection distance to be bump-bonded to prototype Timepix2 or VELOPIX ASICs, to study the performance of the final system.

In parallel we are studying the factors which affect the detector performance, such as metallization, overall active area, wafer thinning, and integration of the diamond sensor into the cooling design of the pixel module.

3D silicon sensors 3D silicon detectors consist of a three-dimensional array of electrodes that penetrate into the detector bulk. The 3D detector is realised by etching holes normal to the surface of the silicon and filling these with dopant to form interposed arrays of n^+ and p^+ holes. In traditional planar detectors the electrodes are implanted in the top and bottom surfaces of the wafer so the maximum drift and depletion distances are set by the wafer thickness. In contrast, 3D detectors deplete laterally, so these distances are given by the inter-column spacing that can be much smaller than the wafer thickness. The reduced electrode distance results in high electric fields and high drift velocities with relatively low bias voltages that reduce the probability of trapping, gives short collection times and makes the devices radiation hard. These devices show very promising radiation resistance, but are difficult to fabricate. The fabrication difficulties can be partially eased with the use of double-sided 3D sensors, where the columns do not extend through the full depth of the silicon bulk [143]. A potential advantage for the VELO upgrade of 3D technology is that the self-shielding geometry and additional processing can allow devices to be active to within $10\mu m$ of their physical edge.

Both strip and pixel 3D devices have been developed. Pixel devices have been fabricated for Medipix/Timepix and ATLAS designs, with most recently quad-Medipix sensors having been produced. Devices have been simulated with ISE-TCAD and the electrode geometry configuration has been optimised [144]. The devices have been tested in the laboratory with LHCb/Medipix and other CERN testbeams and at the Diamond synchrotron [145]. The devices deplete between columns at 2 V, and deplete to the front and back surfaces at 10 V. In the current devices the pores (10 μm diameter) do not collect charge, and hence an inefficiency is obtained for perpendicular tracks. The devices also have considerably higher capacitance than comparable planar devices[2].

The unirradiated 3D devices show 100% charge collection efficiency (22.8k electrons) at full depletion. Only moderate bias voltages, 150 V, are necessary for full charge collection for fluences up to 10^{15} $n_{\mathrm{eq}}/\mathrm{cm}^2$. Higher radiation doses reduce the collection efficiency but for 10^{16} $n_{\mathrm{eq}}/\mathrm{cm}^2$ the collected charge at 150 V is 44% (10k electrons), and higher at 300V. For comparison, a 300 μm-thick n-on-p planar sensor irradiated to the same fluence of 26 MeV protons has a 25% collection efficiency at 900 V bias [146]. Charge multiplication effects have also been observed in the 3D detectors (as in planar devices), and are currently under study.

5.3.3 Electronics R&D

The choice of a pixel detector for the upgraded VELO requires a new front-end chip that satisfies the electronics architecture described in Section 4. A family of pixel chips (Medipix, Timepix [137]) has already been developed based on a 55 μm square pixel, and these have been used successfully in a number of different applications. A new development, Timepix2, is currently underway and many of its features, in particular the analog front-end, are applicable to VELOPIX. Thus VELOPIX will be an adaptation of Timepix2 with a digital readout architecture to match the LHCb requirements.

The technology of choice is the IBM 130 nm CMOS process, which is now widely used in high energy physics and offers the advantages of large component density and an intrinsic tolerance to the total-dose effects of ionising radiation. Recent measurements on Medipix3 [147] indicate that the technology can survive doses of well beyond the $\sim$ 200 Mrad expected in the upgraded VELO.

Table 5.1 lists the main requirements for the VELOPIX chip. The size of the pixel and of the full matrix match well the VELO requirements on track precision and area coverage. The maximum peaking time of 25 ns allows correct identification of hits with the bunch crossing. The requirements on noise and threshold are determined by the signal expected from the silicon sensor after irradiation and also include the expected reduction in signal due to charge sharing between pixels. The ability to measure time over threshold (TOT) per hit is expected to improve the track resolution by allowing more precise hit position reconstruction through charge weighting, as demonstrated by the test beam results described in [138]. All of these features will be implemented in Timepix2.

An extremely important requirement is the sparsification of data, given the requirement of reading all hits from every bunch crossing. In addition to this, the small pitch and track angles mean that charge will often be shared amongst pixels, increasing further the data rate. An architecture has already been developed to minimise the data bandwidth from the pixel matrix [148]. This is based on grouping the digitised data from a 4×4 array (a super-pixel) and transmitting this information as a formatted and encoded cluster. Figure 5.3 shows the

---

[2] The capacitance between one readout strip and the bias columns, which dominates the total capacitance, was measured as 12.5 pF/cm in an 80 μm-pitch strip detector.

Table 5.1: The main requirements of the VELOPIX chip.

Parameter	Requirement
Pixel size	55μm $\times$ 55μm
Array size	256×256
Front-end peaking time	≤ 25 ns
Time-walk for signals 1000 e^- above threshold	≤ 5 ns
Noise for input capacitance up to 25 fF	≤ 100 electrons
Minimum detectable charge	500 electrons
Channel-to-channel threshold spread	< 30 electrons
Time over threshold measurement	4-bit
Readout type	zero suppressed
Power consumption	< 1.5 W/cm^2

super-pixel organization: the 4×4 matrix of analog pixels share a common super-pixel digital block processing the information of all pixels in the matrix. In order to reduce the data rate, the super-pixel data is formatted with a scheme including a header containing the data common to the pixels in the group, such as the beam crossing number, and using the minimum number of bits to transmit the pixel specific information. Various layers of buffering are involved within a super-pixel, within a group of 4 super-pixels, and at the end of the super-pixel column. The preferred method for transmitting the data off the chip is by high-speed serial links. The average ASIC output in the innermost region of the sensor can reach about 13 Gbit/s, and we assume that the serialiser drivers will be capable of delivering 4 GBit/s, hence 4 per chip is sufficient. Hit patterns derived from Monte Carlo events have been used to assess the performance of the chip architectures and it has been shown that losses of less than $< 0.5\%$ are expected for the highest occupancy conditions.

The performance of the Timepix chip for charged particle tracking has been verified with the construction of a dedicated Timepix telescope and the extensive characterisation of a series of hybrid pixel devices, including 300 and 150 μm thick planar sensors and irradiated and non-irradiated 3D sensors. A resolution of 4 μm has been demonstrated for optimum angles in the planar sensor, together with very high efficiencies and accurate charge calibration [149].

5.3.4 Readout Architecture

Four hybrids comprising six VELOPIX ASICs form a pixel plane, as described above. Thus, in the present model featuring four high speed serial links per ASIC, each hybrid comprises 24 high speed data outputs. Assuming 26 pixel detector planes, the total number of data links in this system is 2496. This number can be reduced if ASICs with low occupancy use a smaller number of high speed serializers. As the electronics operates in an a vacuum enclosure, we are planning to use copper data cables inside the detector box. This choice is motivated by the higher radiation tolerance and reliability of this solution. The challenge is to ensure transmission of 5 Gbit/s data rates over about 2 m with low mass cables and several discontinuities introduced by connectors and feedthroughs. The current design of the data receiver boards (TELL40), used

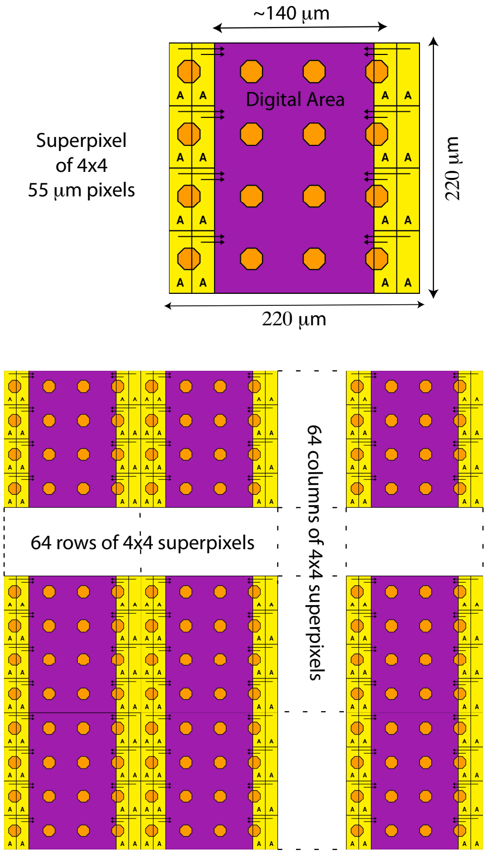

Figure 5.3: VELOPIX super-pixel layout. The orange circles indicate the bump-bonds to individual sensor pixels, and the yellow regions marked A indicate the analogue electronics part. The array of super-pixels making up the chip is shown below.

to transfer data from the front-end devices to the event processing farm, can accommodate up to 24 inputs on each of 4 mezzanine cards. Under this assumption, our “back-end” electronics would comprise 26 TELL40. The readout scheme of a VELO half is illustrated schematically in Fig. 5.4.

There are several R&D items that need to be addressed to validate this overall readout concept. The detailed simulation of the data flow at chip level needs to be complemented by a “system level” study of the data rates needed across a pixel plane. The data-acquisition group provides a framework to perform these studies, which we need to adapt to our description of the “quarter-plane” slice.

The R&D to develop a suitable data transfer scheme is focussing on the following issues:

- Most suitable electrical standard to be adopted in the high speed serializer (CML, LVDS, SLVDS);
- Signal equalisation to compensate for the distortion induced by the high speed signal transmission over ~ 1.5 m low mass cables. One option would be to incorporate suitable elements in the VELOPIX itself (“pre-equalisation”) although this would require modification of the high speed serial drivers currently being developed for other CERN projects.

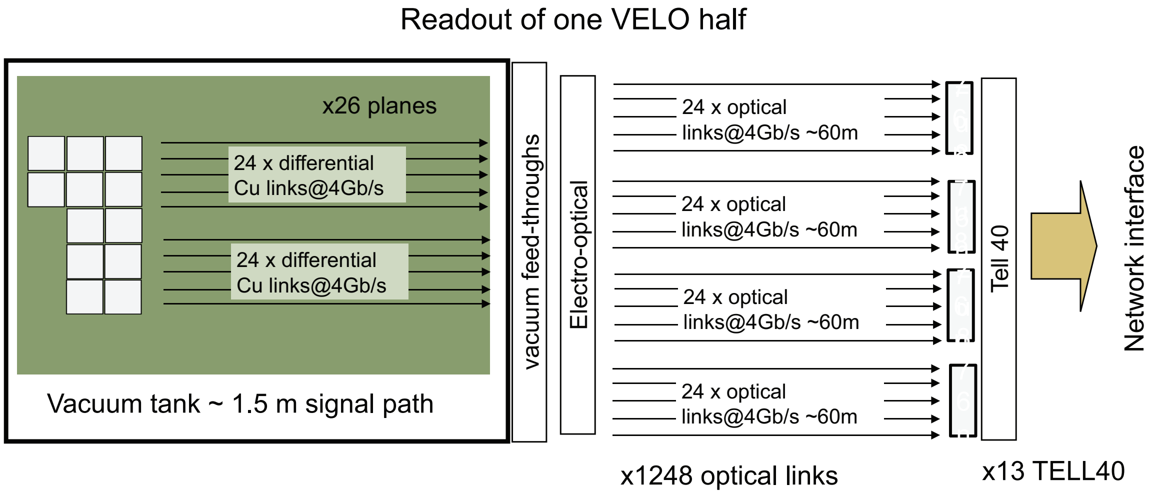

Figure 5.4: Schematic illustrating the readout of one VELO half.

> Another option would be to install "self-adapting" circuits at the receiving end ("post-equalisation"), which would have the advantage of being able to automatically adjust the compensation to match the distortion in each individual line. Commercial devices will be considered, if the radiation tolerance is adequate, or a custom implementation may be necessary.

The VELOPIX readout architecture poses particular challenges to the TELL40 due to the fact that the data are produced as non time-ordered packets. In addition, the super-pixel clusters may contain two individual clusters which must be split before the tracking algorithms are performed, and due to the fact that clusters are not combined across super-pixels in the row direction, clusters may have to be merged. The electronics specifications are designed to remove the majority of time-walk effects from the data, but any residual time-walk could also split clusters across event time-stamps. Gain non-uniformity and offsets in the pixel thresholds will affect the cluster position calculations, as will potential corrections for imperfect charge sharing between pixels. We will study how to use the powerful Stratix IV included in the TELL40 boards, featuring DSPs ideally suited for complex mathematical data manipulations, to address these effects. Potential algorithms could reduce the data rates, provide a first level of event filtering, introduce calibration constants, and reorganize the data into real clusters ready to be combined into tracks.

5.3.5 Foil R&D

The main purpose of the RF foil is to act as a *de facto* beam pipe, with all its attendant functions, i.e. it must: separate the primary (accelerator) and secondary (detector) vacua, carry the image currents of the beams, allow for the close-in VELO sensor geometry with overlap, shield against RF noise pick-up in the VELO, and withstand high radiation levels. The main issues with the current design [150] of the RF foil are that it contributes about half

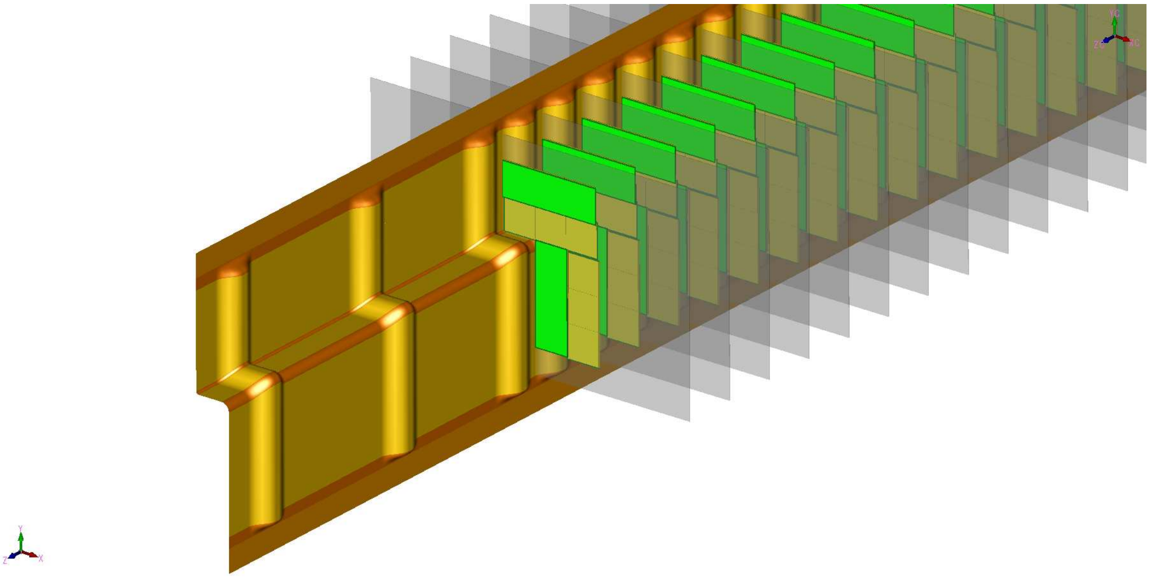

Figure 5.5: The first design of the RF foil for the upgraded VELO, based on the L-shaped straw-man module geometry. Each of the 26 stations is comprised of two VELO modules, with sensors (green), ASICs (yellow), and substrate (transparent grey). The foil (gold and orange) is shown between the modules on each side, and is corrugated to conform with the L-shape of the modules as well as the small overlap of the modules that is required for full acceptance coverage. The first three modules have been removed from this figure to expose the foil geometry. The spatial amplitude is smaller than the current RF foil, but the curvature is more complicated

of the total material thickness of the VELO detector, adding significant Coulomb scattering to the vertex and tracking errors, and its shape must be altered to accommodate the L-shaped VELO module described in Section 5.2. It is assumed that the current overall structure of having two independent movable overlapping halves, moving in the horizontal direction, will be retained. A view of the upgrade RF foil is given in Fig. 5.5.

These functions and issues place many serious requirements on the foil material and design.

- In order to reduce the tracking errors, the radiation length x/X_0 of the new foil material should be smaller than that of the currently-used aluminum alloy (300 μm thick AlMg3). The foil dominates the material before the second measured point, and simulations confirm that the impact-parameter resolution indeed scales with the square root of the radiation length of this section. However the material cannot be too thin, otherwise it will not be stiff enough to prevent deflection onto the sensors nor to prevent material fatigue under repeated vacuum cycles, causing pinhole leaks.

- The foil design and material must be compatible with ultra-high vacuum and dynamic beam effects, such as multipacting and secondary emission yield. This requires NEG coating and low out-gassing. The structure should be impedance tuned to minimize the generation of wake fields. It must withstand a radiation dose of ∼200 Mrad without significant degradation.

- The foil material must be formable to a complicated geometric shape comprised of corrugations, small feature sizes, and a large step required by overlapping L-shaped modules. The plastic deformation technique used in the fabrication of the current RF foil is unlikely to be viable in forming a large step.

The technologies under consideration include either developing a new material such as a carbon-fibre reinforced polymer (CFRP), or using a workable metal alloy similar to AlMg3.

CFRP composites have intrinsically low density and can be made with large-modulus fibers for stiffness, plus space-qualified resin that is radiation-tolerant, low out-gassing and micro-crack resistant. Similar material has been shown to be mechanically stable to above 500 Mrad [151]. Recent advances in CFRP fabrication techniques indicate that the use of carbon nanotubes for polymer reinforcement has the potential to increase the strength of the material considerably [152]. Additionally, the RF foil, box and flange can be fabricated as a single integrated unit, avoiding vacuum sealing problems. Use of this material could reduce the material thickness by a factor of two over the current foil. However its large-area behaviour under vacuum has yet to be established, particularly with long term radiation exposure.

A first set of CFRP samples have been fabricated, consisting of small, flat, 300μm thick pieces, made with various layup techniques in order to optimize material, thickness uniformity and vacuum tightness. Dedicated molds have been made as tooling for layup shaping, with the first shaped samples fabricated having $\sim 300\,\mu$m thickness and good feature definition. A testing program has been developed for determining the resulting curvature profile, uniformity of thickness, mechanical deformation, vacuum sealing, and so on. In addition to measurement of the basic features for a large-area structure, these prototypes will be tested for RF shielding and radiation resistance.

Metal alloy has been used successfully in the current RF foil, and many of its basic features are already known. The focus is on the fabrication technique, such as developing a different deformation technique to form the foil, or machining the foil from a thicker plate, with the use of a 5-axis milling machine. The milling technique can be combined with a new approach in which the full box is machined from a single massive block of homogeneous AlMgMn, with mechanical strength provided during the process by a special filling material. In this way the thickness of the side walls can be graded in an optimum manner, and the difficulties of welding a very thin front foil to create the final box are completely avoided. In a first demonstration step a box with a flat front foil has been machined with a foil thickness of 300 μm and the object has been tested to be leak tight to $< 10^{-9}$ mbar l/s. The next step will be to manufacture a box with an L-shape foil, which will be evaluated for vacuum tightness and thickness uniformity.

5.4 Strip-based alternative design

In case the material budget or power consumption of the pixel detector rise beyond acceptable levels, a strip-based detector is also being prototyped. The silicon strip sensors of the current VELO detector in the LHCb experiment are the result of an R&D programme over a period of six years and four major cycles. The initial approach taken for the upgrade design is to stay as close as possible to the proven design. The following issues have to be taken as main inputs:

- **Signal-to-noise ratio:** After a total integrated luminosity of 40 fb^{-1} the sensor signals are expected to drop to about 10k electrons. In order to maintain a reasonable signal-to-noise ratio at the end of the lifetime of the detector the capacitance of the strips should be kept below 4 pF. The capacitance can be brought down by placing the routing lines so as to minimise the routing line length for the most irradiated inner strips.

- **Number of channels:** Increasing the number of channels can bring an advantage in terms of occupancy. On the current module, there is space to fit 20 Beetle chips around the sensor (the current die size is 5.1 mm along the short edge). The dimensions of a future chip will be further optimised, as the use of 130 nm technology and the removal of the analogue pipeline will bring significant space savings. As an additional benefit, the removal of the intermediate pitch adapter will bring a gain in signal-to-noise ratio.

- **Minimum strip pitch:** Given the flexibility of the strip design, it will be possible to reduce the minimum strip pitch and obtain more precise measurement for the first point on the track, of vital importance for the impact-parameter resolution. This requirement has the additional benefit of lowering the occupancy and giving an improved resolution after high irradiation doses in comparison to the larger pitches, when charge sharing is no longer operational in the sensor. The total resistance presented to the electronics front end must be carefully controlled, to ensure the signal-to-noise ratio is not affected.

- **Minimum radius of first measured point:** Reducing the radius of the first point will improve the multiple scattering term component of the impact parameter resolution, by about 10% per 0.5 mm reduction. This can be achieved by reducing the width of the guard ring.

- **Occupancy:** The occupancy is expected to go up by a factor 1.6, for an increase of a factor five in luminosity. It can be reduced by increasing the number of strips, as discussed above, and by matching the strip pitch precisely to the particle occupancy as a function of radius. Preliminary studies show that at the upgrade the occupancy can be brought below 1%, for operation at the highest luminosity, as shown in Fig. 5.6.

- **Cooling:** As for the pixel option, the cooling is envisaged to be provided by a diamond spine extending to the innermost edge of the silicon. Given that the power consumption is less in the irradiated region due to the absence of readout chips, it is expected that the performance will be at least as good as indicated by the studies for the pixel module.

In the strip prototype detector, the total number of strips will be increased to 2560 (corresponding to 20 instead of 16 readout chips with 128 readout channels), and 23 modules would be employed. The increase in the number of channels and hence power consumption should be within the range of the cooling system, however there will be likely improvements in chip power consumption along the lines of the developments for the ATLAS ABCn chip [153]. The minimum pitch will be decreased from the current 40μm to 25 or 30μm, and the first sensitive strip will be placed at 7.5 mm, assuming that a 500 μm guard ring width will be achievable. The occupancies which can be achieved with such a design are reasonable. Assuming that a material contribution of the upgraded foil of half the current RF foil is achievable, then the layout described here should achieve a nominal impact parameter resolution performance of $(14 + 20/p_{\mathrm{T}})$ μm where p_{T} is the track transverse momentum expressed in GeV/c, and similar efficiency as for the pixel option (see Fig. 5.6). A strip detector has been designed and will

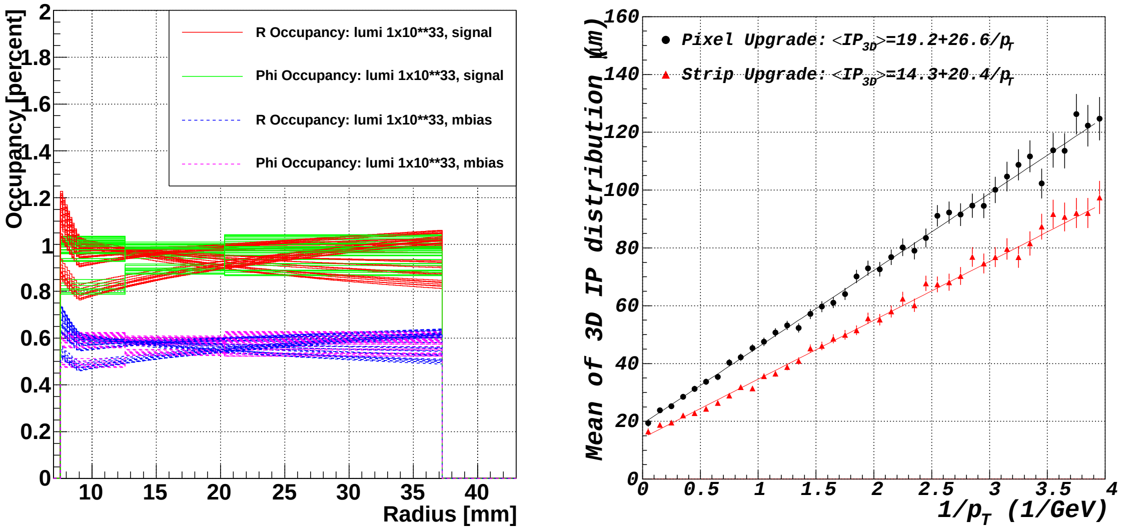

Figure 5.6: Left: the expected occupancies for all 42 sensors in an strip detector design for operation at a luminosity of 1×10^{33} cm^{-2}s^{-1}, for minimum bias events and for $B_s \rightarrow \phi\phi$ signal events. Right: the expected impact-parameter resolution for the upgraded strip design as a function of $1/p_{\mathrm{T}}$, compared to the values for the upgraded pixel design.

be produced, in order to confirm that the basic signal-to-noise performance is sufficient for the upgrade.

Concerning the front-end electronics, the current VELO uses the analogue 128-channel Beetle ASIC that provides four analogue outputs at a 1 MHz L0 rate. The synchronous 40 MHz readout of the LHCb upgrade means that a new radiation-hard readout chip would have to be designed for the new environment able to read at that frequency, suitably adapted to the low detector capacitance to provide the best possible signal-to-noise ratio. In addition, a programmable zero suppression data transmission should be implemented. The design of such a chip would have significant synergies with the strip chip which may be required for the upgraded TT, as described in Section 6.4.

5.5 VELO R&D infrastructure

The VELO upgrade infrastructure comprises three broad classes of equipment that are being developed to aid the qualification of technologies for the VELO upgrade. These are laser (or cosmic-ray) test stands, vacuum chambers and a particle telescope with a fast time-tagging capability for tracks. It is intended that the laser and cosmic test stands and vacuum chambers will exist in several different forms for the development of pixel and strip sensor technologies and the qualification of new module types. The particle telescope will be based at CERN and will be used to prove the sensor and module technologies in tests in charged particle beams.

5.5.1 Laser test stand

The laser test stands will be used to verify the performance of front-end read out chips and sensor technologies in a repeatable manner that does not require the same level of infrastructure as a full beam test. They will comprise a focused red or near IR laser that will deposit charge in very precise locations in the detectors. These will be coupled to accurate motion stages that will allow the laser spot to be scanned with micron accuracy over the detectors. They will be used to study in detail the response of sensors and front-end amplifiers as well as effects such as charge sharing, time walk and cross talk.

It is foreseen that there will be systems of this nature at all the centres developing the new sensor technologies, and there are already active systems existing. These systems have been initially used to characterise the response of Timepix assemblies and 40 μm strip detectors in conjunction with a series of test-beam measurements.

5.5.2 Vacuum chamber

There already exist vacuum chambers at a number of institutes for testing out-gassing of variously sized items. With careful instrumentation these could be used to make limited measurements of the thermal performance of prototype modules. In addition it is intended to construct a more sophisticated chamber dedicated to the VELO upgrade with a window to allow the measurement of both the thermal and mechanical performance of prototype modules. This will have a relatively large volume to allow full sized modules to be tested. It will be instrumented with lasers to measure the mechanical deformation and a thermal camera to measure the temperature performance. It is hoped that the significant synergies with the NA62 Gigatracker project can be exploited to share this resource.

5.5.3 Telescope

The development of an efficient, accurate and convenient particle telescope system for the characterisation of VELO upgrade assemblies forms the core of the R&D characterisation programme. In a first step, a telescope has been constructed using Timepix assemblies which has demonstrated a resolution at the device under test of ~ 2 μm. The time tagging capabilities of the Timepix were exploited to allow tracks to be allocated to scintillator triggers, giving each track a time tagging of better than 1 ns. The shutter mode of operation of the Timepix allowed an instantaneous particle flux of up to 4 kHz to be recorded. The telescope has been used to characterise Timepix assemblies with 300μm and 150μm thick sensors, as well as Timepix 3D (irradiated and unirradiated) assemblies. In addition a synchronisation mechanism was set up to allow the time of the track to be recorded and placed correctly within a 25 ns period, in order to allow the test of strip detectors connected to Beetle chips, and a number of fine pitch devices were tested [149]. A best resolution for angled tracks of 4 μm was demonstrated for the Timepix chip with an efficiency of 99.5%.

The telescope development is planned to continue, building on the strong collaborative links already existing with the Medipix group. It is foreseen that it will be available to other sub-detector upgrade projects within LHCb, as well as collaborations with similar needs, for example NA62 or other Medipix collaboration members. It is planned that the telescope will eventually be developed into a system with two independent arms that could be mounted on either side of any desired device under test, and a TDC unit that will time-align triggers and the device under test with the time-stamped data from the arms. The arms will use the RELAXD Timepix readout system based on Gigabit Ethernet technology. This will also allow a single arm unit to be used as a cosmic test stand. In addition a precise motion platform and mounting for the arms is being developed at CERN, along with infrastructure to provide cooling for irradiated devices and environmental monitoring. This development is planned to exploit synergy with the EU-funded AIDA project, while providing a powerful instrument for the VELO upgrade prototyping work.

Chapter 6

Charged Particle Tracking

6.1 Downstream track reconstruction

The downstream tracking region of LHCb comprises one tracking station (TT) located upstream, and three tracking stations (“T-stations”, T1–T3) at the downstream side of the magnet. The purpose of these tracking stations is twofold:

1. provide a high precision momentum measurement for charged particles resulting in precise mass resolutions of unstable particles;
2. measure the track directions of the charged particles as input to photon-ring searches in the RICH detectors for particle identification.

In the reconstruction sequence of LHCb we distinguish different track-types depending on the sub-detectors they traverse: “long tracks” traverse the full spectrometer (VELO and T-region) and have best momentum and vertexing quality, “downstream tracks” traverse only the TT and T-region and contain good momentum information, and finally “T-tracks” only traverse the T-stations and have precise slope information for RICH-2.

For low and medium momentum tracks (up to about 80 GeV/c) the momentum resolution is mainly limited by multiple scattering, while for higher momentum tracks the detector resolution becomes the limiting factor. To measure track momenta of all particles a T-station track-segment after the magnet is used in the following ways.

- For high momentum long tracks, the momentum is effectively measured by combining the T-station segment with a track slope measurement before the magnet using VELO and TT.
- For lower momentum long tracks as well as for downstream tracks, the momentum is effectively determined by combining the T-station segment with a short TT track-stub.
- For T-tracks the momentum is measured either by assuming the track originates from the primary vertex (for high momentum tracks) or by measuring the curvature in the stray magnet-field in the T-region (for low momentum tracks).

To achieve these goals the T-detectors were designed to provide high efficiency standalone pattern recognition capabilities together with high resolution in the B-field bending plane. The

T-detectors consist of large Outer Tracker straw detectors, covering 98% of the 30m^2 detector surface and smaller Inner Tracker Silicon detectors, covering 0.3m^2 at the small angle—high track density—region. The T-stations are used in the HLT to find long track continuations of VELO track-seeds and provide precision momentum information in the trigger to inclusively select signal events. Alternatively, offline standalone track finding in the T-stations complements the track finding to achieve maximum efficiency for exclusive final state reconstruction.

The TT station covers the full acceptance of 2 m^2 before the magnet and was constructed using the same Si technology as the IT detector. The purpose of the TT-station is four-fold:

1. To reconstruct the trajectories of long-lived tracks that decay outside the fiducial volume of the VELO detector (e.g. K_S decays).

2. To reconstruct low momentum "slow" particles that bend out of the acceptance of the detector before reaching the T-stations.

3. To provide an additional track segment to ease pattern recognition and to improve the connection between the track segments determined by the VELO and the downstream T-stations. In the present high pile-up data taking mode with high track density in the detector, a significant reduction of false tracks ("ghosts") has been achieved, when tracks are required to be validated by TT hits.

4. To allow for selecting high momentum tracks in an early stage of the online track trigger. Since low momentum tracks may scatter and give rise to a large impact parameter, knowledge of the track momentum suppresses the secondary vertex candidates. This feature is not used at present, since in the region between VELO and TT the multiple scattering is higher and the magnetic field is lower than assumed in the original simulations.

The set-up of the tracking detector stations was designed [154, 155] and optimized [156] to provide best performance in a high track-density environment[1] corresponding to instantaneous luminosities in the range of $\mathcal{L} = 2 - 5 \times 10^{32}\text{cm}^{-2}\text{s}^{-1}$. For nominal LHC running $\mathcal{L} = 2 \times 10^{32}\text{cm}^{-2}\text{s}^{-1}$ corresponds to 10 MHz visible interactions with an average number of 0.4 interactions per bunch crossing. At these run conditions the T-stations are expected to observe on average 72 charged particle tracks, of which 26 are long tracks, for a $b\bar{b}$ event [156].

For optimal track reconstruction, each of the stations is equipped with four measurement layers according to the coordinates: X-U-V-X, where X indicates a horizontal measurement and U and V stereo measurements at $\pm 5^\circ$ from X. The presence of two X-layers allows to perform an initial 2-dimensional track search algorithm as an initial step for a full 3-dimensional pattern recognition procedure. Experience with the HERA-B detector, as well as dedicated MC pattern recognition studies demonstrated that optimal ghost rejection performance was obtained for stereo angles in the region of 2.5° to 7.5°. The choice of a stereo angle of 5° provides a y-coordinate measurement with sufficient precision on the track slopes for the RICH pattern recognition [156]. For the TT detector a similar geometry was adopted to ease the reconstruction of K_S decaying downstream of the VELO.

Contrary to the IT, the TT and OT detectors have their on-detector electronics mounted just outside the fiducial volume of the experiment. The read-out systems of the tracking detectors

---

[1] For all simulation studies at various luminosities nominal LHC operation with 25 ns bunch spacing and $\sigma_{\text{inel}}(\sqrt{\text{s}} = 14 \text{ TeV}) = 80$ mb is assumed.

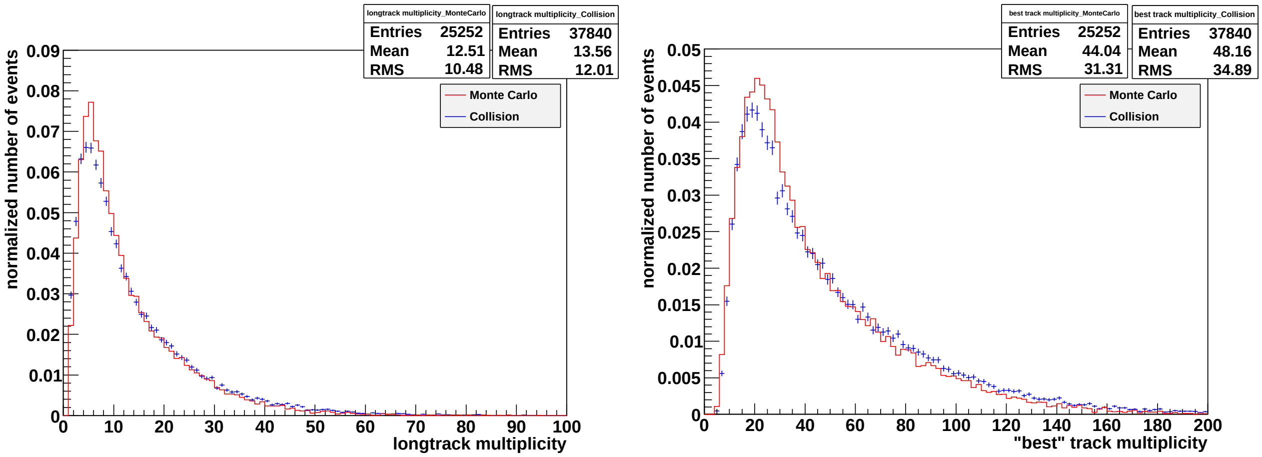

Figure 6.1: A comparison of the track multiplicity in 7 TeV events in the LHC and for real data and MC events, for long tracks (left) and all tracks (right).

allow T and TT station measurement information to be available in the HLT trigger with a 1 MHz readout frequency.

In this section we discuss the strategy to operate the tracking spectrometer in a higher track density environment together with a higher event readout frequency of 40 MHz, while maintaining the excellent resolution performance of the current detector.

6.1.1 Experience with the current detector

Monte Carlo simulations are used to evaluate the performance of the detectors in a high luminosity environment. To verify the correctness of these calculations we present first a comparison between these MC samples and the real data observed in the 2010 run. Due to the limited number of LHC bunches in 2010, spill-over was not present[2]. The 2010 data has been used to validate the reconstruction efficiency of charged tracks in simulations without pile-up, and subsequently the MC is used to extrapolate to the 25 ns bunch structure and high luminosities in the upgrade.

The event track-multiplicity, including primary tracks directly produced in the pp collisions, as well as secondary tracks from interactions with detector material, is directly related to the total number of hits observed in the detectors. In Fig. 6.1 the multiplicity of long tracks per event is compared between data and MC for 7 TeV collisions. The plot shows a good agreement between the data and MC distributions, with only a 9% higher multiplicity in data, indicating that the LHCb PYTHIA tuned MC events provide a reliable simulation of the multiplicity of real data. It should be noted that the observed hit multiplicity in the TT and T detectors are approximately 30% higher than predicted by MC, due to detector hits that are not assigned to tracks. In the MC such hits originate from low momentum secondary particles.

The pattern-recognition capabilities of the detectors are expressed in the track-finding efficiency and the probability to reconstruct ghosts. The pattern recognition algorithms were

---

[2] The arrival time of each particle and electronic response may span more than the time interval between consecutive bunches. The MC for the upgrade takes this into account, also generating interactions several bunches around the bunch of interest.

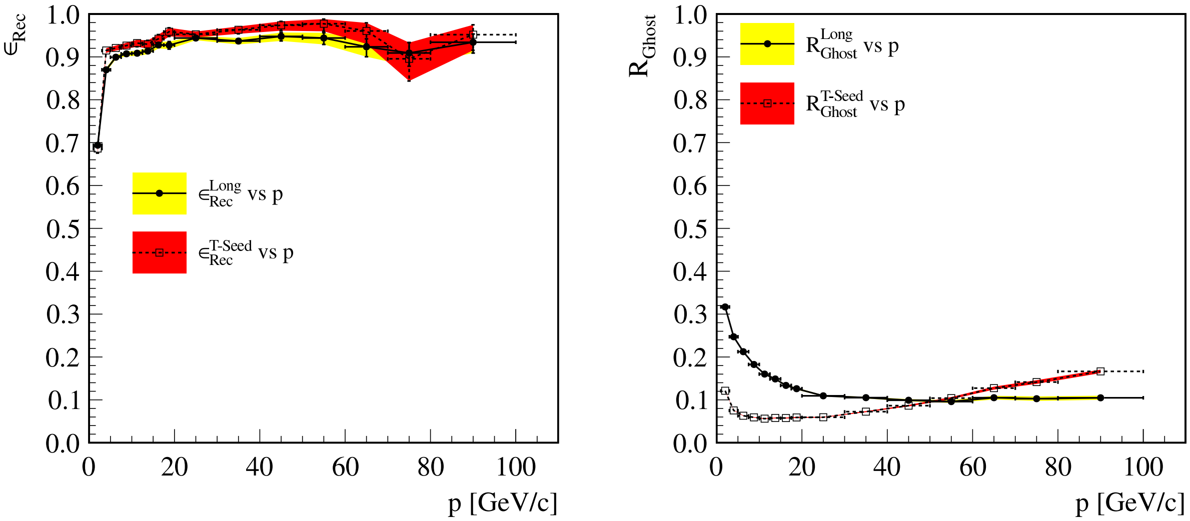

Figure 6.2: MC results for (left) track finding efficiency for long tracks and T-station seeds as a function of momentum, (right) ghost rates for long track finding and T-station seeds as a function of momentum.

tuned to provide maximal efficiency for an acceptable fraction of ghost tracks. To demonstrate the capabilities of the current T and TT detector setup we present the efficiency and ghost rate of the T-seed track and the long track finding methods. In the case of MC events the track reconstruction efficiency and ghost rate is easily determined using MC truth information. The track-finding efficiency and corresponding ghost-rates for long tracks, as well as for T-station segments are shown in Fig. 6.2 for B-decay events at 25 ns LHC operation at a luminosity of $2\times10^{32}\mathrm{cm}^{-2}\mathrm{s}^{-1}$. The track finding efficiency is better than 90% for tracks with momenta higher than 5 GeV/c, while the ghost rate is less than 10% for these tracks.

For real data, the track-finding efficiency for tracks in the downstream region can be determined using K_S decays [157] in which one pion is required to be fully reconstructed as a long track, while the second pion is only required to be observed in the VELO and in the calorimeter. The method is illustrated in Fig. 6.3. The comparison between the reconstruction efficiency for real data and MC data for tracks with $p_{\mathrm{T}} > 0.2$ GeV/c yields agreement within 3%. Alternatively, the track finding efficiency for long tracks can be obtained from a comparison of the observed relative yield between decays with known branching fraction, $D \to K\pi$ with respect to $D \to K\pi\pi\pi$. This method yields a consistent ratio of 1.0 ± 0.03 between data and MC [12]. From these results it is concluded that reconstruction efficiencies can be reliably determined with our Monte Carlo simulations.

The hit resolution of the tracking detectors for real data is found by calculating unbiased residual distances between detector hits and the reconstructed trajectory. The residual plots for the OT hits and IT hits are shown in Fig. 6.4 and show that the average resolution is 230 μm for OT hits, 73 μm for IT hits and 93 μm for TT hits. The expected values from the MC are respectively 200 μm (OT) and 50 μm (IT and ST). The remaining difference are contributed to remaining systematic calibration, misalignment and magnetic field-mapping imperfections, which affect the TT-station in particular. The corresponding momentum resolution is expected

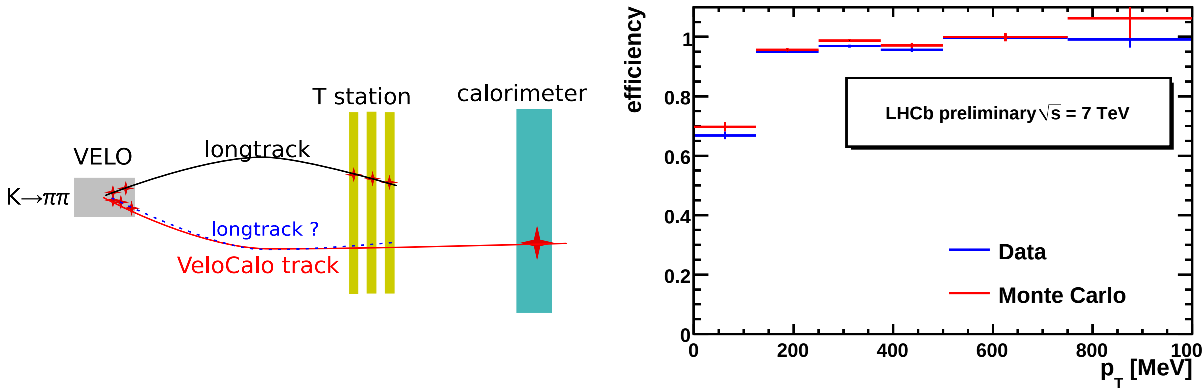

Figure 6.3: Left: the method to determine the track reconstruction in the downstream region using K_S decays. Right: the resulting efficiency plotted as function of the p_{T} of the K_S, compared for data and MC.

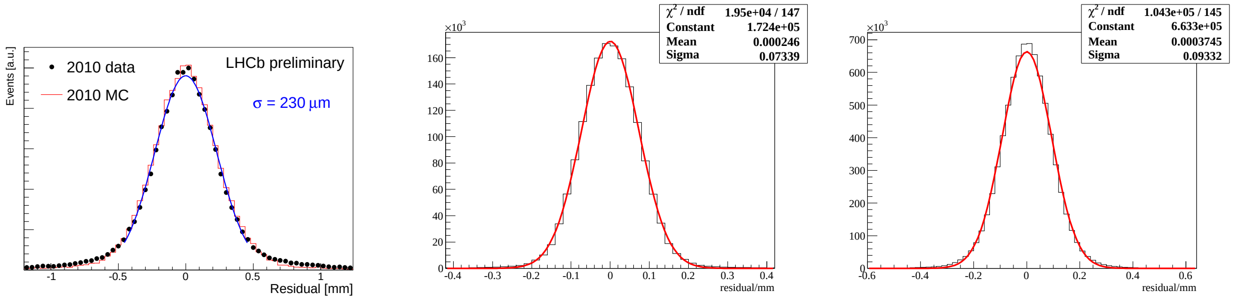

Figure 6.4: The unbiased residual distance between a track and a detector measurement for OT (left), IT (middle) and TT (right) detector hits. The observed resolutions are respectively 250, 73 and 93 μm.

to be in the range $\delta(p)/p = 0.3\% - 0.5\%$. To compare the momentum reconstruction performance of real data with MC simulation the dimuon invariant mass distribution at the J/ψ peak and the Υ-resonances are plotted in Fig. 6.5. The observed resolutions are 13.6 MeV/c^2 for the J/ψ and 47 MeV/c^2 for the $\Upsilon(1S)$, deviating about 25% from the corresponding MC expectations of respectively 10.9 MeV/c^2 and 40 MeV/c^2. A small systematic offset of the reconstructed J/ψ mass of 2.5 MeV/c^2 is observed.

6.1.2 Detector occupancies

The geometry of the IT and OT detectors were chosen to limit the occupancy of the hottest regions in the OT detector to below 10% for nominal run conditions at $\mathcal{L} = 2 \times 10^{32}\mathrm{cm}^{-2}\mathrm{s}^{-1}$ [156]. The 5 mm cell diameter of the straws is chosen to limit the drift time within the period of two bunch crossings, while maintaining a manageable number of readout channels. Figure 6.6 shows the distribution of the impact point distribution of particles traversing a station. The distribution shows that the most hits are observed in an elliptical area around the beam-line. The elliptical shape is caused by the dipole magnet which bends the tracks in the horizontal plane. From the plot it can be concluded that the straw occupancy in the detector is dominated by the hits at small $|y|$ coordinate.

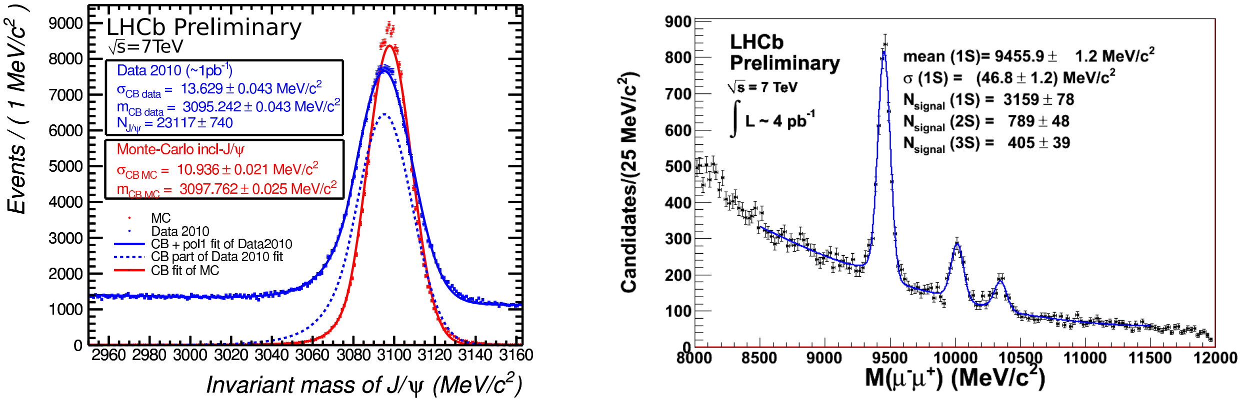

Figure 6.5: The dimuon mass spectrum showing the (left) J/ψ mass and (right) the $\Upsilon(1S)$, $\Upsilon(2S)$ and $\Upsilon(3S)$ resonances.

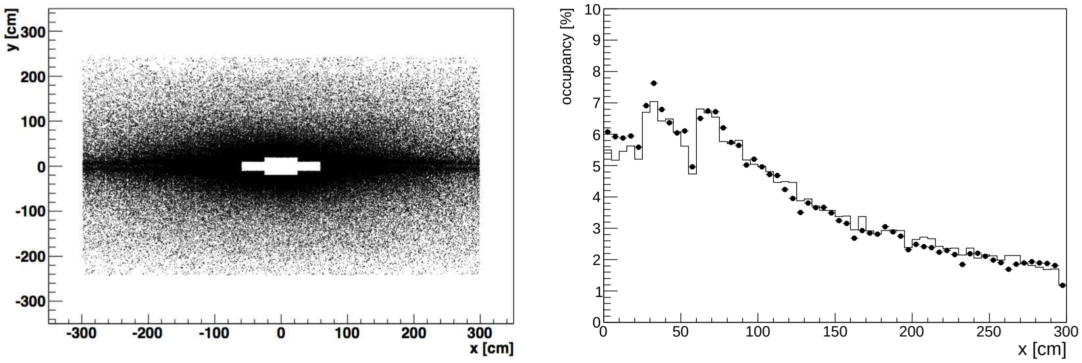

Figure 6.6: Left: hit distribution across the surface of the OT station T2 using MC. The resulting distribution is obtained by summing over many interactions. Right: a comparison of the occupancy distribution between data and MC for minimum bias events with a pile-up of $\mu = 2$, where the MC distribution is scaled by a factor 1.34.

OT Occupancy The OT straw detectors have a maximal drift time of 42 ns, roughly corresponding to the time of two bunch crossings. In the present detector conservatively all detected hits in a three bunch-crossing period of 75 ns are accumulated in a read-out event. For a data run with an average of μ=2 interactions per crossing, the occupancy distribution is compared to MC in Fig. 6.6, averaging over events in a minimum bias trigger. A comparison with the MC shows that the overall occupancy, as mentioned before, is about 30% lower than the data. Further MC studies demonstrate that the occupancy depends on the hardness of the interaction. B events have, on average, an occupancy that is about a factor two higher than minimum bias events. The corresponding data volume, folded with the luminosity, sets a requirement for data transfer capabilities of the electronics, while the event occupancy affects the pattern recognition in both online and offline environments.

Occupancy limit for data transmission In the current LHCb detector, the OT is read out on a positive Level-0 trigger decision, with a maximum trigger rate of 1.1 MHz. Such

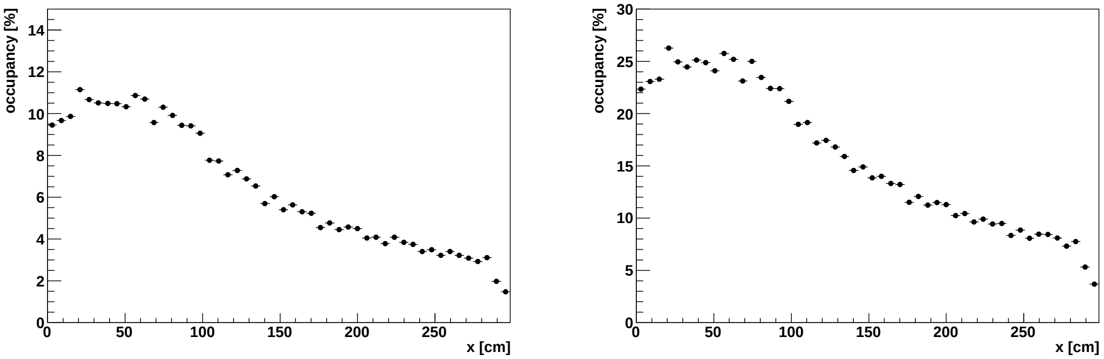

Figure 6.7: Occupancy distribution using MC for $b\bar{b}$ events *vs* the x-coordinate in the OT detector with the current detector for a luminosity of (left) $\mathcal{L} = 2 \times 10^{32}\mathrm{cm}^{-2}\mathrm{s}^{-1}$, (right) $\mathcal{L} = 10^{33}\mathrm{cm}^{-2}\mathrm{s}^{-1}$.

triggered events contain on average more hits than minimum bias events. To calculate the resulting read-out data volume the assumption is made that each triggered event is a B event. In Fig. 6.7 the occupancy distribution versus the x-coordinate in the detector is shown for two data taking scenarios under nominal LHC bunch operation: a luminosity of $\mathcal{L} = 2\times10^{32}\mathrm{cm}^{-2}\mathrm{s}^{-1}$ and $\mathcal{L} = 1 \times 10^{33}\mathrm{cm}^{-2}\mathrm{s}^{-1}$.

The readout electronics can, at a maximal rate, transfer 450 bytes of data from the TELL1 into the HLT farm at maximal readout rate of 1.1 MHz, corresponding to an average occupancy of 17%. A comparison with the occupancy plot in Fig. 6.7 shows that operation of the current detector can be achieved up to a luminosity close to $\mathcal{L} = 1 \times 10^{33}\mathrm{cm}^{-2}\mathrm{s}^{-1}$, perhaps requiring global event cuts to remove a tail of high occupancy events.

For the option of 40 MHz electronics untriggered (minimum bias) events can be used to calculate the expected detector occupancy. As described in the OT electronics section 6.2.1 below, the proposed 40 MHz readout scheme can accommodate events up to very high occupancy. Alternatively, the electronics can be configured to read out the full data (without zero suppressing), providing a readout independent of occupancy.

Occupancy limits for track reconstruction Although the IT/OT detector border was designed to operate with 10% - 15% occupancy [158] for nominal luminosity, the current online and offline pattern recognition algorithms have been shown to be able to efficiently find tracks in events with on average 2.5 interactions, which indeed have occupancies of 20% - 25% in the hottest regions of the OT detector. The High Level Trigger track reconstruction has been demonstrated to be able to reconstruct such events. Events with higher multiplicities were rejected using global event cuts.

Occupancy with shorter straw modules To see the effect on occupancy of the (small) high occupancy region close to the $y = 0$ plane, a case study has been made to calculate the occupancy in the OT detector using modules at a larger distance from the beam in part of the OT detector surface. The cases that are modelled in the simulations are the modifications of the geometry as shown in Fig. 6.8. The figure shows, in addition to the current OT geometry, two studies that have been done for modules that are shortened by either 20 cm or 30 cm

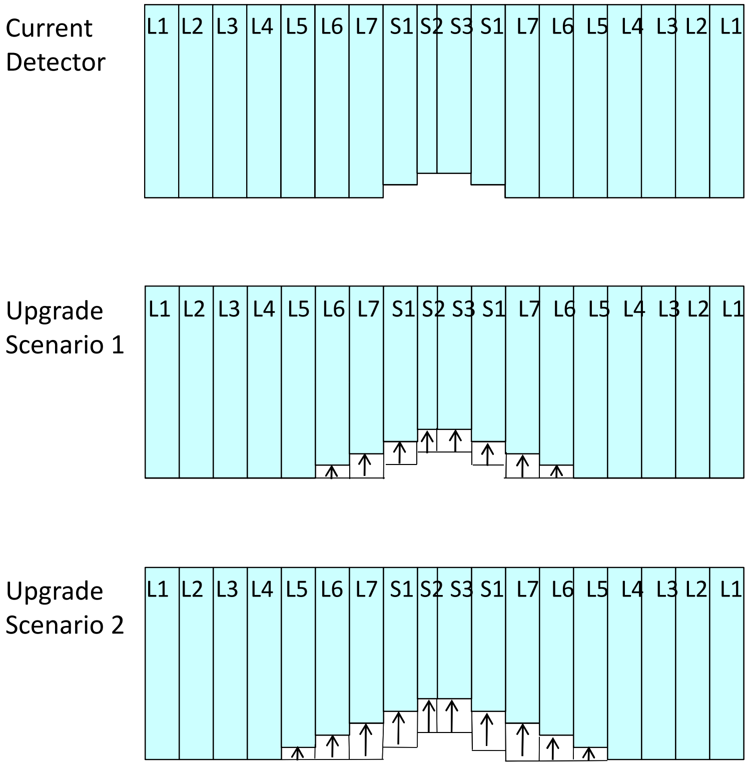

Figure 6.8: Schematic representation of the (top) current OT straw module geometry and possible modifications that are considered in which several detector modules are shortened by (middle) 20 cm in Scenario 1 or by (bottom) 30 cm in Scenario 2. The drawings are not to scale.

as shown in the figure, filling the space with an expanded IT detector. In Fig. 6.9 we show the resulting occupancy along the horizontal detector x-coordinate for luminosities of $\mathcal{L} = 1 \times 10^{33}\mathrm{cm}^{-2}\mathrm{s}^{-1}$ and $\mathcal{L} = 2 \times 10^{33}\mathrm{cm}^{-2}\mathrm{s}^{-1}$. The plot illustrates how reducing the OT module size and consequent enlargement of the Inner Tracker region could limit the Outer Tracker occupancies to an acceptable level for the luminosities and layouts indicated.

IT Occupancy The present IT is positioned close to the beam line and has strips which are 10 to 20 cm long and 200 μm wide. Similar to the Outer Tracker, the granularity of the proposed Inner Tracker solution is based on Monte Carlo simulations emulating high luminosity running. To validate the simulations the IT occupancy distributions of the current detector are compared to those obtained from LHC collision data at low pile-up conditions, Figure 6.10 shows the occupancy distribution for the x-layer of the side detector-box of station T1 for minimum-bias triggered data. The MC distribution has been scaled by a factor of 1.4 to correct for the higher observed multiplicity in data. We conclude that after this correction the MC distribution is reliable. From several simulations done with PYTHIA and FLUKA we have estimated the occupancy in the most exposed regions, at the right and at the left of the beam pipe. The predicted occupancies for B-events with nominal luminosity (with 0.4 interactions

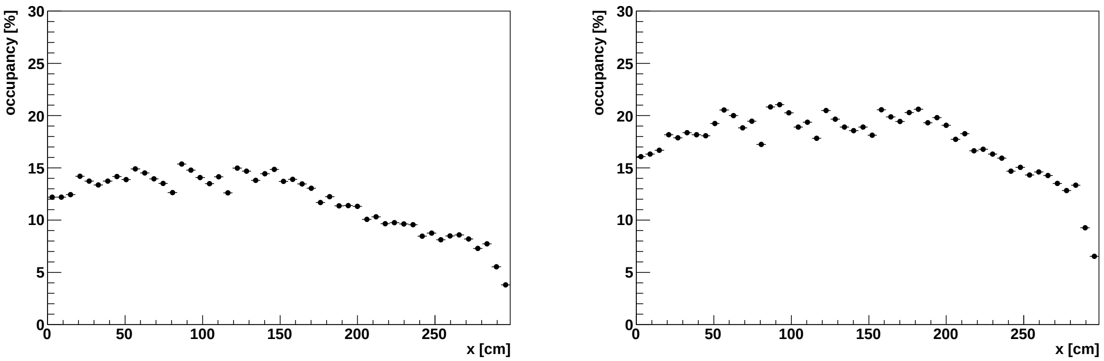

Figure 6.9: MC Occupancy distribution *vs* the x-coordinate in the OT detector (left) with the modified detector geometry Scenario 1 for a luminosity of $\mathcal{L} = 10^{33}\mathrm{cm}^{-2}\mathrm{s}^{-1}$ and (right) with the geometry Scenario 2 for a luminosity of $\mathcal{L} = 2 \times 10^{33}\mathrm{cm}^{-2}\mathrm{s}^{-1}$.

on average while including spill-over effects) varies from <1% up to to 2.3% in the innermost sensors adjacent to the beam pipe [159].

The detection efficiency of the current IT detector has been tested in a high track density environment during LHC injection tests in 2009 in which 450 GeV protons from the SPS were dumped on a beam stopper (the "TED"), located 350 m downstream of LHCb. This resulted in intense illumination of the IT detectors consisting predominately of O(10) GeV/c muons. Typically 3000–4000 IT clusters were observed, corresponding to an occupancy of 3–4%. A dedicated reconstruction of these muon tracks resulted in an efficiency of 97.6%.

At the end of the 2010 LHC run data was collected with an average of μ=2.5 interactions per crossing. This implies effectively running at $7 \times 10^{32}\mathrm{cm}^{-2}\mathrm{s}^{-1}$ under nominal conditions. For this luminosity the measured occupancy is 6 to 7%, rather close to the predicted MC occupancy of 5 %.

In conclusion, although the conditions in the 2010 run were close to "upgrade" occupancies, the IT occupancy was not critical. It should be noted, however, that there was no spill-over effect present, due to the limited number of bunches in the LHC machine.

For the upgraded IT fibre tracker option discussed below, with a 250 μm pitch, we expect the relative occupancy to increase by maximally 25% compared to the current detector with a pitch of 200 μm. In case the multiplicity is too high, there is the possibility to reduce the occupancy by a factor of two by splitting some of the modules that are lateral to the beam pipe into an upper and lower readout section.

TT occupancy The TT detector uses silicon strips of 183 μm pitch with readout sectors of 1, 2, 3 or 4 sensors, depending on their location in the detector [13]. The occupancy distribution of single interaction LHC events is compared to Monte Carlo in Fig 6.10, where the MC is scaled by an overall factor of 1.3 to correct for the track mulitiplicity difference. For B events with nominal luminosity the occupancy of the TT sensors varies from less than 1% in most of the outer regions of the detector up to 3.3% in the sensors closest to the beam-line [160].

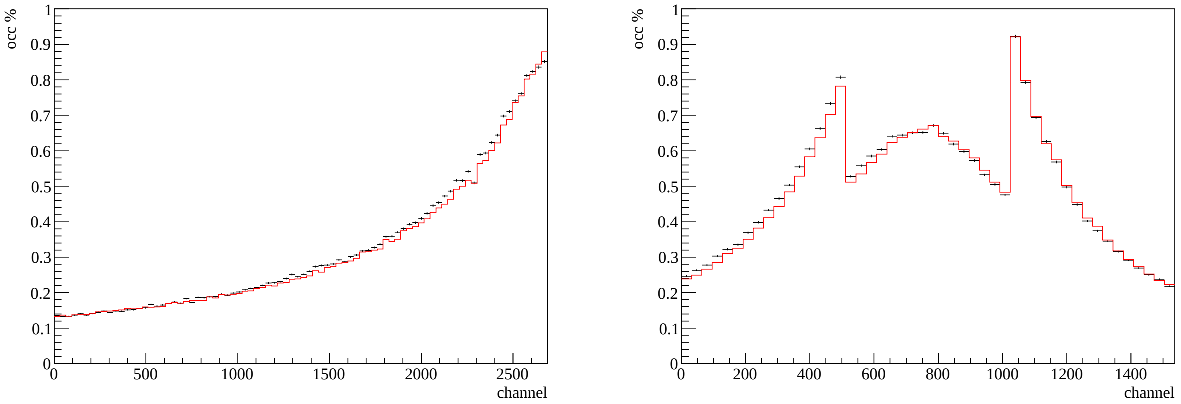

Figure 6.10: Occupancy distribution for data (points) and MC (histogram) as function of the x-coordinate in (left) the IT detector and (right) the TT detector for single interaction events seen by LHC data taken in early 2010.

6.1.3 Design considerations for the upgrade

The tracking spectrometer was designed to balance track finding redundancy and measurement precision with the amount of material in the acceptance. At the same time the detector segmentation was optimized versus cost for efficient track finding operating at luminosities in the range of $2-5\times10^{32}\text{cm}^{-2}\text{s}^{-1}$. The following considerations are made for operation at luminosities in the range 1–2 $\times\, 10^{33}\text{cm}^{-2}\text{s}^{-1}$.

Measurement redundancy and material budget In the "re-optimization" of the LHCb spectrometer design before it was constructed, an effort was made to minimize the amount of material in the acceptance [156]. A reduction of multiple scattering, photon conversions and hadronic interactions was given priority over extra measurement redundancy [161]. A comparison of the current detector set-up to a detector layout with more stations yielded similar tracking efficiency and ghost rates, while perturbing effects of additional material were avoided. The momentum resolution was not improved by adding measurement planes. The robustness of the detector setup was demonstrated by a Monte Carlo study that simulated additional hypothetical detector inefficiencies as well as higher occupancies, but with close to identical performance [156].

The total material budget of the current detectors is on average 4% (TT), 3.5%(IT) and 3%(OT) X_0 per station, leading to a total average material budget of about 14% X_0 for the tracking region. The material distribution of the TT and OT detectors is relatively uniform, that of the IT distribution is much less uniform, due to readout hybrids, mechanical supports, cooling pipes and readout cables that are located in the acceptance. A map of the total radiation length in the T-region is shown in Fig. 6.11. The contribution of the infrastructure can clearly be seen, in particular cooling balconies, cabling and support structures of the Inner Tracker. For the upgrade we envisage to maintain the same layout of one TT-station and 3 T-stations, however we aim as much as possible for a further reduction of material, in particular from inactive infrastructure.

For higher instantaneous luminosity the average number of simultaneously occurring proton-

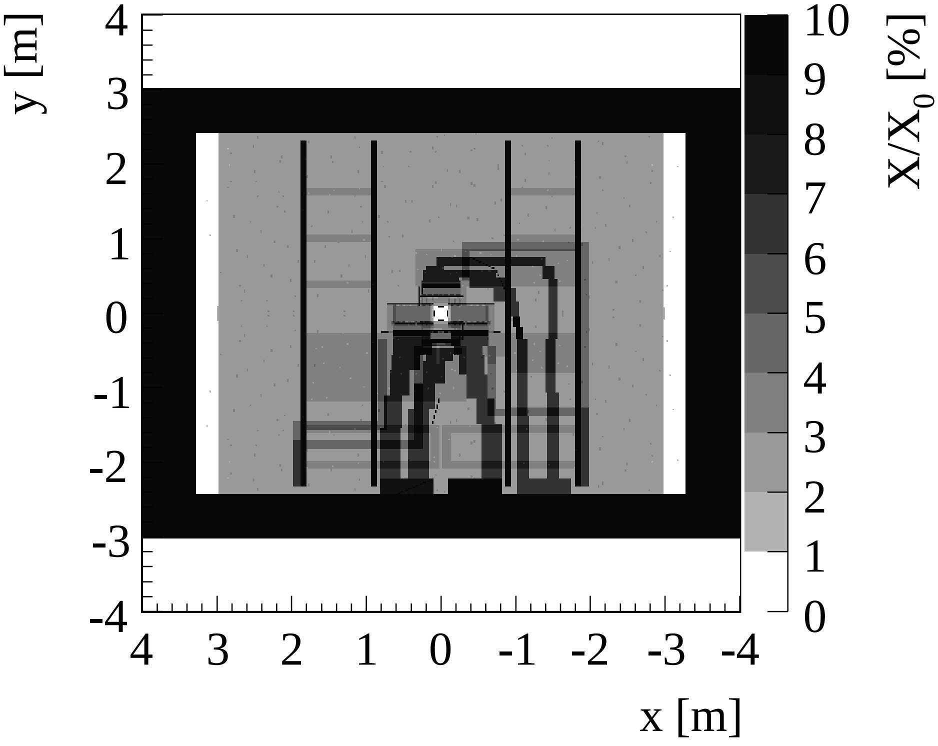

Figure 6.11: The radiation thickness map of station T3 as seen by straight tracks from the interaction point (Geantino particles). The light grey indicates 3% X_0, while the dark structures represent the more massive infrastructure material.

proton interactions ("pile-up") increases, and with it the number of tracks in the event. In addition, the detectors see effects from hits in previous (silicon strips) or previous and subsequent bunches (drift tubes), so-called "spill-over". To evaluate the robustness of the current tracking-stations setup, the performance of the current LHCb track finding pattern recognition is studied as function of the track multiplicity in the events. Figure 6.12 shows the efficiency (left) and ghost rate (right) for both the T-station track segment and the long track finding algorithms. The plots are obtained without any retuning of the algorithms used as a function of multiplicity. The total number of tracks reconstructed depend relatively strongly on a χ^2/ndf quality criterion, since such a criterion allows to reject tracks connecting hits originating from an incorrect spill. At a nominal luminosity of $2 \times 10^{32}\text{cm}^{-2}\text{s}^{-1}$ the number of long tracks in a B event is 35 on average, of which 30 have a $\chi^2/\text{ndf} < 3$. Alternatively, at a luminosity of $1 \times 10^{33}\text{cm}^{-2}\text{s}^{-1}$ the average long track multiplicity is expected to be about 71, of which only 46 have a $\chi^2/\text{ndf} < 3$.

The plot shows that the spectrometer continues to find tracks in a high density environment with only a small drop in efficiency. The ghost rate is seen to increase for these higher multiplicity events. While the origin of these ghost tracks has been traced to multiple causes [162] an important class of ghost tracks corresponds to track segments correctly reconstructed in the VELO that are matched to segments produced by other tracks in the downstream stations.

In the reconstruction of exclusive B decays the ghost rates are not expected to contribute

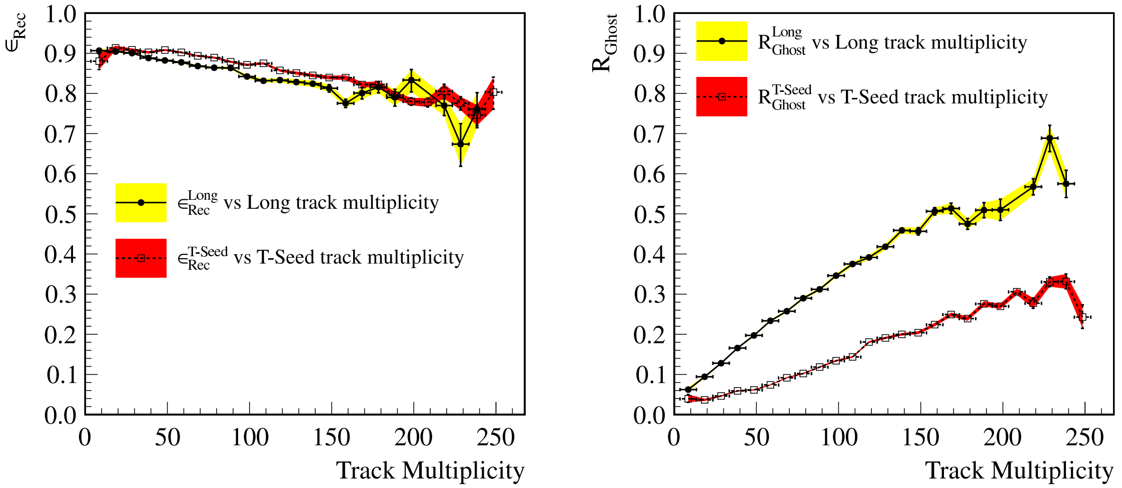

Figure 6.12: The efficiency and ghost rate for T-seed tracks and long tracks plotted *vs* the number of tracks in the event.

significantly to the background in the event selection. For several inclusive reconstructions a reduced signal over noise performance was observed, see Fig. 6.13, using standard track selection criteria at conditions with high pile-up, as was the case during most of the 2010 run. However, it was observed that the ghost rates could be suppressed in two ways at a small loss in efficiency: by requiring the presence of TT hits on the track and by applying a tighter χ^2/ndf track quality criterion.

Figure 6.14 shows how ghost tracks differ from real tracks by comparing the χ^2/ndf distribution, the number of hits on the track and the pseudorapidity distribution. Based on these quantities a likelihood criterion is available [162] that can be used to further suppress ghosts. In addition, requiring the presence of TT hits on long tracks further reduces the ghost rate at the cost of slightly reducing the acceptance, as is discussed in a dedicated section below. In summary, the LHCb spectrometer, perhaps with a slightly expanded acceptance of the TT detector, continues to provide sufficient redundancy for track finding in the high luminosity environment of the upgrade.

Hit resolution The detector hit resolutions were designed to be approximately 200 μm for an OT measurement and 50 μm for an IT or TT measurement [163]. Relying on accurate alignments, these hit-resolutions lead to x-coordinate measurements in a station of 80 μm for the OT and 25 μm for the IT, yielding a similar momentum resolution for high momentum tracks traversing the IT and lower momentum tracks traversing the OT. The relative momentum resolution of the current detectors is in the range $\delta(p)/p = 0.3\% - 0.5\%$. The fact that it does not increase proportional to the hit resolution indicates it is limited by multiple scattering.

Good hit resolution aids the pattern recognition performance as it allows for small search windows in the search for candidate trajectories. The ±5° stereo planes provide a y-coordinate resolution that is 12 times worse than the x-coordinate, but is sufficient for pattern recognition.

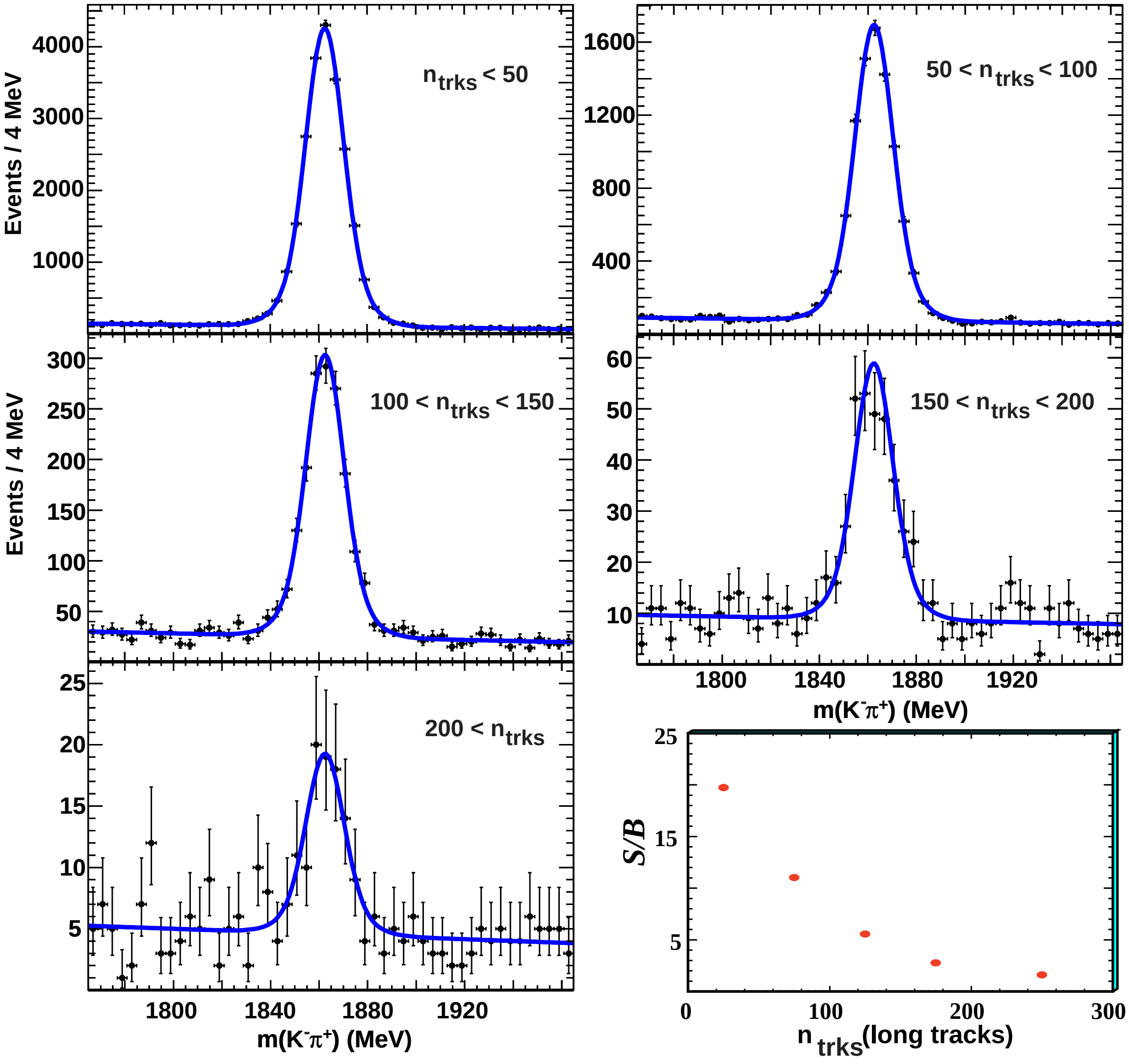

Figure 6.13: The invariant mass of $K^-\pi^+$ tracks forming a common vertex that form a candidate semileptonic b decay with a μ^- as a function of the number of reconstructed long tracks. The lower right hand plot shows the signal-to-background ratio as determined by a fit to the mass peak. (The error bars are smaller than the size of the points.)

Detector occupancy The boundary between of the Inner Tracker and Outer Tracker was chosen to provide efficient track reconstruction for a minimal IT detector surface. As shown in Section 6.1.2 the occupancy of the OT straw detectors becomes too high at a luminosity above $1 \times 10^{33}\text{cm}^{-2}\text{s}^{-1}$. Operation at such luminosity would require either replacing the current OT modules in the high occupancy region by shorter ones, or replacing them with detectors of higher granularity.

Radiation Tolerance The current IT and OT detectors are designed to withstand radiation levels corresponding to at least 20 fb^{-1} over 10 years of operation. The upgraded detector should be able to withstand irradiation levels in the hottest region corresponding to 50 fb^{-1} for 10 years of operation. Irradiation studies will be discussed in Section 6.2.2.

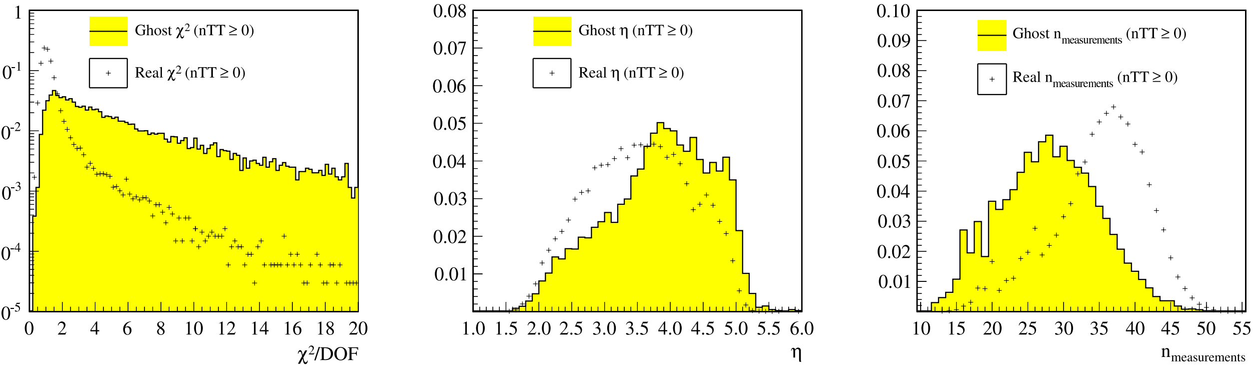

Figure 6.14: A comparison between real tracks and ghost tracks. Left: the distribution of the χ^2/ndf resulting from the track fit. Centre: the pseudorapidity distribution. Right: the number of hits assigned to the track.

Table 6.1: Summary of fractions of long tracks outside the detector acceptance with different shapes of the inner contour of the TT detector. The long track sample consists of tracks from generic b decays satisfying the criteria $\chi^2/\text{ndf} < 5$ and $p_\text{T} > 0.3$ GeV/c.

Inner edge geometry	Good track missed (%)	Ghost tracks missed (%)
Square (±37) mm [no change]	3.08	6.10
Octagon (side 30.7 mm)	1.62	3.64
Circle (radius 37 mm)	1.20	2.90
Circle (radius 32 mm)	0.09	0.045

An upgraded TT detector For TT an effort is underway to use real data as well as Monte Carlo simulations to study possible improvements of its acceptance and layout.

The TT detector is important in reducing the population of ghost tracks within its nominal acceptance. Figure 6.15 shows the long track projections to a hypothetical "TT" plane, located between the two TT stations, at $z = 2485\,\text{mm}$. The red rectangles represent the geometrical acceptance of the present system, illustrating that in many cases small angle track candidates miss the acceptance of the current TT detector. Although an effort was made to minimize the gap close to the beam-pipe, covering the region down to $\eta = 4.8$, there still is lack of sensitivity due to a required 5 mm safety gap and 3 mm gap for insulation purposes. For the upgraded TT detector it will be attempted to increase the acceptance in this high η region. While clearance requirements imposed because of the Be beam pipe are not likely to be eliminated in the upgraded detector, one could consider shaping the outer edge of the innermost sensors to provide a better coverage. This strategy is adopted successfully in the present VELO detector. To quantify the gain in acceptance, Table 6.1 summarizes the fractional increase of good tracks that can be confirmed, as well as the increase of ghost candidate tracks that could be rejected, as achieved by changes of different inner detector geometry shapes.

An additional improvement on ghost track rejection could be obtained by introducing a finer TT segmentation in the y (non-bending) direction. Although the finer segmentation is mainly relevant for the inner part of the detector, a first estimate of the importance of

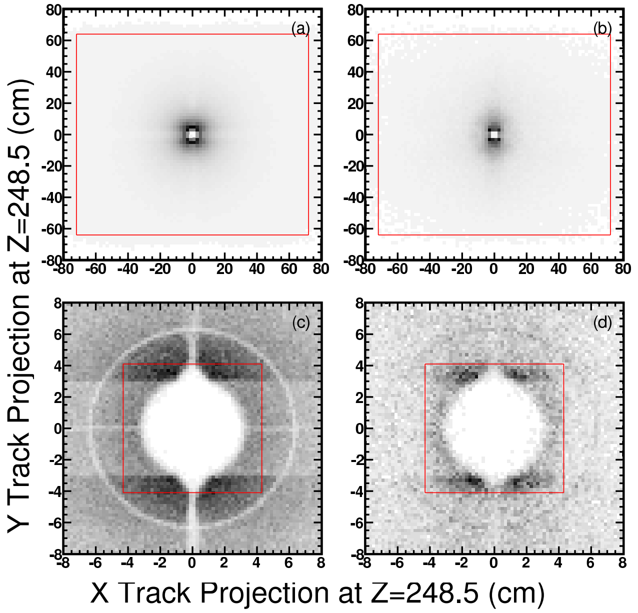

Figure 6.15: Track projections at the mid-plane between the two TT stations: scatter plots (a) and (c) correspond to tracks matched to a Monte Carlo particles (good tracks), and (b) and (d) include ghost tracks. Red lines define the inner TT geometrical acceptance. The bottom plots (c) and (d) show a zoomed view near the beam pipe to show the higher occupancy and the density of missed tracks near the beam pipe.

such segmentation is obtained from a MC simulation of the present TT, making its overall segmentation respectively 2, 10, 100 times higher. In this study, simulating inclusive b events with an average number of interactions per crossing $\mu = 3$ the reduction of ghost tracks is studied on a sample of tracks with a $p_{\mathrm{T}} > 300$ MeV/c and χ^2/ndf < 5. To isolate the effect of the TT, all tracks considered have correctly reconstructed VELO parts. Figure 6.16 summarizes the findings for the default TT and the higher segmentation scenarios. Requiring TT hits with the current segmentation is seen to reduce the ghost rate by 40% to 60%, depending on the track multiplicity in the VELO. The best performance results in a ghost suppression between 60% and 80% and is achieved with an assumed y-segmentation about 100 times finer than the present one. The results obtained from this study are encouraging, and demonstrate that a higher segmentation, especially in the inner region of the detector, is valuable. These studies will be refined with a dedicated simulation in the framework of the new MC tools developed for the upgrade.

TT layout The following aspects are being explored in relation to the layout of the TT measurement planes.

- As it is foreseen that the RICH-1 Aerogel will be removed from the upgrade detector setup, the multiple scattering in the upstream tracking region decreases accordingly. In addition reducing the pitch in the innermost part of the TT detector will be studied. Both of these effects may lead to an improved momentum resolution.

- The optimal position resolution of the detector as a function of x: if two different resolu-

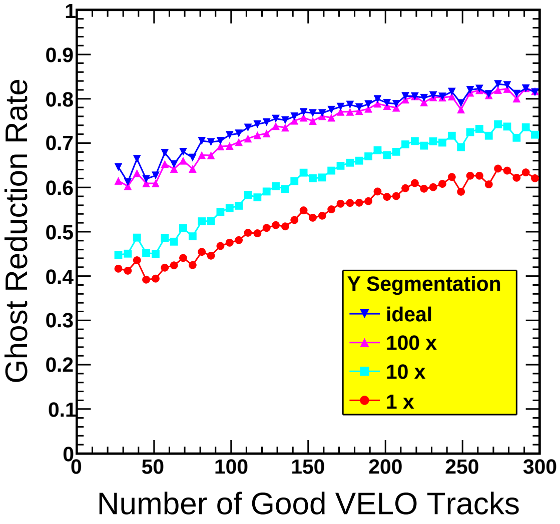

Figure 6.16: Relative ghost reduction fraction for different assumptions in the TT y segmentation. The curves show the performance for 1×, 10× and 100× the current TT segmentation.

tions for the inner and outer parts are envisaged, what is the optimal dividing line (e.g. a circle of 20 cm) between the two sections, and what are the optimal pitch sizes?

- The optimal number of detection layers. An increase of the number of layers could provide reliable track segments for the pattern recognition and might increase the track detection efficiency. However, more layers would also increase the material budget.
- The optimal distance between the TT-layers, and their best location with respect to the magnet.
- Increasing the magnetic field in the region of TT, which may allow for a "momentum matching" ghost suppression algorithm. The effect of the magnetic field has been seen to lead to higher occupancies in tracking stations due to low momentum "curler" tracks [164] and needs to be revisited for this study.

6.1.4 Summary

A series of possible improvements for the T-stations and the TT are being considered. The layout optimization for such a detector goes in parallel with the R&D studies required for the technological solutions. The current detector layout of three T-stations and one TT detector is maintained as the baseline in the upgrade. As more material would lead to a degradation of the momentum resolution, no additional detectors are proposed.

For the T-stations moving the IT readout system outside of the acceptance region is proposed, which leads to a potential reduction in interaction and radiation lengths. The pattern recognition studies show that the current OT detector can accept occupancies up to 25% in the hottest regions. This implies that operation at a luminosity of $10^{33}\text{cm}^{-2}\text{s}^{-1}$ is still possible, but without much safety margin. Therefore, we propose that the upgraded IT covers a larger detection surface. The OT modules could be replaced, if required, by shorter modules covering less of the hot region at small $|y|$. In that scenario running at luminosities higher than $1 \times 10^{33}\mathrm{cm}^{-2}\mathrm{s}^{-1}$ would be possible. Both straw detectors for the hottest OT modules, and scintillating fibres with thick fibres are being considered. Such a detector would be constructed of lightweight detector boxes of similar modularity to the current OT boxes, allowing detector integration to be performed using the existing infrastructure. More detail is given concerning the OT upgrade in the next section.

Since the current LHCb IT and TT detectors use silicon technology and provide excellent performance, we recognize that the use of scintillating fibres would be a more challenging detector option, requiring an R&D program to demonstrate their suitability in the dense radiation environment. Therefore, while R&D on the fibre option is discussed below in Section 6.3, we also maintain the possible option of a silicon-based IT and TT detector upgrade with a readout at 40 MHz. The silicon option for the TT is described in Section 6.4.

6.2 Straw tracker upgrade

The current T-station detection surface is largely covered by 12 double layers of Kapton straw detectors organized in three stations with stereo views. The straws have a diameter of 5 mm and are approximately 2.5 meter long and organized in modules of 256 straws. At the far end of the detector boxes, outside the fiducial volume, replaceable electronic boxes are mounted that house the analogue (pre-amplifiers) and digital (TDCs) read-out electronics. The detector is constructed within geometrical tolerances of 100 μm. An internal alignment precision of the full T-station better than 50 μm has been obtained using cosmic ray data. The overall alignment within the LHCb frame is in progress and still affecting the mass resolution performance.

The hit resolution of the current detector and the mechanical tolerances of the modules are well suited for the upgrade. The granularity of the detector is designed to operate within a luminosity range of $2-5\times10^{32}\mathrm{cm}^{-2}\mathrm{s}^{-1}$. The development of the pattern recognition algorithms and experience with the current detector gives us confidence that the granularity of the current detector is sufficient to operate at a luminosity up to $\mathcal{L} = 1 \times 10^{33}\mathrm{cm}^{-2}\mathrm{s}^{-1}$. At such luminosity the detector occupancy becomes critical in the region closest the beam-line where the track density is highest. The resulting occupancy situation is presented below.

Meanwhile we have observed in the laboratory that the OT detector modules suffer from gain loss after they have been locally irradiated with a radioactive source. The origin of the gain loss mechanism has been traced and possible remedies are discussed below. In case of unrecoverable damage, straw modules can be replaced by shorter and more radiation hard modules.

6.2.1 OT electronics

The task of the Front-End Electronics is to provide a precise ($\sim$1 ns) drift-time measurement. The tracking procedure requires high efficiency (low thresholds), while at the same time putting stringent limits on the noise level. The modular detector structure (a module consists of two staggered layers of 64 straws, electrically floating at the centre and read out at the two ends) [13, 155, 156, 158] reflects on the FE electronics: the signals from 128 straw tubes are analyzed and digitized by one "FE-Box", a set of specially designed PCBs, hosted in a metallic housing that fits to a module end. Straw tube modules and their FE Electronics are attached to mobile metallic structures (C-Frames) that provide mechanical support, as well as the distribution of the various services to the modules and the FE-Boxes: Low-Voltage (LV), High-Voltage (HV), slow (ECS) and fast control (TFC), etc.

For the present straw-tubes detector, 480 FE-Boxes were produced and installed (432 used, 10% spares). Quality checks have been performed in several stages, at the level of individual boards and at the global level with dedicated test systems mimicking the real detector and capable of simulating all the readout functionalities [165]. The OT FE-Boxes were stably operational during the entire 2010 data taking period. Thanks to the high threshold uniformity achieved in production, all 6720 discriminator thresholds (the thresholds of the 53,760 OT channels can be set with a granularity of 8 channels) could set to the common value of 800 mV, roughly corresponding to a charge of 3.5 fC. This guaranteed virtually no loss of detection efficiency (above 98%) and very low noise (typically corresponding to a 0.01% occupancy). The fraction of dead channels is well below 1% (the vast majority due to shortcuts or frequent dark pulsing in the straw tubes).

Present Design Each FE-Box channel consists of a preamplifier/shaper and a discriminator, a Time-to-Digital Converter (TDC) and a data serializer and optical link transmitter, as shown schematically in Fig. 6.17. So, each FE-Box contains all the electronics necessary to read out the hit signals from the straws, determine their times with respect to the LHC clock, and ship them to the off-detector electronics if a positive trigger (L0) decision arrives.

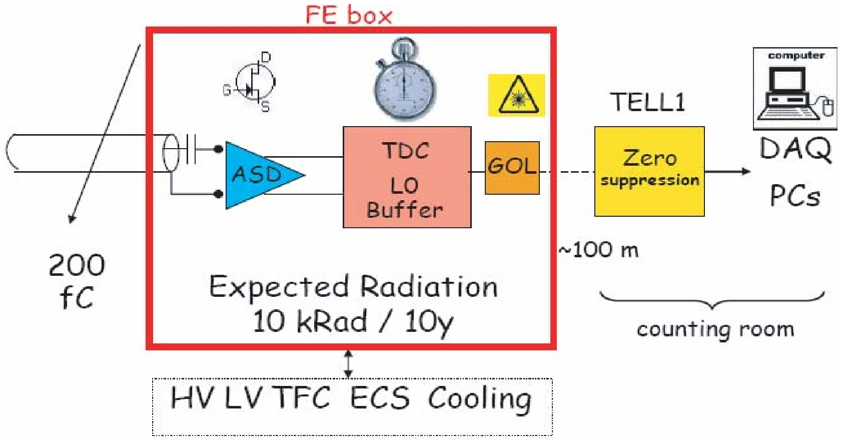

Figure 6.17: Schematic view of the OT Electronics.

These functionalities are implemented in a modular way through various boards: the HV Board (hosting 32 capacitors, each of 330 pF, to decouple the small hit charges to the preamplifiers from the positive HV supplied to the anode wires), the ASDBLR Board (hosting two 8-channels ASDBLR chips [166], produced using the radiation-hard DMILL process and featuring a fast peaking time of about 7 ns and baseline restoration to eliminate the long ion tail), the OTIS Board (hosting one OTIS chip [167], a 32-channel clock-driven TDC especially designed for OT and produced using a 0.25 μm CMOS process), and the GOL/AUX Board (that provides the bias voltages by means of radiation-hard voltage regulators and hosts one

GOL chip [168], which receives the 8-bits data from four OTIS chips, serializing and optically transmitting them to the TELL1 boards in the counting house.)

Each FE-Box contains 4 HV Boards, 8 ASDBLR Boards, 4 OTIS Boards and 1 GOL/AUX Board. The data flow is schematically shown in Fig. 6.18. On an L0 accept, each of the four OTIS sends all data (no zero suppression) to the GOL: each of the 32 OTIS channels contribute 8 bits (6 bits drift-time and 2 bits to signal its position inside the the 3-BX search window). Together with a 32 bits header, this gives a total of 288 bits [167]. Therefore, on each L0 accept the GOL sends 1152 bits to the TELL1 board: at an average L0 rate of 1.1 MHz, this corresponds to an output bandwidth of 1.27 Gb/s per FE-Box.

In addition to the outgoing data fibre, each FE-Box has high-voltage feed-throughs to the straw-tubes, two ($+6\,$V and $-6\,$V) low-voltage bias lines to supply the on-board voltage regulators, and a high-speed connector providing slow- and fast-control signals.

FE-Box Upgrade The strategy for the upgrade of the OT FE-Boxes to the 40 MHz readout scheme is based on the following observations:

- We choose to maintain as much as possible of the present infrastructures (support C-Frames, LV and HV power supplies and distribution system, front-end electronics cooling, slow and fast-control systems, etc.), given the very significant time and resources that would be required to redesign and produce them.
- The present solution based on one FE-box per module end still represents an optimal segmentation in terms of geometry, interfaces to the modules services (gas and HV), cooling, grounding and shielding: all PCB boards in the FE-box can be replaced by boards with “upgraded” functionalities, but the same geometrical dimensions.

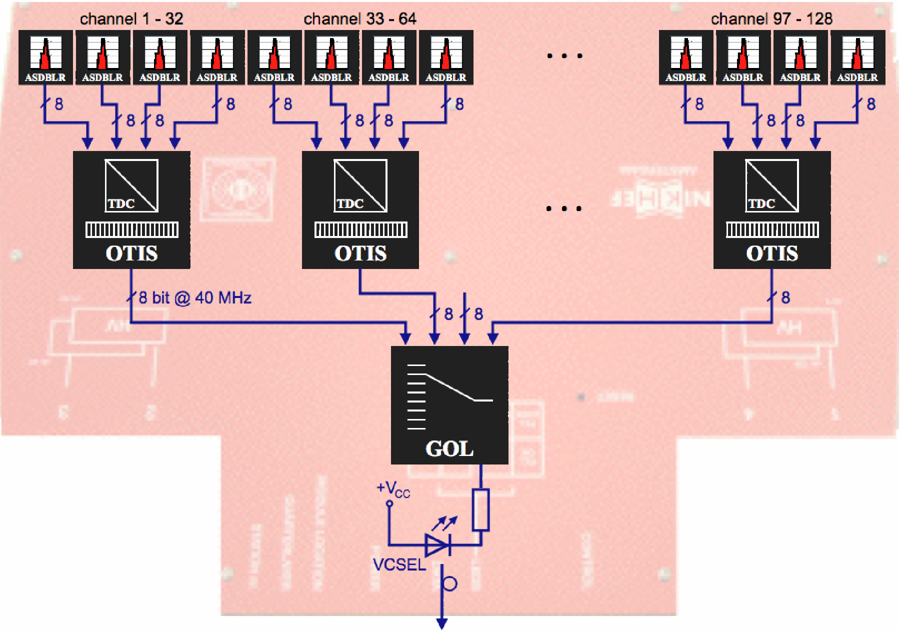

Figure 6.18: Schematic view of the data flow in the present FE-Box design.

- The present HV and ASDBLR boards already fulfill the needs of the 40 MHz readout scheme. The fast peaking and recovery time of the ASDBLR amplifier [166], which practically guarantee the capability of detecting at least one hit per bunch crossing. permit its usage at higher hit rates. Increased radiation levels are also not a concern, given the intrinsic radiation hardness of the production technology [166].
- Analogous considerations hold for the TDC core of the OTIS chip, designed to digitize one hit per bunch crossing in a dead-time free fashion [167]. However, the derandomizing buffer and the readout sequence have been designed to cope with an average L0 accept rate of 1.1 MHz and "trains" of up to 15 consecutive events [129]. Therefore, the OTIS chip (or at least its control logic), and consequently the OTIS Board, need to be redesigned in order to accommodate for the needs of the 40 MHz readout.
- Since its bandwidth is already fully exploited at the present L0 accept rate of 1.1 MHz, the GOL chip, and consequently the GOL Board, need to be redesigned in order to accommodate for the bandwidth requirements of the 40 MHz readout.

Therefore, we propose a straightforward approach to upgrade the OT FE-Boxes based on the following main concepts:

- we retain the FE-Box chassis and cover, the HV Board, and the ASDBLR Board;
- we design and produce new versions of the OTIS and GOL/AUX Boards compatible with the 40 MHz readout scheme. The new PCBs shall have the same geometrical dimensions as the present ones; the new OTIS Boards shall also adopt the same input connector to interface to the existing ASDBLR Boards;
- the interfaces to the cooling, LV, and HV distributions will remain unaltered;
- modifications to the data and control (slow and fast) distribution systems will become necessary, depending on the choice of the TDC and the serializer chips.

We believe this "minimalistic" upgrade to be feasible in terms of resources (the FE-Box components that are retained made up for more than 70% of the total FE-Box costs) and time scale. In the rest of this section, we will consider more closely the options for the upgrade of the TDC and the serializer board.

40 MHz TDC The performance of the TDC core of the OTIS chip is more than satisfactory (dead-time free digitization of one hit per bunch crossing and time resolution more than 3 times better than required to achieve a $200\,\mu$m space resolution). However, the readout sequence of 36 clock cycles is incompatible with a 40 MHz readout scheme. Moreover, at present a 3 bunch-crossings window of the L0 pipeline is searched for hit on an L0 accept (required by time-of-flight differences, the $\sim$40 ns maximum drift time, signal propagation along the anode wire, etc.), and only the first hit found in this search is transmitted to the TELL1 board; this single-hit feature becomes the more undesirable at higher instantaneous luminosities. A redesign of the OTIS chip focused around a modification of these features of the control logic, while retaining the main functionalities of the TDC core, appears feasible.

In addition, we explored an alternative that would allow us to avoid the costly and time-consuming iterations of an ASIC design, based on previous experience in TDC implementation with high-bandwidth FPGAs [169]. In particular, the Actel "ProASIC3" family of low-cost, low-power FPGAs [171], already used in multiple applications at LHCb [170], offers a reasonably radiation-tolerant (>30 krad) solution. Our R&D program resulted in a 16-channel TDC implementation based on a Phase-Locked-Loop (PLL) at 320 MHz clock speed to generate 16 phase-shifted bins of 1570 ps, as shown in Fig. 6.19. Data from the ProASIC3 TDC were collected using input pulses with random or synchronously shifting time phases: our implementation exhibited quite uniform bin sizes (differential non-linearity $\simeq 0.8$) and a linear response to timing scans. We also implemented the capability to perform zero-suppression to reduce the output bandwidth to an acceptable level.

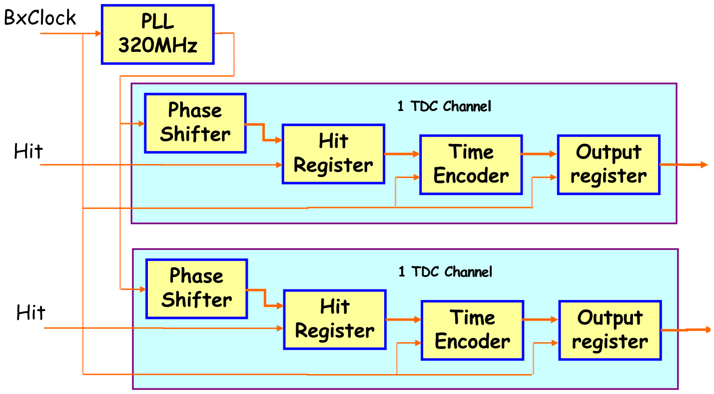

(a) TDC Schematics

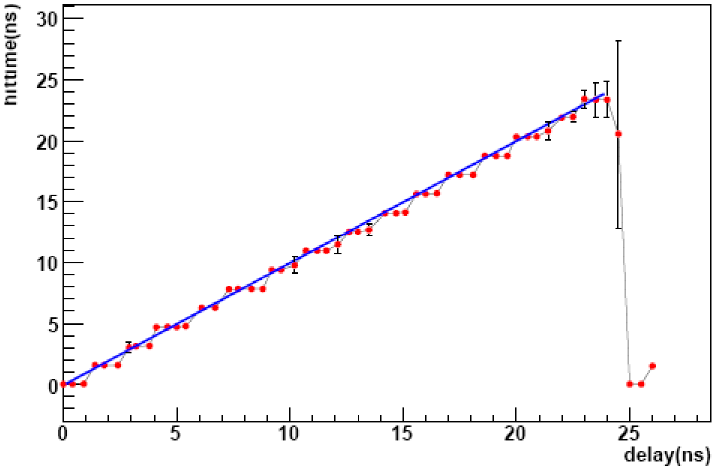

(b) Linearity Scan

Figure 6.19: TDC implementation in an Actel ProASIC3 FPGA (a), and results of a timing scan showing the linearity of the TDC response to an input pulse with a shifting phase synchronous to the FPGA clock (b).

40 MHz serializer/transceiver The Giga-Bit Transceiver (GBT) being developed for the LHC experiments upgrades [132] will be a suitable replacement of the GOL chip. It is based on an architecture and transmission protocol capable of sustaining high data rates (up to 4.8 Gb/s) and high radiation doses. It also includes the capability to provide slow and fast control signals; therefore, while the cooling, LV and HV interfaces will remain unchanged in the upgraded design, the slow and fast control interface (at present electrical differential signals, decoded and fanned out to 18 FE-Boxes by a dedicated "Control-Box", and routed through a high-speed multi-wire cable of SCSI-2 type) can be realized through an additional GBT per FE-Box.

Optical data transmission is foreseen via a system of opto-electronics components produced by the Versatile Link project [133]. We are also exploring the possibility to adopt multi-channel transmitter arrays of vertical cavity surface emitting lasers (VCSEL), participating to an R&D project for the development of a compact optical package for mounting a VCSEL PIN array and couple it to a fibre ribbon [172].

Data flow and output bandwidth A schematic view of a possible design of an upgraded FE-Box, based on the ProASIC3 TDC, the GBT and a VCSEL array, is shown in Fig. 6.20 (to be compared with the present architecture shown in Fig. 6.18). We studied the bandwidth implications of different TDC output data formats: the results shown in Fig. 6.21 indicate that very large occupancies can be sustained, provided that zero-suppression is performed.

If one maintains the present connection scheme (9 FE data links per TELL1 board), then the architecture in Fig. 6.18 implies a total of 8 × 9 optical data inputs per TELL40 board, roughly corresponding to a total bandwidth of 140 Gb/s at an average occupancy of 25 %, which appears entirely compatible with the present TELL40 R&D.

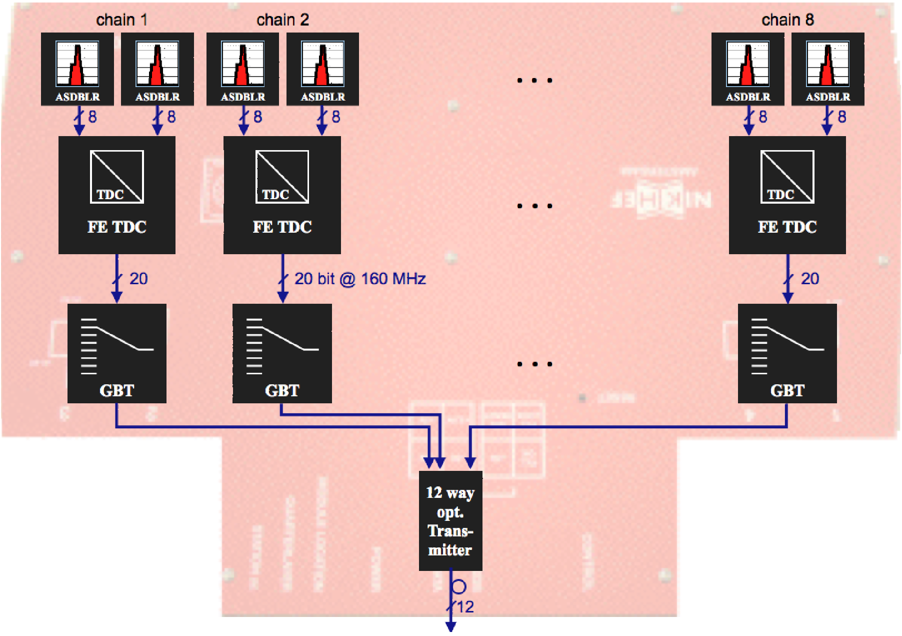

Figure 6.20: Schematic view of the data flow in the proposed upgraded FE-Box design.

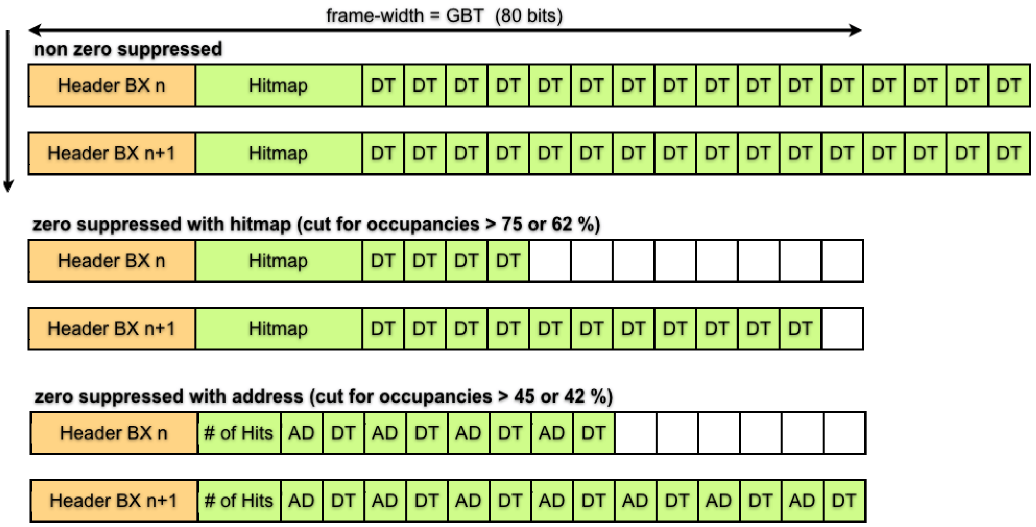

(a) TDC output data in non-zero suppressed and zero-suppressed mode (two alternative formats with and without hit pattern are shown).

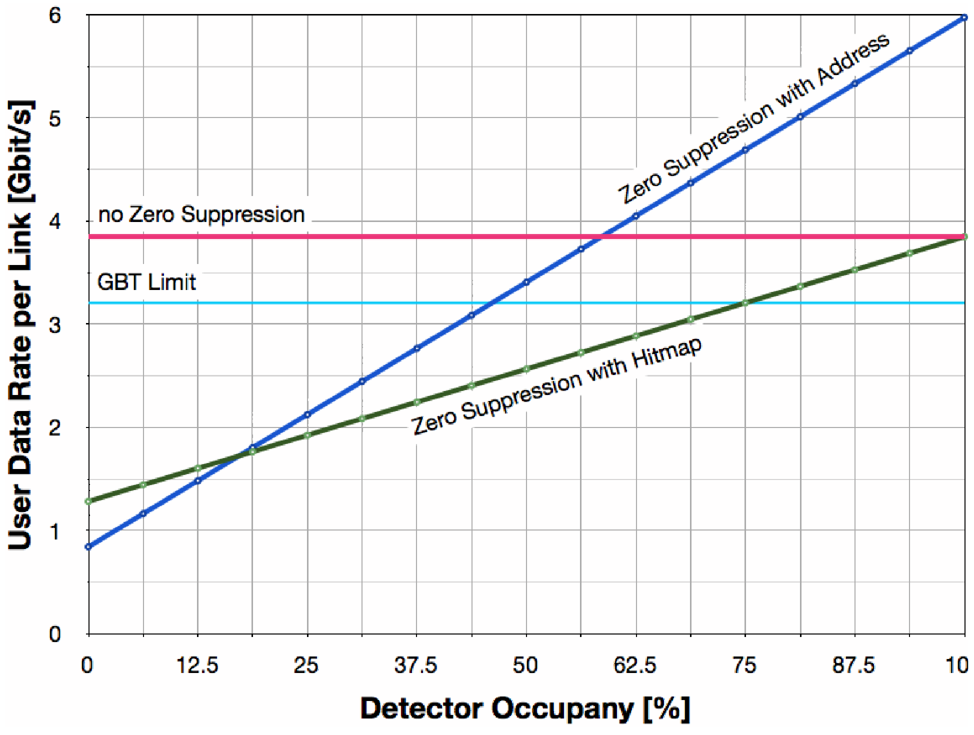

(b) TDC output bandwidth as a function of channel occupancy.

Figure 6.21: TDC data format (a) and bandwidth (b).

Summary of proposed upgrade In summary, we propose a partial redesign of the OT FE-Boxes compatible with the 40 MHz readout scheme, consisting in the design and production of new TDC and serializer/transceiver boards. An R&D program, based on the Actel ProASIC3 FPGA, the GBT and the versatile link, is well under way and the results indicate the proposed solution to be technically feasible.

6.2.2 Radiation tolerance of OT straws

The OT detector has been designed to withstand irradiation intensities that correspond to an incident rate of 250 kHz per cm wire length at a nominal luminosity of $2 \times 10^{32}\mathrm{cm}^{-2}\mathrm{s}^{-1}$. That corresponds to an integrated charge dose of 2.5 C/cm after collecting $20\,\mathrm{fb}^{-1}$ (10 years of 10^7s running/year) [158].

Current measurements during the first high intensity beam of the LHC in October 2010 showed a current of about 50 nA in the hottest straw, at an instantaneous luminosity 10 times lower than the design luminosity of $2 \times 10^{32}\,\mathrm{cm}^{-2}\mathrm{s}^{-1}$, corresponding to an irradiation intensity of approximately 15 nA/cm in the hottest region of the OT at nominal luminosity. This would imply an integrated dose of 2.5 C/cm after collecting $33\,\mathrm{fb}^{-1}$.

Ageing effects It was discovered that, despite extensive ageing tests in the R&D phase [173], the OT suffers from gain loss after moderate irradiation [174]. Subsequently, a large number of irradiation tests have been carried out in the laboratory, revealing several distinguishing features:

- The gain loss is not proportional to the source intensity: directly under the source the gain loss is less severe compared to the periphery. The shape of the dependency of the gain loss on the irradiation intensity remains unchanged when parameters of the irradiation tests are changed, such as: high voltage, source type, source intensity, gas flow, gas mixture, humidity, irradiation time, or flush time.
- The gain loss occurs mainly upstream the source position, and is worse for larger gas flow. Presumably due to the creation of ozone in the avalanche region, the gain loss is prevented downstream.
- The gain loss is large, up to 25% for an integrated dose of 0.1 mC/cm at an intensity of 2 nA/cm.
- The relation of gain loss versus intensity does however depend on the size of the irradiated area. This hampers solid predictions of irradiation damage for the operation at the LHC.

The origin of the gain loss is traced to an insulating layer on the anode wire, caused by glue components inside the gas volume. The glue used at construction is the epoxy AY103-1 with hardener HY991 containing the aromatic hydrocarbon di-isopropyl-naphthalene as plastifier. The plastifier does not take part in the curing process, and is expected to remain volatile close to the surface of the hardened epoxy. The plastifier di-isopropyl-naphthalene is identified as the cause of ageing in the OT [175].

Beneficial treatment A number of beneficial treatments have been identified to decrease the ageing rate:

- Flushing. Long term flushing is expected to transport away the glue vapours from the gas volume, and indeed the ageing rate is observed to decrease over time. All OT modules are therefore continuously being flushed.

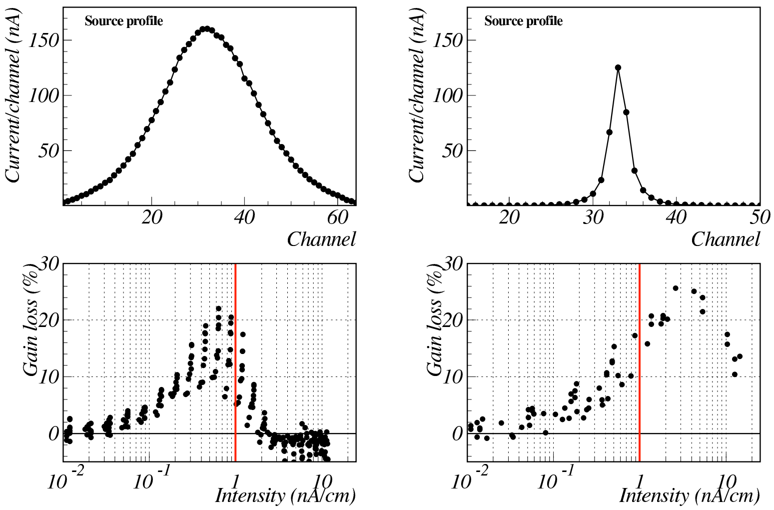

Figure 6.22: Irradiation damage versus source intensity, shown for two different source profiles.

- Oxygen. The addition of oxygen to the counting gas has shown to reduced the ageing rate by about a factor two. The nominal gas mixture is Ar/CO_2/O_2 70/28.5/1.5.

In addition to preventive treatments, also a curative treatment has been found:

- HV training. The insulating deposits can be removed by applying a large positive high voltage between 1850 V and 1920 V. This leads to dark currents of about 10 μA per wire. Potential damage to the anode wire has been investigated in the scanning electron microscope and no signs of mechanical damage to the gold plated wires were observed.

Extrapolation to high luminosity running The dependency of gain loss as a function of intensity depends on the size of the irradiated area. Figure 6.22 shows two examples of irradiation tests in the laboratory, one test with the irradiation source far from the module surface, with wide collimation, and one test with the source close to the module surface with narrow collimation. The relation between the gain loss and source intensity is different for both cases, which hampers solid predictions of irradiation damage induced by the LHC.

Secondly, the dependency of the gain loss as a function of irradiation time is poorly known. Long term irradiation tests on various OT modules seem to indicate that the decrease of gain shows a flattening behavior.

Ageing results with Trabond 2115/Araldite AY105 modules Three full scale OT modules have been constructed with different epoxy glues [176]. One module was constructed with AY105-1, which consists of identical epoxy and hardener as compared to AY103-1, but without any plastifier. In addition, two modules have been built with Trabond 2115.

These modules have been irradiated for approximately 1000 hours, resulting in a maximal accumulated charge of 0.25 C/cm at the point of highest intensity with an anode current density of 70 nA/cm. A negligible gain loss of $(5 \pm 2)\%$ was observed, indicating that this gain loss is not related to the fast ageing caused by AY103-1. These results demonstrate that usage of a different glue leads to more radiation hard modules, which are candidates for replacements in case serious gain reductions are observed in the current OT modules.

6.3 Fibre Tracker Upgrade

The current IT detectors implement 12 layers of silicon detectors in three stations following the same stereo geometry as the OT detectors. Each station consists of 4 detector boxes installed around the beam pipe providing a “swiss-cross” shaped acceptance. The silicon strip detectors are built of wafers with a strip pitch of 198 μm that are mounted on ladders. The readout electronics, as well as the cooling infrastructure, are mounted inside the detector boxes, introducing material in the active region of the Outer Tracker. The granularity and the resolution of the silicon detectors lead to an average occupancy of 1–2% for nomial luminosity operation, allowing usage in a higher density environment. In the injection tests the IT has been operated in an high density environment, illustrating that track reconstruction at an occupancy of 10% is possible for the IT.

Operation at a readout speed of 40 MHz requires replacement of the electronics. Since the electronics of the current IT detectors cannot be replaced independently of the detectors, new detectors have to be built. Given the tight occupancy requirement of the OT straws the proposed upgrade IT detector should cover a larger area than the current detector.

For a new, larger, Inner Tracker a scintillating fibre detector is considered. A scintillating fibre inner tracker offers two attractive features over a silicon detector. Firstly, the scintillating fibre cooling requirements are less stringent than for silicon detectors under intense irradiation. Secondly, the fibre option allows optical signal transportation to readout electronics outside the fiducial volume. These two options allow for an important reduction of mass of dead material (electronics, cooling balcony, connectors, cables, see Fig. 6.11) in the acceptance of the spectrometer. In addition, the length of the scintillating fibres can be relatively easily adjusted to the required dimension of the IT detectors. The electronics solution for fibre readout at 40 MHz would be developed in a common project with the RICH group.

The high occupancy foreseen at high luminosity in the innermost part of the Outer Tracker suggests to explore the scenario of alternative solutions for the LHCb upgrade. The use of a more granular and faster fibre detector, capable to sustain radiation and also to satisfy the requirement of covering the relatively large area (i.e. 4×4.5 m^2) currently occupied by the straw tubes, is under consideration.

The scintillating-fibre technology has been applied in high rate environments [177, 178, 179, 180]. In this section a scintillating-fibre detector option is considered for LHCb; “thin” fibres as a possible replacement for silicon in the IT and the TT, and “thick” fibres as a possible replacement in (part) of the OT.

6.3.1 Scintillating-fibre detectors for the IT and TT

A possible layout for a fibre tracker is shown in Fig. 6.23. It makes use of a carbon fibre supports similar to those of the present IT. The new IT boxes containing layers of fibres are suspended to the frames. The FE chips are not in the box like in the present IT, but the scintillator light is transported outside the acceptance by clear fibres, at about 3 m from the beam pipe

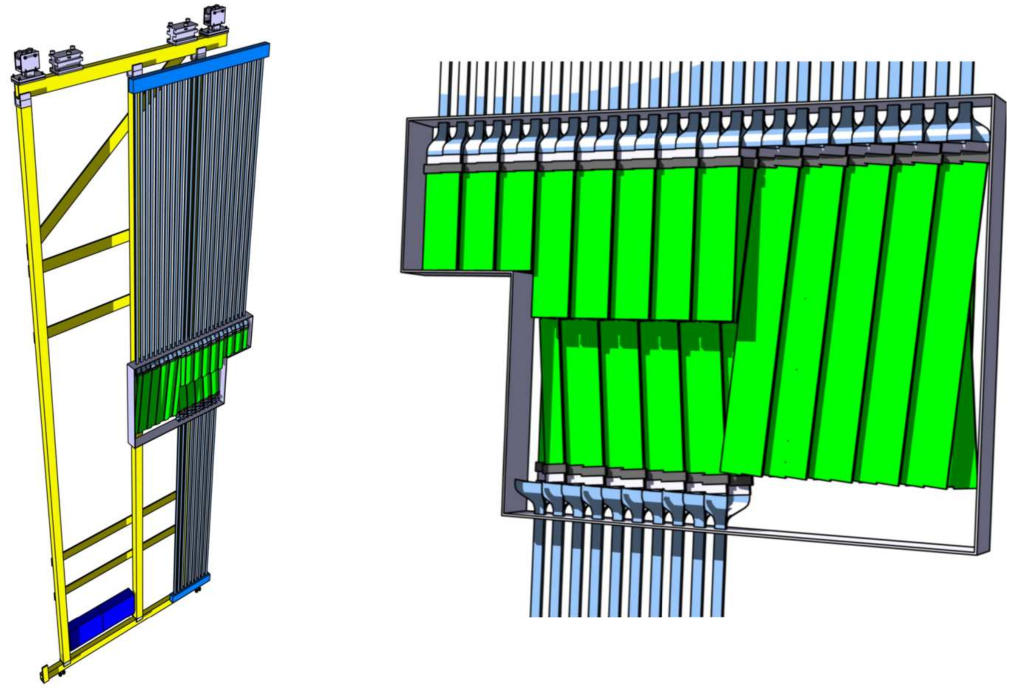

Figure 6.23: Possible configuration of the IT layout.

in a region with lower radiation. There, we have electronics service boxes, containing the light sensors, digitization, and optical line drivers.

The area covered by the scintillating fibres will be similar to the present IT, or larger, to decrease the occupancy in the OT. In the following we will assume a size of boxes and topology close to the present IT configuration. The readout pitch is also similar ($\sim 250\ \mu$m), which implies about the same number of channels to read out (120k). A two layer prototype for stereo view is shown in Figure 6.24.

The present idea for the readout of the scintillating fibres is to use Silicon Photomultipliers (SiPM) [181]. SiPMs with 128 sensors per chip are being developed by Hamamatsu (dubbed MPPC for Multi-Pixel Photon Counter). Each channel consists of a sensitive area of 250 μm width (230 μm active), and 1.32 mm height, well suited to efficiently detect the light from layers of densely packed scintillating fibres with a diameter of about 250 μm. An example illustrating the single photon resolution obtained with SiPM (a 32 channels prototype) is shown in Fig. 6.25.

Several tests have been performed on the radiation resistance of such devices. The discussion in Section 6.3.1 shows that these devices have to be placed in a protected area: their performances seriously degrades after an irradiation of the order $10^{11}\ n/\mathrm{cm}^2$, dying after $10^{12}\ n/\mathrm{cm}^2$. From FLUKA simulations we expect $3 \times 10^{-4}\ n/\mathrm{collision}/\mathrm{cm}^2$ in a region 3 m above the beam pipe. With a luminosity of $2 \times 10^{33}\mathrm{cm}^{-2}\mathrm{s}^{-1}$ we have 2×10^{15} collisions/year hence we expect an irradiation of $6 \times 10^{11}\ n/\mathrm{cm}^2$.

These predictions indicate a lifetime of about one year for the SiPM. Hence it is necessary to absorb the neutron flux at the source and/or to protect the devices with a shield (see below). At the same time the companies are studying how to increase the radiation hardness of the

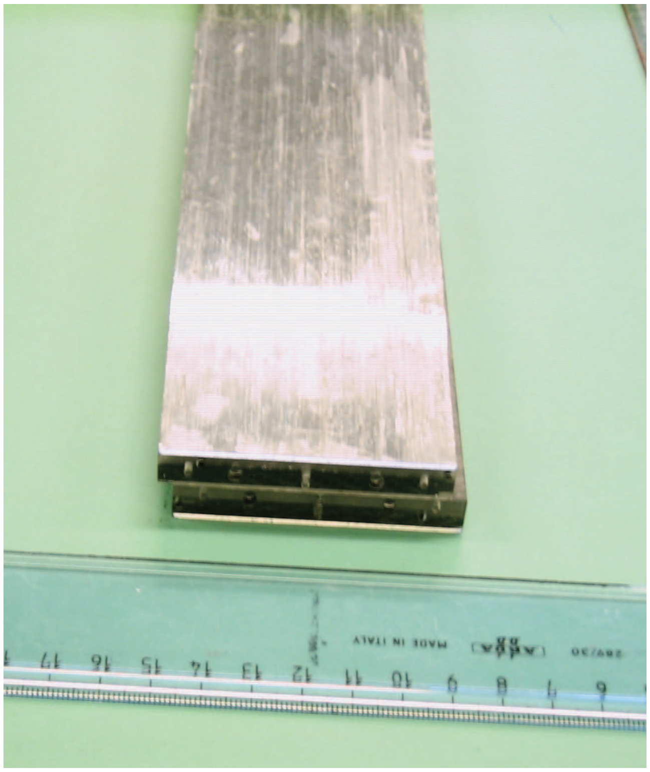

Figure 6.24: Photograph of a fibre tracker prototype made of two sensors 40 cm long and 6.35 cm wide. The two sensors are glued together with the fibres at the top and at the bottom, making an angle of 1 degrees. The two extremes have been polished in such a way that an unique hybrid with SIPMs can be placed to read out both stereo views at one side. A flat mirror can be placed at the other side. The total thickness of the detector is 1.9 cm (two sci-fibre layers of 1 mm each on carbon-fibre/polystyrene foam supports), corresponding to about 1.6% X_0. The weight is 190 g. New prototypes will be produced with the stereo angle of 5 degrees, and a lighter structure (1.4% X_0 or less).

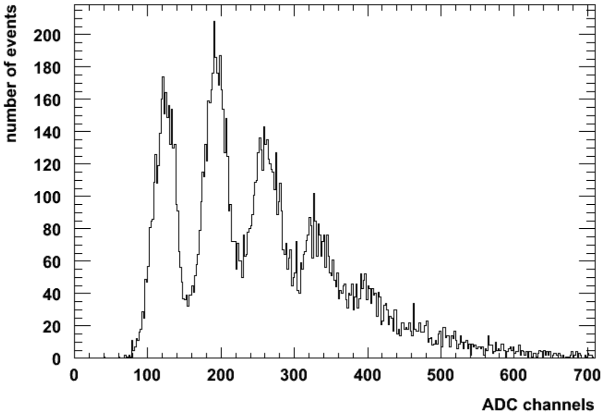

Figure 6.25: SiPM response to a very low flux of light. The peaks correspond to single cells firing, demonstrating the single photo-electron sensitivity of the sensor.

devices.

The technology of fibres is now tested in the context of the Positron Electron Balloon Spectrometer experiment (PEBS) [183]. Several prototypes have been built using Kuraray SCSF-78MJ fibres with diameter of 250 μm. The measured precision for the fibre diameter is of 6 μm. The light emission wavelength is in the blue, around 450 nm, the decay time is 2.8 ns, and the attenuation length in the fibre larger than 4 m.

To produce reliable detector modules with a sufficient spacial resolution, an adequate method of positioning and gluing fibres is crucial. The fibres have to be laid and stacked very precisely with a given pitch. During the production process any damaged to the sensitive fibres must be prevented. A stack of layers for a total of about 1 mm thickness is found to optimize the detection efficiency versus material budget. With our choice of diameter this corresponds to 5 layers. Two methods of producing fibre matrices are considered.

The first, which is already proven, was developed by RWTH Aachen for the PEBS experiment. The fibres are wound on a cylindrical surface with a screw thread to guide the fibres of the first layer. The fibres of further layers are guided by the grooves between the fibres of the underlying layer. To get a flat fibre module after detaching the glued fibres from the cylinder, the tension of the fibres has to be increased with each layer. The alignment precision of the fibres around their nominal position was measured by a pattern recognition procedure: a precision of 25 μm rms was found.

The second method is designed by TU Dortmund and still under development. The fibres are wound around a long cuboid with a half cylinder at each end (Fig. 6.26). The positioning is done by stepping motors and grooves at the half cylinder surface. The main advantages are the possibility to produce bigger modules and the constantly low fibre tension in the production process.

For the PEBS beam-tests a readout using a prototype of 32-channel SiPMs arrays was tested. The detection efficiency for minimum ionizing particles was found close to 100%. The signal yield was larger than 20 p.e. (photo-electrons) per MIP in the hit SiPM channel, with a noise of 0.3 p.e. rms, providing a very comfortable S/N ratio. The hit position is computed as the center of gravity of clusters. The obtained spatial resolution was estimated to be 50 μm, consistent with the simulations.

Assuming the light yield and noise observed with the PEBS prototypes a simulation has been performed to study the performances of a new IT, with the structure described above: 1 mm thick scintillating fibres detector, prolonged by about 3 m of clear fibres, the SiPMs at the end. Notice that the radiation length of 1 mm fibre sensor is about equivalent to a 300 μm Si sensor. A light structure will contain the scintillating fibres with a material budget not very different to the present detector. The clear fibre will also contribute to the material budget, but reductions will be achieved by replacing copper cables and pipes. Clear fibres from Kuraray have an attenuation length greater than 10 m (500 dB/km at 450 nm), so we are not limited by the length and an optimized path in front of the OT can be chosen.

At present we are considering to read out the scintillating layer only at one end, a mirror will be placed at the other end.

Studies are ongoing to understand if it is possible to prolong the scintillating fibre by a clear one, reaching a transmission efficiency close to 100%. We have made a simulation in which the scintillating layers are put in contact with the clear fibre ribbon introducing alignment errors. The simulation contains information about:

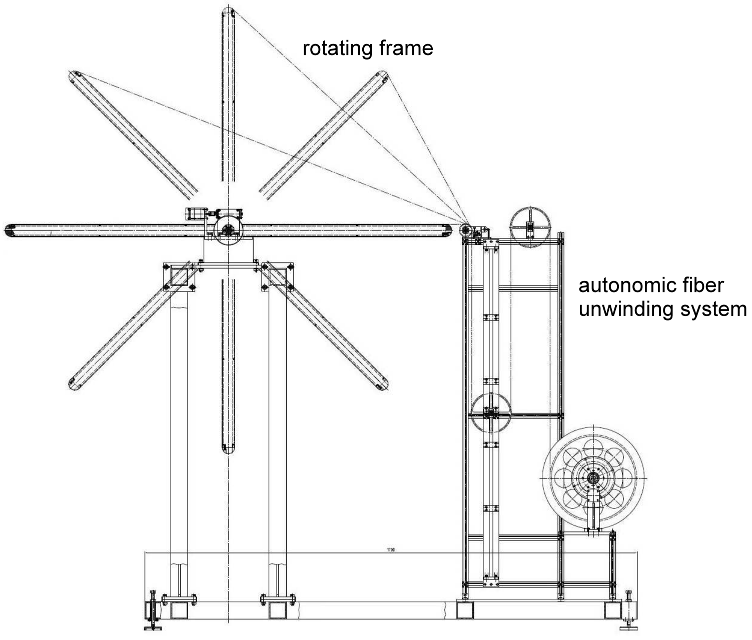

Figure 6.26: Lathe-prototype to wind fibre matrices.

1. the average p.e. yield (20 p.e. per MIP);
2. the channel saturation (80 micropixels/channel, for instance);
3. the intrinsic signal noise and resolution (in units of p.e., parametrized by $0.3 + N \times 0.02$ p.e., where N is the number of detected p.e.);
4. the relative fibre to fibre alignment precision (7 μm, see Fig. 6.27);
5. an absolute misalignment of clear and scintillating layers (up to 60 μm).

The simulation did not include light attenuation in the clear fibres. In the case of a 60 μm misalignment, the measured p.e. signal is reduced by 28%. At the same time the spatial resolution deteriorates from 50 μm rms to 80 μm.

We will perform simulation with scintillating fibres and clear fibres of different sizes. Kuraray also produces fibres with a quasi-square cross-section. We will see if these can better match the SiPM geometry of a channel. We are also investigating the possibility to obtain from Kuraray quasi-rectangular shaped clear fibres of the size of a SiPM channel. Kuraray is now trying to produce ribbons made of 5 of such clear fibres lined-up.

Fibre R&D The error of an over- or under-sized fibre propagates and builds up through the layers of the matrix. An automatic fibre quality control system has been developed in Dortmund. It checks the fibres delivered by the manufacturer with regard to their diameter, light guidance and losses.

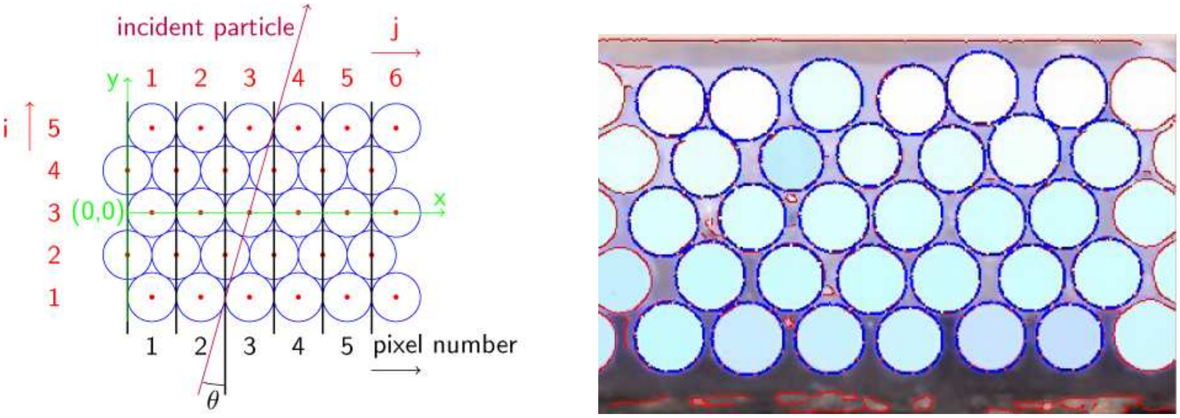

Figure 6.27: Left: ideal configuration of 5 layers of fibres. Right: picture of a portion of a fibre tracker prototype built for the PEBS experiment, seen from one end. The contour of each fibre was drawn by a pattern recognition program which is used to measure the alignment precision of each fibre with respect to its nominal position.

To produce a high-performance tracking system several properties must be checked. The influences of humidity, temperature and radiation to the fibres, the glue and in particular their combination have to be analyzed. There are many studies available concerning the radiation hardness of organic scintillators and especially scintillating fibres. The quantitative results differ significantly, hence it is necessary to perform own investigations. A summary of concluded studies can be found in [182].

First fibre irradiations took place in December 2010 at Forschungszentrum-Garching near Munich. Single fibres were irradiated with a 20 MeV proton beam at different doses. Figure 6.28 shows a first qualitative result. The measured fibre was irradiated homogeneously over a length of 50 mm with a total dose of 10^5 Gy (corresponding to the order of magnitude of ten years of LHC irradiation at the inner edge of the IT with a luminosity of $10^{33}\,\mathrm{cm}^{-2}\mathrm{s}^{-1}$). A deterioration of the attenuation length in the irradiated area can be seen. Further investigations will show whether the lower light yield is acceptable. Alternatively there is the possibility to switch to more radiation hard fibres which emit in the green. The possible usage of such fibres requires additional R&D effort since the detection efficiency of the SiPMs peaks in the blue. Further analysis of the irradiated fibres and the consequences for the tracking resolution are ongoing.

Sensor radiation issues FLUKA simulations indicate that the main component of the radiation in the region at 3 m above or below the beam pipe are neutrons with a spectrum centered around 1 MeV. The major source of the flux originates from the back of the detector, in the region of M1. More detailed simulations are in preparation. With a luminosity of $10^{33}\,\mathrm{cm}^{-2}\mathrm{s}^{-1}$ we expect a neutron fluence of $3 \times 10^{11}\ n/\mathrm{cm}^2$.

It has been reported (by Toru Matsamura, KEK) that SiPMs suffer from radiation damage. In particular tests performed on MPPC samples (S10362-11-100CK) indicate that these device die after an irradiation of 10^{12} neutrons/cm^2. The test were done with neutrons from a reactor with a dominant component of the spectrum in the range of 0.1 to 1 MeV.

To confirm these results, we have also performed irradiation campaigns with 65 MeV protons

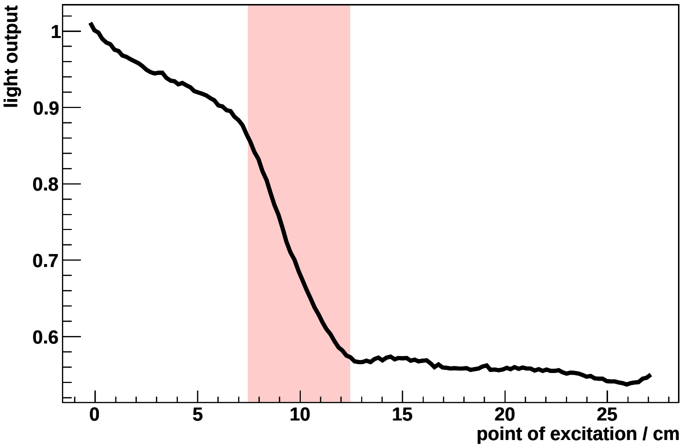

Figure 6.28: The light output of a scintillating fibre as a function of the distance between the point of excitation and the end of the fibre where the light yield is measured. The fibre was irradiated with a dose of 10^5 Gy in the marked area.

and with a PuBe neutron source.

Tests with protons The suitability of the SiPM-arrays is determined by their ability to distinguish different numbers of photons. This is necessary to use the centre of gravity method to improve the resolution. A first irradiation of SiPM-arrays with 20 MeV electrons at the ELBE-Quelle near Dresden showed that this ability decreases already at low doses. To quantify the influence on the parameters of the SiPMs (dark counts, photon detection efficiency, gain, crosstalk, etc.), irradiations with protons were performed at the end of 2010. These tests were done at Centre Antoine-Lacassagne in Nice (65 MeV) and Forschungszentrum-Garching near Munich (24 MeV). SiPM spectra with different number of photons and the leakage current were taken at varied bias voltages. The detailed analysis of the data is ongoing. First qualitative results are shown in Fig. 6.29. Before irradiation (left) the dark-count spectrum (mainly the pedestal) and the LED-spectrum (about 8 photons) are well separated. Figure 6.29 (right) shows the same measurement after an irradiation with 8.3×10^{10} protons/cm^2. Converted to 1 MeV neutrons this number corresponds to approximately 50 days at the top of the current IT at $2 \times 10^{32}\text{cm}^{-2}\text{s}^{-1}$. The result indicates that the radiation close to the beam-pipe is too high for the SiPM-arrays.

Tests with a PuBe source The PuBe neutron spectrum extends up to about 10 MeV, mainly in the interval from 3 to 6 MeV. Our source has an activity of 10^7 neutrons/s. There is a contamination of 10^6 gammas/s with a maximal energy of 4.4 MeV. We irradiated three SiPM placed in a small box at distances of 7, 12, and 17 cm from the center of the source. The response of the SiPMs could be tested by shining three LEDs. The neutron flux was about 13×10^3, 4.5×10^3, and 2.2×10^3 neutrons/cm^2/s respectively. The dark current was monitored at different times of exposure, see Fig. 6.30, showing a constant degradation process, of about 2×10^{-7} nA per n/cm^2 for the three positions.

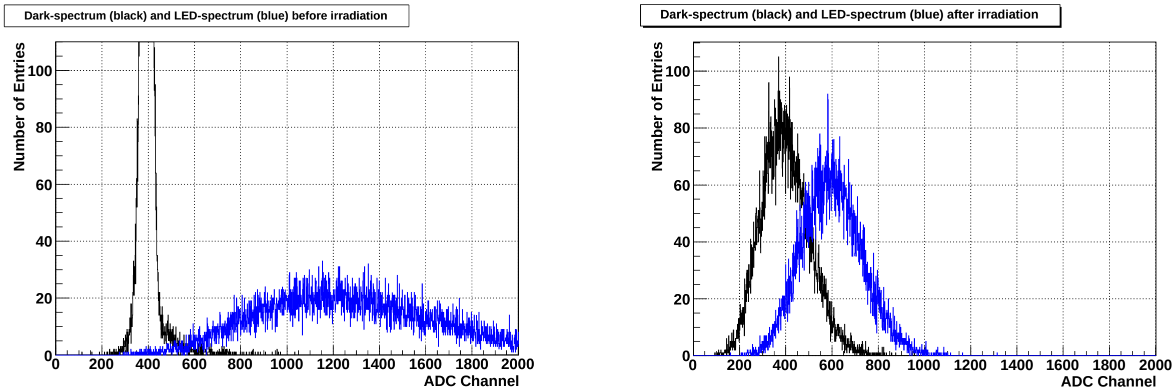

Figure 6.29: Left: dark- and LED-spectrum of one channel of an unirradiated SiPM-array. Right: dark- and LED-spectrum of the same channel after an irradiation with 8.3×10^{10} protons/cm^2.

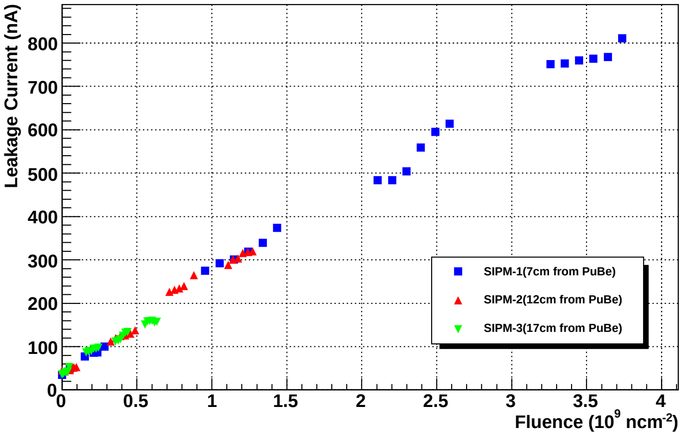

Figure 6.30: Dark current in the three SiPMs as a function of the integrated neutron flux. The slope is about 2×10^{-7} nA per n/cm^2, identical for the three positions (the rate is 10 nA/h for the SiPM placed at 7 cm).

To check the role of the gamma rays we have also performed irradiation with a 3 mm lead shield placed between the source and the box. No change was observed in the slope, and we conclude that there is a negligible contribution of gamma rays in the degradation of the sensor.

Neutron shielding The design of a shielding structure for neutrons is ongoing using FLUKA, and assuming the FLUKA predicted neutron spectrum in LHCb.

To validate the procedure, some test are performed with the PuBe source and SiPMs protected by different layers of Polyethylene with 5% boron. Some results are shown in Fig. 6.31, for the irradiation of a shielded SiPM (in fact it is the third SiPM of the preceding irradiation experiment). The box with one SiPM was covered by 1.8 cm of borated Polyethylene and irradiated. The SiPM distance from the source was of 7 cm. The different slopes correspond to different amount of shielding: no shielding, 1.8 cm thick shield as described above, idem plus

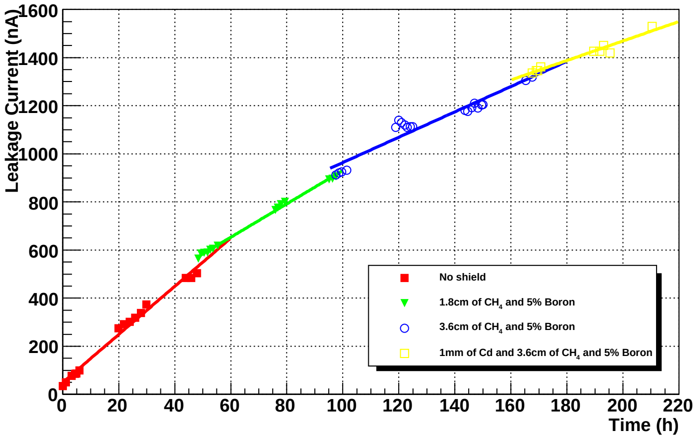

Figure 6.31: Dark current as a function of time in one SiPM, partially protected by neutron shielding of different size. The three slopes correspond to no shielding and shielding by 1.8 and 3.6 cm of Polyethylene with 5% boron. For the last portion of the curve a 1 mm Cd layer has been added to check the effect of the absorption of quasi-thermal neutrons. The four slopes are 10.0 nA/h (identical to the the result seen above), 6.9 nA/h, 5.2 nA/h and 4 nA/h.

an additional 1.8 cm layer (but only on the front side of the box), and the last test was done with the addition of a 1 mm Cd. The Cd layer is used to clean up the low energy neutrons. These results show a global reduction by about a factor of 2 of the degradation. As previously stated, these studies will be used to validate the FLUKA simulation.

Absorber layers placed at strategic positions in the LHCb detector should also be considered, with a structure similar to the shielding described above. From FLUKA, a hot spot is the M1 region close to the beam pipe. More detailed simulations are needed, and we also foresee tests on site: several SiPM samples have been placed in LHCb, close to the existing radiation monitoring devices.

Electronics For on-detector electronics an upgrade to a 40 MHz readout and correspondingly higher output data rate would either mean a significant increase of data transmission bandwidth between the detector and counting house, or an introduction of data compression (including zero suppression) electronics on the detector. A fibre detector offers the attractive feature of installing the active 40 MHz readout electronics outside the acceptance of the OT. This has the advantages that the readout can be localized in a less intense irradiation environment (similar to the present OT electronics) and that the presence of additional dead material related to electronics, readout and cooling systems in the active area can be avoided.

Because of the Geiger-Mueller mode of operation a SiPM signal is intrinsically much larger than the one from a silicon strip detector. The gain is typically 7.5×10^5 electrons per photon for a SiPM with $50 \times 50\mu$m micropixels, compared to 2.2×10^4 for a 300 μm-thick silicon detector. As a consequence the preamplifier and shaper circuit is much less sensitive to noise. Circuits suited for SiPM detectors have been successfully implemented in several FE chips. An adaptation to the short integration time required at the LHC should not be problematic. The dynamic range for the measurement of up to 3 MIP signal requires a dynamic range of 1 to 30 photons and a signal-to-noise ratio of about 10 to guarantee a good noise suppression.

The most challenging part for the FE electronics is the signal digitization. As the particle impact point is determined by the centre of gravity of the hit cluster, a good position resolution requires each channel amplitude to be recorded with at least a 5 bit resolution. With 5 bits the dynamic range of 0 to 30 photons can be covered and due to the single photon detection capability the noise can be suppressed to a value below the least significant bit. The signal digitization requires a custom designed ASIC with for example 128 or 64 5-bit ADCs followed by an FPGA that provides zero suppression and electrical interfacing to GBT. The system shown in Fig. 6.32 will be placed outside the acceptance of the LHCb detector and protected by some shielding, as described above. Therefore the requirements to the electronics are less problematic concerning cooling, space and radiation environment, as is the case for the current, silicon based, IT.

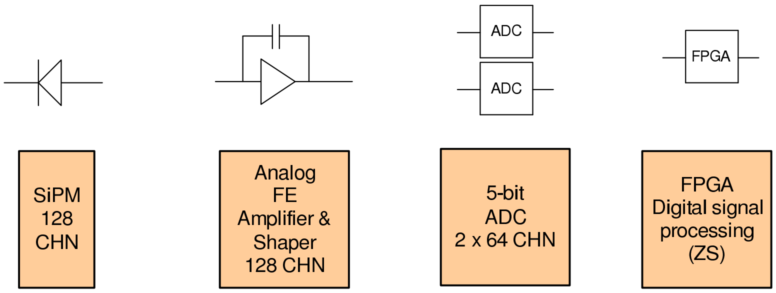

Figure 6.32: Signal processing chain for the SiPM detector with analogue FE, ADC and digital signal processing on the FPGA.

6.3.2 R&D for a scintillating-fibre OT

For the innermost, high-occupancy, part of the Outer Tracker a possible alternative to straw detectors is the use of relatively thick scintillating fibres (in the range of 0.7 to 1 mm) to be coupled with photosensor detectors (either multi-anode PM or SiPM). Existing literature [177, 178, 179, 180] suggests that for either single or double cladding scintillating fibres the primary requirements of the OT can be met. The fibres show a good light yield, resistance to radiation, ease of operation and construction, a space resolution at the level required by the LHCb tracking and a minimal dead time. The minimal dead time will avoid pile-up effects in the detector.

In a configuration under study, a certain amount of fibre layers are glued longitudinally one on top of the other, to replace a single coordinate (X or U,V) of the current straw tube setup (Fig 6.33). The number of layers of fibres has to be optimized, considering the obtainable light yield, and the material budget. From preliminary evaluations, it is expected that in the case of 1 mm fibres, 4 to 6 fibre layers would guarantee enough light at the photosensor and maintain the current material budget of 1% of X_0 per coordinate layer.

These layers of fibres are glued on a mechanical support of low mass (carbon fibre). Each column of fibres is ganged and brought to a single element of the photosensor, where the

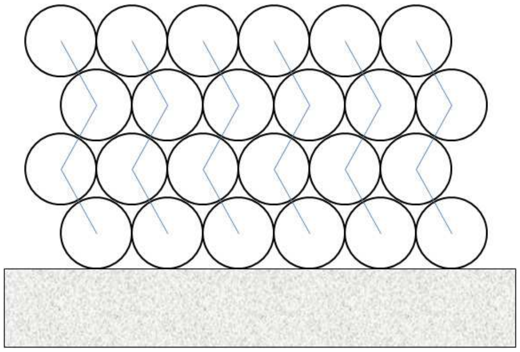

Figure 6.33: A possible schematic layout of an active layer of fibres (one coordinate). Fibres connected by a line would be sent to the same photosensor element.

collected charge is recorded. The charge centroid will provide the transversal coordinate, with a resolution better than the one coming from the simple binary information.

As photosensors, SiPM have very appealing photon detection efficiencies and ease of operation, although their radiation resistance is not yet verified (as discussed above). The level of noise of these detectors could be a drawback in a high track density environment. On the other hand, new multi-anode PMTs from Hamamatsu (64 channels each) with high quantum efficiency based on SBA or UBA photocathodes are also very good candidates for fibre readout.

In a digital readout scheme with a 1 mm fibre diameter one expects space resolutions of approximately 0.35 mm per single coordinate. From preliminary results of simulations, the resolution can be improved when the charge centroid readout method is applied. Other arrangements of fibres are under study in order to reach the required granularity, and a complete simulation of the set-up based on GEANT4 has been prepared.

A study of a fibre prototype is currently undergoing at the Frascati Laboratories (Fig. 6.34). One fibre module, 2.5 m long, 60 mm wide, made of 6 layers of fibres ganged to a 64 channel MaPMT H8500 is currently under test. The fibres used are single-clad SCSF-81 from Kuraray, 1 mm in diameter, and are expected to have a light yield of 4–6 p.e./mm and an attenuation length of 4 m. In the prototype the fibre pitch is 1.35 mm and the average track length in the fibre for an orthogonal track is 3.5 mm. Including the PM quantum efficiency, the average number of p.e./track is approximately 10. This setup will be used to continue resolution studies, while it is planned to build another prototype, shorter (1 m), with 128 readout channels and 4 layers of 1 mm fibres and pitch of 1 mm, to be equipped with higher quantum efficiency PM, and to be exposed to a beam in the summer of 2011.

6.4 Silicon Tracker Upgrade

The present IT and TT systems are built with Si strip detector modules. The geometry and station arrangements were optimized for a low luminosity operation of the tracking system (μ = 0.4). While R&D is needed to identify a silicon detector system that meets the requirements dictated by the different event environment expected in the LHCb upgrade, Si still represents a very appealing option for this application. It provides a radiation-hard solution for the innermost portion of the detection planes, that will experience a maximum fluence of

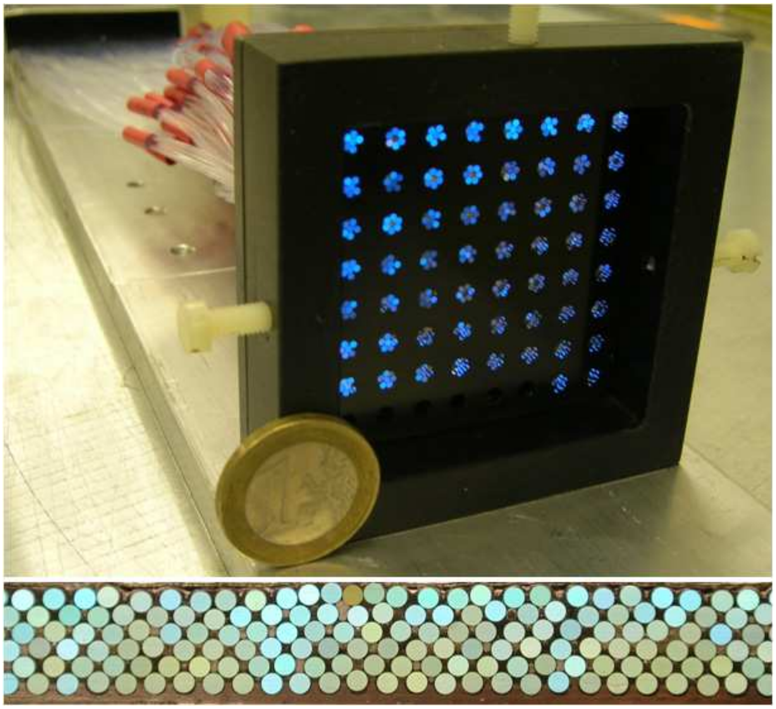

Figure 6.34: Photographs of the 1mm-fibre prototype during construction: mechanical setup for the coupling of fibres to the MaPMT Hamamatsu 8500 at one end (top) and the fibres at the other end, after polishing (bottom).

$2{\times}10^{14}$ $n_{\mathrm{eq}}\mathrm{cm}^{-2}$. Three decades of experience in the use of this detector technology in experimental particle physics and other fields [184] have led to remarkable technological advances, which we can exploit. For example, relatively large sensors with different shapes have been produced, and almost edgeless devices [185, 186] minimize the guard ring dead area. Strip patterns with segmentation changing with the expected occupancy can be implemented, as in the current VELO, with a range of shapes and orientation. The main challenge with this technology are in the system integration, namely the minimization of the material budget while ensuring mechanical stability and adequate cooling, and bias and signal distribution optimized for speed and low noise without excessive power dissipation. Although the technology can be used both for the TT as well as IT trackers, we focus here on a silicon implementation for TT. The desired detector geometry needs to be optimized in concomitance with system design criteria. The studies described before, showing how an increased segmentation in the y coordinate and a larger acceptance in the TT lead to a reduced number of ghost tracks at higher occupancies, will be refined and extended to determine the best sensor pattern consistent with a manageable number of data lines and low mass implementation.

In addition, a front-end device suitable for 40 MHz readout needs to be developed. While the general structure of this ASIC is common to the front-end systems built for other LHCb detector systems, some of its building blocks need to be tuned for this specific technology. For example, if we maintain the front-end electronics location at the top and bottom periphery of the active area, the analogue front end needs to be optimized for relative high input capacitance. In addition, low mass electrical connectivity with high reliability and low common mode noise

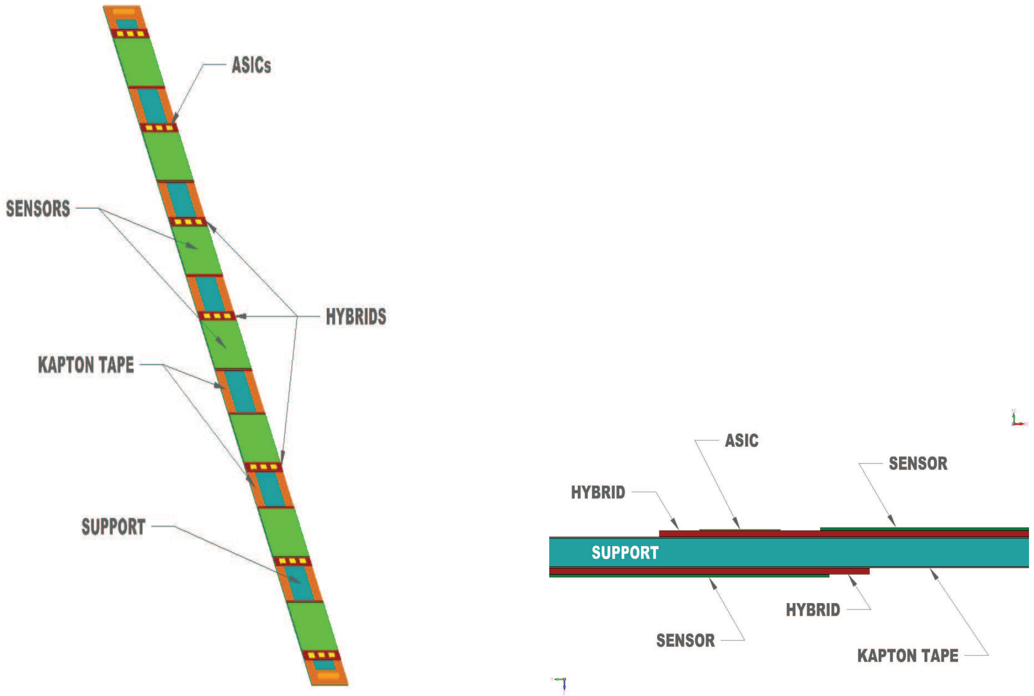

Figure 6.35: Conceptual design of an integrated module assembly for a Si TT layer. Left: assembly of one side of the stave, where a composite substrate (shown in blue) provides mechanical stability and cooling for the hybrid circuit hosting the silicon detectors and the front-end electronics. Kapton tapes (shown in orange) bring the serial digital outputs to the back-end electronics and distribute power and HV to the hybrid circuits. Right: details of the double-sided assembly with sensor overlap.

needs to be implemented.

Clearly the innermost portion of the plane poses more complex challenges: it suffers more radiation, thus it determines the maximum temperature at which the detector can operate efficiently and reliably. In addition, it is farthest from the region where cooling can be implemented without increasing significantly the material budget of the system. Finally, this is the detector segment that benefits most from an increased segmentation due to the high track density. A non-traditional edge shape allows best coverage of the region near the beam pipe. Thus a separate optimization of the innermost TT region is very important.

The main components of the R&D towards the silicon tracker include the development of "integrated module" building block of the sensor plane, the silicon sensor optimization and front-end electronics providing the 40 MHz readout.

6.4.1 Straw-man integrated module

A "straw-man" integrated module concept based on ideas developed for the ATLAS SCT upgrade [187] has been developed. The Si detector size and overall module length in Ref. [187] are comparable in size to the modules needed to cover the TT detector acceptance. Other interesting module concepts are being developed for the Belle II upgrade [188]. Thus we can exploit synergistic R&D development to optimize our design.

Figure 6.35 shows the conceptual design of our integrated module. We are exploiting a double-sided mechanical assembly to achieve full detector acceptance. The baseline stave concept consists of a mechanical support implemented in carbon honeycomb or foam, a bus cable (copper-aluminum-kapton tape flex-circuit to distribute electrical signals, power and high-voltage) laminated on each side of the mechanical core, silicon detector modules mounted on low-mass hybrid circuits hosting the detectors and the front-end electronics. The mechanical support will include integrated cooling if deemed necessary to maintain the desired temperature in the innermost sensors. This design has the advantage of minimizing the capacitance seen by the input line of the front-end electronics. This allows the use of 300 μm sensors. Positioning the front-end electronics close to the sensor does not need to have a significant impact on the overall material budget as the electronics may be thinned down to $\sim$ 100 μm. Thinning is planned also for the VELOPIX ASIC. Several R&D efforts geared towards HL-LHC [189] and Belle II [188] aim at achieving even thinner front-end devices. Table 6.2 shows a summary of the material budget per plane assumed in this initial estimate, it corresponds to a total radiation length of 1.5% per plane.

Table 6.2: TT Si integrated module material budget.

Component	Radiation length (%)
Sensor	0.34
Hybrid + FE electronics	0.44
Substrate, Cooling, and Kapton tape	0.73
Total	1.51

We are planning to undertake mechanical and thermal studies to assess the cooling needed to prevent thermal runaway throughout the detector lifetime. Thermal studies similar to the ones described for the VELO are under way. A mechanical mock-up will be constructed to validate these studies. However, the advanced HL-LHC R&D work gives confidence that this can be achieved.

Similarly, the electrical integrity of data transmission, and the overall power and grounding scheme to prevent the addition of common mode noise, are key system-design R&D items. We are assuming that the copper to optical transition occurs at a distance of about 2 m from the front-end hybrids like in the present design. An electrical signal transmission model will be constructed, utilizing fast serial drivers to transmit high data rate signals through prototypes of the proposed interconnect system.

The investigation of the system issues described here constitutes critical R&D work to optimize the performance of Si-based upstream (and possibly downstream) tracking susbsystems.

6.4.2 Sensor technology R&D

Radiation hard Si strip devices are our baseline detector elements. The radiation level expected is at most the one envisaged for innermost tracking elements after few years of operation at nominal LHC luminosity, as a fluence of $2{\times}10^{14}$ $n_{\rm eq}{\rm cm}^{-2}$ is predicted by our background simulation studies at the innermost radius (assumed to be 3.7 cm) after collecting an integrated luminosity of 100 fb^{-1} , thus we are relying on a well known technology. We anticipate using 300 μm thick n-in-p devices, studied extensively in the framework of the RD50 collaboration [190]. This technology is the one chosen for the VELO replacement modules [191]. The main R&D items concerning the sensor design are:

1. optimum strip geometry;
2. guard ring design to maximize sensor active area;
3. inner detector shape to optimize acceptance in the high η region.

The availability of 2–3 routing layers in current Si devices can be exploited to refine the segmentation along the strip in the innermost devices.

6.4.3 Electronics R&D

Dedicated front end electronics featuring 40 MHz readout needs to be developed for this application. Table 6.3 summarizes the main requirements.

Table 6.3: TT Si-strip front-end electronics requirements.

Parameter	Requirement
equivalent noise charge (C_{in}=10-40 pF)	$\leq 1500\ e^-$
analogue response peaking time	$\leq$ 25 ns
readout architecture	binary zero-suppressed
discriminator time walk (4–40 ke^-)	$\leq$ 10 ns

The building blocks of this ASIC are common to other subsystems, featuring analogue front end, zero suppression, and digitization with high speed serializer with data format consistent with the GBT protocol [132]. Presently the strip pitch envisaged is $\sim$ 200 μm, as in the present TT system, thus a binary readout is adequate. The ASIC will be implemented with the same C-MOS 130 nm technology adopted for the VELOPIX ASIC. Sub-micron C-MOS technologies are inherently radiation hard and require lower bias voltages, reducing the power consumption.

The analogue front end needs to be tuned to the detector capacitances envisaged for the final system (ranging from 2.5 to 25 pF depending upon the y segmentation). Zero suppression is critical to reduce the amount of information transmitted through the optical links. Presently, there is no strong motivation to introduce a finer readout pitch, and thus a binary readout is probably sufficient to achieve the desired spatial resolution. For calibration and monitoring purposes it would be desirable to have a switchable analogue output, for example on one specific channel per ASIC.

The digitized information needs to be transmitted through a fast serializer block, which provides the necessary data throughput consistent with the requirements of 40 MHz readout. Thus signal integrity is an important consideration, and discontinuities in the signal path, with the related losses and distortion, need to be minimized.

We are developing a R&D strategy that maximizes synergy with other LHCb sub-detectors, and with similar ongoing development at CERN. In parallel to the ASIC design and electrical characterization, thinning of the readout ASIC is an important R&D item if we consider putting the electronics close to the sensor.

6.4.4 Mechanical Support and Cooling

The salient mechanical features for the module have been described above. The design includes cooling lines embedded in the mechanical core to handle the thermal load, using either liquid or bi-phase cooling medium. Studies are underway to determine the cooling power needed.

As the module mounts at the top and bottom similarly to the present TT module, the mechanical superstructure that is in place now can likely be re-used in large part for this design, with some modifications to the beam pipe region, support plates and cable routing.

Infrastructure All the items described above need prototyping and testing. The module components need to be exposed to adequate levels of irradiation, and the detector performance needs to be assessed before and after irradiation. The tools described in the section on the VELO upgrade can be used towards this goal. In particular, the infrared laser set-up and cosmic ray test stand at Syracuse are available. In addition, the excellent TIMEPIX telescope is an ideal environment to qualify the spatial resolution of prototype detectors.

Chapter 7

Particle Identification

Introduction

The particle identification (PID) system is a vital component of the upgraded LHCb detector. Several key physics channels which involve kaons rely on the RICH PID to reject copious backgrounds from multiple-track combinatorics and events with similar decay topologies. Especially important are the rare decays $B_s \to \phi\phi$, $B_s \to \phi\gamma$, $B \to \phi K^0_S$, as well as the gamma-measurement family of channels $B \to DK$. The PID is also crucial for the kaon tagging performance of the experiment, especially for momenta up to $10\,\text{GeV}/c$.

The baseline PID system will consist of the two existing RICH detectors, to be augmented by a novel detector based on time-of-flight to identify low momentum particles. As for the current detector, the key momentum range is from $p \sim 2\,\text{GeV}/c$ up to $\sim 100\,\text{GeV}/c$ [13]. The upstream RICH-1 detector, shown in Fig. 7.1 (left), currently has aerogel and C_4F_{10} gas radiators, covering momenta from ~ 2 to $10\,\text{GeV}/c$ and ~ 10 to $60\,\text{GeV}/c$, respectively. The downstream RICH-2 detector, shown in Fig. 7.1 (right), has a CF_4 gas radiator and covers

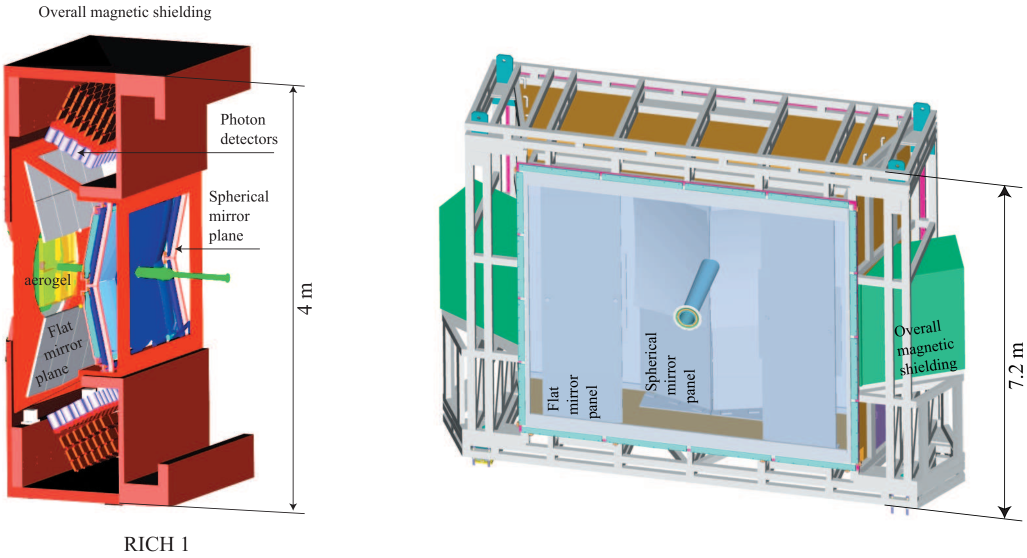

Figure 7.1: Schematic layout of the (left) RICH-1 and (right) RICH-2 detectors.

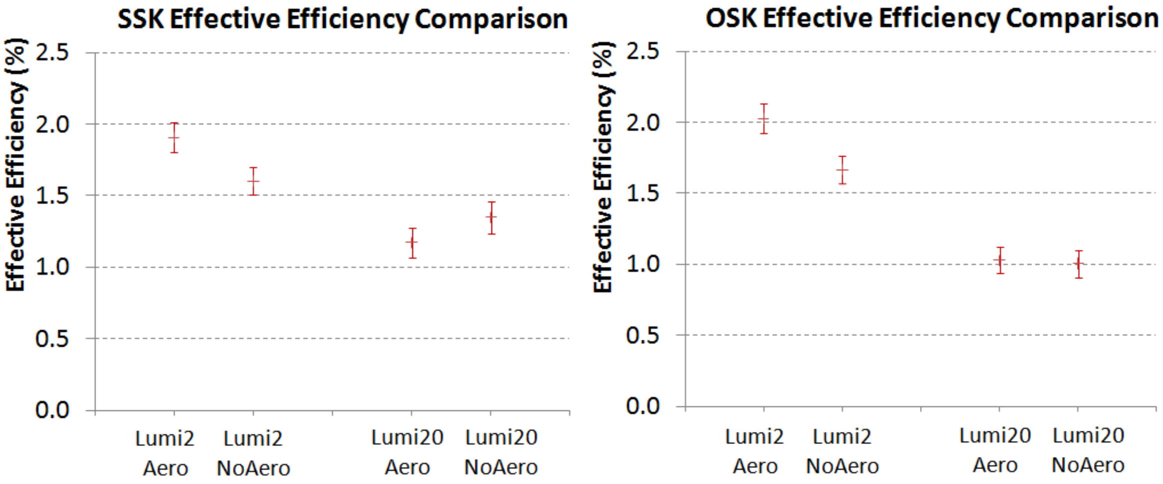

Figure 7.2: The SSK and OSK tagging powers in $B_s \rightarrow \phi\phi$ events, with and without aerogel. Lumi2 and Lumi20 represent the LHCb luminosities of $2\times10^{32}\,\mathrm{cm}^{-2}\mathrm{s}^{-1}$ (current LHCb) and $2\times10^{33}\,\mathrm{cm}^{-2}\mathrm{s}^{-1}$, respectively.

momenta up to $\sim 100\,\mathrm{GeV}/c$.

The philosophy adopted has been to re-use as much as possible all existing RICH mechanical and optical components. The current RICH system employs custom-built photon detectors, the Pixel HPDs [192], which operate very successfully. However these cannot be re-used in the upgraded RICH detector since the HPD readout electronics are limited to a 1 MHz event readout rate, incompatible with the upgrade rate of 40 MHz. The fact that the HPD readout chip is integrated within the vacuum envelope of the HPD tube therefore precludes simply replacing the chip and retaining the photon detectors. It is therefore proposed to replace the HPDs with multi-anode photomultipliers (MaPMTs) with external 40 MHz readout electronics. The upgrade of the existing RICH detectors will be described in Section 7.1.

From simulation studies it has been concluded that the low photon yield of the aerogel radiator (a mean of 5.5 photons per saturated track [13]), coupled with the increased background at high luminosity, will be inadequate in the harsh environment of the LHCb upgrade. This would compromise the crucial low-momentum PID, for which the key physics performance indicators are the same-side kaon (SSK) and opposite-side kaon (OSK) tagging powers in $B_s \rightarrow \phi\phi$ events. The contribution to the tagging performance with and without aerogel is shown for SSK and OSK taggers in Fig. 7.2. Two luminosities are shown, $2 \times 10^{32}\mathrm{cm}^{-2}\mathrm{s}^{-1}$ (current LHCb) and $2 \times 10^{33}\mathrm{cm}^{-2}\mathrm{s}^{-1}$ (twice the planned luminosity of the upgraded detector). It can be seen that the presence of aerogel does not improve the tagging performance at high luminosity, nor does it have the necessary robustness. The low-momentum PID efficiency, and robustness at this higher luminosity, can be restored with a time-of-flight system discussed below.

In the current detector, the aerogel is located in the middle of the tracking system, and its removal will reduce the material budget by about 5% of a radiation length. In addition, the aerogel gives much larger rings than the gas radiator of RICH-1, so about half of the photodetector area of RICH-1 is currently devoted to the aerogel. The area to be covered by the upgraded photodetectors of RICH-1 will therefore also be significantly reduced.

In the upgraded detector, it is proposed to remove the aerogel from RICH-1, and instead

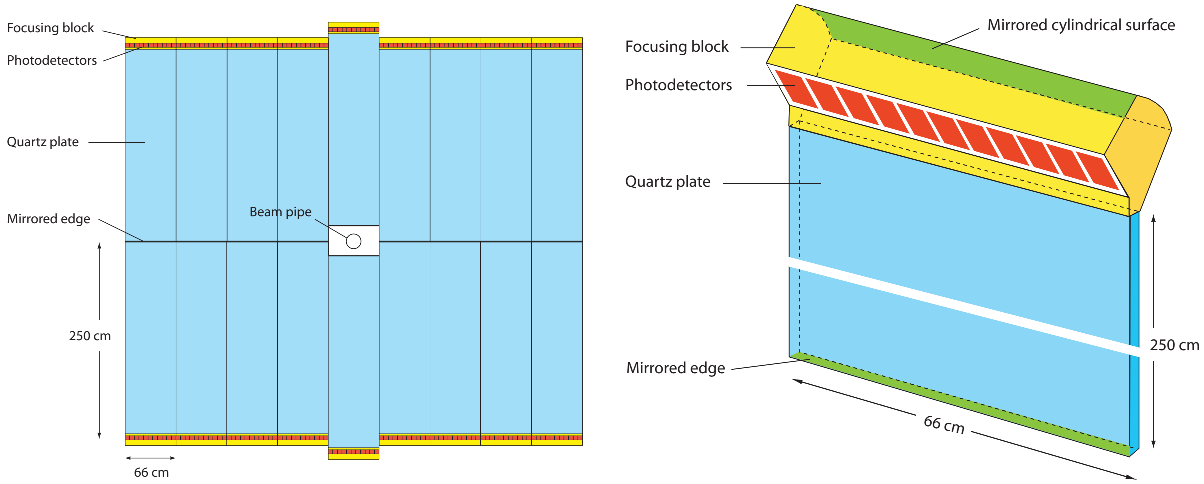

Figure 7.3: Schematic layout of the TORCH detector, showing the front view of the 18 identical modules, and an isometric view of a single module.

use a system based on time-of-flight to cover the low momentum range below $\sim 10\,\mathrm{GeV}/c$ (i.e. below the kaon threshold in the $\mathrm{C_4F_{10}}$ gas radiator). Three sigma K/π separation and positive proton separation up to $10\,\mathrm{GeV}/c$ requires a time-of-flight resolution of about 15 ps per track, at a distance of ~ 10 m from the interaction region. The proposed detector combines time-of-flight and RICH detection techniques, and is named the TORCH [193]. It relies on the detection of Cherenkov photons from a 1 cm-thick plane of quartz, illustrated in Fig. 7.3, to measure the time-of-flight of tracks. The photons propagate by total internal reflection to the edge of the plane, in a manner similar to a DIRC detector [194]. They are then focused onto an array of Micro-Channel Plate photon detectors (MCPs) at the periphery of the TORCH detector. The time-of-propagation of the photons in the quartz plate also depends on the particle type that produced them, as different velocity particles give a different Cherenkov angle and therefore a different path length. This effect is coherent with the time-of-flight difference, and enhances the separation power. The goal of achieving a time resolution of 15 ps per track, together with the expected number of detected photons per track of around 30, dictates a 70 ps resolution in the single-photon time measurement. This detector will be described in Section 7.2.

Figure 7.4 shows the calculated performance of the different components of the PID system, for isolated tracks, in terms of the significance (in number of Gaussian sigmas) for K/π separation as a function of momentum. Excellent particle identification can in principle be achieved over the full momentum range of interest. The actual performance that will be obtained depends on the background and pattern recognition, and a preliminary simulation study has been performed. Identification efficiencies and misidentification fractions will be discussed in Section 7.3.

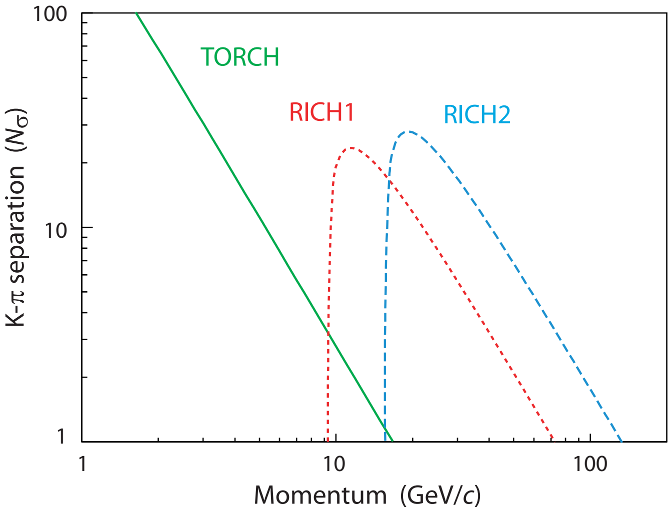

Figure 7.4: Calculated performance (in sigma separation) of the different components of the PID system versus momentum, for isolated tracks. The assumed resolutions per photon and photon yields per track are (70 ps, 1.6 mrad, 0.7 mrad) and (30, 16, 12) for (TORCH, RICH-1, RICH-2) respectively.

7.1 The RICH system

7.1.1 Design considerations

The current RICH system deploys Pixel Hybrid Photon Detectors (HPDs) to detect and reconstruct the Cherenkov rings [13, 192]. A total of 484 HPDs cover the ~ 3.3 m^2 total photon detection area and, with 32×32 channels per HPD, give an effective granularity of $2.5 \times 2.5\,\mathrm{mm}^2$ at the photocathode surface. With the current RICH-1 granularity, the contribution in C_4F_{10} to the Cherenkov angle resolution from the HPD pixellization is approximately equal to those contributions from the photon emission point error and chromatic dispersion. Since the HPDs must be replaced, we must use a photon detector to match at least the granularity of the current HPD. A photon detector to meet these requirements is the Multi-Anode Photomultiplier tube (MaPMT).

An important design consideration is that the superstructures of both the current RICH detectors, shown in Fig. 7.1, are to be retained in the LHCb upgrade. However, since the MaPMT photon detectors have a very different geometry to the current HPDs, the photon-detector mounting frames to house the MaPMTs and their local magnetic shielding will need to be re-designed, with the modularity and pitches of the mounts important factors. Cooling schemes and service routing of cables will also be re-modelled. The R&D work will culminate in prototype mounting frames that will later be used in a test-beam to demonstrate the performance of the MaPMT modules. Most of the current heavy installation equipment can also be re-used.

We expect that the optical system of both RICH detectors can largely be re-used. However, the geometrical size of the current RICH-1 photon detector plane is dictated by the need to accommodate aerogel rings. In the absence of aerogel, the size of the photon-detector plane, and the hence number of MaPMTs, can in principle be significantly reduced. Nevertheless, it will be investigated with the simulation whether the RICH-1 granularity and multi-hit capabilities are improved by increasing the size of C_4F_{10} rings with a new focusing system. If this proves to be advantageous, we will re-establish our liaison with industrial contacts in carbon-fibre and glass mirror structures to decide the best optical design in terms of compactness, material structure, and cost effectiveness.

7.1.2 Photodetector and readout

The baseline photon detector for the upgraded RICH is the MaPMT. The RICH group has wide experience with the R7600 generation of Hamamatsu MaPMTs [195, 196]. The R7600 is a 64-channel (8×8) pixel device of active area $18.1 \times 18.1\,\mathrm{mm}^2$, a pixel size of approximately $2 \times 2\,\mathrm{mm}^2$, and a pixel pitch of 2.3 mm. The border of the R7600 is $25.7 \times 25.7\,\mathrm{mm}^2$, hence the device suffers from a poor active-area fraction of $\sim 50\%$. However all other properties serve well the requirements of the LHCb RICH.

A new generation of R7600, the Hamamatsu R8900, is currently available as a 16-channel (4×4) pixel device, but not yet as a 64-channel device that would be required for the RICH. In a similar housing of size $26.2 \times 26.2\,\mathrm{mm}^2$, it features a slimmer mounting of the window which allows the active area to increase to $23.5 \times 23.5\,\mathrm{mm}^2$, giving a fractional cover of 80%. Another new generation of the metal-channel product line, the R11265, is under development at Hamamatsu (expected around spring 2011). It uses the same housing as the R7600 and the slimmer window mount, and features a higher photoelectron capture efficiency than the R8900. In a prototype the active area is reported to be $23 \times 23\,\mathrm{mm}^2$ giving a 80% fractional coverage, while the pixel pitch increases to 2.9 mm.

Given that the MaPMT square cross-sectional geometry allows close packing of approximately 90%, we estimate that 1152 units of R7600/R11265 would be required to equip RICH-1 (increased by about 45% if the aerogel is present) and 2560 R7600/R11265 to equip RICH-2. This gives approximately 238k readout channels in total. Due to its improved active-area coverage, the photon-detector baseline is the R11265 series of MaPMT, with the R7600 as backup. However in the latter case, lenses would need to be employed to improve the effective active area.

The R7600 has been characterized in the laboratory [197], and a summary of the results are shown in Fig. 7.5. Excellent single-photon response is observed, however a channel-to-channel variation in gain up to a factor of two is measured. We plan to correct for this effect on a channel-by-channel basis in the front-end electronics readout. It can also be seen that the cross-talk characteristics are excellent, at a negligible level below 1%. The MaPMT response to longitudinal and transverse magnetic fields is shown in Fig. 7.6, as measured inside a Helmholtz coil and a solenoid. This shows reductions of gain up to $\sim 10\%$ for longitudinal fields up to 50 gauss. (Note that maximum longitudinal fields of 25 gauss are expected in RICH-1, provided local magnetic shielding is incorporated.) These tests will be repeated when the new generation of R11265 tubes becomes available. Considering the increase in overall active-area coverage, the sensitivity to magnetic field for pixels at the periphery of the anode will also be studied. In addition, long-term measurements have started to study possible ageing effects on those tubes, at rates expected at their maximum occupancies. To limit ageing effects, the supply voltage to the MaPMT is minimized.

We have also tested the H9500 flat-panel 16×16 pixel MaPMT from Hamamatsu [198]. This device has an active area of $49 \times 49\,\mathrm{mm}^2$ and a border of $52 \times 52\,\mathrm{mm}^2$, which gives about a

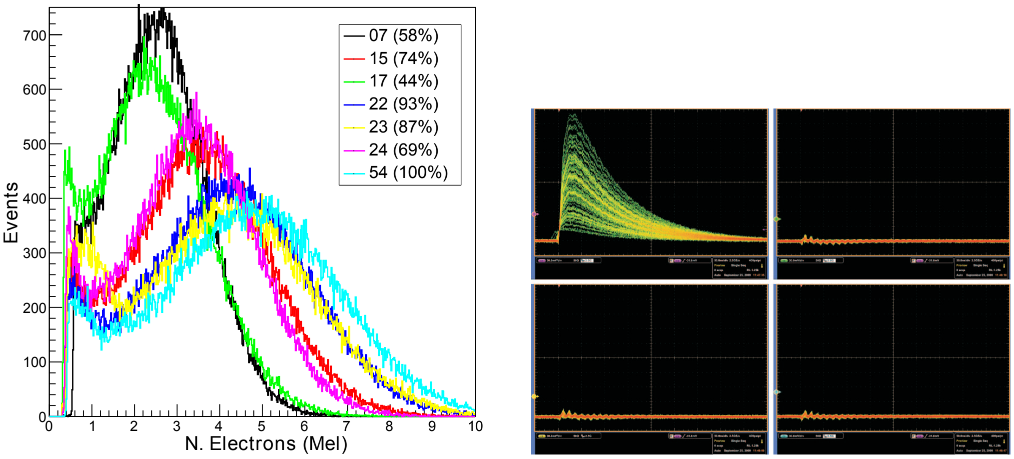

Figure 7.5: Preliminary measurements of R7600 properties: (Left) response to single photons in a central pixel demonstrating a significant channel-to channel gain variation, (Right) cross-talk response on adjacent channels compared to the central pixel which has the photon hit.

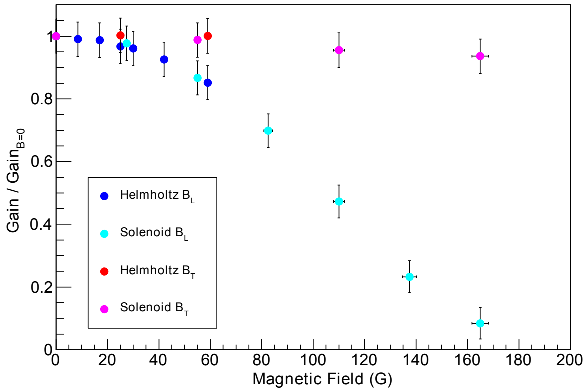

Figure 7.6: Response of the MaPMT gain to longitudinal and transverse magnetic fields.

90% active region (the pixel pitch is about 3.05 mm). In the tests we observed a small number of electrons generated at the first dynode from a single photon. This leads to cross-talk observable in around 10% of signals. Also the H9500 has significantly poorer response to single photon signals than the R7600, and suffers from increased dark counts. Since we are not reliant on the compact nature of the H9500 in the longitudinal dimension, we believe the R7600 is the better option for the LHCb RICH detectors.

The MaPMT readout must conform to the upgraded 40 MHz LHCb electronics architecture. The front-end chip will be an ASIC and must provide the shaping and amplification as well as discrimination and digitisation. We have chosen binary readout as baseline, which is the cheapest option and minimizes the off-detector data throughput. The binary choice requires the ability to adjust channel-to-channel gain variations of the MaPMTs prior to discrimination on the front-end ASIC. It is advantageous that the readout provides baseline recovery of the signal ideally within 25 ns, in order to suppress signal spill-over (which can give dead-time into adjacent bunches for binary readout). With these criteria in mind, we are proceeding with the front-end electronics R&D on two fronts: we have started development of a custom front-end

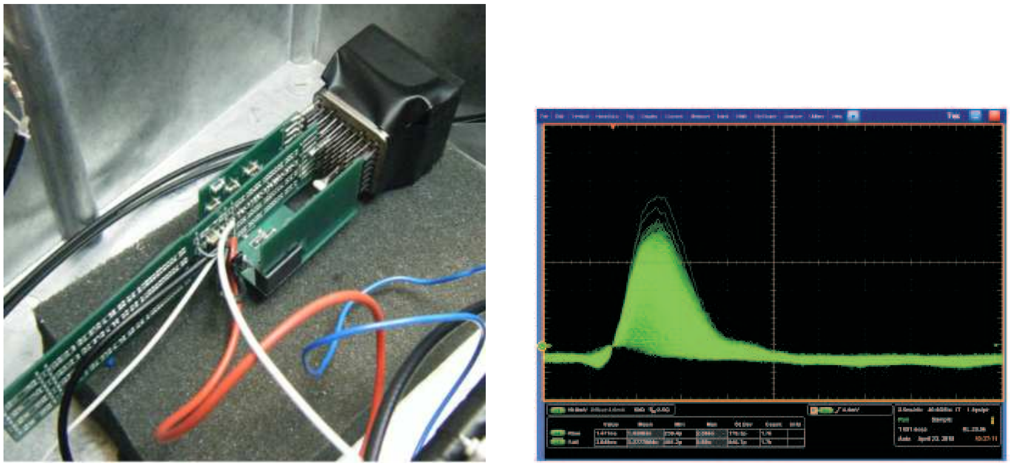

Figure 7.7: (a) Photograph of a discrete-component prototype mounted on the R7600, (b) oscilloscope trace showing the performance in response to single photons (the horizontal scale is 2.5 ns/div, the vertical scale is 10 mV/div).

electronics readout chip, and we are investigating a currently-available chip for its suitability, the Maroc-3 [199].

We are currently designing a customized readout chain which is tailored for the R7600 or R11265, comprised of an analogue pulse shaper amplifier and a binary discriminator. A prototype with discrete components has been fabricated with commercial transistors in Silicon-Germanium (SiGe) Heterojunction technology [200]. Four channels per side have been placed on each board, which then read out a line of eight channels on the R7600. This scheme allows several MaPMTs to be placed side by side. A photograph of the board mounted on the R7600 is shown in Fig. 7.7(a). The prototype has been tested with single photons sent to an MaPMT pixel via a commercial blue LED and from Cherenkov photons from a PbF_2 crystal. Very good performance is demonstrated, shown in Fig. 7.7(b). The peak amplitudes are about 50 mV with rise-times of 1.4 ns. The fall-times of the pulses are set to about 3 ns and thus the baseline is restored well before 25 ns, thus eliminating possible spill-over/dead-time effects at the LHC event rate. The total power dissipation for the analogue section of the front-end is measured to be 3 mW.

Furthermore, we have performed SPICE simulations of an MaPMT front-end ASIC chip, fabricated in SiGe 0.35μm-CMOS technology, and based on the discrete-component prototype. These simulations indicate that a 300 ps rise-time, 3 ns $(1/e)$ fall-time at 0.3 mW per channel power dissipation, and 1500 electron noise RMS should be achievable for the preamplifier. The discriminator has been also designed showing about 500 ps transition time when loaded with a few pF at its output. Power dissipation per channel is expected to be close to 1 mW. The layout of a prototype 4-channel chip is under development and we expect a customized chip to be available on the timescale of late 2011.

As a parallel activity, we will evaluate the new 40 MHz Maroc-3 readout chip, developed by the OMEGA Collaboration specifically for MaPMTs. We will investigate whether this chip, or a variation of it, suits the LHCb RICH requirements. In the present version, the Maroc-3 has a 25 ns fast-signal shaping time, and its power dissipation is 3.5 mW per channel. Simulations will be made to investigate whether such a shaping time is compliant with the expected maximum occupancy and whether spill-over/dead-time effects are tolerable.

Both the customized ASIC and the Maroc-3 developments will contain only the analogue sections of the readout: the amplifier, the discriminator and slow-control logic. The rest of the decision logic will be implemented in a separate commercial Field-Programmable Gate Arrays (FPGAs) assuming they are proven to resist the radiation environment. As a consequence, this latter part of the readout sequence will be independent of the front-end chip chosen.

As well as developing MaPMT readout, we are closely following alternative technologies. One such technology is based on standard HPDs but with external readout electronics. This has the advantage of decoupling photon detector from electronics developments [201]. The overall design of the tube would be similar to the current HPDs equipping the RICH detectors, allowing to keep a significant fraction of the existing photon detector infrastructure. The output signal from the preamplifier would be subsequently fed to a discriminator and processed through back-end electronics similar to what is required for the MaPMTs. The key challenge is to maintain an acceptable signal-to-noise ratio in this configuration. A second alternative technology is a novel hybrid MCP with a Medipix/Timepix readout chip, developed at CERN, and based on an original development at Berkeley [202]. An on-going collaboration with the Burle-Photonis company [203] will encapsulate the Timepix chips into vacuum tubes. The major advantage of this photon detector technology would be its readout synergy with the VELO group. At present we are tracking developments, and hope to compare the properties of HPD and MCP devices to those of the MaPMT, once the former photon detectors become available.

7.1.3 R&D plans

An R&D programme is underway to evaluate RICH technologies for the LHCb upgrade. The next-generation R11265 MaPMT will be studied in the laboratory and compared to the R7600. The electronics readout and photon-detector mechanical mounting will be designed. The required time for baseline recovery of the front-end readout will be critical in the design-choice of the front-end, and will be assessed in simulation.

Following further laboratory characterisation, an array of R7600 MaPMTs will be tested in a prototype RICH detector in a CERN test-beam. The RICH gas enclosure and optical system for the demonstrator already exists, and this will be equipped with a column containing photon detectors, and the ancillary electronics. The beam components: telescope, trigger etc, will be assembled from existing infrastructure. In the first phase, the current LHCb DAQ system will be adapted; we will first configure existing LHCb TELL1 boards for readout with the Maroc-3 chip, together with standard LHCb ODIN boards. This will then be compared with the front-end fabricated in discrete components. In the second phase, the DAQ system for the test-beam will conform to the new LHCb readout architecture, which will follow a common LHCb-wide protocol. This is also the phase where the prototype ASICs for full 40 MHz data transmission will be used in the RICH detector. Key measurements will include photon counting and Cherenkov angle resolution.

Work will be started to design and prototype an upgraded front-end DAQ-interface (to replace the “Level-0” board in the current RICH) which will be based on FPGA technology, and to investigate possible compatibility between MaPMT and MCP (TORCH) applications. We will use the new generation of radiation hard Giga-bit optical link (GBT) chipset and rad-hard FPGAs necessary to format and (possibly) zero-suppress data, and interface with the

GBT optical readout. Once the data have been transmitted off-detector, the RICH DAQ will be provided via TELL40 boards.

In parallel to the test-beam and read-out developments, simulation studies will continue to further optimize the PID performance. Performance metrics will include RICH efficiency and purity, low momentum PID response, flavour tagging performance, and the ability to cope with high occupancy.

7.2 The TORCH detector

7.2.1 Detector operation and layout

The TORCH is a novel detector which uses Cherenkov photons from a 1 cm-thick plane of quartz to measure the time-of-flight of tracks. The thickness of the plate is a compromise between photon yield, the contribution to the resolution from the uncertainty on the photon emission point, the cost in terms of quartz volume, and the material budget ($\sim 8\%\ X_0$ for 1 cm of quartz). The overall detector thickness, including photodetectors, is only about 15 cm, so it should be easy to integrate into the existing LHCb spectrometer. The initial choice of position was at $z = 13\,\mathrm{m}$, taking the place currently occupied by the M1 station which will be removed in the upgrade (see Fig. 1.6). The final position of TORCH will be determined by optimising performance against cost, and could well be moved upstream to $z = 9.5\,\mathrm{m}$, i.e. just in front of RICH-2 (but still after the tracking system).

Quartz is used because it is optically dense to maximise the photon yield, is radiation hard, has high transmission length, and can be polished to maintain very accurate optics to preserve total internal reflection and angular precision. However, the chromatic dispersion of quartz is large, hence we must measure not only the time-of-flight, but also correct for the spread of photon speed due to the variation of refractive index with photon wavelength. This is achieved by focusing the photons onto pixellated photodetectors, allowing the angle of the photon to be measured accurately, and when combined with the known track direction the Cherenkov emission angle can then be determined. The wavelength of the photon is effectively determined from this information, allowing the dispersion to be corrected for. This concept is closely related to other ongoing R&D projects for future PID detectors, the TOP detector for Belle II [204] and the endcap DIRC for PANDA [205], which similarly rely on the recent development of fast photodetectors. The distinction of the TORCH approach is the focus on time-of-flight rather than time-of-propagation, and the performance at higher momenta.

The initial TORCH simulations assumed a full plane of quartz covering the spectrometer acceptance, apart from a small cut-out around the beam pipe. This was used for the simulation studies of performance reported below. However, to move towards a more realistic detector design, a modular arrangement has been introduced as shown in Fig. 7.3, which will be discussed below. The conceptual design for reconstructing the photon paths is illustrated in Fig. 7.8: the angle of the photon within the plane of the quartz plate, θ_x, is determined from knowledge of the emission point on the track and the detection point at the photodetector, as in (a). The angle perpendicular to the plane, θ_z, shown in (b), is determined by focusing the photons onto the pixellated photodetectors using the optical element shown in Fig. 7.9 (left) at the edge of the plate. This relies on the fact that the photon angle is unchanged as it reflects off the two faces while travelling across the plane, via total internal reflection.

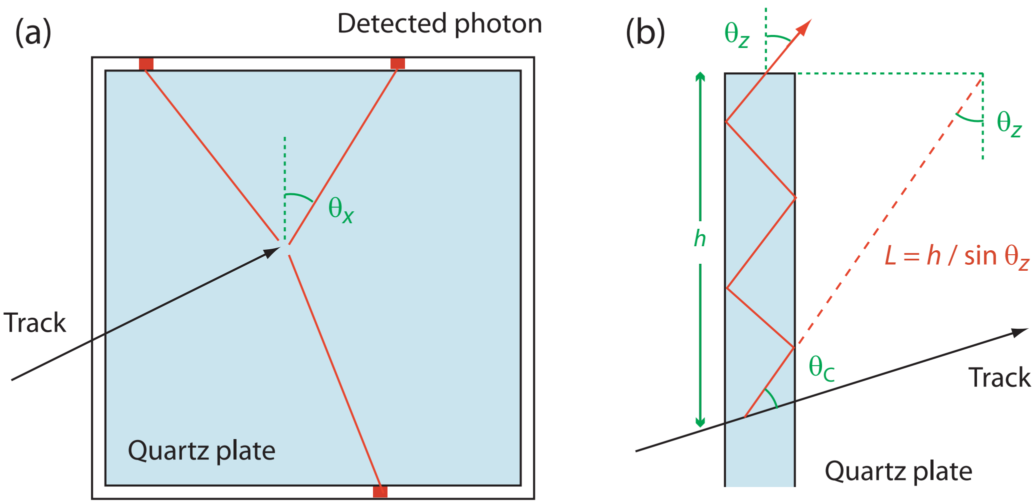

Figure 7.8: Schematic to illustrate the concept of the reconstruction of photon trajectories (a) in the transverse (x, y) projection, where the filled squares indicate detected photon hits, (b) in the (y, z) projection.

Both angles need to be determined with a precision of about 1 mrad, in order to reconstruct the photon propagation time with a precision of about 50 ps. This angular precision can be easily achieved in θ_x with coarse pixellization of $\sim$ 1 cm pitch, due to the long lever arm. In the other projection the pixel size needs to be finer by a factor of 10 or more. The total resolution on the photon propagation time includes contributions both from the uncertainty on the trajectory coming from the finite pixel size, and from the intrinsic time resolution of the photodetector. We assume that Micro-Channel Plates (MCPs) are used. MCPs with a 10 μm pore size (i.e. the diameter of the microchannel) have been demonstrated to provide a resolution of 30 ps for single photons [206]. To develop the design of the detector we have taken the parameters of an existing commercially-available MCP, as illustrated in Fig. 7.10, but adjusting the anode pixel size to suit our application.

Our aim is to measure the time-of-flight of individual photons to within $\sim$ 70 ps. Given around 30 detected photons per track, the arrival time of the particle at the TORCH can be determined to an estimated precision of 10–15 ps. The production time of the particle (t_0) can be precisely determined from the combination of times measured by TORCH from the other particles produced at the same vertex in the interaction, as discussed below.

Being a new detector, significant R&D is clearly required to demonstrate the feasibility of the TORCH concept. Whereas the upgraded RICH system is required to be ready at the start of operation of the upgraded experiment, the TORCH could in principle be added at a later stage.

7.2.2 Pattern recognition

Following the approach outlined above, the reconstruction is relatively straightforward: we measure the arrival time and position of a photon on the photodetector plane, infer θ_z, and calculate its trajectory assuming it was emitted by the track at the midpoint in z of its path through the quartz plate. Given measurements of the track path and momentum from the

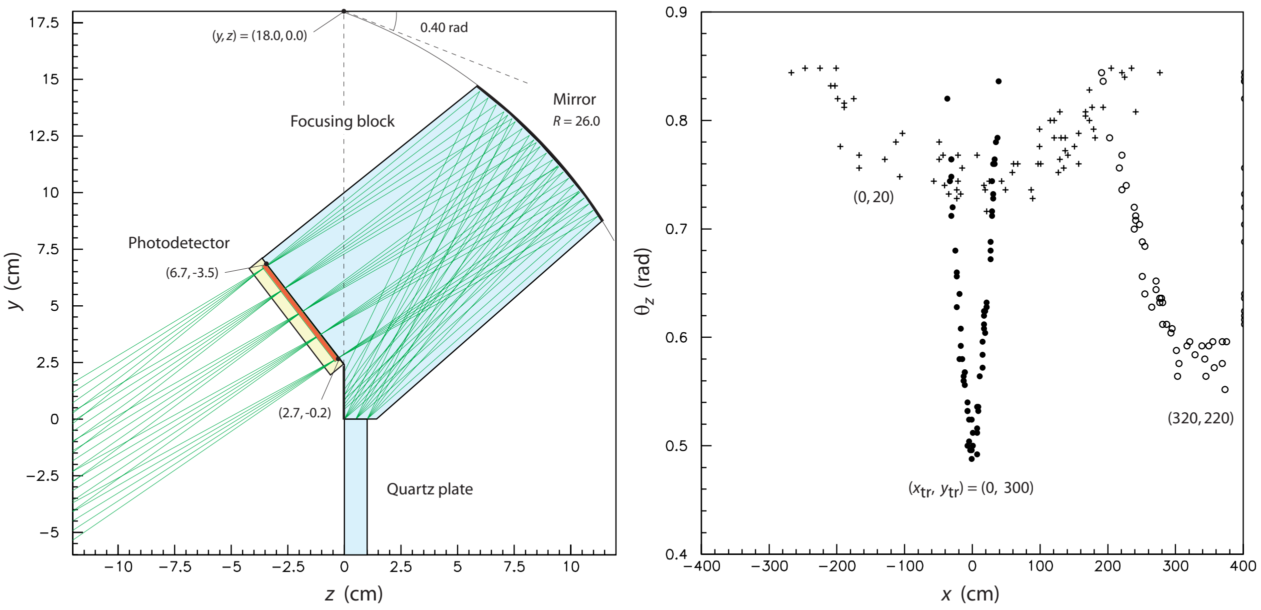

Figure 7.9: (Left) Cross-section through the focusing element, attached to the edge of the quartz plate. The focusing of photons is indicated for five illustrative angles between 450 and 850 mrad, emerging at different points across the edge of the plate. (Right) Event display of detected photons from simulated tracks passing through the TORCH detector, showing their angle θ_z at the edge of the plate versus their position along one edge of the plate. Different symbols are used for the photons from three tracks, hitting the plate at different positions.

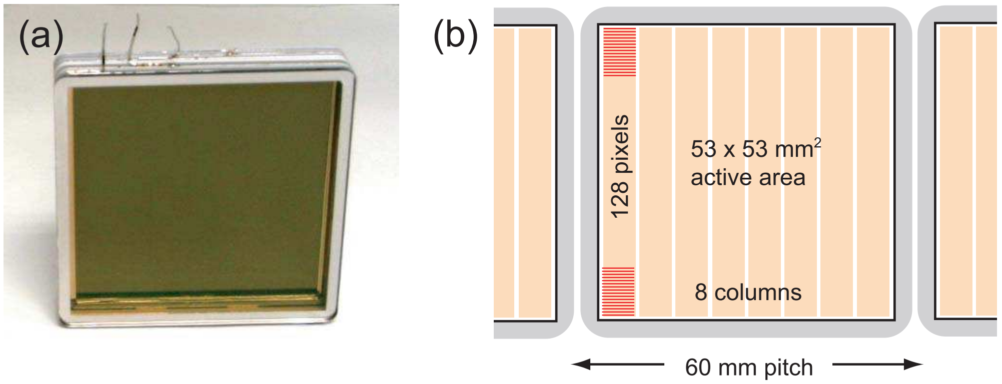

Figure 7.10: (a) Photograph of the Planacon XP85022 MCP from Burle-Photonis, which has 32×32 square pixels. (b) Schematic of the photodetector layout for TORCH, with Planacon-sized MCPs placed side-by-side, with pixellization adjusted to be fine in one direction and coarse in the other.

tracking system and knowledge of the optical properties of quartz, this is sufficient information to extract the mass from the time difference between the track leaving the primary vertex (PV) and the photon being detected. There are two principal challenges: first, association of photons to tracks (pattern recognition) and second, determining the time when the track left the PV.

In the environment of the upgraded LHCb luminosity, there will be $\mathcal{O}(100)$ fully reconstructed tracks plus a large number of secondaries passing through the TORCH in an event.

However, most photon-track pairs can be rejected as unphysical. We take advantage of the limited range of photon wavelengths to which the photodetector is sensitive and reject candidates outside this range. This is equivalent to a restriction on θ_C: for our geometry, this means that relevant photons lie along arcs on the photodetector plane, as shown in Fig. 7.9 (right). Additionally, we can ignore photon-track pairs with unphysical timing. Instead of attempting to measure the mass of the particle directly, we assume (e, μ, π, K, p) hypotheses and test for consistency with each in turn. Background photons whose timing is not consistent with these masses can be ignored.

The "start time" of the track must also be determined. We take advantage of the high pion multiplicity and use other tracks from the same event primary vertex to fix the relative timing. The same reconstruction procedure described above is used except that the last step is inverted: for each track from the event primary vertex, we assume the pion mass and deduce the total time elapsed (time-of-flight of the track plus time-of-propagation of the photon). Subtracting this from the measured photon detection time gives a per-photon estimate of the track start time. For a primary vertex with N_π fully reconstructed pion tracks, the start time resolution is smaller than the per-track time resolution by roughly $\sqrt{N_\pi}$.

This simulation has used the simple conceptual design of a single plane of quartz. In practice the plane would need to be constructed from smaller plates, and a first design of a modular layout has been made, as was shown in Fig. 7.3. In this case the additional reflection of photons off the lower edge and sides of each module will lead to extra ambiguities in the reconstruction, but that is balanced by the much lower number of tracks traversing each module, and the excellent performance is expected to be maintained. Detailed simulation of this modular layout is in progress.

7.2.3 Photodetector and readout

An MCP photon detector potentially suitable for the TORCH detector is the Burle-Photonis XP85022. This is a 59 mm square unit with $\sim 80\%$ active coverage. There are 32×32 pixels/unit, each 1.6 mm square in the commercial version. The channel gain-uniformity of the XP85022 is excellent ~1:1.5 and it is robust against magnetic fields (~1 T). Another great advantage, in contrast to the MaPMT, is that the anode pixel layout can in principle be designed as required. The current plans for the granularity of the TORCH is 128×8 (the customization of granularity will involve collaboration with industry). We are currently exploring a modular design for the TORCH as in Fig. 7.3, with 18 identical modules and 11 Planacon-sized MCPs per module. This gives a total of 198 MCP units.

R&D is in progress to test the suitability of the MCP to meet the TORCH requirements. We have acquired a pair of 64 channel 8×8 XP85012-A1's to test in the laboratory using commercially-available single-channel electronics. The pore size of the XP85012-A1 is 25 micron, which is the size readily available commercially at an affordable cost. The timing properties of a single tube are currently under investigation with a pulsed blue (400 nm) laser from PiLas, which has a $\sim$ 20 ps resolution, and set up to emit single photons. The laser and MCP are used to start/stop a fast NIM-based ORTEC time-to-amplitude converter. The laboratory set-up is shown in Fig. 7.11(left). First results from the laboratory tests are shown in Fig. 7.11(right). An excellent timing resolution of 46 ps is achieved.

We are actively investigating MCP readout. A potentially suitable front-end chip has al-

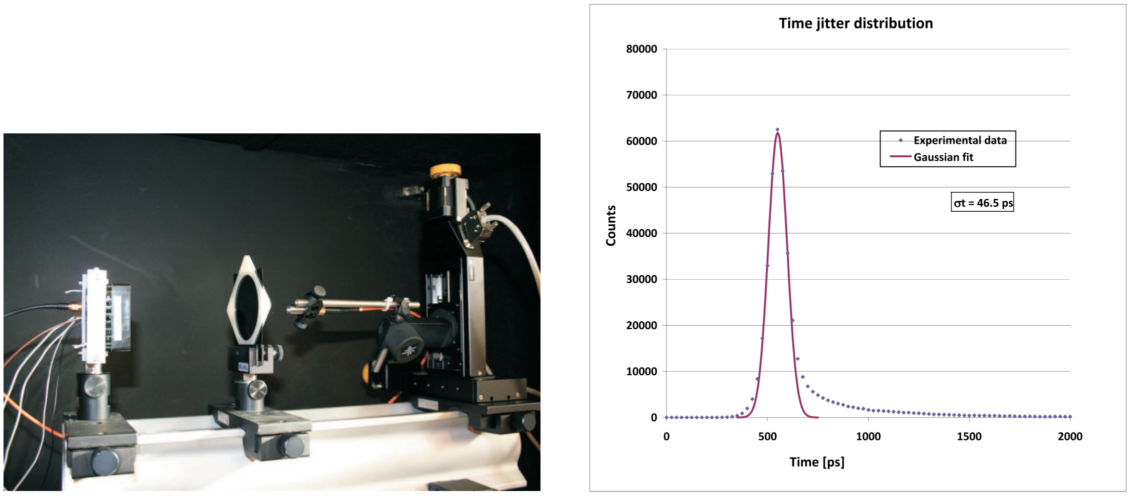

Figure 7.11: (Left) A photograph of the laboratory test set-up to study the timing properties of the XP85012-A1 MCP, (Right) the MCP timing distribution measured with a blue laser operating in single photo-electron mode, demonstrating a 46 ps resolution when fitted with a simple Gaussian.

ready been developed for the ALICE TOF system. The NINO and HPTDC chip-sets [209], produced at CERN, have been used to measure time-of-flights down to a resolution of 30 ps by independent researchers in space/medical applications [210]. Current NINO chips have 8 channels, however 32-channel versions have also been tested, possibly progressing to 64 channels in the next iteration. To provide proof-of-principle verification of the MCP readout, we have fabricated a multi-layer PCB test board incorporating eight NINO/HPTDC chips. A photograph of the readout card coupled to an MCP is shown in Fig. 7.12. This NINO/HPTDC system will be available in the coming weeks and will first be used to read out the pair of XP85012-A1 MCPs in the laboratory.

As a parallel electronics development, we will maintain synergies with the RICH front-end electronics. As explained above, SPICE simulations show that rise-times of 300 ps with 5 ps RMS jitter can be achieved with the new RICH readout chip currently being developed in SiGe 0.35μm-CMOS technology, making it potentially compatible with TORCH MCP requirements.

7.2.4 R&D plans

The verification of the TORCH operation will be achieved in a number of stages. After proof of principle of the 8×8 MCP timing properties in the laboratory, a test rig will be fabricated for test-beam operation. A quartz bar will be coupled to a machined plastic or quartz focusing element, read out by a single MCP with the NINO/HPTDC front-end in the first instance. A second MCP will be used to provide the beam timing. TELL1 boards will be configured for analogue and digital-time readout, together with standard LHCb ODIN boards for DAQ. Precise timing measurements of the demonstrator TORCH will be taken as a function of beam energy and angle of incidence in the quartz. Key measurements will include measurement of photon energies using the dispersion relationship of quartz, and verifying the time-of-flight resolution. Possible instrumental effects such as angular aberration, cross-talk, and noise will also be verified.

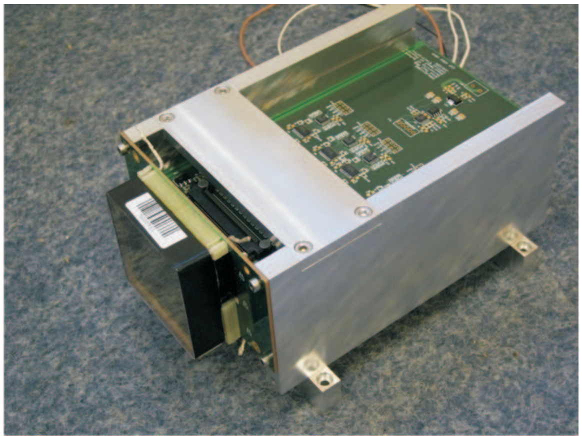

Figure 7.12: A photograph of the NINO/HPTDC readout card coupled to 8×8 Burle-Photonis XP85012-A1.

Customisation of MCPs to an 8×128 pixellization will involve collaboration with industry. Possible industrial partners are Photek (UK) [207], Burle-Photonis (France) [203], and Hamamatsu (Japan) [211]. An investigation on the MCP pore size will be made; 25 micron is currently commercially available, however 10 micron would improve the timing resolution and magnetic field response. It is also essential to ensure good lifetime for the tubes, which has been an issue with MCPs in the past [208], and which depends on the working point chosen for the gain of the tubes. This R&D work will culminate in a sample of prototype tubes for qualification.

For the 1024-channel MCP, a single device would need sixteen 64-channel NINO chips, and this modularity would need to be studied, and possibly improved, for the LHCb upgrade. Hence, we will work with the developers of the NINO chip-set and the RICH electronics group to optimise the overall modularity. Any fabrication of a new MCP readout chip would also invoke a 2-year programme.

The DAQ interface for the TORCH will be developed in conjunction with the RICH. For this, the TORCH will also implement an FPGA, the new generation of radiation hard Giga-bit optical link (GBT) chipset, FPGAs for data suppression, and off-detector TELL40 boards.

Finally, an intensive R&D programme will focus on the TORCH modularity. The quartz thickness is a crucial parameter, and the compromise will be between good photon yield, minimizing the uncertainty on the position of the photon emission, and overall mechanical stability. The ability to polish the quartz surface over a large area, in order to maintain less than a 1 mrad uncertainty after multiple internal reflections will also be investigated in collaboration with industry. The mechanical mounting of the quartz will be crucial, as well as its coupling to the focussing block. The mechanical prototyping will be a multi-stage process, finally culminating in a full-scale module, focussing block and MCPs to demonstrate the timing resolution and photon count.

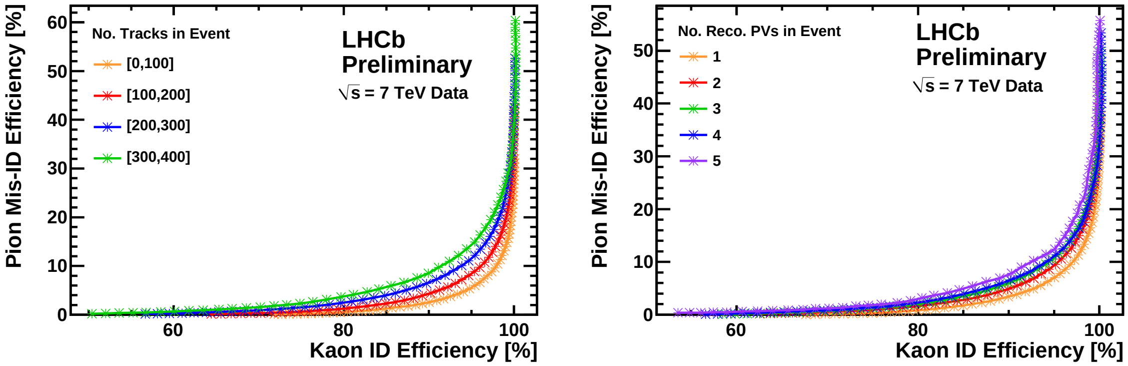

Figure 7.13: The pion misidentification fraction versus the kaon identification efficiency for the RICH gas radiators as measured in 7 TeV LHC collision data: (left) as a function of track multiplicity, and (right) as a function of the number of primary vertices).

7.3 Expected performance of the PID system

The performance of the upgraded PID system has been studied, both in 7 TeV LHC collision data and in Monte Carlo.

We have estimated the performance of the upgraded RICH system by studying the π/K separation as a function of measured track multiplicity and the number of primary vertices, as measured in data. A very pure sample of π's and K's can be extracted in data by using the D^* calibration sample and selecting $D^* \rightarrow D(K\pi)\pi$ decays, with no recourse to particle ID information. Fig. 7.13 shows the pion misidentification fraction versus the kaon identification efficiency as a function of track multiplicity and the number of primary vertices, as the likelihood for the kaon hypothesis is varied. The aerogel photons have been removed from the analysis, hence this is the performance for gas radiators only. Whilst there is clearly some degradation of performance observed at higher track multiplicities, the π/K performance remains extremely robust, giving confidence that the current RICH detectors are suitable for operation at higher luminosities.

The performance of the particle identification using TORCH has been studied using a simple simulation of the detector, coupled to the full simulation of events in the LHCb spectrometer. We compare two luminosities, $2 \times 10^{32}\text{cm}^{-2}\text{s}^{-1}$ and $2 \times 10^{33}\text{cm}^{-2}\text{s}^{-1}$. The efficiencies and misidentification fractions for pions and kaons are shown in Fig. 7.14. Excellent π-K separation is achieved up to 10 GeV/c and beyond, as required. The good performance of the TORCH at high intensity running is also apparent, showing robustness in performance up to $\times 10$ the current LHCb luminosity, i.e. twice that for nominal running of the LHCb upgrade.

Whilst initial data analysis indicates the RICH performance should be robust at higher luminosities, simulation of the new detector geometry must be completed to draw firm conclusions. The current Monte Carlo incorporates HPDs, and therefore the MaPMT geometrical structure must be implemented into the upgraded LHCb Monte Carlo. This work is in progress. The PID performance will be studied as a function of MaPMT granularity and active/dead area fraction, versus luminosity. The contributions to the Cherenkov angle resolution from pixellisation, chromatic error, and photon emission point uncertainty will also be determined. The performance of the SSK and OSK tagging powers in $B_s \rightarrow \phi\phi$ events will be evaluated when

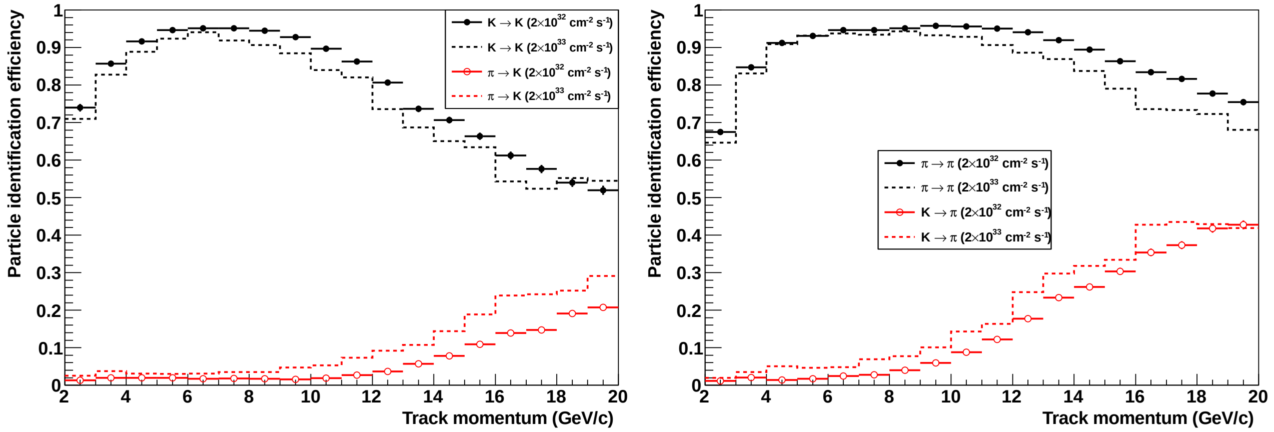

Figure 7.14: Identification efficiency for the subset of well-measured, truth-matched charged tracks in the simulation which are matched to a primary vertex. The plots show the efficiency for a kaon (left) or pion (right) track to be identified correctly (black, upper points) or incorrectly (red, lower points). The ID and mis-ID efficiencies are shown for two different luminosities, $2 \times 10^{32}\,\mathrm{cm}^{-2}\mathrm{s}^{-1}$ (points) and $2 \times 10^{33}\,\mathrm{cm}^{-2}\mathrm{s}^{-1}$ (dotted histograms). Tracks are assigned as pions or kaons depending on which hypothesis maximizes the likelihood, ignoring other mass hypotheses.

adding the TORCH detector.

Optimized photon pattern recognition and ring reconstruction will be vital to maximize the PID performance at the highest luminosities. The necessary software tools for pattern recognition will be developed for the upgraded RICH and TORCH detectors. Finally we will also study the possibilities of a global PID algorithm incorporating both RICH and TORCH.

Chapter 8

Calorimetry

Introduction

The present calorimeter system of LHCb is composed of a Scintillating Pad Detector (SPD), a Preshower (PS), an Electromagnetic Calorimeter (ECAL) and a Hadronic Calorimeter (HCAL). The HCAL is based on the Tilecal technology and contains 1488 cells. It is preceded by the ECAL based on the Shaslik technology and containing 6016 cells. In front of the ECAL, the PS is composed of 6016 tiles matching the geometry of the ECAL. The PS is placed after a lead sheet of 2.5 radiation length and is preceded by another layer of 6016 scintillator tiles, the SPD. The detailed description of the calorimeter system can be found in [212].

The calorimeter system plays a role in photon reconstruction (ECAL), in photon and electron identification (ECAL, PS, SPD), and in the trigger system (HCAL, ECAL, PS, SPD).

For this document we have concentrated the studies on the upgrade of the ECAL and HCAL readout at 40 MHz, since the removal of the SPD and PS is being considered for the upgrade.

- The Low Level Trigger (LLT), foreseen to replace our present L0 trigger, does not require a very strict selection and therefore it can be operated without the PS and SPD.
- It remains to be studied whether the necessary electron and photon identification needed for parts of our upgrade physics program can be achieved without the SPD and PS.

If an upgrade of the SPD and PS is needed, the modifications to the Front-End (FE) cards would be very similar to the modifications of the ECAL/HCAL FE-cards described below.

To minimize the required modifications, it is planned for the upgrade to keep the present ECAL and HCAL calorimeter modules, their photomultipliers (PMT), Cockroft Walton bases (CW) and coaxial cables. However, to keep the same average anode current of the phototubes at the higher luminosity, their high voltage (HV) is reduced and therefore the gain of the amplifier integrator in the Front-End card will be increased. This is described in Section 8.1.

The racks and crates situated at the top of the calorimeter can be kept as they are, however of course the FE-cards have to be modified to allow a read out at 40 MHz. To minimize the number of fibres necessary to read the calorimeters, the ADC information is packed using an algorithm similar to the one presently used in the TELL1 calorimeter cards. The new FE-cards are described in Section 8.2.

The decision to keep the calorimeter modules, their PMTs and CW bases assumes that they can operate with the radiation damage corresponding to the foreseen integrated luminosity. This is discussed in Section 8.3.

Because of the higher luminosity, there will be a higher occupancy in the calorimeter cells. This will cause an increase in calorimeter noise due to statistical fluctuation in these underlying events. While the effect is small for the measurement of high E_T photons it is important in the case of low E_T photons. In Section 8.4 an estimate of this equivalent noise is given.

8.1 ECAL/HCAL electronics upgrade: analogue FE

The analogue signal processing in the present ECAL FE-board [212,13,213] is mostly performed by a shaper ASIC that integrates the PMT pulse, which has been clipped at the PMT base. The PMT is located at the detector; the signal is transmitted through a 12 m 50 Ω coaxial cable to the FE-board located in the crates at the calorimeter platform.

Table 8.1: Summary of the requirements for the calorimeter analogue FE.

Parameter	Requirement
Energy range	$0 \leq E_\mathrm{T} \leq 10\,\mathrm{GeV}$ (ECAL)
Calibration/Resolution	4 fC/2.5 MeV per ADC count
Dynamic range	$4096 - 256 = 3840$ cnts: 12 bits
Noise	$\lesssim 1$ ADC cnt (ENC < 5–6 fC)
Termination	$50 \pm 5\,\Omega$
Baseline shift prevention	Dynamic pedestal subtraction
Max. peak current	4–5 mA over 50 Ω
Spill-over correction	Clipping
Linearity	< 1%
Cross-talk	< 0.5%
Timing	Individual (per channel)

The PMT gain has to be decreased by a factor 5 with respect to the present operation HV in order to keep the same average current after the increase in luminosity[1]. Therefore, this has to be compensated in the electronics and the preamplifier input equivalent noise must be decreased accordingly.

The noise after integration and pedestal subtraction should be at the level of 1 ADC count approximately, corresponding to an input charge of 4 fC RMS (compared to 20 fC in the present system). Detailed noise analysis shows that the total input referred noise voltage of the Front-End should be smaller than $1\,\mathrm{nV}/\sqrt{\mathrm{Hz}}$. This requirement includes not only the input referred noise of the amplifier but any other noise source, i.e. the 50 Ω termination resistor; therefore, a passive termination is not acceptable. Active termination schemes are under study. Because

---

[1] According to Hamamatsu PMT specifications, a 20% gain reduction may be expected per integrated charge of 100 C (the expected charge per year in present conditions and worst PMT position).

the implementation of an active termination requires a transistor level approach and because the FE-board has 32 channels, an ASIC development is under study. It will be described below.

There is another approach however, since currently the PMT signal is clipped in the base, and about 2/3 of the signal charge is lost. An alternative solution would consist of removing the clipping at the PM base and perform it after amplifying the signal in the FE-card. This would relax by a factor 3 the noise requirement of the FE-amplifier, thus allowing a passive termination. Although this solution requires intervention in the detector, the operation is feasible. Thus, such a solution, based on Commercial Off-The-Shelf (COTS) Op. Amps and analogue delay lines is also described.

After analogue signal processing, either with an ASIC or using COTS, the signal must be digitized through a 12 bit ADC at 40 MHz. Baseline candidate is the AD9238 ADC, which is a dual pipeline ADC. Its sampling frequency ranges from 20 to 65 MHz.

Table 8.1 summarizes the main requirements for the analogue FE of the calorimeter system. Except for the PMT current and noise, the other requirements are similar to the ones for the current ECAL Front End [212, 13, 213].

8.1.1 Integrated implementation

Active termination, avoiding resistor termination and its thermal noise is usually referred as "electronically cooled termination". Conventionally it is created by an operational amplifier with capacitive feedback. This solution works well, provided that the input signal amplitude is not so large as to produce significant changes in the input amplifier transconductance. In the case of calorimeters for high energy experiments, this may not be the case as a large dynamic range is usually required. The ATLAS LAr calorimeter preamplifier creates the electronically cooled termination through a "super common base" input stage with an additional feedback loop [214]. An ASIC in IBM's 8WL 130 nm SiGe process is being designed for the LHC upgrade [215].

The LHCb Preshower chip relies also on a super common base stage [212], however no cooled termination is used in this case because the chip is located in the PM base. The input current is amplified and converted to differential signalling in order to be integrated through a fully differential amplifier with capacitive feedback. Since no dead time is allowed and high quality delay lines cannot be easily integrated, the solution adopted for the PS is to alternate every 25 ns between two integrators and to reset one integrator when the other one is active.

The proposed implementation of the ASIC for the calorimeter electronics upgrade is based on a combination of the two previous solutions. In the first place a "super common base" input stage with additional current feedback creates the electronically cooled termination as shown in Fig. 8.1. Then two alternated switched signal paths are used to integrate and sample the input current with no dead time, as in the Preshower sub-detector.

A first prototype of input stage of the chip including preamplifier and switched integrators has been designed in Austria-microsystems 0.35 μm SiGe BiCMOS technology and submitted to the foundry in June 2010 (Fig. 8.2). There are a number of key issues to be tested, corresponding to some innovations with respect to the ASICs referred above. On the one hand the amplifier uses current feedback (Fig. 8.1, left) for several reasons:

- The output is a mirrored current.

- Additional I/O pads are needed for standard voltage feedback [216], but not for current feedback. This makes easier the implementation of a fully differential channel (with pseudo differential input), which may be critical in a FE-board with large amount of digital circuitry.
- All nodes have low impedance, and hence less prone to pick up noise.
- ESD robustness is improved since no MOS transistor gate or bipolar base is connected to the input pad (series resistors are not allowed for noise reasons).

Current mirrors are based on active cascode circuits in order to be able to achieve the required linearity, noise and bandwidth.

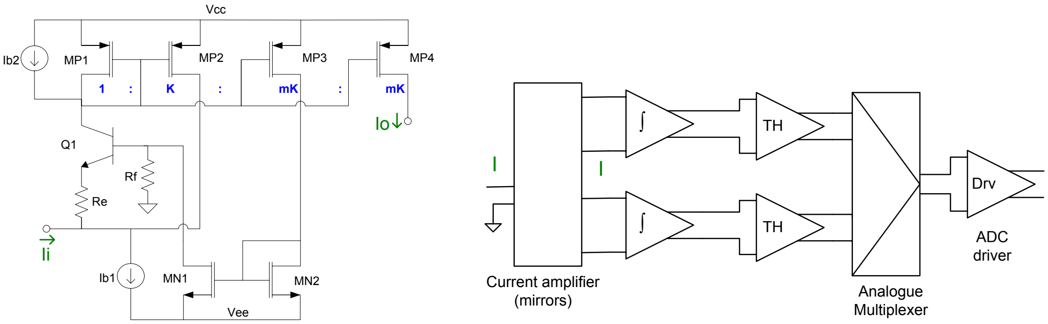

Figure 8.1: Super common base amplifier with current feedback (left) and interleaved switched paths (right).

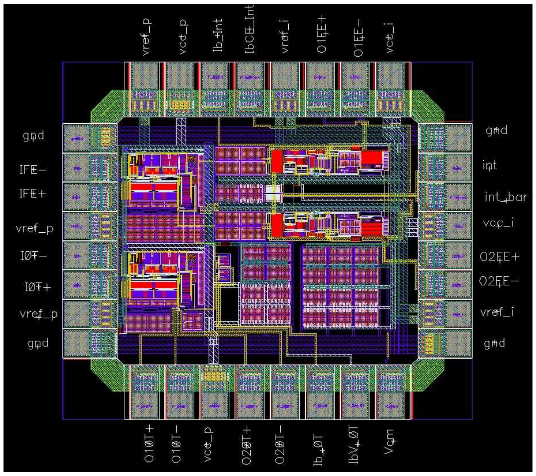

Figure 8.2: First ASIC prototype of the input part of the channel.

8.1.2 Discrete component implementation

Provided that the clipping line in the base of the PMTs (Fig. 8.3, left) is removed, noise requirements can be relaxed and line termination can be performed with a resistor. With

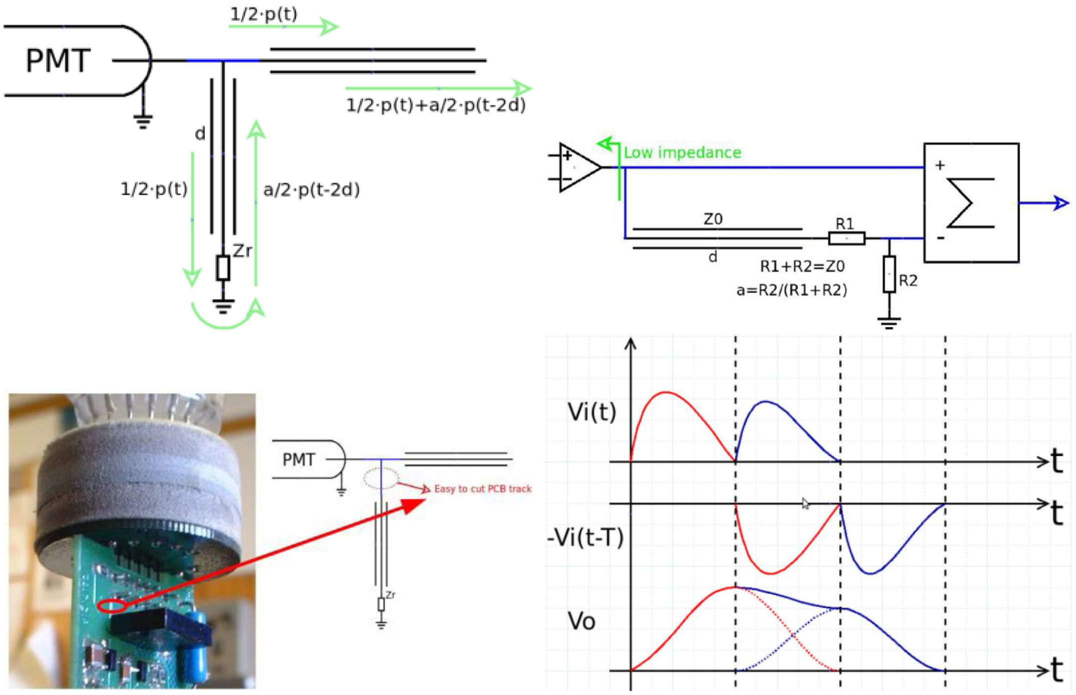

Figure 8.3: Principles of operation for the COTS solution. The left drawing and picture show the clipping system (top) and the trace in the PMT base that has to be cut to remove the clipping (bottom). The schematics and curves on the right show the system that is used in the COTS implementation to reset the integrator (top) and the resulting integrator output signal (bottom).

COTS it is possible to implement a similar scheme as the one already working in the current ECAL. However, there are two modifications compared to the present design: an input low noise amplifier is used, thus reducing the total noise, and the clipping is performed on the electronic card after the input amplifier rather than in the PMT's base. The clipping principle is preserved but the scheme must be adapted because the operational amplifier has a much lower output impedance than the PMT tube.

This option implies an intervention on the PMT's base, but it is reasonably easy to cut the trace on the PCB (Fig. 8.3, bottom left). This reduces the contribution of the Cockcroft-Walton induced noise, in case it was coupled after the clipping, since the outgoing signal is larger. The integration of the signal is done in an operational amplifier and 25 ns later a “disintegration” is performed in such a way that at the sampling instant the result of the previous integration is cancelled (Fig. 8.3, right). The circuit is made with differential operational amplifiers. This gives two polarities of the signal easing the implementation of the circuit described in Fig. 8.3. This scheme helps reducing the pedestal and helps the subtraction algorithm. It also avoids switching currents in the analogue power supplies.

A first prototype of the board is already built and the first measurements are being performed.

8.2 ECAL/HCAL electronics: new FE card

The present FE-cards are each connected to 32 PMT signals. They are described in the note [217]. The main card components are

- 8 ASICs each with 4 amplifier integrators.
- 32 Analog devices ADC AD9042.
- 8 FPGA AX250 of Actel (FePGA) for signal processing (pedestal subtraction and gain correction in the trigger path). A latency buffer and a derandomiser are used for preparing the data to be read-out after reception of a L0 trigger. Injection of test pattern instead of ADC data is foreseen. Each FPGA processes 4 channels.
- 1 FPGA AX500 of Actel (TrigPGA) which collects data at 40 MHz, processed in the FEPGAs, from the 32 cells of the card and from $8 + 4 + 1$ cells from neighbouring cards. It selects the highest transverse energy in a cluster of 2×2 cells and sends this information to the trigger path, through the crate backplane and through two trigger validation cards per crate.
- 1 FPGA APA300 of Actel (SeqPGA) gathers the data readout from the 8 FEPGAs, serializes them and sends them through the backplane to a controller board and then through a fibre to the TELL1 cards.
- 1 FPGA APA150 of Actel (GluePGA) is used as an interface for ECS between the control board of the crate and the FE-card to load constants into the FPGA, to load test patterns, to perform spying of data and other functions.

In the cards foreseen for the upgrade, the TrigPGA functionality and therefore probably the FPGA and its firmware will be kept unchanged. This will allow to transmit the high E_{T} clusters to be used in the low level trigger (see Chapter 3).

The GluePGA and its functionality for ECS will probably be kept, while the SeqPGA has no role in a 40 MHz readout system.

In the new cards the 32 channels will be grouped in 4 groups of 8 channels (see Fig. 8.4). In each of the four groups the PMT pulses are amplified and integrated as explained in Section 8.1. They are then converted with a 12 bit ADC running at 40 MHz. The ADCs' data will be processed by a single reprogrammable Flash-based FPGA of Actel. Preliminary studies show that the A3PE1500 has the necessary resources for an 8 channel group. The data will then be sent to the TELL40 boards (see Chapter 4) by one GBT Fibre system per 8 channel group with a useful bandwidth of 3.2 Gbit/s or 80 bits every 25 ns. A schematic diagram of one such group is shown in Fig. 8.4.

If one would send the 12 bits for each channel, 96 bits/25ns would be needed together with extra information such as the BXID and link identifier. One GBT would then not be enough. However in most cases the ADC data corresponds only to small pulses due to pedestal fluctuation (noise or pile-up). One possibility would be to send only data above a certain zero-suppression threshold; however this zero suppression can cause non linearity when measuring the calorimeter energy in a 3×3 cluster.

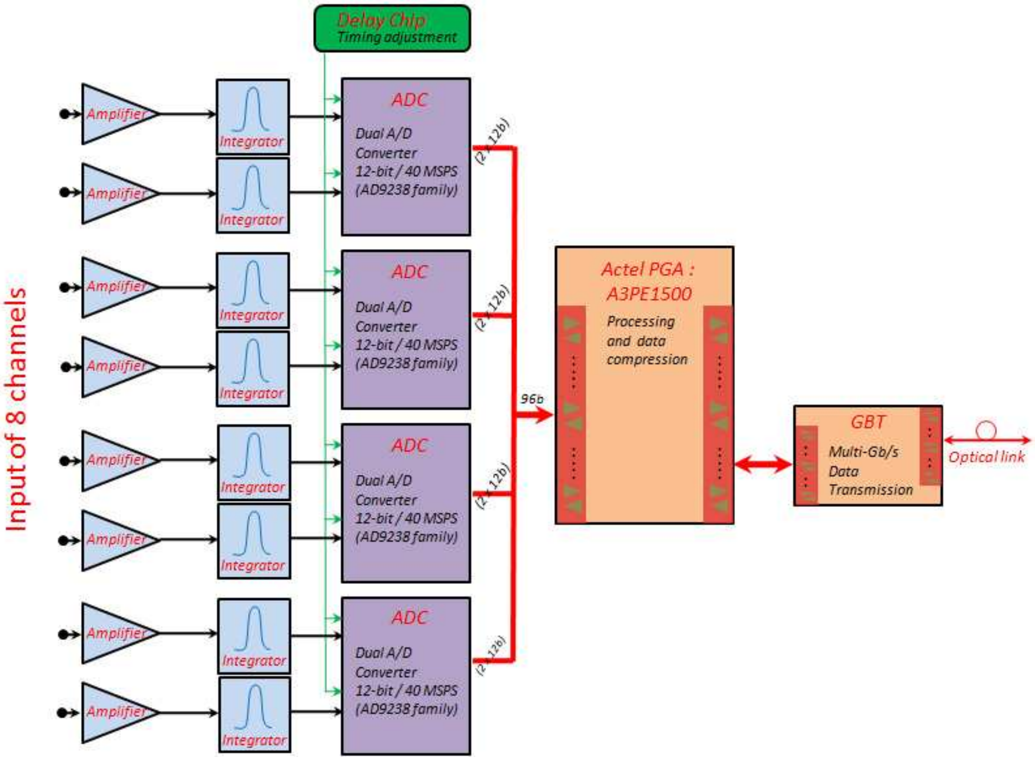

Figure 8.4: One FE-block of 8 channels.

In the upgraded cards we propose to compress the ADC information of 8 channels, in the A3PE1500 FPGA. For each event an 8-bit pattern word describes if the ADC information is made of short data (5 bits transmitted) or long data (the full 12 bits are transmitted). Simulations have shown that using this scheme one GBT per 8 channels is sufficient to transmit the information even in the highest occupancy region of the calorimeter and at the highest luminosity, if the event to event fluctuations are averaged over a large number of events, including events with empty proton bunches in the LHC. It has been verified that the multiplexer cells and memory blocks of the A3PE1500 are sufficient to implement such a scheme.

A prototype of an 8 channel slice of the FE-card has been built for tests of the analogue and digital part in 2010, and is undergoing the first tests at present. The prototype is shown in Fig. 8.5.

8.3 Radiation issues

At high luminosity operation, the central cells of the ECAL and HCAL will receive significant radiation doses, and their performance will deteriorate. The HCAL is essentially used for the trigger and the requirements on its resolution are not so severe as for the ECAL. The expected radiation will not significantly affect its present resolution. We consider hereafter only the ECAL performance degradation. The ECAL and HCAL FE-electronics is located above the detector. The dose expected after an integrated luminosity of $5\,\text{fb}^{-1}$ is 1 krad in the crate vicinity. The components will be radiation tested and chosen to cope with this level [212].

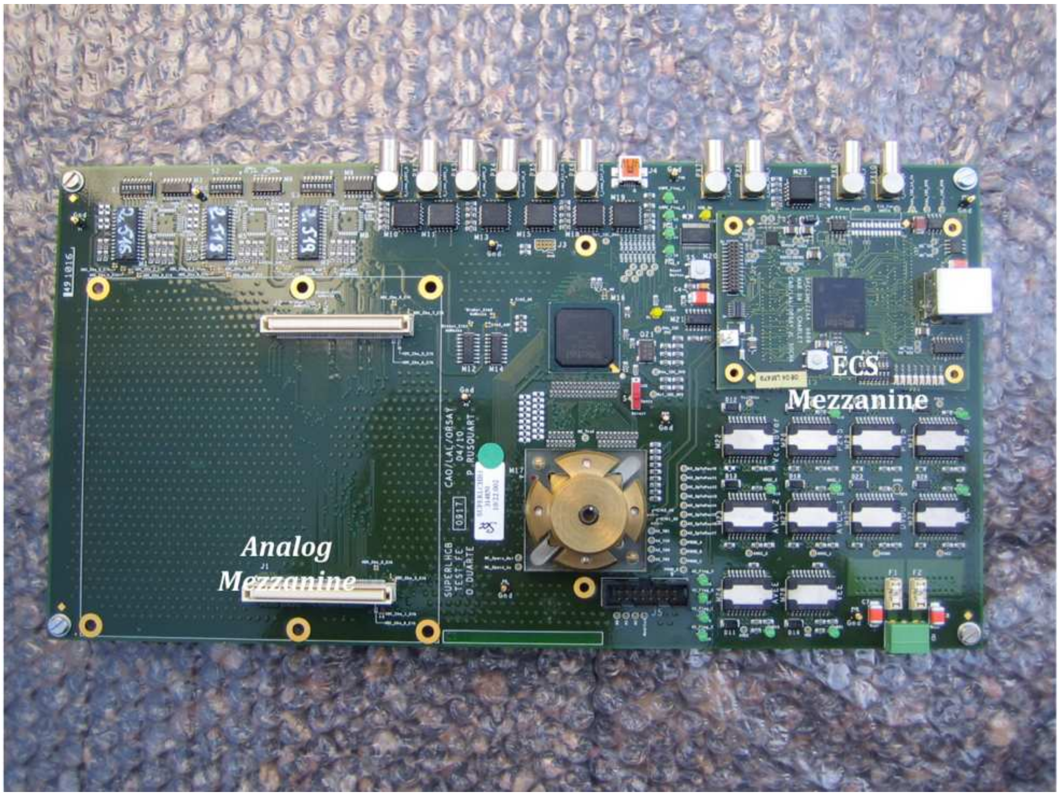

Figure 8.5: Photograph of the first prototype of the digital electronics.

The predictions for the doses received by ECAL can be found in [212, 218]. After $10\,\mathrm{fb}^{-1}$, at the innermost cells it reaches $\sim$ 1.2 Mrad at the depth of 6–10 cm from the front face of the detector (electromagnetic shower maximum), and is $\sim$ 0.6 Mrad at its rear surface, where photomultipliers are installed (see Fig. 3.10 of [212]). Most of the dose ($\sim$ 70%) comes from hadrons.

From the point of view of radiation tolerance, the following parts of ECAL should be considered:

- Optical elements of the calorimeter modules: loss of transparency and light yield of the scintillator tiles and wavelength shifting fibres (WLS);
- Photomultipliers: degradation of entrance window transparency;
- CW bases of photomultipliers: radiation damage of electronic parts.

The radiation damage of the optical elements of the modules, as well as that of the PMT entrance window, will lead to the degradation of the detector sensitivity and energy resolution (now $N_{\mathrm{pe}} \sim 3000$ p.e./GeV and according to test-beam measurements on a single module, $\sigma(E)/E = 10\%/\sqrt{E(\mathrm{GeV})} \oplus 0.8$ [219]).

In case of degradation above a certain limit, the innermost modules can be replaced: such a possibility is implemented in the mechanical design of ECAL [212]. The radiation damage of the CW bases leads to incorrect (and, in general, unstable) HV values for the PMTs.

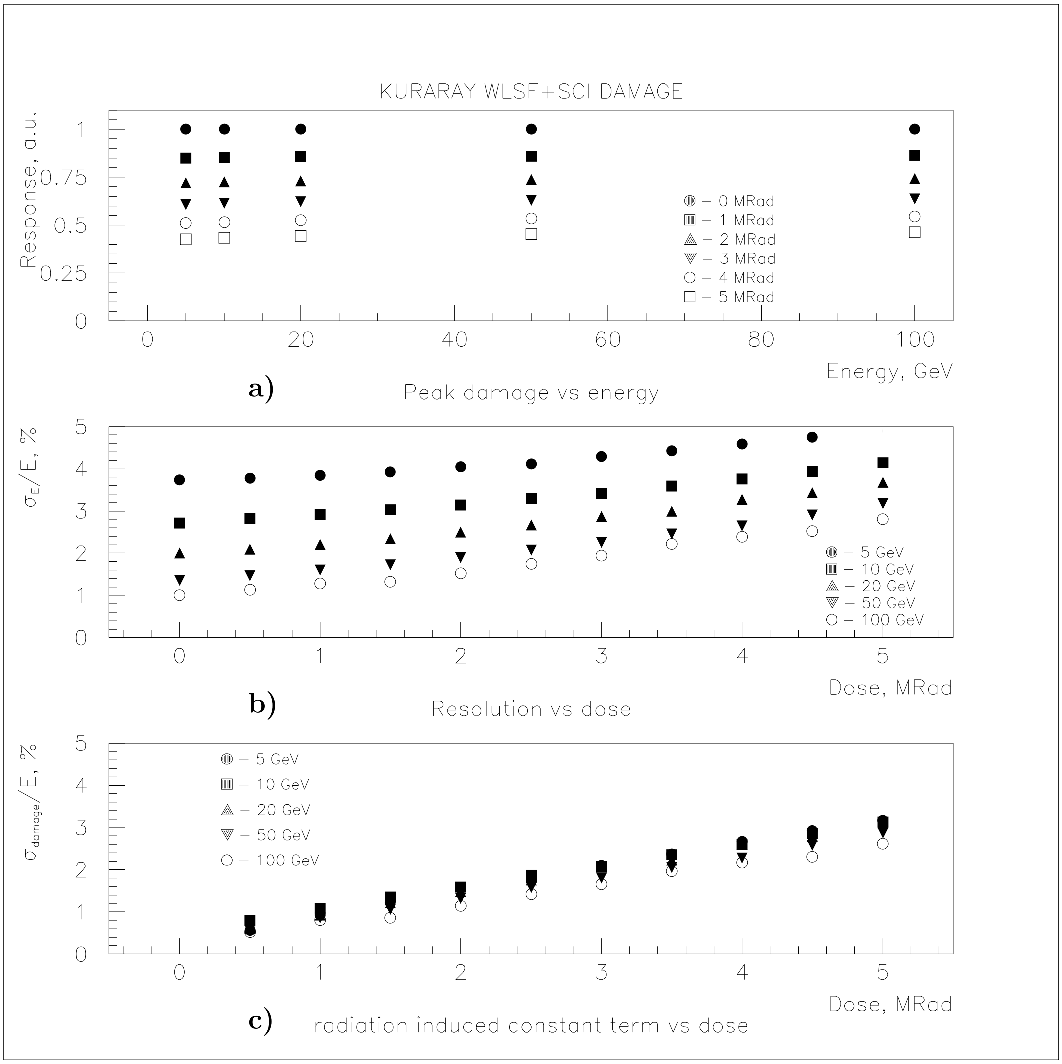

Figure 8.6: Simulation studies of the radiation induced module performance degradation, using GEANT4 (see text). Shown are the peak damage versus energy for various accumulated doses (a); the energy resolution degradation for various energies (b); the constant term degradation for various energies (c). The horizontal line corresponds to a constant term of 1.5%.

8.3.1 Outcome of the previous tests

Module optics

The radiation resistance of the LHCb ECAL modules was studied during the R&D phase of the project [220]. The most important test was carried out at LIL (LEP Injector Linac) in 2002.

Two modules were irradiated with a 500 MeV/c electron beam up to a dose of $\sim$ 5 Mrad at the shower maximum, which, according to the simulation, corresponds to an integrated luminosity of 40 fb^{-1}. Then the light yield and transparency of the scintillator tiles and WLS fibres were determined by means of a radioactive source scan. The measurements were performed several times from 7 to 2000 hours after the irradiation; a significant annealing effect was observed.

The values taken after 2000 hours annealing were used as an input to the simulation of response to electromagnetic showers, obtained with GEANT4. For the calculation of the light yield at intermediate doses, an exponential interpolation was used. The results are shown in Fig. 8.6 [212]. One can see that at 5 Mrad the predicted degradation is such that the light yield becomes 40% of that before irradiation. The degradation of the resolution consists mainly in an increase of the constant term, showing an approximately linear dependence on the dose. At 5 Mrad the constant term becomes $\sim 3\%$ (0.8% before irradiation).

There are 32 spare modules of the inner type, which is, according to these results, enough for the replacement of the most irradiated modules, if it would become necessary.

PMT entrance window and CW bases

The Hamamatsu R7899-20 PMTs used in the LHCb ECAL are specially designed to work in high radiation background and their entrance window is made of special material. The CW generator circuit is also radiation tolerant: it is designed such that it is not sensitive to the characteristics of its active elements, and remains operational even with significantly damaged components. In addition, the components with lower degradation rates were specially selected [221].

In order to measure the radiation tolerance of photomultipliers and CW bases, irradiation tests were conducted at IHEP (Protvino) in 2010. The samples were installed behind a 22 cm-thick steel converter and irradiated by the 50 GeV proton beam of the IHEP U-70 accelerator up to the doses of 1–2 Mrad, depending on the sample position. The duration of the test was 3 days; the parameters of the samples were then measured within a few days after the end of the irradiation, without a long annealing period. These results can be considered as a lower limit for the radiation tolerance.

During the test, the Hamamatsu PMT sample received ~ 1.9 Mrad, equivalent to 6 years of operation at $5\,\mathrm{fb}^{-1}$ per year; then, after 11 days, its window transmittance was measured with a spectrophotometer and compared to the window of an unirradiated sample. In the wavelength range from 500 to 550 nm the loss of transmittance did not exceed 5%. The conclusion is therefore that the radiation tolerance of the PMT entrance window is sufficient to work during the full upgrade period.

To study the radiation hardness of CW bases, three samples were installed at the beam and powered up. The output voltage (initially $\sim 950\,\mathrm{V}$) was monitored during the tests and stable until failure. The failure occurred at doses between 1.4 and 1.7 Mrad. Our conclusion is that the CW bases of the photomultipliers are radiation tolerant at least up to a dose of 1 Mrad, which is sufficient even for the innermost cells to survive during 2 years at $5\ \mathrm{fb}^{-1}$. The replacement of CW bases can be performed during annual shutdown periods, and 500 spare CW bases are sufficient for the full upgrade program.

8.3.2 Future tests

Following these initial tests, there remains some uncertainty on the radiation tolerance of the ECAL modules for the following reasons. First, the tested optical components are not of exactly the same type as the ones finally used in the ECAL construction. Second, the irradiation was performed in an electron beam, while in real conditions it will be mostly hadronic radiation;

this may imply a different degree of damage and a different annealing behavior. The light yield and transmission of the optical components is affected as function of the z coordinate along the module. Simulations are used to combine these effects with fluctuations in shower depth, thus calculating the degradation in resolution. This simulation is a third cause of inaccuracy. In practice, this translates into an uncertainty on when modules need to be replaced, and on the number of required spares.

Taking into account all the facts mentioned above, it was decided to perform a new series of tests, irradiating spare ECAL modules in a hadron beam. Two ECAL modules of inner type were placed for irradiation into the LHC tunnel. The position (near the LHCb interaction point, at a distance of $\sim 4\,\mathrm{m}$ along the Beam 2 direction, and at 15 cm from the beam line) is chosen such that the dose received by the test modules during the LHC operation is ~ 10 times larger than that for the innermost modules of ECAL. It is therefore expected that by the end of 2011 the test modules will get a dose corresponding to approximately 1 or 2 years at 5 fb^{-1}. The situation will be reviewed after having measured the characteristics of the test modules, which could take place in 2012–13 at the SPS electron test beam. At this point there would still be enough time to produce extra spare modules, if necessary.

8.4 Effects of pile-up

The luminosity increase foreseen for the LHCb upgrade will lead to a large average number of interactions per crossing and therefore to an increase of the event multiplicity. This may affect the ECAL energy and position resolutions by shifting on average the energy measurements and smearing the reconstructed energy and position of the clusters.

Several methods have been used to estimate the effect, and the one presented here relies on real data recorded with the calorimeter system at 3.5 TeV. The energy is lower than that expected for the upgrade, but the estimate is based on real data and is therefore more realistic than simulations[2].

8.4.1 Noise estimation method

The method consists in storing the signal seen by the 6010 cells of the ECAL for a large minimum-bias data sample before zero suppression. This is possible as the LHCb electronics and acquisition perform a compression of the data without loss of information, the zero suppression being done at the reconstruction level. Using the raw data that are presently available, the reconstruction is run again after relaxing the zero-suppression threshold. To generate a high luminosity event, several minimum-bias events are piled-up by adding the ADC counts measured for each cell of the calorimeter.

The number of minimum bias events added depends on a random number of interactions per beam crossing given by a Poisson law as a function of the luminosity. Two quantities are finally extracted per cell: the average number of ADC counts seen, which is a measurement of the transverse energy (the photomultiplier gains are adjusted with a $\sin\theta$ law in order to provide at the trigger level an E_{T} measurement), and the RMS of the fluctuations of this signal.

---

[2] The event p_{T} spectrum should not change strongly with the energy, but we expect an increase of the multiplicity of $\approx 20\%$, according to the PYTHIA simulations, between 3.5 TeV and 7.0 TeV in beam energy.

The ECAL cells are such that a typical electromagnetic shower is contained in a cluster of 3x3 cells. The same quantities as previously mentioned are also extracted for such clusters.

8.4.2 Results

Figure 8.7 shows the results at the maximum luminosity expected for the first phase of the upgrade, i.e. $10^{33}\mathrm{cm}^{-2}\mathrm{s}^{-1}$. The electromagnetic calorimeter energy resolution may be expressed as

$$\frac{\sigma(E)}{E} = \frac{10\%}{\sqrt{E(\mathrm{GeV})}} \oplus 1.5\% \oplus \frac{0.0025 \times \mathrm{RMS}}{E \sin\theta}(\mathrm{Pile-up}) \oplus \frac{0.01}{E\sin\theta}(\mathrm{Noise}), \tag{8.1}$$

where the pile-up contribution is extracted from the present analysis and the noise contribution is the one measured at the pit with the present system. Notice that the ADC count being in E_T, those contributions depend on the angle of the cell with respect to the beam axis. The extra energy measured can on average be removed, but the resolution is degraded according to the RMS of the pile-up contribution. Table 8.2 lists the numerators of the pile-up contribution to the ECAL resolution for luminosities ranging from 2×10^{32} up to $2 \times 10^{33}\mathrm{cm}^{-2}\mathrm{s}^{-1}$ and averaged over the calorimeter cells.

$\mathcal{L}$ ($\mathrm{cm}^{-2}\mathrm{s}^{-1}$)	2×10^{32}	5×10^{32}	10^{33}	2×10^{33}
RMS	12	15	18	22
$0.0025 \times \mathrm{RMS}$	0.030	0.038	0.045	0.055

Table 8.2: Average RMS of the pile-up contribution to the signal of the ECAL cell signal at different luminosities. The numerator of the contribution to the resolution is also given.

$\mathcal{L}$ ($\mathrm{cm}^{-2}\mathrm{s}^{-1}$)	2×10^{32}		10^{33}	
Resolution	Total	Pile-up	Total	Pile-up
$B \to D^*(D\gamma)K$	7.4%	4.7%	14.3%	13.1%
$B \to \phi\gamma$	2.3%	0.5%	2.7%	1.5%

Table 8.3: Energy resolution for two types of photon reconstruction at low (400 MeV, $B \to D^*K$) and high (3.5 GeV, $B \to \phi\gamma$) E_T at an angle of 100 mrad. The overall resolution and the pile-up contribution are given at the present nominal luminosity and at the expected one for the first phase of the upgrade.

The degradation on the resolution could also be viewed for two different photon reconstructions, at low and high E_T, and depends on the photon angle (according to Eq. 8.1), and the RMS of the pile-up contribution (Table 8.2). The typical E_T for the channel $B \to D^*K$ is 400 MeV and is around 3.5 GeV for the $B \to \phi\gamma$ decay. Table 8.3 shows the degradation of the energy resolution at an angle of 100 mrad (the total angular acceptance of the ECAL covers the region 30–250 mrad), and for luminosities of 2×10^{32} and $10^{33}\,\mathrm{cm}^{-2}\mathrm{s}^{-1}$. As expected, the high E_T reconstruction does not suffer from the pile-up effect. At low E_T, it becomes the largest contribution to the resolution.

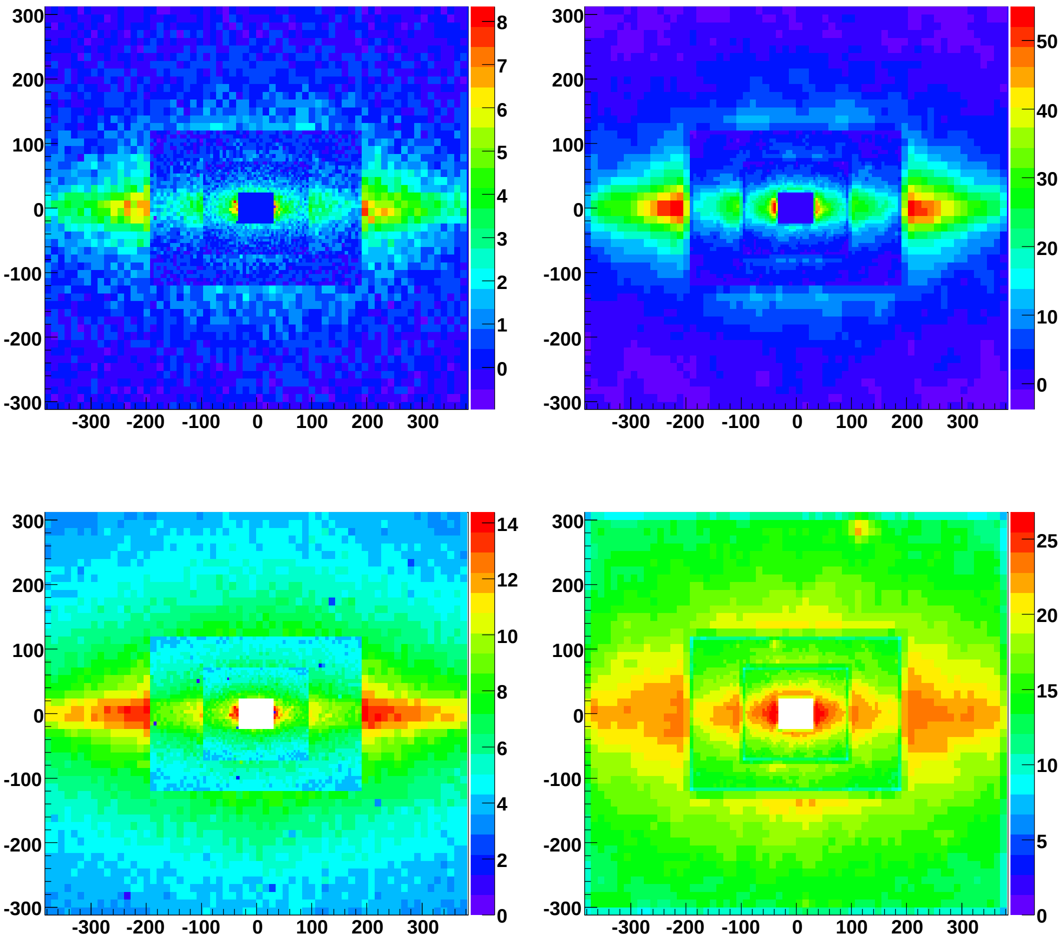

Figure 8.7: 2D maps (x and y axes are in cm) of the average signal in ADC counts (top) and of its distribution RMS (bottom) for the 6016 cells of the ECAL. The maps are produced from a sample of 100,000 events that have been generated by piling-up real data events (see text), corresponding to a luminosity of $10^{33}\,\mathrm{cm}^{-2}\mathrm{s}^{-1}$. The left maps show the average signal and RMS per cell, the right ones represent the same quantities for 3×3 clusters, the position of the cluster on the map being the one of the central cell of the cluster. The bottom right plot gives the p_{T} fluctuations (in ADC counts) that we can expect on the calorimeter surface. Multiplying by 2.5 MeV gives the corresponding information in MeV.

Chapter 9

Muon System

Introduction

The muon system [222, 13, 223] is the most shielded sub-detector of LHCb and the primary component of particle flux is less dominant than in other subsystems. Nevertheless, ageing of detectors, their rate capabilities, the long term reliability of the present electronics and the performances of muon identification in a high rate environment are concerns for the system when operated with a luminosity of 10^{33} $\mathrm{cm}^{-2}\mathrm{s}^{-1}$. Muon station M1 will not be needed in the upgrade, as the improvement in the Low Level Trigger (LLT) muon momentum resolution will be performed by the tracking stations, and the expected high rate will make it less useful.

Most of the hits recorded by the muon chambers in the stations M2–M5 are produced by secondary particles coming from electromagnetic and hadronic showers and by the low energy neutron background. The actual values of these components, simulated in the LHCb Monte Carlo with safety factors, have been studied in the first year of operation of the detector. This will be discussed in more detail in Section 9.1.

The muon system Front-End (FE) electronics is already read out at 40 MHz, as it is currently sending data at this rate to the L0 trigger, while the full TDC information is sent at 1 MHz to the DAQ system. This scheme has to be slightly modified, in order to have a system fully integrated with the general LHCb LLT and with the rest of the upgraded DAQ. As a global strategy, it is planned to have a minimal set of changes for the muon system and its FE-electronics. Details on the muon electronics upgrade are discussed in Section 9.2.

A key element for a successful running of the system at high luminosity will be a good understanding of the high rate performance of the MWPCs and of detector ageing effects. These aspects will be presented in Section 9.3, together with the MWPC detector operation stability, considerations about spare chambers and ongoing R&D of large-area GEM detectors.

Finally, Section 9.4 summarizes the expectations for the muon identification performance in the high luminosity environment.

9.1 Particle flux in the Muon System

The particle rates in the muon system are estimated on the basis of a full GEANT simulation [224] of proton-proton interactions at the nominal LHC energy of 14 TeV and at the nominal

Table 9.1: Deposited charge (C/cm of wire) in the most irradiated chamber after 50 fb^{-1} (left); rates on a single FE-electronics channel (MHz) in the most irradiated chamber at 10^{33} $\text{cm}^{-2}\text{s}^{-1}$(right).

	R1	R2	R3	R4
M2	0.67	0.42	0.10	0.02
M3	0.17	0.08	0.02	0.01
M4	0.22	0.06	0.01	0.004
M5	0.15	0.03	0.01	0.003

	R1	R2	R3	R4
M2	0.81	0.55	0.12	0.10
M3	0.24	0.11	0.03	0.04
M4	0.09	0.07	0.04	0.03
M5	0.07	0.07	0.04	0.02

LHCb luminosity of $2 \times 10^{32}\,\text{cm}^{-2}\text{s}^{-1}$. The simulation uses a detailed description of the LHCb detector and the cavern hosting it. Great attention has been paid to the choice of the low energy physics processes included in the simulation, since a large fraction of particles crossing the muon detector have very low energy. Due to large uncertainties in the low energy spectrum of the neutron flux, a safety factor of 5 has been applied in the calculations, which gives in turn safety factors of 2 (M1) and 3 (M2–M5) in the total radiation dose. The same simulation has been used to estimate the rates at the level of the FE-electronics. The deposited charge in the chambers is estimated taking into account the particle rate per gap in the most irradiated MWPC of each region. The charge released by a MIP crossing a gap perpendicularly is assumed to be 0.8 pC. The results for the ageing and for the rate at the level of the FE-electronics are reported in Table 9.1.

The simulated amount of radiation expected in the muon system has been compared with direct measurements coming from the LHCb operation. The rates of muon hits in the various detector regions have been measured during the 2010 run for luminosity values ranging from 10^{27} to 10^{32} $\text{cm}^{-2}\text{s}^{-1}$. The measured rate R is scaled for the nominal luminosity of 2×10^{32} $\text{cm}^{-2}\text{s}^{-1}$.

The resulting values of R are found to be independent of luminosity within a few %, except for the regions affected by back-scattering, where R also depends on the average number of visible interactions per bunch crossing and on the LHC filling scheme. For the most irradiated chambers in regions M1R1 and M2R1 we find 130 and 45 kHz/cm^2, respectively.

In Figure 9.1 we compare the values of the average R in each region for three different luminosities with the predictions of two simulations: the Monte Carlo data previously mentioned, produced with the full GEANT simulation in the nominal LHCb configuration at 14 TeV including spillover, and more recent Monte Carlo data produced in the 2010 configuration at 7 TeV, not including spillover. The safety factor has not been applied to the Monte Carlo for this comparison.

Rates are reasonably well reproduced by the simulation for the outer regions, while they are underestimated for the inner regions and M1 by up to a factor 2, hence well within the safety factors indicated above.

9.2 Muon System Electronics

The basic architecture of the muon electronics can be maintained for the the upgrade. From the FE-board CARDIAC [225] to the Off-Detector Electronics (ODE) board [226] no modifications are foreseen with respect to the current layout [13]. At present the signals from the ODE boards

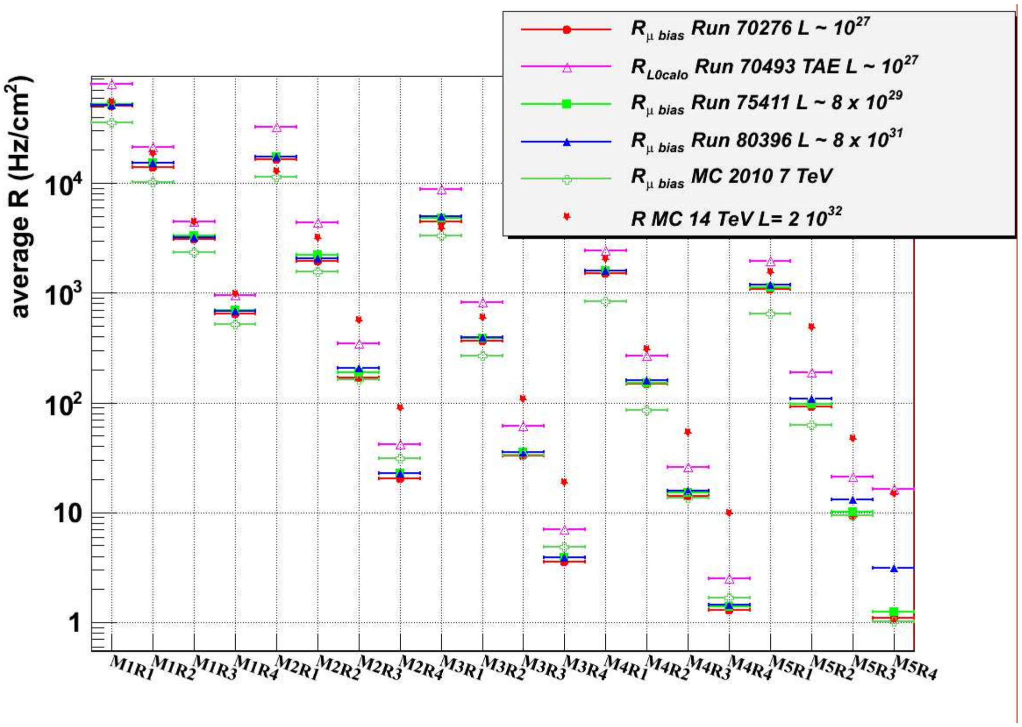

Figure 9.1: Evaluation of the average muon hit rate R for the different detector regions.

are sent at 1 MHz to the TELL1 boards [13], which will be upgraded to the TELL40 boards to cope with a 40 MHz data rate. As described in the following, all the modifications of the muon electronics architecture foreseen for the upgrade will be done on the TELL40 board.

9.2.1 Front-end electronics

In the current layout the signals generated on the muon chambers are digitized at the FE-level by the CARDIAC board. The two ASICs CARIOCA [227] and DIALOG [228] mounted on the CARDIAC boards are realized in IBM 0.25 μm technology, using specific layout techniques (enclosed gate structures) suitable for radiation resistance up to 10 Mrad without significant performance loss. Therefore under the conditions presently foreseen for the upgrade, the current FE-electronics layout will be maintained.

9.2.2 Off-detector electronics

The ODE board is synchronous with the LHC clock. The 192 ODE input channels are processed every 25 ns by the SYNC ASIC [229]. The information is sent on optical links to the L0 trigger processor at 40 MHz, using 12 GOL [230] chips as data serializers. The information is used by the L0 trigger algorithm to generate the trigger decision (L0-yes signal). In addition a time measurement is done for each input channel by the SYNC ASIC using a custom 4 bit TDC. The L0-triggered events are sent to the TELL1 boards at the maximum rate of 1 MHz through one GOL chip on the DAQ link.

The main requirement for the electronics upgrade is to process and save the data coming

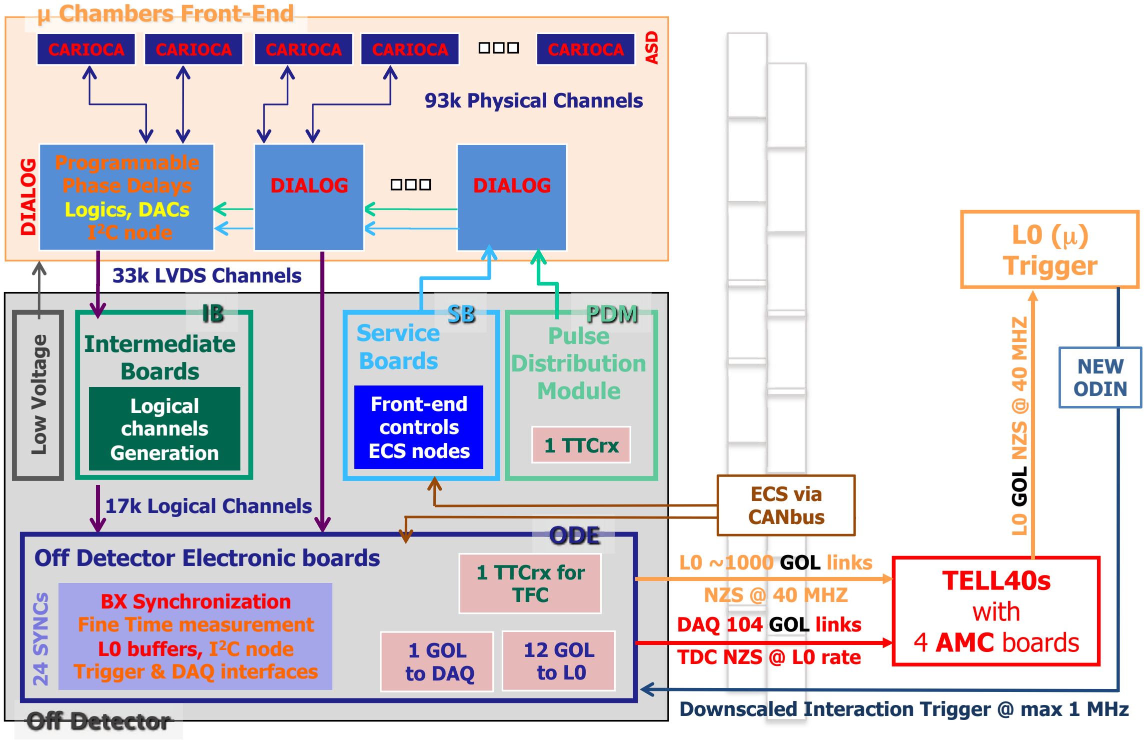

Figure 9.2: Block scheme of the muon electronics architecture in the upgrade layout.

from the detector at 40 MHz, instead of the nominal 1 MHz of the current layout. As described, the ODE boards already process the muon detector signals at 40 MHz. For this reason no changes are foreseen at the level of the ODE boards for the upgrade. Moreover, the L0 muon trigger will be maintained in the upgrade as in the present configuration. Finally, all the synchronous signals are transmitted to the ODE board with the TTCrx data format as in the current layout [231]. The maximum trigger rate received by the ODE board is 1 MHz. However, the L0-yes signal currently received will be upgraded to the logical AND of the foreseen Low Level Trigger and the L0 muon trigger.

9.2.3 TELL40 implementation via AMC board

The block diagram of the muon electronics architecture in the upgrade layout is shown in Fig. 9.2. A new muon data bank to be sent to the farm is foreseen. The muon bank is created at the LLT rate (expected up to 30 MHz) and contains the data carried by the L0-links, used in the current layout only by the L0 muon trigger processor. Moreover, at the maximum rate of 1 MHz also the timing data carried by the DAQ-link is added to the muon bank. The muon bank is set up by a dedicated Advanced Mezzanine Card (AMC), to be installed on the TELL40 board. One TELL40 board will embed 4 AMC boards, while each AMC board will be connected to only one ODE. A block scheme of the AMC board is shown in Fig. 9.3. The AMC board takes as input the L0-links and the DAQ-link transmitted from the ODE board with the 40 bits GOL data format. Since the L0 muon trigger processor will not change with respect to the current implementation, it must receive the L0-links as they exit from the ODE board.

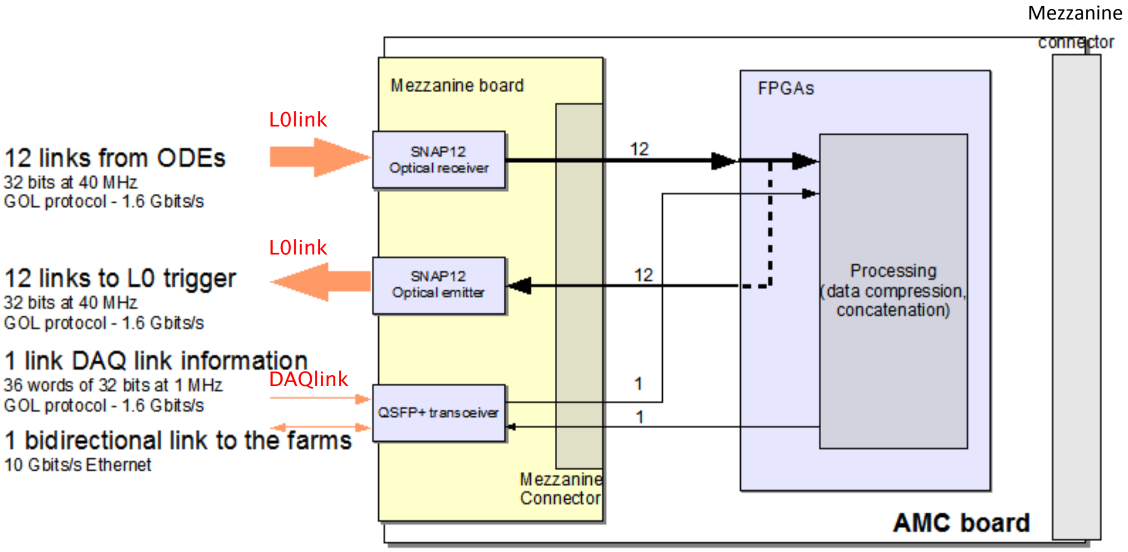

Figure 9.3: Block scheme of the AMC board.

Therefore a L0-links duplication is provided by the AMC board which outputs a copy of the L0-links to the L0 muon trigger processor. The detail of the duplication of this information is still under study.

The second copy of the L0-links data is processed, together with the DAQ-link data, by the programmable logic (FPGA) of the AMC board. First the data are checked every 25 ns in order to be validated. Finally, for each triggered event, the muon bank is created and sent from the AMC board to the farm.

9.3 Detector studies for high luminosity

9.3.1 Rate limitations of chambers and electronics

The high-rate performance of a MWPC was tested [232] using a 100 GeV muon beam superimposed to the 662 keV γ flux of variable intensity produced by the ^{137}Cs radioactive source at the CERN-GIF. One of the main results of the test is that no evident saturation effect is present up to the tested current density of approximately 30 nA/cm^2. This value must be compared with the one expected in the M2–M5 stations at 10^{33} cm^{-2}s^{-1}, which is below 15 nA/cm^2. Therefore we expect that no significant space charge effect will deteriorate the chamber performance.

By means of the muon beam it was also possible to study the behaviour of the Front-End electronics in the high rate environment. The muon detection efficiency and the response time resolution were studied as a function of the hit rate up to 1 MHz per Front-End electronics channel. Once the detection efficiencies have been corrected for the effect of dead time (2.0 to 2.5% at 1 MHz), both parameters show a behaviour in the presence of high particle fluxes that is very similar to the one measured without photon background. Therefore, except for dead time effects, no deterioration is expected in the performance of the FE-electronics.

9.3.2 MWPC tests

Extensive ageing tests were performed on MWPC prototypes at the CERN-GIF and at the ENEA-Calliope gamma irradiation facilities [233, 234]. In two tests charges of 0.25 C/cm and 0.44 C/cm, respectively, were accumulated without any apparent loss of performance. compared with the doses expected at 10^{33} $\text{cm}^{-2}\text{s}^{-1}$ (Table 9.1) these values suggest that most of the chambers of the muon stations M2–M5 should sustain the dose at high luminosity.

On the other hand, HV trips have been observed in some chambers already at a luminosity much lower than the one foreseen for the upgrade of LHCb. A careful investigation of the trips showed that they are not related to effects on the wires, which manifest themselves typically by sparks, but rather due to a thin film on the cathodes, which leads to self-sustaining Malter-like currents, exceeding the trip current. Similar effects have been observed during the testing phase of the chambers at GIF. After conditioning the chambers under irradiation, the self-sustaining currents could be fully suppressed. More details are reported in [235].

Given this situation, it seems appropriate to investigate further about the effects seen using the present CERN-GIF source, and later on the upgraded facility providing 10 times larger particle fluxes. The upgraded facility should be available from 2012 onwards and will be suited for an ageing test in which the limit of operation of this type of MWPCs is established. Based on the experience acquired so far in operating the MWPCs, the technology should sustain an integrated luminosity of 50 fb^{-1} with about 1–2% of the chambers being replaced every year, which we consider is reasonable maintenance for such a large system.

9.3.3 R&D on GEM detectors

The overall experience with GEM chambers in the first year of LHCb operation has been satisfactory, and most of the chambers worked efficiently. However, two chambers showed problems, which requires further investigation.

The expertise acquired by LHCb groups [236] in the design and production of GEM detectors has been merged into the common framework of the RD51 Collaboration [237]. This effort has been finalized to make the GEM technology available for large area detectors. In order to overcome the size limitation due to the troublesome alignment of the two masks, and thus fulfilling the demand of large area foils from the GEM community, a single-mask procedure has been developed by the TS DEM-PMT group at CERN. Large area GEMs are now available in dimensions up to detectors for inner regions of M2–M3 and represent a possible backup solution in case of unexpected ageing of chambers in these regions.

A characterization of the operating performance of the new GEM foils has been obtained building a planar triple GEM chamber with an active area of 300×700 cm^2, equipped with 20×25 mm^2 pad readout anode. A full prototype using this new technology has been built at the Frascati Laboratory and was tested in current mode with a ^{137}Cs photon source, showing good uniformity and stability when compared with the standard technology [238].

9.3.4 HV and LV systems

The HV system will be completed in the coming year in order to connect each gap of the MWPC system to an independent HV channel. In the present layout, four gaps of R4 chambers are connected to a single HV channel. To increase the operational efficiency of the system and to minimize the number of disconnected gaps during data taking, the UF/PNPI HV system will double the number of available channels, from the current 1920 to 3840. The construction of the modules will start in 2011, so to have the full system installed by the restart of data taking in 2012. This will be very useful also for the operation at high luminosity, and no further changes to the HV-system will be required for the LHCb upgrade. The high voltage systems presently used (UF/PNPI and CAEN) are expected to stand more than 50 Gy radiation dose in the area of the M2–M5 racks. The dose foreseen at standard luminosity in the hottest region is approximately 20 Gy (with a safety factor of 10).

The LV system supplies electrical power to the FE-electronics (CARDIAC boards) and to the Off-Detector Electronics (ODE system). The present LV scheme is based on Wiener Maraton power supplies, which are foreseen to be used also in the upgrade. The higher rate on the FE-electronics will cause an increase in power consumption of less than 10%. In the present configuration, the hottest channels of power supplies are used at 80% of full load, and therefore the power increase is not a major concern.

9.4 Muon ID performance at high luminosity

One of the main concerns of operating the muon system at high luminosity is related to the capability of the detector to perform an adequate muon identification, by maintaining high efficiency for muons and by keeping the muon misidentification (mis-ID) probability for hadrons and electrons very low [239].

In a high luminosity environment where the average number of visible interactions per crossing is considerably larger than one, the high number of tracks coming from multiple primary vertices (PV) enhance the probability of mis-ID, primarily due to the number of accidental associations to hits in the muon chambers coming from decays in flight or punch-through of pions and kaons. This effect has been studied with the data collected between July and October 2010 in runs with an average number of visible pp interactions per crossing above 2. The muon mis-ID probability was studied using the abundant sample of pions coming from K_S decays. The muon mis-ID increased by a factor 2 going from events with one PV to events with ≥ 4.

However, a proper retuning of the algorithm, mostly based on tighter cuts on the association between the extrapolated track and muon hits, recovered the performance observed in low pile-up conditions. In particular the S/B ratio of J/ψ candidates has been studied as a function of the number of reconstructed PV after the retuning of the Muon ID algorithm. The result can be seen in Fig. 9.4 where the invariant mass distribution of inclusive $J/\psi \to \mu\mu$ sample is presented for $N_{\mathrm{PV}} = 1$ and for an average $N_{\mathrm{PV}} = 2.3$: the worsening of the S/B ratio is $\leq 15\%$ with an efficiency loss of $\leq 5\%$, for an increase of the average number of primary vertices of more than a factor 2.

The main sources of concern at high luminosity are the increased multiplicity of hits in the inner regions of M2–M3 stations, where a high level of background could deteriorate the muon mis-ID and the unknown level of spillover in the muon system at high luminosity. Both phenomena could also influence the efficiency of the L0-muon rejection power. A detailed evaluation of these effects on the overall performance of the muon identification is still ongoing and will benefit from the LHC operation in 2011 at 50 ns.

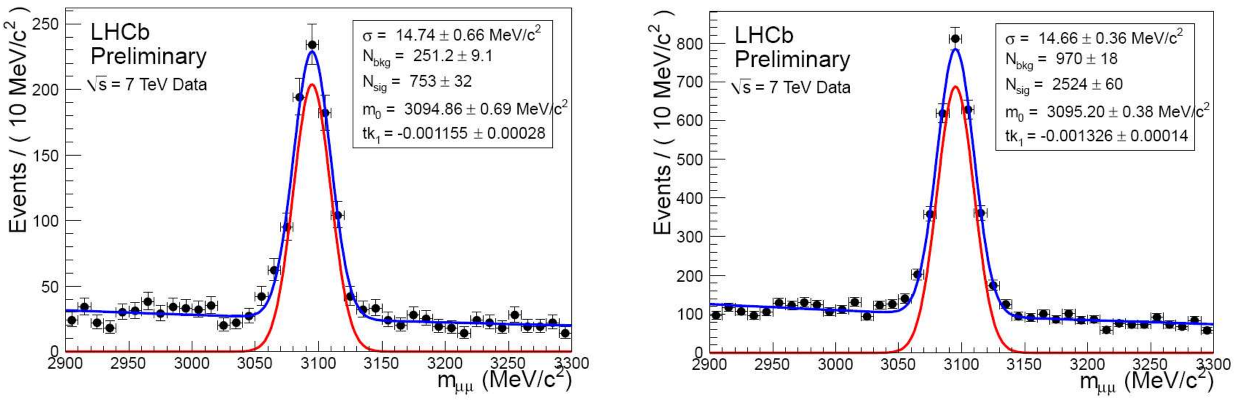

Figure 9.4: $J/\psi \rightarrow \mu\mu$ signal and background distribution in case of event data with a single PV reconstructed (left) and with the whole sample (right) having an average number of PV equal to 2.3.

Chapter 10

Online system and Offline computing

The Online system consists of the Experiment Control System (ECS), the Timing and Fast Control (TFC), the Data Acquisition (DAQ) and the Online IT infrastructure (OIT).

The architecture and the basic principles were described in the LHCb Online TDR [240]. They are: a unified control system for all hardware and software components required to run the experiment, a single stage readout using a large, dedicated local area network, driven by a central fast control system, which provides synchronous commands and timing. Wherever possible industry standard hardware and software are used and the number of different protocols and technologies is intenionally kept as small as possible.

Based on these principles the Online system of the current LHCb detector has been designed and commissioned. Fig. 10.1 gives a schematic overview. In this system data are pushed from the detector into the readout boards (TELL1/UKL1) shown at the top of the figure. The Timing and Fast Control (TFC) system, shown in the left upper part, broadcasts a destination address to the readout boards, which then send their data via the network, shown in the middle, to one of the computers in the event-filter farm (EFF) shown in the bottom. The computers in the EFF process the event data, select a small fraction of them and send these to the storage, shown at the lower left of the figure. The EFF computers then announce themselves to the TFC system as being available for new data, closing the cycle of data acquisition and high-level triggering.

All components are monitored and controlled by the experimental control system (ECS) indicated on the right-hand side of the figure.

While many components will need to be changed or upgraded, either to accommodate the higher trigger-rate or naturally because of component obsolescence, the basic architectural choices described here briefly have been found to be successful and will be kept for the upgrade.

10.1 Experiment Control System

A uniform control system, the ECS [241], is in charge of configuring, monitoring and controlling both the data acquisition and the various detector elements, the classical slow control. Its physical backbone is a large private local-area network, where all essential services such as domain control and user accounts are replicated, respectively mirrored from the CERN domain to ensure completely independent operation. Its logical functions are realised using a distributed SCADA system (PVSS2) running on over 100 servers. The most important of its functions is

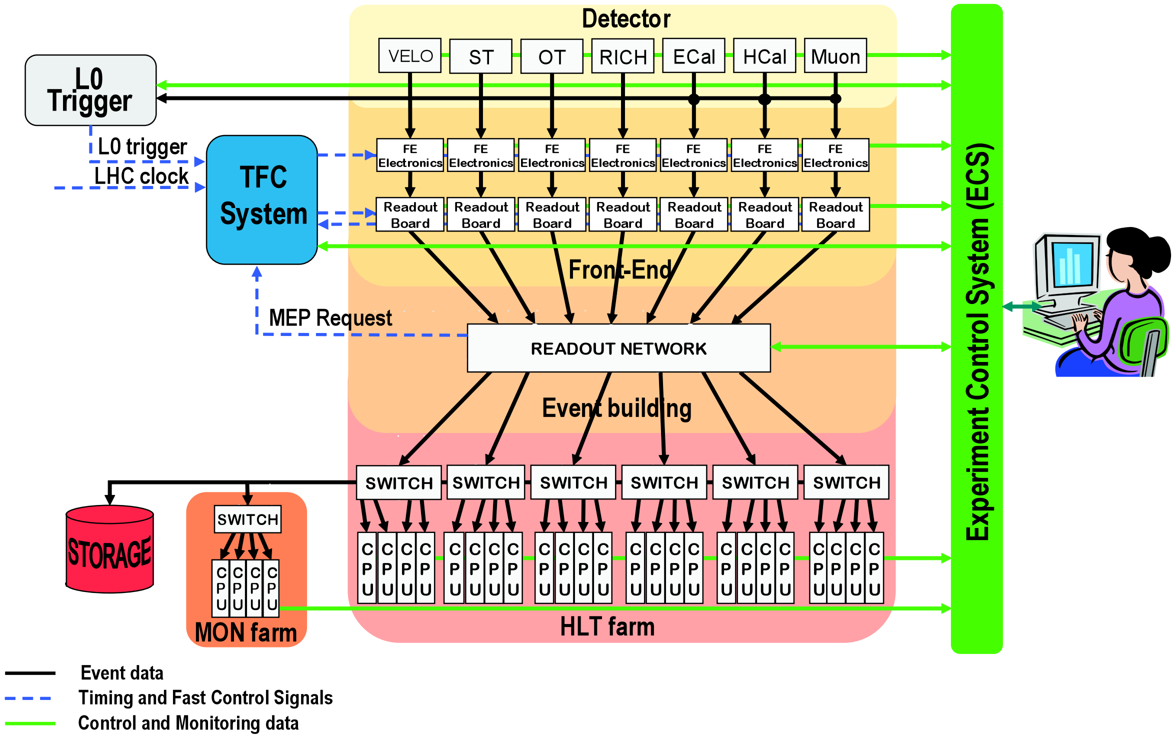

Figure 10.1: The LHCb Online system as from 2009. The individual components are explained in the text.

a behavioural modeling of any software or hardware device in the system as a finite state machine [242], which allows for automation and uniform operation. In this manner a single operator can run the entire experiment, assisted by a second person, who monitors the data quality.

Apart from obvious upgrades in the software (operating system, PVSS) the future of the controls interfaces might necessitate new developments. In general any controls interface must be controllable from a standard PC (personal computer). Ideally no internal cards (PCI, PCIe or similar) should be required—this allows virtual machines to be used. Virtualization will be important as the overall load on the control system is not expected to grow as much as the power of individual servers. The integration of the GBT [132] as a controls interface will need to be done, and it could in principle replace the SPECS [243] protocol currently in use for electronics in radiation areas. New or modified detectors will need to be integrated, but can build on the experience gained to date, and (partially at least) on the use of the existing frameworks.

10.2 Timing and Fast Control

Synchronous, fast signals such as the trigger decisions and the clock are transmitted by the Timing and Fast Control System (TFC) [244] which physically is implemented around the optical, radiation-hard TTC (Timing, Trigger and Control) technology developed for the first generation of LHC experiments. The TFC protects the fixed-latency buffers of the LHCb hardware trigger (L0) and allows other elements in the system to protect their buffers from overflow by sending a throttle signal.

Furthermore in LHCb, unlike the other LHC experiments, the TFC system is also used to regulate the data-flow by assigning destination addresses in the event-filter farm to the readout boards. This is implemented using custom-made FPGA based electronics.

While the basic principles are kept, the full readout at 40 MHz, and consequently the new readout architecture and technologies, requires a complete redesign of the TFC hardware and a redesign of the readout control functions.

The details of the TFC upgrade are described in [245] and in Chapter 4. In place of the current system of Readout Supervisors, switch modules, and optical encoder/transmitter modules, the new TFC system will contain a single TFC multi-master with an internal switch fabric to support the possibility to run autonomously any set of sub-systems in parallel for commissioning, calibration and test purposes. The TFC multi-master incorporates interfaces towards the LHC RF system, the LHC beam-synchronous timing and control, and the new Low Level Trigger (LLT) sub-triggers. During global data-taking, only one sub-master drives the readout electronics of all sub-systems by transmitting control and reset commands, including special commands for calibration and non-zero suppressed readout. In order to optimize the readout band-width, protect against data congestion, and allow flexibility during the commissioning phase, the TFC master incorporates a readout rate control which is based on the LHC collision scheme, the LLT and buffer status information collected from TELL40 boards.

An interface board in each TELL40 crate assures the connection with the Front-End electronics via the GBT link and the fan-out/fan-in requirements towards the Back-End modules. The TFC interface board will also incorporate optional TFC master logic such that it can be used to drive a test bench or a local test during installation.

The aim is also to maintain the interface towards the current TFC distribution network in order to support the current trigger and readout electronics in parallel during the upgrade phase. If the DAQ will employ a push-architecture, as in the current system, the TFC master will drive the DAQ by transmitting to the Back-End modules the destination identifier of the farm node to which the next batch of events should be sent.

Similar to the TELL40, the TFC multi-master will have output links towards the event-filter farm in order to transmit a TFC data bank for each event, which is appended to the event during the event building. It will contain information about the identity of the event, UTC time, event type, trigger information etc. Since the TFC master holds all the global information about the data taking and trigger, it will also produce running and performance statistics, and online luminosity.

10.3 Data Acquisition

The data acquisition of the current experiment is based on Gigabit Ethernet and a push-architecture, where data are buffered in the network devices [246]. The readout-boards (TELL1 [247]) are connected directly to a core-network, which provides the necessary buffering to cope with the massive inrush of packets from these boards. The boards push the data as soon as they receive a destination, which happens at the same moment, since the TFC system synchronously assigns this information. Several triggers are coalesced and sent to one of 1350[1] servers in the event-filter farm. Events are re-assembled there and distributed to worker-threads which run the trigger algorithms. An adjustable fraction of the events, nominally 2 kHz, is retained and written to a high-performance storage system, consolidated into files and then sent on to the Tier-0 at CERN/IT.

Keeping the basic architecture of a single stage read-out over a dedicated local area network, in the following the key characteristics of the upgraded DAQ will be described.

10.3.1 Network

110 TELL40 boards as introduced in Chapter 4 will generate a raw input data rate into the TELL40s of roughly 34 Tbit/s. Since the events are zero-suppressed in the front-end, in this chapter no significant data-reduction in the TELL40 boards is assumed. In this sense the numbers in the following are worst-case. Assuming 10-Gigabit/s links, as is the case for 10-Gigabit/s Ethernet, we arrive at 5280 10-Gigabit/s links into the DAQ network assuming a link-load factor of about 0.7.

The baseline technology for the readout-network is 10-Gigabit Ethernet. An alternative readout based on Infiniband is also studied. Infiniband offers higher link-speed and switches are very cheap however it potentially requires more buffering in the TELL40 boards.

Full connectivity between the event-filter farm nodes is not required so the network can be split into several smaller networks ("slices"), where each TELL40 board is connected to every slice. This is ideal for staging the deployment of the readout network and the farm. Several readout-networks and farms will thus be operated in parallel, as has been demonstrated by the CMS experiment. This is made easily possible in LHCb as the TELL40 boards must have many outputs to cope with the traffic. Each output link (or group of output links) is connected to an independent readout network, with its own farm attached, as shown in Fig. 10.2.

A single slice can then be implemented either using a monolithic core-router as is done in LHCb today or as an aggregate of smaller (and cheaper) switches. The choice between these two solutions is subject to R&D to demonstrate the technical feasibility and will ultimately be based on the overall cost and performance.

It is not clear that a push-protocol will be maintainable at the data-rates in question and so pull architectures (and more generally traffic-shaping methods) will be studied as well. This requires significant buffering on the TELL40s. Details on readout protocol studies and possible network architectures can be found in [248].

---

[1] Status at the end of 2010.

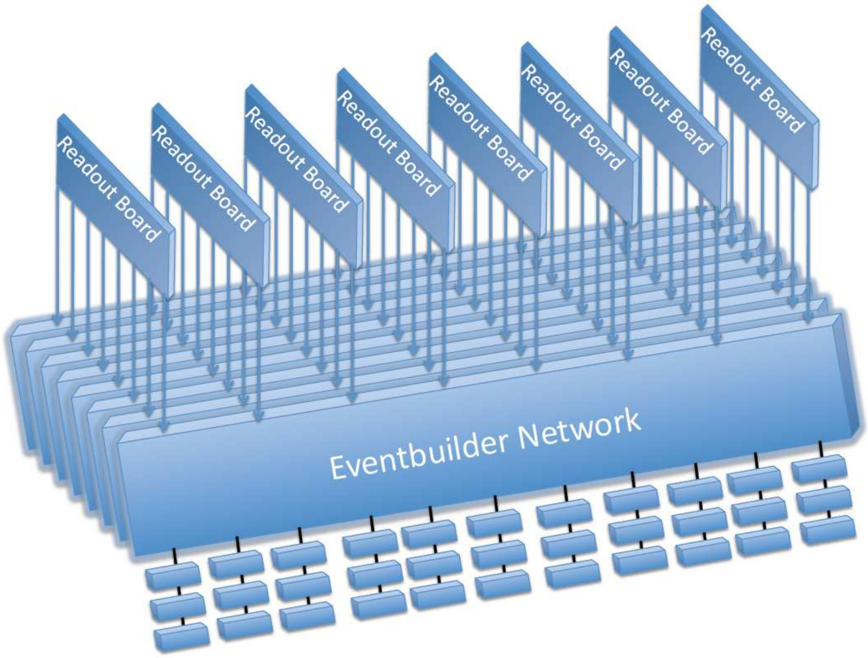

Figure 10.2: Upgrade readout-network with eight slices (and eight independent event-filter farms).

10.3.2 Farm

The event-filter farm will need to grow significantly. Assuming that Moore's "law" will continue to hold, this will give a factor 7 to 8 increase in performance of a single node over the roughly seven years until the upgrade is installed. Moreover the current installation at in UX85A (at Point 8 of the LHC) is limited in cooling power, space and electrical power. On the timescale of the upgrade a farm sufficient for a LLT rate of 5 MHz can easily be housed in the current farm location at Point 8. Higher LLT rates would require additional CPU power elsewhere, or an upgrade of the facilities in UX85A.

10.3.3 Storage

The storage system already today can store more than 1 GB/s, far beyond what is required. Experience has shown that peak-loads can be much higher than average and that it is important to be able to evacuate the large buffers in the farm very quickly (which requires fast storage). Assuming a worst case scenario of 20 kHz to storage of events of 100 kB size a system which can handle 4 GB/s is required (to be able to write and at the same time read the data for checks and copying to the Grid). This capacity can be easily acquired at moderate cost, even today.

10.4 Online IT Infrastructure

The Online IT infrastructure consists of servers for general purpose work, terminal stations, data-bases and all services required for an independent running of the Online system at Point

8. Apart from usual modernization no changes are foreseen. To ease management and reduce administration and hardware cost the virtualization program already started for the experiment will be continued and extended. Operational experience has shown that there is a significant need for general purpose CPU power for "non-standard" calibration jobs and quick analyses which are currently done on a small dedicated online cluster. This facility will need to be maintained and extended.

10.5 Offline Computing

The resources required for offline computing, described in [249], will need to grow with the amount of data produced by the upgraded LHCb.

An HLT output rate of 20 kHz, with a raw event size of 100 kB, corresponds to an instantaneous data rate of 2 GB/s to offline storage, similar to the Alice data rate during heavy-ion running. The LHCb data recording capacity at CERN-Tier0 must be upgraded to accommodate this rate. With 5×10^6 seconds per year of data taking, the storage requirement for two copies of the raw data is 20 PB/year. We assume that improvements in the reconstruction program will allow us to reconstruct events in the upgraded detector (at 14 TeV centre-of-mass energy, pile-up $\mu = 2$, with spillover from adjacent beam crossings) in about the same time as events taken in 2010 at 7 TeV, $\mu = 2$, without spillover, i.e. 25 HepSpec06 (HS06) seconds per event. In order to keep up with the 20 kHz event rate, the prompt reconstruction requires a CPU capacity of 250 kHS06 (about 25,000 cores in 2010) if one accepts that the reconstruction results become available after a time which is twice the duration of the corresponding physics fill. This is roughly 12 times the capacity available to LHCb at CERN-Tier0 in 2010. If the reconstruction adds 100 kB/event (compared to 60 kB in 2010), each reconstruction pass will produce 10 PB per year to be kept on tape; with a stripping reduction factor of 10 (as in 2010), the raw+reconstructed data reduces to 2 PB of stripped DST per year. If we assume one full reprocessing per year and a minimum of two copies for each dataset, we estimate a disk storage requirement for DST of 8 PB/year. Further data reduction is required to produce datasets whose size is manageable for end-user analysis. If one wants to produce datasets of comparable size to that expected in 2011, a further reduction of a factor 10 would be required in the stripping.

We expect that resources for reprocessing, stripping and end-user analysis will continue to be provided outside CERN and we envisage that the necessary network capacity will be provided by the natural evolution of the OPN and national networks. The factor 10 increase in trigger rate leads to a corresponding increase in the global CPU requirements. The increase in disk requirements, taking into account the bigger DST event size, is a factor 15, but this could be reduced if a more aggressive stripping strategy can be achieved.

Chapter 11

Simulations

Full simulation software for the present LHCb detector provided a starting point for simulations of the upgraded LHCb detector. Monte Carlo data were generated for luminosities of up to 10 times larger than the design luminosity of the existing detector. Each sub-detector was inspected for increase in occupancy. Since the present MC has been proven to somewhat underestimate occupancies in certain subsystems, we stretched the range of luminosities covered by the upgrade MC to values higher than the upgrade luminosity goal. Deteriorations in reconstruction efficiencies and HLT timing were also measured. These exercises identified bottlenecks in the present detector layout, in addition to those already known from readout electronics and radiation tolerance. Furthermore, real LHCb data taken with beam conditions producing a large number of primary interactions per crossing offered more insight into the present limitations. Overcoming these limitations is an iterative and on-going process.

Various upgrade options are often first investigated with simplified stand-alone simulations or private modifications of the public LHCb software. The selected options are being put under more scrutiny. We are working towards full simulation of a complete upgraded detector. We chose to implement the upgrade as an option to the existing LHCb software applications, rather than starting new ones. This way the upgrade software stays up to date with rapidly evolving software for the existing detector. Improvements being implemented for the MC generators and in the sub-detector modelling automatically propagate to the upgrade software. The existing software applications (Gauss, Boole and Brunel) were designed to be modular [249]. The upgrade simulations exploited and improved this structure. The existing sub-detectors can be replaced by their upgraded versions in the configuration phase. As part of official LHCb software releases, the upgrade software gets automatically distributed over the LHC Computing Grid, which allows generation of large statistics data samples via normal production procedures.

Our first implementation of the upgrade option in the LHCb software was based on changes which could be implemented without major modifications of the detector geometry definition and reconstruction software. We call this model the "Minimal Upgrade Layout". The thickness of the RF foil inside the vertex detector was cut in half, as indicated by the preliminary upgrade design studies. We generated MC data with and without aerogel radiator in RICH-1. Lighter beam-pipe supports in the magnet region were implemented. Positions of Inner and Outer Tracker (IT/OT) in each T-station were swapped to decrease occupancy in the OT straws. The OT gate was changed from 75 ns to 50 ns assuming better time alignment of individual channels. All silicon detectors were assumed to sample the signal in each strip at 40 MHz. A

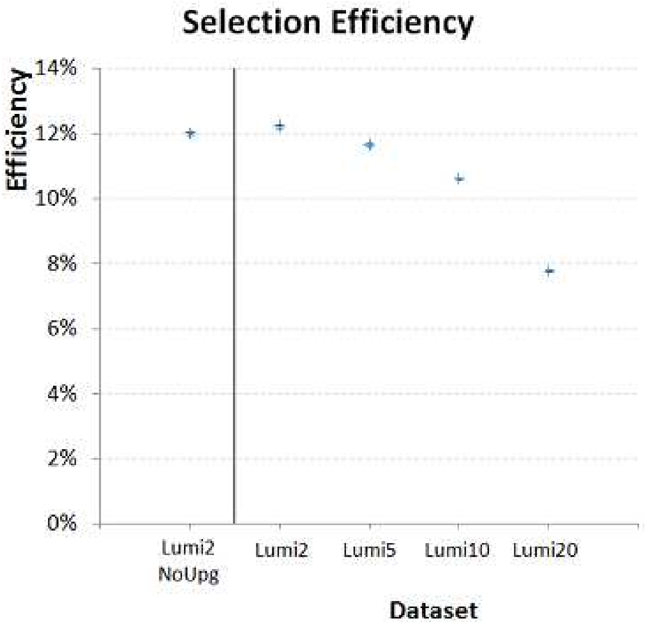

Figure 11.1: Reconstruction efficiency for $B_s \rightarrow \phi\phi$ for the present LHCb detector (the point on the left), and for Minimal Upgrade Layout simulations for the various luminosities (the points to the right of the vertical bar). The luminosity labels on the horizontal axis are given in units of 10^{32} cm^{-2} s^{-1}.

model of spill-over subtraction taking advantage of this rapid sampling rate was implemented. For the IT it was sufficient to subtract a fraction of a pulse from the previous bunch crossing. For VELO and TT we also subtracted a fraction of the pulse seen in the next bunch crossing. The spillover subtraction reduced the occupancy at a luminosity of 2×10^{33} cm^{-2}s^{-1} and 25 ns bunch-crossing spacing by 22%, 42% and 20% in VELO, TT and IT, respectively. The remaining spillover contributions are 3%, 7% and 4%, correspondingly. The same reconstruction software was used as applied to the real LHCb data.

From these simulations we learned that while the Inner Tracker occupancy would be well under control even at 2×10^{33} cm^{-2}s^{-1}, the OT occupancy becomes a limiting factor for luminosities above 1×10^{33} cm^{-2}s^{-1}. This is illustrated in Fig.11.1, in which the reconstruction efficiency for $B_s \rightarrow \phi\phi$ is plotted as a function of the luminosity. The rapid deterioration at the highest luminosity was traced to a loss of hits in the Outer Tracker, since only the first hit in a straw can be recorded within the 50 ns readout gate.

Work to replace the existing VELO detector (based on R- and phi-strips) with a pixel detector in the full simulation is fairly advanced. The geometry of the most recent design has been implemented as illustrated in Figs. 11.2 and 11.3. Charge spread in the sensor is taken from the existing VELO software and produces results which are in good agreement with the TIMEPIX test beam results (see Fig. 11.4). A more sophisticated charge-spread simulation is also pursued, which will allow better understanding of possible radiation damage effects. The detector dead-time and time-walk effects are simulated. An idealized read-out chain and temporary raw data formats are used. A realistic read-out chain is being studied in stand-alone simulation by taking individual pixel hits from full simulation for input. The pixel hits have been integrated with the existing track fitting software. So far, we have been using idealized pattern recognition using MC truth information. Real pattern recognition algorithms are being developed in order to evaluate gains from the 3-dimensional nature of the pixel hits in the track reconstruction, as are used in the current trigger and offline analysis (the simulations presented above and in the other chapters are based on the existing strip vertex detector and the true pattern recognition used on the real data). Comparison between upgrade simulations with the present VELO detector and VELOPIX shows that similar momentum, vertex and direction resolutions are expected as illustrated in Figs.11.5 and 11.6.

Implementing changes in the other sub-detectors in full simulation is as yet subject to working-out design details. Full simulation of all of the upgraded sub-detectors is in progress.

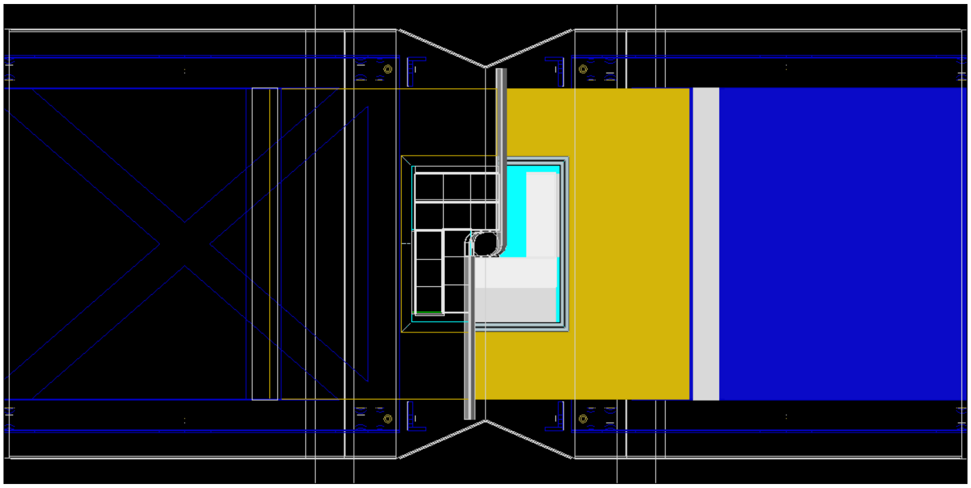

Figure 11.2: (x, y) view of the pixel station as implemented in LHCb upgrade simulation (based on GEANT4 [250]). The left half-plane shows the layout of the VELOPIX chips on the L-shaped sensor. The support structure is also shown.

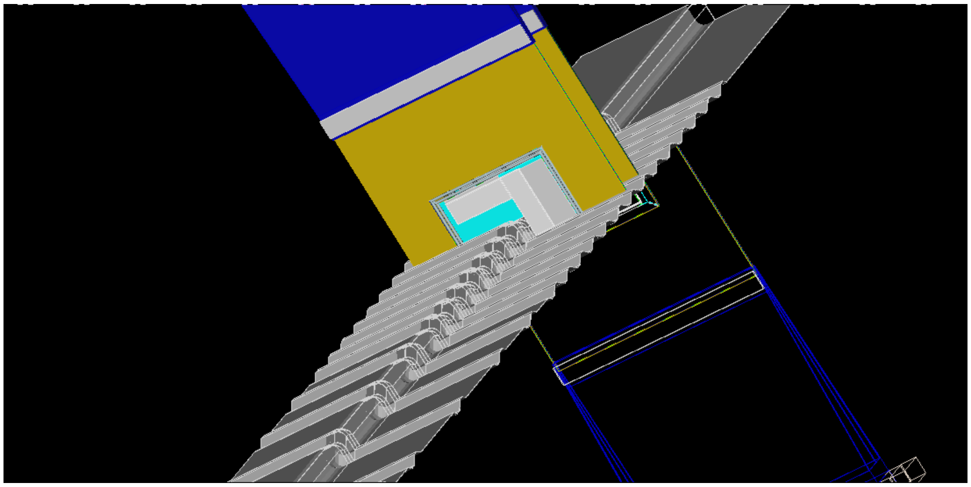

Figure 11.3: 3D view of the RF foil as implemented in the LHCb upgrade simulation. Three selected sensor planes together with the mechanical support are also shown.

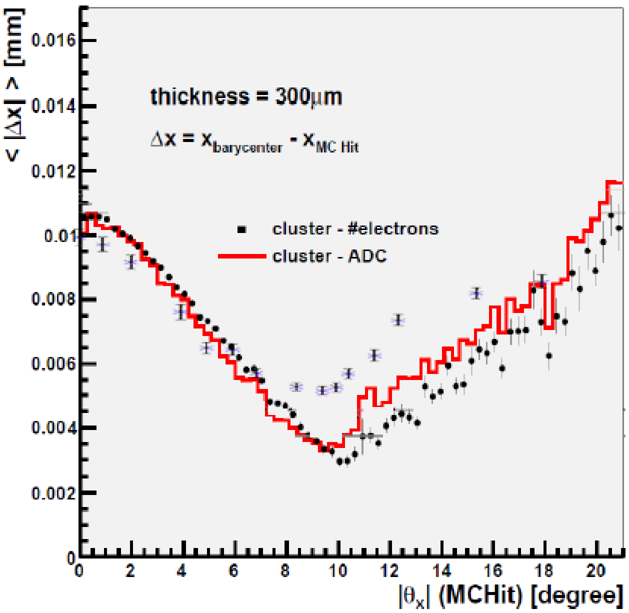

Figure 11.4: Single hit resolution for the VELOPIX detector as a function of the inclination angle to the sensor. The red line shows the simulation results when 4 bits are used to encode the charge measured in each pixel (the black point with error bars were obtained without degrading the charge resolution). The grey points with crosses and error bars represent the hit resolution measured in the VELOPIX with test beam.

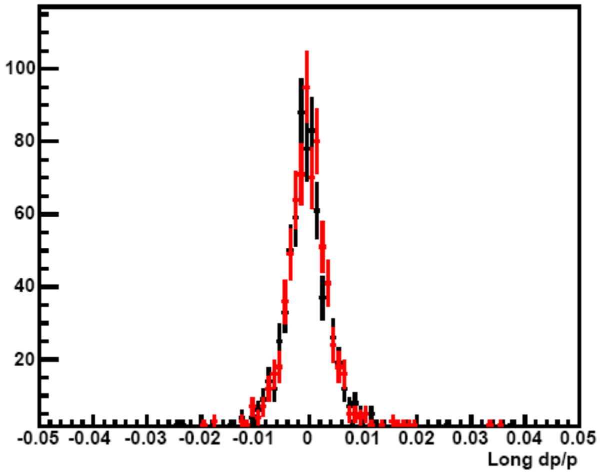

Figure 11.5: Comparison of the momentum resolution ($\Delta p/p$) for long tracks (i.e. reaching the T-stations behind the magnet) for the upgrade simulation, between the VELOPIX detector (red points) and the present VELO detector (black points).

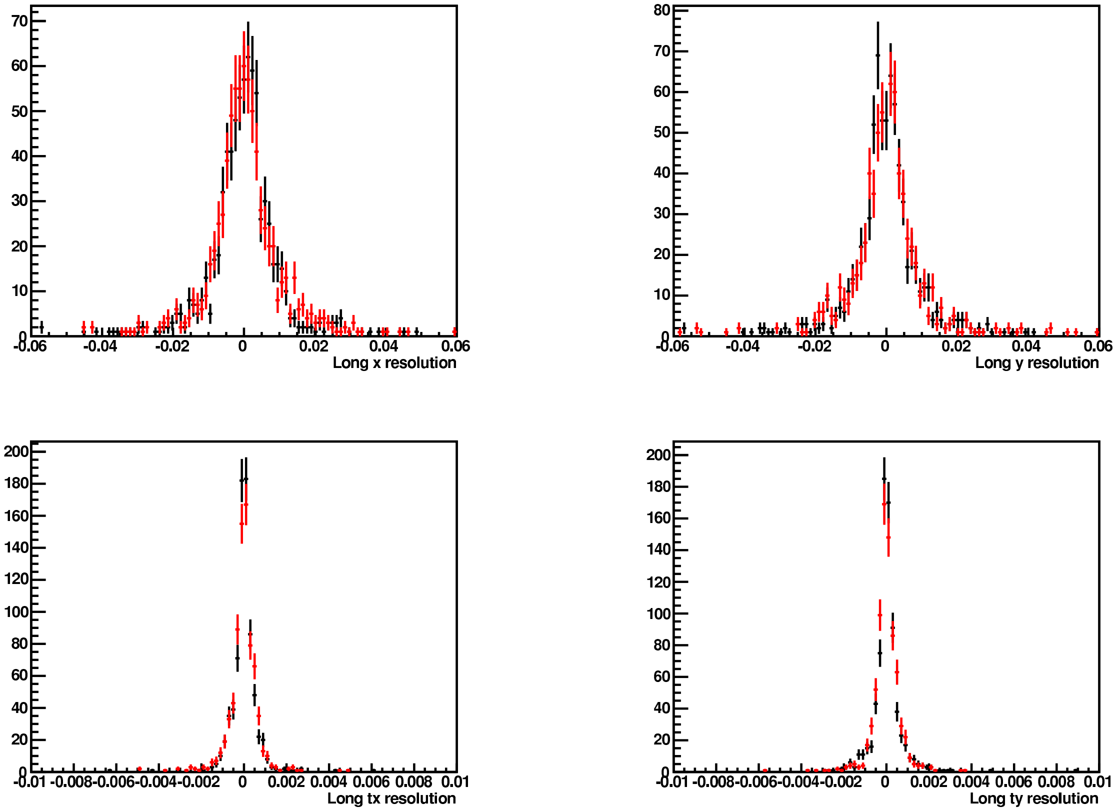

Figure 11.6: Comparison of position (top plots: Δx and Δy) and slope (bottom plots) resolutions at the track origin for the upgrade simulation, between the VELOPIX detector (red points) and the present VELO detector (black points).

Chapter 12

Conclusion

The LHCb experiment is currently taking data successfully at the LHC. After the experiment has run for about five years at its design luminosity it is proposed to upgrade the experiment to run at higher luminosity. The upgraded detector is planned to be installed in the second long shutdown of the LHC machine, that is foreseen in the second half of this decade. Since the LHCb detector is spread out along the beam line, it is possible to work on several detectors at the same time, so that the total time for disassembly of the existing components and installation of the new ones is minimized. Nevertheless, in the first long shutdown we intend to do as much of the infrastructure work as possible in order to speed up the eventual installation.

The main focus of the upgrade is to increase the read-out of the experiment to 40 MHz, so that the increase in luminosity can be exploited with an improved trigger. All detector elements are needed to achieve full performance with the 40 MHz readout. A staging strategy has been developed that will allow individual elements to be installed when received and when installation time is available, so that experience can be gained in running them. This will be achieved by reading out all the detectors at the current 1 MHz readout rate, even if they have 40 MHz capabilities, until the upgrade installation is complete. The TORCH detector could be installed later if it is not available on time, with some impact on the particle identification performance at low momentum. R&D has started to verify the feasibility of this and other detector developments.

The physics case for the LHCb upgrade points to the compelling necessity for the experiment to measure the effects of any new particles seen by any of the LHC detectors. Such New Physics will require thorough study to identify and classify, and the upgraded LHCb would be the ideal experiment to perform this task using flavour physics observables, especially since B_s decays are an important element of this work. The forward geometry, particle-identification capabilities and flexible trigger of the upgraded detector will also give LHCb unique and complementary capabilities in important topics beyond flavour physics.

That LHCb has taken data and demonstrated its abilities even under the challenging circumstances of many interactions per crossing, and is at a machine that will provide the needed luminosity, points to the LHCb Upgrade as being a golden opportunity for high energy physics.

Bibliography

[1] H. Baer *et al.*, Phys. Rev. D**71** (2005) 095008; H. Baer *et al.*, JHEP **0507** (2005) 065; J.R. Ellis, K.A. Olive and P. Sandick, Phys. Rev. D **78** (2008) 075012.

[2] G.L. Bayatian *et al.* (CMS Collaboration), "CMS Technical Design Report, Volume II: Physics Performance", CERN-LHCC-2006-021.

[3] O. Buchmueller *et al.*, arXiv:0907.5568 [hep-ph].

[4] T. Hurth and M. Nakao, Ann. Rev. Nucl. Part. Sci. **60** (2010) 645 [arXiv:1005.1224 [hep-ph]].

[5] J. Charles *et al.* (CKMfitter Group), Eur. Phys. J. C **41** (2005) 1 [arXiv:hep-ph/0406184]. Updated results and plots available online at `http://ckmfitter.in2p3.fr`

[6] M. Bona *et al.* (UTfit Collaboration), JHEP **0610** (2006) 081 [arXiv:hep-ph/0606167]. Updated results and plots available online at `http://www.utfit.org/`

[7] CDF public note 10206, `http://www-cdf.fnal.gov/physics/new/bottom/100513`; see also: T. Aaltonen *et al.* (CDF Collaboration), Phys. Rev. Lett. **100** (2008) 161802 [arXiv:0712.2397 [hep-ex]].

[8] D0 conference note 6098, `http://www-d0.fnal.gov/Run2Physics/WWW/results/`; see also: V. M. Abazov *et al.* (D0 Collaboration), Phys. Rev. Lett. **101** (2008) 241801 [arXiv:0802.2255 [hep-ex]].

[9] V. M. Abazov *et al.* (D0 Collaboration), Phys. Rev. D **82** (2010) 032001 [arXiv:1005.2757 [hep-ex]].

[10] V. M. Abazov *et al.* (D0 Collaboration), Phys. Rev. Lett. **105** (2010) 081801 [arXiv:1007.0395 [hep-ex]].

[11] B. Adeva, *et al.* (LHCb Collaboration), "Roadmap for selected key measurements of LHCb," arXiv:0912.4179 [hep-ex].

[12] R. Aaij *et al.* (LHCb Collaboration), Phys. Lett. B **694** (2010) 209 [arXiv:1009.2731 [hep-ex]].

[13] A. A. Alves Jr. *et al.* (LHCb Collaboration), "The LHCb Detector at the LHC", JINST **3** (2008) S08005.

[14] N. Cabibbo, Phys. Rev. Lett. **10** (1963) 531; M. Kobayashi and T. Maskawa, Prog. Theor. Phys. **49** (1973) 652.

[15] G. Buchalla *et al.*, Eur. Phys. J. C **57** (2008) 309 [arXiv:0801.1833 [hep-ph]].

[16] M. Antonelli *et al.*, Phys. Rept. **494** (2010) 197 [arXiv:0907.5386 [hep-ph]].

[17] G. D'Ambrosio, G. F. Giudice, G. Isidori and A. Strumia, Nucl. Phys. B **645** (2002) 155 [arXiv:hep-ph/0207036].

[18] G. Isidori, Y. Nir and G. Perez, arXiv:1002.0900 [hep-ph].

[19] A. Lenz *et al.*, arXiv:1008.1593 [hep-ph].

[20] S. R. Choudhury and N. Gaur, Phys. Lett. B **451** (1999) 86 [arXiv:hep-ph/9810307]; K. S. Babu and C. F. Kolda, Phys. Rev. Lett. **84** (2000) 228 [arXiv:hep-ph/9909476]; C. S. Huang, W. Liao, Q. S. Yan and S. H. Zhu, Phys. Rev. D **63** (2001) 114021 [Erratum-ibid. D **64** (2001) 059902] [arXiv:hep-ph/0006250].

[21] A. J. Buras, Prog. Theor. Phys. **122** (2009) 145 [arXiv:0904.4917 [hep-ph]].

[22] V. M. Abazov *et al.* (D0 Collaboration), Phys. Lett. B **693** (2010) 539 [arXiv:1006.3469 [hep-ex]].

[23] D. M. Straub, arXiv:1012.3893 [hep-ph].

[24] A. Soni, A. K. Alok, A. Giri, R. Mohanta and S. Nandi, Phys. Rev. D **82** (2010) 033009 [arXiv:1002.0595 [hep-ph]]; A. J. Buras, B. Duling, T. Feldmann, T. Heidsieck, C. Promberger and S. Recksiegel, JHEP **1009** (2010) 106 [arXiv:1002.2126 [hep-ph]]; W. S. Hou and C. Y. Ma, Phys. Rev. D **82** (2010) 036002 [arXiv:1004.2186 [hep-ph]].

[25] S. Nandi and A. Soni, arXiv:1011.6091 [hep-ph].

[26] I. Dunietz, R. Fleischer and U. Nierste, Phys. Rev. D **63** (2001) 114015 [arXiv:hep-ph/0012219].

[27] L. Wolfenstein, Phys. Rev. Lett. **51** (1983) 1945; A. J. Buras, M. E. Lautenbacher and G. Ostermaier, Phys. Rev. D **50** (1994) 3433 [arXiv:hep-ph/9403384].

[28] LHCb Collaboration, LHCb-CONF-2011-005.

[29] K. Nakamura *et al.*, (Particle Data Group), J. Phys. **G 37**, 075021 (2010)

[30] R. Aaij *et al.* (LHCb Collaboration), arXiv:1102.0206 [hep-ex], submitted to Phys. Lett. B.

[31] S. Stone and L. Zhang, Phys. Rev. D **79**, 074024 (2009) [arXiv:0812.2832 [hep-ph]].

[32] Y. Xie, P. Clarke, G. Cowan and F. Muheim, JHEP **0909**, 074 (2009) [arXiv:0908.3627 [hep-ph]].

[33] S. Faller, R. Fleischer and T. Mannel, Phys. Rev. D **79** (2009) 014005 [arXiv:0810.4248 [hep-ph]].

[34] K. De Bruyn, R. Fleischer and P. Koppenburg, arXiv:1012.0840 [hep-ph].

[35] R. Fleischer, Nucl. Phys. B **659** (2003) 321 [arXiv:hep-ph/0301256].

[36] A. Lenz and U. Nierste, JHEP **0706** (2007) 072 [arXiv:hep-ph/0612167].

[37] R. Aaij *et al.* (LHCb Collaboration), arXiv:1102.0348 [hep-ex], submitted to Phys. Lett. B.

[38] R. W. Lambert, CERN-THESIS-2009-001.

[39] N. Brook, N. Cottingham, R. W. Lambert, F. Muheim, J. Rademacker, P. Szczypka and Y. Xie, CERN-LHCB-2007-054.

[40] W. S. Hou, Phys. Rev. D **48** (1993) 2342; M. Tanaka, Z. Phys. C **67** (1995) 321 [arXiv:hep-ph/9411405]; K. Kiers and A. Soni, Phys. Rev. D **56** (1997) 5786 [arXiv:hep-ph/9706337].

[41] B. Grzadkowski and W. S. Hou, Phys. Lett. B **283** (1992) 427; R. Garisto, Phys. Rev. D **51** (1995) 1107 [arXiv:hep-ph/9403389]; C. H. Chen and C. Q. Geng, JHEP **0610** (2006) 053 [arXiv:hep-ph/0608166]; U. Nierste, S. Trine and S. Westhoff, Phys. Rev. D **78** (2008) 015006 [arXiv:0801.4938 [hep-ph]].

[42] LHCb Collaboration, LHCb-CONF-2011-011.

[43] Heavy Flavour Averaging Group, arXiv:1010.1589 [hep-ex], `http://www.slac.stanford.edu/xorg/hfag/`

[44] Y. Grossman and M. P. Worah, Phys. Lett. B **395** (1997) 241 [arXiv:hep-ph/9612269]; R. Fleischer, Int. J. Mod. Phys. A **12**, 2459 (1997) [arXiv:hep-ph/9612446]; D. London and A. Soni, Phys. Lett. B **407**, 61 (1997) [arXiv:hep-ph/9704277]; M. Ciuchini, E. Franco, G. Martinelli, A. Masiero and L. Silvestrini, Phys. Rev. Lett. **79** (1997) 978 [arXiv:hep-ph/9704274].

[45] M. Raidal, Phys. Rev. Lett. **89** (2002) 231803 [arXiv:hep-ph/0208091].

[46] M. Bartsch, G. Buchalla and C. Kraus, arXiv:0810.0249 [hep-ph]; M. Beneke, G. Buchalla, M. Neubert and C. T. Sachrajda, Nucl. Phys. B **591**, 313 (2000) [arXiv:hep-ph/0006124].

[47] N. Styles *et al.*, LHCb-PUB-2009-025.

[48] R. Fleischer, Phys. Rev. D **60** (1999) 073008 [arXiv:hep-ph/9903540]; M. Ciuchini, M. Pierini and L. Silvestrini, Phys. Rev. Lett. **100**, 031802 (2008) [arXiv:hep-ph/0703137].

[49] A. V. Gritsan and J. G. Smith, “Polarization in B Decays,” in Ref. [29]; H. Y. Cheng and J. G. Smith, Ann. Rev. Nucl. Part. Sci. **59** (2009) 215 [arXiv:0901.4396 [hep-ph]].

[50] N. G. Deshpande, N. Sinha and R. Sinha, Phys. Rev. Lett. **90** (2003) 061802 [arXiv:hep-ph/0207257]; M. Ciuchini, M. Pierini and L. Silvestrini, Phys. Rev. D **74** (2006) 051301 [arXiv:hep-ph/0601233]; M. Ciuchini, M. Pierini and L. Silvestrini, Phys. Lett. B **645** (2007) 201 [arXiv:hep-ph/0602207]; I. Bediaga, G. Guerrer and J. M. de Miranda, Phys. Rev. D **76** (2007) 073011.

[51] M. Gronau and D. London, Phys. Lett. B **253** (1991) 483; M. Gronau and D. Wyler, Phys. Lett. B **265** (1991) 172; D. Atwood, I. Dunietz and A. Soni, Phys. Rev. Lett. **78** (1997) 3257 [arXiv:hep-ph/9612433]; D. Atwood, I. Dunietz and A. Soni, Phys. Rev. D **63** (2001) 036005 [arXiv:hep-ph/0008090]; A. Giri, Y. Grossman, A. Soffer and J. Zupan, Phys. Rev. D **68** (2003) 054018 [arXiv:hep-ph/0303187].

[52] I. Dunietz, Phys. Lett. B **270** (1991) 75; M. Gronau, Phys. Lett. B **557** (2003) 198 [arXiv:hep-ph/0211282]; T. Gershon, Phys. Rev. D **79** (2009) 051301 [arXiv:0810.2706 [hep-ph]]; T. Gershon and M. Williams, Phys. Rev. D **80** (2009) 092002 [arXiv:0909.1495 [hep-ph]].

[53] R. Aleksan, I. Dunietz and B. Kayser, Z. Phys. C **54** (1992) 653.

[54] J. Shigemitsu, at CKM workshop 2010, Warwick
`http://indico.cern.ch/contributionDisplay.py?contribId=3&confId=96378`

[55] A. J. Buras, M. V. Carlucci, S. Gori and G. Isidori, JHEP **1010** (2010) 009.

[56] J. R. Ellis, K. A. Olive and V. C. Spanos, Phys. Lett. B **624** (2005) 47 [arXiv:hep-ph/0504196].

[57] R. Aaij *et al.* (LHCb Collaboration), in preparation.

[58] CDF Collaboration, CDF Public Note 9892.

[59] V. Abazov *et al.*, (D0 Collaboration), Phys. Lett. B **693** (2010) 539.

[60] R. Hodgkinson and A. Pilaftsis, Phys. Rev. D **78** (2008) 075004.

[61] P. Urquijo, "Open charm and beauty production at LHCb," presented at "Charm and bottom quark production at the LHC," CERN, Dec. 3, 2010, `http://indico.cern.ch/conferenceOtherViews.py?view=standard&confId=111524`

[62] R. Fleischer, N. Serra and N. Tuning, Phys. Rev. D **82** (2010) 034038 [arXiv:1004.3982 [hep-ph]]; R. Fleischer, N. Serra and N. Tuning, arXiv:1012.2784 [hep-ph].

[63] T. Hurth, G. Isidori, J. F. Kamenik and F. Mescia, Nucl. Phys. B **808**, 326 (2009) [arXiv:0807.5039 [hep-ph]]; W. Altmannshofer, A. J. Buras, S. Gori, P. Paradisi and D. M. Straub, Nucl. Phys. B **830** (2010) 17 [arXiv:0909.1333 [hep-ph]].

[64] T. Aaltonen *et al.* (CDF Collaboration) Phys. Rev. Lett. **103** (2009) 031801 [arXiv:0812.4271 [hep-ex]].

[65] M. Beneke, T. Feldmann and D. Seidel, Nucl. Phys. B **612** (2001) 25 [arXiv:hep-ph/0106067]; M. Beneke, T. Feldmann and D. Seidel, Eur. Phys. J. C **41** (2005) 173 [arXiv:hep-ph/0412400].

[66] B. Aubert *et al.* (BABAR Collaboration), Phys. Rev. D **79** (2009) 031102 [arXiv:0804.4412 [hep-ex]]; J. T. Wei *et al.* (BELLE Collaboration), Phys. Rev. Lett. **103** (2009) 171801 [arXiv:0904.0770 [hep-ex]]; T. Aaltonen *et al.* (CDF Collaboration), arXiv:1101.1028 [hep-ex].

[67] F. Kruger and J. Matias, Phys. Rev. D **71** (2005) 094009 [arXiv:hep-ph/0502060]; W. Altmannshofer, P. Ball, A. Bharucha, A. J. Buras, D. M. Straub and M. Wick, JHEP **0901** (2009) 019 [arXiv:0811.1214 [hep-ph]]; A. K. Alok, A. Dighe, D. Ghosh, D. London, J. Matias, M. Nagashima and A. Szynkman, JHEP **1002** (2010) 053 [arXiv:0912.1382 [hep-ph]]; U. Egede, T. Hurth, J. Matias, M. Ramon and W. Reece, JHEP **1010** (2010) 056 [arXiv:1005.0571 [hep-ph]].

[68] U. Egede, T. Hurth, J. Matias, M. Ramon and W. Reece, JHEP **0811** (2008) 032 [arXiv:0807.2589 [hep-ph]].

[69] C. Bobeth, T. Ewerth, F. Kruger and J. Urban, Phys. Rev. D **64** (2001) 074014 [arXiv:hep-ph/0104284]; C. Bobeth, G. Hiller and G. Piranishvili, JHEP **0712** (2007) 040 [arXiv:0709.4174 [hep-ph]].

[70] Q. S. Yan, C. S. Huang, W. Liao and S. H. Zhu, Phys. Rev. D **62** (2000) 094023 [arXiv:hep-ph/0004262]; G. Hiller and F. Kruger, Phys. Rev. D **69** (2004) 074020 [arXiv:hep-ph/0310219].

[71] D. Atwood, M. Gronau and A. Soni, Phys. Rev. Lett. **79**, 185 (1997) [arXiv:hep-ph/9704272]; D. Atwood, T. Gershon, M. Hazumi and A. Soni, Phys. Rev. D **71** (2005) 076003 [arXiv:hep-ph/0410036].

[72] F. Muheim, Y. Xie and R. Zwicky, Phys. Lett. B **664** (2008) 174 [arXiv:0802.0876 [hep-ph]].

[73] D. Melikhov, N. Nikitin and S. Simula, Phys. Lett. B **442** (1998) 381 [arXiv:hep-ph/9807464]; Y. Grossman and D. Pirjol, JHEP **0006** (2000) 029 [arXiv:hep-ph/0005069].

[74] M. Gronau, Y. Grossman, D. Pirjol and A. Ryd, Phys. Rev. Lett. **88** (2002) 051802 [arXiv:hep-ph/0107254]; M. Gronau and D. Pirjol, Phys. Rev. D **66** (2002) 054008 [arXiv:hep-ph/0205065]; E. Kou, A. L. Yaouanc and A. Tayduganov, arXiv:1011.6593 [hep-ph].

[75] D. Atwood, T. Gershon, M. Hazumi and A. Soni, arXiv:hep-ph/0701021; V. D. Orlovsky and V. I. Shevchenko, Phys. Rev. D **77** (2008) 093003 [arXiv:0708.4302 [hep-ph]].

[76] C. D. Lu, Eur. Phys. J. C **24**, 121 (2002) [arXiv:hep-ph/0112127].

[77] L. Hofer, D. Scherer and L. Vernazza, arXiv:1011.6319 [hep-ph].

[78] D. Pirjol and J. Zupan, JHEP **1002** (2010) 028 [arXiv:0908.3150 [hep-ph]].

[79] I. I. Bigi, M. Blanke, A. J. Buras and S. Recksiegel, JHEP **0907** (2009) 097; Y. Grossman, Y. Nir and G. Perez, Phys. Rev. Lett. **103** (2009) 071602; M. Bauer, S. Casagrande, U. Haisch and M. Neubert, JHEP **1009** (2010) 017.

[80] Y. Grossman, A. L. Kagan and Y. Nir, Phys. Rev. D **75** (2007) 036008 [arXiv:hep-ph/0609178].

[81] I. Bediaga, I.I. Bigi, A. Gomes, G. Guerrer, J. Miranda, A.C. dos Reis *et al.*, Phys. Rev. D **80**, 096006 (2009).

[82] I.I. Bigi, in Proceedings of KAON2001: International Conference on CP violaton, Pisa, Italy, 12-17 June 2001, p. 417 (hep-ph/0107102).

[83] A. Bondar, A. Poluektov and V. Vorobiev, Phys. Rev. D **82**, 034033 (2010).

[84] J. Libby *et al.* (CLEO Collaboration), "Model-independent determination of the strong-phase difference between D^0 and $\bar{D^0} \to K^0_{S,L}h^+h^-$ $(h = \pi, K)$ and its impact on the measurement of the CKM angle γ/ϕ_3 ", arXiv:1010.2817 [hep-ex].

[85] M. Petric *et al.* (Belle Collaboration), Phys. Rev. D **81**, 091102(R) (2010).

[86] G. Burdman, E. Golowich, J. Hewett and S. Pakvasa, Phys. Rev. D **66**, 014009 (2002).

[87] I. Dorsner, S. Fajfer, J. F. Kamenik and N. Kosnik, Phys. Lett. **B682**, 67 (2009).

[88] J.C. Pati and A. Salam, Phys. Rev. **D10** (1974) 275; R.N. Mohapatra and J.C. Pati, Phys. Rev. **D 11** (1975) 566, 2558; G. Senjanovic and R.N. Mohapatra, Phys. Rev. **D 12** (1975) 1502.

[89] N. Arkani-Hamed, S. Dimopoulos, G. Dvali and J. March-Russel, Phys. Rev. **D 65** (2002) 024032; Y. Grossman and M. Neubert, Phys. Lett. **B 474** (2000) 361; K. R. Dienes and I. Sarcevic, Phys. Lett. **B 500** (2001) 133; S.J. Huber and Q. Shafi, Phys. Lett. **B 544** (2002) 295; G. Perez and L. Randall, JHEP 01 (2009) 077.

[90] T. Asaka and M. Shaposhnikov, Phys. Lett. **B 620** (2005) 17; T. Asaka, S. Blanchet and M. Shaposhnikov, Phys. Lett. **B 631** (2005) 151; F. Bezrukov, D. Gorbunov, JHEP **1005** (2010) 010. [arXiv:0912.0390 [hep-ph]]; A. Roy, M. Shaposhnikov, Phys. Rev. **D82** (2010) 056014. [arXiv:1006.4008 [hep-ph]].

[91] A. Boyarsky, O. Ruchayskiy and M. Shaposhnikov, Ann. Rev. Nucl. Part. Sci. **59** (2009) 191 [arXiv:0901.0011 [hep-ph]]

[92] M. Shaposhnikov, JHEP **0808** (2008) 008 [arXiv:0804.4542 [hep-ph]].

[93] A. Atre, T. Han, S. Pascoli, and B. Zhang, JHEP, 0905:030 (2009) [arXiv:0901.3589]; A. Atre, V. Barger and T. Han, Phys. Rev. D**71**, 113014 (2005) [arXiv:hep-ph/0502163].

[94] J.-M. Zhang, and G.-L. Wang, arXiv:1003.5570 [hep-ph].

[95] D. Gorbunov and M. Shaposhnikov, JHEP **0710** (2007) 015 [arXiv:0705.1729 [hep-ph]].

[96] A. M. Cooper-Sarkar *et al.* (WA66 Collaboration), Phys. Lett. B **160** (1985) 207; F. Bergsma *et al.* (CHARM Collaboration), Phys. Lett. B **166** (1986) 473; G. Bernardi *et al.*, Phys. Lett. B **166** (1986) 479; G. Bernardi *et al.*, Phys. Lett. B **203** (1988) 332; A. Vaitaitis *et al.* (NuTeV Collaboration), Phys. Rev. Lett. **83** (1999) 4943.

[97] L. Canetti and M. Shaposhnikov, arXiv:1006.0133 [hep-ph].

[98] B. Aubert *et al.* (BABAR Collaboration), Phys. Rev. Lett. **104** (2010) 021802 [arXiv:0908.2381 [hep-ex]]; K. Hayasakai *et al.* (Belle Collaboration),' Phys. Lett. B **687** (2010) 139 [arXiv:1001.3221 [hep-ex]].

[99] B. O'Leary *et al.* (SuperB Collaboration), arXiv:1008.1541 [hep-ex].

[100] H. K. Dreiner, M. Kramer and B. O'Leary, Phys. Rev. D **75**, 114016 (2007) [arXiv:hep-ph/0612278]; M. Raidal *et al.*, Eur. Phys. J. C **57**, 13 (2008) [arXiv:0801.1826 [hep-ph]].

[101] Y. Miyazaki*et al.* (Belle Collaboration), Phys. Lett. B **682**, 355 (2010) [arXiv:0908.3156 [hep-ph]].

[102] The ALEPH, DELPHI, L3, OPAL, SLD Collaborations, the LEP Electroweak Working Group, the SLD Electroweak and Heavy Flavour Group, Phys. Reports **427** 5-6 (2006) 257, hep-ex/0509008.

[103] V. Buge *et al.* (CMS Collaboration), J. Phys. **G 34** (2007) 995; N. Besson *et al.*, arXiv:0805.2093 [hep-ex].

[104] M.W. Krasny, F. Dydak, F. Fayette, W. Placzek and A. Siodmok, Eur. Phys. J. C69 (2010) 379, arXiv:1004.2597 [hep-ex].

[105] K. Zurek, "TASI 2009 Lectures: Searching for Unexpected Physics at the LHC," arXiv:1001.2563v1 [hep-ph].

[106] M. Cvetic, P. Langacker and G. Shiu, Phys. Rev. D **66**, 066004 (2002) [hep-ph/0205252], and references therein; N. Arkani-Hamed, S. Dimopoulos and S. Kachru, [hep-th/0501082]; V. Barger, P. Langacker and G. Shaughnessy, [hep-ph/0702001].

[107] M. J. Strasser and K. M. Zurek, Phys. Lett. B **651**, 374 (2007) [hep-ph/0604261].

[108] M. J. Strasser and K. M. Zurek, Phys. Lett. B **661**, 263 (2008) [hep-ph/0605193].

[109] F. de Campos, O. J. P. Eboli, M. B. Magro, and D. Restrepo, Phys. Rev. D **79**, 055008 (2009)

[110] L. Carpenter, D. Kaplan, and E.-J. Rhee, Phys. Rev. Lett. 99, 211801, (2007) [hep-ph/0607204].

[111] T. Aaltonen *et al.* (CDF Collaboration), Phys. Rev. Lett. **99** (2007) 242002.

[112] T. Aaltonen *et al.* (CDF Collaboration), Phys. Rev. **D 77** (2008) 052004; V. Abazov *et al.* (D0 Collaboration), arXiv:1009.2444 [hep-ex].

[113] T. Aaltonen *et al.* (CDF Collaboration), Phys. Rev. Lett. **102** (2009) 242001.

[114] `http://projects.hepforge.org/superchic`

[115] J.W. Lämsaä and R. Orava, 2009 JINT **4** P11019.

[116] M. Albrow *et al.*, JINST **4** (2009) T10001.

[117] L.A. Harland-Lang, V.A. Khoze, M.G. Ryskin and W.J. Stirling, Eur. Phys. J. **C 69** (2010) 179.

[118] S. Heinemeyer, V.A. Khoze, M.G. Ryskin, M. Tasevesky and G. Weiglein, arXiv:1012.5007 [hep-ph].

[119] L.A. Harland-Lang, V.A. Khoze, M.G. Ryskin and W.J. Stirling, arXiv:1011.0680 [hep-ph].

[120] E. Aslanides *et al.*, Nucl. Instrum. And Meth. A 579 (2007) 989.

[121] J. Albrecht, L. de Paula, A. Pérez-Calero Yzquierdo and F. Teubert, "Commissioning and performance of the LHCb HLT1 muon trigger", LHCb-PUB-2011-006.

[122] V. Gligorov, "A single track HLT1 trigger", LHCb-PUB-2011-003.

[123] M. Williams *et al.*, "The HLT2 topological lines", LHCb-PUB-2011-002.

[124] O. Callot and S. Hansmann-Menzemer, "The forward tracking: algorithm and performance studies", LHCb-2007-015.

[125] X. Cid and J.A. Hernando, "What triggers the Hadron Alley", LHCb-PUB-2011-007.

[126] G. Lanfranchi *et al.*, "The muon identification procedure of the LHCb experiment for the first data", LHCb-PUB-2009-013.

[127] L. Shchutska, A. Golutvin and I. Belyaev, "Study of radiative penguin decays $B^0 \to K^*\gamma$ and $B^0_s \to \phi\gamma$ at LHCb", LHCb-2007-030.

[128] SLD Collaboration, K. Abe *et al.*, "Measurement of R_b using a Vertex Mass Tag", Phys. Rev. Lett. 80:660-665, 1998.

[129] J. Christiansen, "Requirements to the L0 front-end electronics", LHCb Technical Note, LHCb 2001-014.

[130] K. Wyllie *et al.*, "Electronics architecture of the LHCb Upgrade", LHCb-PUB-2011-011, in preparation.

[131] `www.actel.com`

[132] P. Moreira *et al.*, “The GBT Project”, Proceedings of the Topical Workshop on Electronics for Particle Physics, Paris, France, 21 - 25 September 2009, CERN-2009-006.

[133] J. Troska *et al.*, “The Versatile Link Proof of Concept”, Proceedings of the Topical Workshop on Electronics for Particle Physics, Paris, France, 21–25 September 2009, CERN-2009-006.

[134] `http://www.picmgeu.org`

[135] A. Gabrielli *et al.*, “The GBT-SCA, a radiation tolerant ASIC for detector control applications in SLHC experiments”, Proceedings of the Topical Workshop on Electronics for Particle Physics, Paris, France, 21–25 September 2009, CERN-2009-006.

[136] The LHCb Trigger System Technical Design Report, CERN LHCC 2003-031, September 2003.

[137] M. Campbell, “10 years of the Medipix2 collaboration”, Nucl. Instrum. and Meth. A, in print.

[138] P. Collins et. al., “The LHCb VELO Upgrade”, Nucl. Instrum. and Meth. **A** 51628.

[139] M.G. van Beuzekom, “Status and prospects of the LHCb vertex locator”, Nucl. Instrum. and Meth., 21 October 2008, pages 21–24, ISSN 0168-9002.

[140] A. Papadelis, “Characterisation and commissioning of the LHCb VELO detector”, CERN-THESIS-2009-044.

[141] `http://www.ansys.com`

[142] G. Casse, “Radiation hardness of p-type silicon detectors”, Nucl. Instrum. and Meth. A, 612 (2010) 464.

[143] D. Pennicard *et al.*, Nucl. Instrum. and Meth. A **598** (2009) 67.

[144] D. Pennicard *et al.*, Nucl. Instrum. and Meth. A **592** (2008) 16.

[145] D. Pennicard *et al.*, IEEE Trans. Nucl. Sci., **57** (2010) 387.

[146] A. Affolder *et al.*, Nucl. Instrum. and Meth. A (2010), doi:10.1016/j.nima.2010.02.187.

[147] R. Plackett *et al.*, “Measurement of the radiation damage to 130 nm hybrid pixel detector readout chips”, Proc. of the Topical Workshop on Electronics for Particle Physics, Paris, France, 21–25 September 2009, CERN-2009-006.

[148] T. Poikela, “Design and verification of digital architecture of 65K pixel readout chip for high energy physics”, MSc. in Tech. Thesis, Univ. of Turku, October 2010.

[149] K. Akiba *et al.*, “Charged particle tracking with the Timepix ASIC”, to be submitted to Nucl. Instrum. and Meth. A; Mac Raighne *et al.*, “Precision scans of the pixel cell response of double sided 3D sensors to pion and X-ray beams”, to be submitted to Journal of Instrum.

[150] NIKHEF Mechanical Engineering Group (Amsterdam, NL), `http://www.nikhef.nl/pub/departments/mt/projects/lhcb-vertex`

[151] M. Tavlet *et al.*, “Compilation of radiation damage test data, Part 2”, CERN 98-01.

[152] X.-F. Li *et al.*, Composites Science and Technology 68 (2008) 2876.

[153] J. Kaplon, “The ABCN front-end chip for ATLAS inner detector upgrade”, Published in Naxos 2008, Electronics for particle physics, 116–120.

[154] K. Kirsebom *et al.* (LHCb Collaboration), LHCb Letter of Intent: “A Dedicated LHC Collider Beauty Experiment for Precision Measurements of CP-Violation”, CERN/LHCC 95-5, 25 August 1995.

[155] S. Amato *et al.* (LHCb Collaboration), LHCb Technical proposal: “A Large Hadron Collider Beauty Expriment for Precision Measurements of CP-Violation and Rare Decays”, CERN/LHCC 98-4, 20 February 1998.

[156] R.A. Nobrega *et al.* (LHCb Collaboration), Technical Design Report: “LHCb Reoptimized Detector and Performance”, [CERN-LHCC 2002-029], 8 November 2002.

[157] R. Aaij *et al.* (LHCb Collaboration), “Prompt K^0_S production in pp collisions at $\sqrt{s} = 0.9$ TeV”, Phys. Lett. B **693** (2010) 69.

[158] P.R. Barbosa *et al.* (LHCb Collaboration), Technical Design Report: “LHCb Outer Tracker”, [CERN-LHCC-2001-024], September 2001.

[159] M. Needham, “Updated Occupancies for the LHCb Inner Tracker”, LHCb-2005-006, 2005.

[160] M. Needham, “Silicon Tracker Occupancies and Clustering”, LHCb-2007-024, 2007.

[161] R. Hierck, PhD. Thesis, “Optimisation of the LHCb Detector”, NIKHEF (2005).

[162] M. Needham, “Identification of Ghost tracks using a Likelihood Method”, LHCb-2008-026 (2008); M. Needham, “Classification of Ghost Tracks”, LHCb-2007-128 (2007).

[163] J. van Tilburg, “Studies of the Silicon Tracker resolution using data”, LHCB-PUB-2010-016, 2010.

[164] R. Hierck, M. Merk and M. Needham, “Outer Tracker occupancies and detector optimisation”, LHCb-2001-093, 2001.

[165] A. Pellegrino (on behalf of the OT Collaboration), “The Front-End Electronics of the Straw Tube Tracker for the LHCb Experiment”, Nucl. Instrum. and Meth. A **623** (2010), 469.

[166] M. Newcomer *et al.*, “Radiation Hardness: Design Approach and Measurements of the ASDBLR ASIC for the ATLAS TRT”, [Nuclear Science Symposium Conference Record], 2002 IEEE 10-16 Nov. 2002, Volume 1.

[167] H. Deppe, U. Stange, U. Trunk and U. Uwer, “The OTIS Reference Manual”, EDMS 859585, March 2008; U. Stange, “Development and Characterisation of a Radiation Hard Readout Chip for the LHCb Outer Tracker Detector”, PhD. Thesis 2005.

[168] G. Cervelli, A. Marchioro and P. Moreira, “A 0.13 μm CMOS serializer for data and trigger optical links in particle physics experiments”, IEEE Trans. Nucl. Sci., vol. 51, no. 3, pp. 836-841, 2004.

[169] Project MuonLab II, B. van der Heijden, afstudeer verslag, March 30 2006.

[170] D. Breton, D. Charlet, P. Robbe, I. Videau, “SPECS: a serial protocol for experiment control system in LHCb”, 10th ICALEPCS Int. Conf. on Accelerator & Large Expt. Physics Control Systems, Geneva, Switzerland (2005).

[171] ProASIC3 FPGA, `http://www.actel.com/products/pa3`

[172] K.K. Gan, “An MT-style optical package for VCSEL and PIN arrays”, Nucl. Instrum. and Meth. A **607** (2009), 527.

[173] S. Bachmann *et al.*, “The straw tube technology for the LHCb outer tracking system”, Nucl. Instrum. and Meth. A **535** (2004) 171.

[174] S. Bachmann *et al.*, “Ageing in the LHCb Outer Tracker: Phenomenon, Culprit and Effect of Oxygen”, Nucl. Instrum. and Meth. A **617** (2010) 202.

[175] N. Tuning *et al.*, “Ageing in the LHCb Outer Tracker: Aromatic Hydrocarbons and Wire Cleaning”, to appear in Nucl. Instrum. and Meth.

[176] M. Capeans, “Ageing and materials: Lessons for detectors and gas systems”, Nucl. Instrum. and Meth. A **515** (2003) 73.

[177] H.B. Dreis *et al.*, arXiv:hep-ex/9805004.

[178] E.C. Aschenauer *et al.*, arXiv:physics/9801003.

[179] M.Adinolfi *et al.*, Nucl. Instrum. and Meth. A **482** (2002) 364.

[180] P. Achenbach *et al.*, arXiv:0802.2830.

[181] G. Roper Yearwood *et al.*, “A scintillating Fiber Tracker with SiPM Readout”, Nucl. Phys. B **197** (2009) 245; B. Beischer *et al.*, “A high-resolution scintillating fiber tracker with silicon photomultiplier array readout”, Nucl. Instrum. and Meth. A **622** (2010) 542.

[182] J. Bähr and R. Nahnhauer and S. Nerreter and R. Shanidze, “A Fiber Detector Radiation Hardness Test”, Nucl. Instrum. and Meth. A **449** (2000) 260.

[183] H. Gast *et al.*, “Indirect dark matter search with the balloon-borne PEBS detector”, PoS(idm2008) 023.

[184] H. Spieler, Nucl. Instr. and Meth. A **623** (2010) 63.

[185] G. Ruggiero *et al*, Nucl. Instr. and Meth. A **604** (2009) 242.

[186] E. Verbitskaya, V. Eremi, G. Ruggiero, Nucl. Instr. Meth. A **612** (2010) 501

[187] M. Cepeda *et al.*, ATL-UPGRADE-PUB-2008-001 (2008).

[188] C. Irmlera, M. Friedla and M. Pernicka, In TWEPP009 (2009).

[189] R. Lipton, Nucl. Instr. and Meth. A **579** (2007) 690.

[190] G. Casse, Nucl. Instr. and Meth. A **579** (2007) 318.

[191] A. Affolder *et al.*, Nucl. Instr. and Meth. A **583** (2007) 18.

[192] S. Amato *et al.* (LHCb Collaboration), "LHCb RICH Technical Design Report", CERN LHCC 2000-037 (2000).

[193] M. Charles and R. Forty, "TORCH: time-of-flight identification with Cherenkov radiation", proceedings of RICH2010, to be published in Nucl. Instrum. Meth. A, arXiv:1009.3793v1 [physics.ins-det].

[194] B. Aubert *et al.* (BABAR Collaboration), Nucl. Instrum. and Meth. A **479** (2002) 1.

[195] J. Bibby *et al.*, "Performance of Multi-anode Photomultiplier Tubes for the LHCb RICH detectors", Nucl. Instrum. and Meth. A **546** (2005) 93.

[196] N.J. Smale, "Multi-anode photon-multiplier readout electronics for the LHCb ring imaging Cherenkov detectors", PhD. Thesis, St Anne's College, University of Oxford (2004).

[197] C. Arnaboldi *et al.*, "Characterization of a multianode photon multiplier tube with single photon signal", to be published in the Proc. of the 2010 NSS Conference; A. Giachero *et al.*, "Current feedback operational amplifiers as fast charge sensitive preamplifiers for photomultiplier readout", accepted for publication in JINST.

[198] C. Arnaboldi *et al.*, "Cross-talk study of the single-photon response of a flat-panel PMT for the RICH Upgrade at LHCb.", IEEE Transaction on Nuclear Science, V 57, pp 2267-2272, 2010.

[199] MAROC readout chip manual: `http://omega.in2p3.fr`

[200] C. Arnaboldi *et al.*, "An ultra fast, low power readout chain for single photon sensitivity with multi-anode photomultiplier tubes for the RICH upgrade at LHCb", accepted for publication in NIMA, doi:10.1016/j.nima.2010.10.051.

[201] See for example: E. Albrecht *et al.*, Nucl. Instrum. and Meth. A **411** (1998) 249; E. Albrecht *et al.*, Nucl. Instrum. and Meth. A **442** (2000) 164; R.J. Mountain, Nucl. Instrum. and Meth. A **502** (2003) 183; P. Cushman *et al.*, Nucl. Instrum. and Meth. A **442** (2000) 289.

[202] B. Mikulek *et al.*, “A noiseless kilohertz frame rate imaging detector based on microchannel plates read out with the Medipix2 CMOS pixel chip”, Nucl. Instrum. and Meth. A **567** (2006) 110.

[203] Burle-Photonis (Merignac, France), `http://www.photonis.com/`

[204] K. Nishimura (Belle Collaboration), Proc. of RICH2010, 3–10 May 2010, `http://rich2010.in2p3.fr/`

[205] C. Schwarz (PANDA Collaboration), Proc. of RICH2010, 3–10 May 2010, `http://rich2010.in2p3.fr/`

[206] J. Va’vra *et al.*, “A 30 ps timing resolution for single photons with multi-pixel Burle MCP-PMT”, Nucl. Instrum. and Meth. A **572** (2007), 459.

[207] Photek (Hastings, UK), `http://www.photek.com/`

[208] T. Jinno *et al.*, “Lifetime-extended MCP-PMT”, Nucl. Instrum. and Meth., in press, `http://dl.dropbox.com/u/8396580/NIM-A.pdf`

[209] F. Anghinolfi *et al.*, “NINO: an ultra-fast and low-power front-end amplifier/discriminator ASIC designed for the multigap resistive plate chamber”, Nucl. Instrum. and Meth. A **533** (2004) 183.

[210] J.S. Lapington *et al.*, “A high-throughput, multi-channel photon-counting detector with picosecond timing”, Nucl. Instrum. and Meth. A **604** (2009) 199.

[211] Hamamatsu (Japan), `http://www.hamamatsu.com/`

[212] S. Amato *et al.* (LHCb Collaboration), “LHCb calorimeters technical design report”, CERN-LHCC-2000-036.

[213] C. Beigbeder-Beau *et al.*, “The front-end electronics for LHCb calorimeters”, LHCb-2000-028.

[214] R.L. Chase and S. Rescia, “A linear low power remote preamplifier for the ATLAS liquid argon EM calorimeter”, IEEE Trans. Nucl. Sci., 44:1028, 1997.

[215] N. Dressnandt, M. Newcomer, S. Rescia and E. Vernon, “LAPAS: A SiGe Front End Prototype for the Upgraded ATLAS LAr Calorimeter”, TWEPP-09: Topical Workshop on Electronics for Particle Physics, Paris, France, 21–25 Sep 2009.

[216] F. Yuan, “Low-Voltage CMOS Current-Mode Preamplifier: Analysis and Design”, IEEE Transactions on Circuits and Systems, Vol. 53, No. 1, 2006.

[217] C. Beigbeder-Beau *et al.*, “Description of the ECAL/HCAL front-end card”, LHCb-2003-036 (EDMS 909465).

[218] G. Corti and L. Shekhtman, “Radiation background in the LHCb experiment”, LHCb-2003-83, 22 September 2003.

[219] A. Arefev *et al.*, “Design, construction, quality control and performance study with cosmic rays of modules for the LHCb electromagnetic calorimeter”, LHCb-2007-148.

[220] A. Arefev *et al.*, “Beam Test Results of the LHCb Electromagnetic Calorimeter”, LHCb-2007-149.

[221] A. Arefev *et al.*, “Design of PMT base for the LHCb electromagnetic calorimeter”, LHCb-2003-150.

[222] The LHCb Collaboration, “LHCb Muon System Technical Design Report”, CERN/LHCC 2001-010 and “Addendum to LHCb Muon System Technical Design Report”, CERN/LHCC 2003-002.

[223] M. Anelli *et al.*, “Performance of the LHCb muon system with cosmic rays”, JINST 5:P10003, 2010.

[224] G. Martellotti *et al.*, “Particles rate in the LHCb muon detector”, LHCb note 2005-075.

[225] W. Bonivento *et al.*, “Production of the front-end boards of the LHCb muon system”. LHCb Note 2007-150.

[226] A.Balla *et al.*, “The Off Detector Electronics of the LHCb muon Detector”, Nuclear Science Symposium Conference Record, IEEE , vol. 2, (2006) 1296. doi: 10.1109/NSS-MIC.2006.356080.

[227] W. Bonivento *et al.*, “Development of the CARIOCA frontend chip for the LHCb muon detector”, Nucl. Instrum. and Meth. A **491** (2002) 233.

[228] S. Cadeddu *et al.*, “The DIALOG chip in the front-end electronics of the LHCb muon detector”, IEEE Trans. Nucl. Sci., vol. 52 (2005) 2726-2732. doi: 10.1109/TNS.2005.862862.

[229] S. Cadeddu *et al.*, “The SYNC chip in the electronics architecture of the LHCb muon Detector”, to be published on journal IEEE Trans. Nucl. Sci. (2010). doi: 10.1109/TNS.2010.2056930.

[230] P. Moreira *et al.*, “A radiation tolerant gigabit serializer for LHC data transmission”, Proc. of the 7th Workshop on Electronics for LHC Experiments, Stockholm, Sweden (2001) p145.

[231] J.Christiansen *et al.*, “Receiver ASIC for Timing, Trigger and Control Distribution in LHC Experiments”. IEEE Trans. Nuclear Science, vol. 43, (1996) 1773. doi: 10.1109/23.507220.

[232] M. Anelli *et al.*, “High-rate performance of the MWPCs for the LHCb muon system”, Nucl. Instrum. and Meth. A **593** (2008) 319.

[233] V. Souvorov *et al.*, “First results of an aging test of a full scale MWPC prototype for the LHCb muon system”, Nucl. Instrum. and Meth. A **515** (2003) 220.

[234] M. Anelli *et al.*, “High radiation tests of the MWPCs for the LHCb muon system”, Nucl. Instrum. and Meth. A **599** (2009) 171.

[235] K. Mair *et al.*, “Conditioning of MWPCs for the LHCb Muon System”, 2005 IEEE Nuclear Science Symposium, Puerto Rico, Conference Record.

[236] G. Bencivenni, *et al.*, “Performance of a triple-GEM detector for high rate charged particle triggering”, Nucl. Instrum. and Meth. A **494** (2002) 156.

[237] RD51 Proposal, CERN-LHCC-2008-011 (2008).

[238] M. Alfonsi *et al.*, “Activity of CERN and LNF groups on large area GEM detectors”, Nucl. Instrum. and Meth. A **617** (2010) 151.

[239] G. Lanfranchi *et al.*, “The Muon Identification Procedure of the LHCb experiment for the first data”, CERN-LHCb-PUB-2009-013.

[240] P.R. Barbosa-Marinho *et al.*, “LHCb Online system technical design report: Data acquisition and experiment control”, CERN-LHCC-2001-040.

[241] C. Gaspar, “The LHCb Run Control System”, Proc. of IEEE RealTime 2010.

[242] B. Franek and C. Gaspar, “SMI++ object-oriented framework used for automation and error recovery in the LHC experiments”, Proc. of CHEP 2009.

[243] D. Breton, D. Charlet, P. Robbe and I. Videau, “SPECS : a serial protocol for experiment control system in LHCb”, Proc. of the 10th Int. Conf. on Accelerator and Large Experimental Physics Control Systems, Geneva, Switzerland, 2005.

[244] F. Alessio *et al.*, “The LHCb readout system and real-time event management”, IEEE Trans. Nucl. Sci. **57** (2010) 663.

[245] F. Alessio *et al.*, “Timing and Fast Control and readout electronics Aspects of the LHCb Upgrade”, LHCb-PUB-2008-072.

[246] N. Neufeld, *et al.*, “The LHCb event-builder”, IEEE Trans. Nucl. Sci. to appear in 2011.

[247] G. Häfeli, *et al.*, “The LHCb DAQ interface board TELL1”, Nucl. Instrum. and Meth. A **560** (2006).

[248] G. Liu and N. Neufeld, Proc. of CHEP 2010.

[249] R. Antunes *et al.*, “LHCb computing technical design report”, CERN-LHCC-2005-019.

[250] S. Agostinelli *et al.*, Nucl. Instrum. and Meth. A **506** (2003) 250.